Boise State University
Dept. of Electrical and Computer Engineering
1910 University Dr.
Boise, ID 83725

Final Report

Reconfigurable Electronics and Non-Volatile Memory Research

October 14, 2011

Reporting Period: **July 15, 2007 – July 14, 2011**

Prepared for
Air Force Office of Scientific Research
875 N. Randolph St. Room 3112
Arlington VA 22203

Under Contract No.
FA9550-07-1-0546

Submitted by
Kristy A. Campbell, Ph.D., Principle Investigator
(208) 426-5968, email: kriscampbell@boisestate.edu

REPORT DOCUMENTATION PAGE

Form Approved
OMB No. 0704-0188

1. REPORT DATE *(DD-MM-YYYY)*	**2. REPORT TYPE**	**3. DATES COVERED** *(From - To)*
14-10-2011	Final	15-07-2007 – 14-7-2011

4. TITLE AND SUBTITLE
Reconfigurable Electronics and Non-Volatile Memory Research

5a. CONTRACT NUMBER

5b. GRANT NUMBER
FA9550-07-1-0546

5c. PROGRAM ELEMENT NUMBER

6. AUTHOR(S)
Dr. Kristy A. Campbell

5d. PROJECT NUMBER

5e. TASK NUMBER

5f. WORK UNIT NUMBER

7. PERFORMING ORGANIZATION NAME(S) AND ADDRESS(ES)

Department of Electrical and
Computer Engineering
Boise State University
1910 University Ave.
Boise, ID 83725

8. PERFORMING ORGANIZATION REPORT NUMBER

9. SPONSORING / MONITORING AGENCY NAME(S) AND ADDRESS(ES)
USAF, AFRL
AFOSR
875 N. Randolph St. Room 3112
Arlington VA 22203

10. SPONSOR/MONITOR'S ACRONYM(S)
AFOSR

11. SPONSOR/MONITOR'S REPORT NUMBER(S)
AFRL-OSR-VA-TR-2012-0624

12. DISTRIBUTION / AVAILABILITY STATEMENT
DISTRIBUTION STATEMENT A. Approved for public release; distribution is unlimited.

13. SUPPLEMENTARY NOTES

14. ABSTRACT
This is a final report for the DEPSCoR grant titled "Reconfigurable Electronics and Non-Volatile Memory Research." The primary purpose of this work was to investigate materials and fabricate devices that may display electronic properties useful for reconfigurable electronics applications and/or non-volatile memory. The grant enabled the development of microfabrication processes for exotic materials at Boise State University including material synthesis. Single-bit devices, 10 x 10 cross point arrays, 150 x 150 cross point arrays, and 24-pin DIP packaged parts were fabricated with over 10 different materials systems that showed promise for non-volatile memory and reconfigurable electronics. Materials explored included chalcogenides doped with transition metal ions and organics. Devices were discovered that displayed tunable capacitance. Additionally, devices displaying memristive behavior were discovered. This work resulted in two additional AFRL collaborations, an AFRL Educational Partnership Agreement, an SBIR Phase I and an STTR Phase I grant.

15. SUBJECT TERMS
Non-volatile memory, reconfigurable electronics, memristive device, neuromorphic computing

16. SECURITY CLASSIFICATION OF:			**17. LIMITATION OF ABSTRACT**	**18. NUMBER OF PAGES**	**19a. NAME OF RESPONSIBLE PERSON**
a. REPORT	**b. ABSTRACT**	**c. THIS PAGE**			Karen Henry
Unclassified	Unclassified	Unclassified		143	**19b. TELEPHONE NUMBER** *(include area code)* 208-426-1571

Objectives

The project objectives were:

(1) design, fabrication, and study of phase-change memory devices consisting of stacked chalcogenide (S-, Se- or Te-containing material) thin films;
(2) design, fabrication and study of new concepts in materials for reconfigurable electronics;
(3) design and fabrication of a test array structure for optical and electrical characterization of new materials concepts

Status of Effort Summary

Status of Objectives 1 and 2. Two-terminal devices were fabricated with several new memory concept materials synthesized in the lab, including ion-conducting organic and chalcogenide memories, and a novel electron spin-based zero-field splitting memory concept. Memristor-like devices were fabricated and tested, along with programmable resistance and capacitance devices with potential in reconfigurable electronics applications. Circuit designs were initiated to test reconfigurable electronics applications.

Status of Objective 3. An array structure for testing materials properties under confined conditions was designed, fabricated and tested. Some processed wafers were sent to collaborators for materials characterization and EXAFS measurements.

Significant Results

(1) Development of a memristor-like device based on chalcogenide materials. A collaboration between the AFRL Rome, NY group led by Dr. Robinson Pino was established.
(2) Development of chalcogenide devices that are programmable to discrete resistance values (phase-change and ion-conducting); measurement of the temperature dependence of these devices.
(3) Development of chalcogenide devices that have tunable capacitance values.
(4) Arrays of phase-change material for EXAFS measurements to determine the structure of the phase-change materials under various operating conditions have been fabricated and tested. EXAFS measurements were completed and determined that the chalcogenide material as fabricated in the arrays contained oxygen impurity.
(5) Synthesis of chalcogenide-transition metal ion materials for potential use in a new spintronics memory application.

Accomplishments/New Findings

Major accomplishments:

1. Developed microfabrication processes for all processes needed for this project, including bringing two new tools online and functional (ion-mill for etching and a thermal evaporator).
2. Synthesized materials for new memory investigations.

3. Fabricated devices with organic and chalcogenide based materials.
4. Developed testing platforms and electrically tested devices.
5. Developed a memristive-based device.
6. Developed a tunable capacitor device.
7. Filed two patent applications based on the developed devices.
8. Began an investigation into a new memory concept based on electron spin, referred to as the Zero-Field Splitting memory.
9. Established several government, industrial, and university collaborations on this research.
10. Part of this work led to an SBIR Phase I project and an STTR Phase I project.

In addition to the major accomplishments listed above, there are several notable points to mention:

1. Full nanodevice fabrication with exotic materials was developed. Prior to the initiation of this project, Boise State could not fully fabricate two-terminal electronic devices with exotic materials, such as chalcogenides. To complete device fabrication, outside sources, such as Micron Technology, were used for many of the steps. At the end of this DEPSCoR grant, the foremost accomplishment has been the establishment of a full fabrication line for the incorporation of chalcogenides and other exotic materials into nanodevices and many of the other accomplishments and collaborations stem from this success. The fabrication capabilities developed by this DEPSCoR project have already benefited other projects and other researchers within Boise State University by allowing them to use these developed processes and tools for their research.

2. Practical application learning opportunities for students performing semiconductor processing and photolithography layout design. Fabrication work over the course of the granting period afforded a large number of graduate and undergraduate students with the opportunity to learn how to approach the problems of semiconductor fabrication using tools available within the Idaho Microfabrication Laboratory, and to apply critical thinking and failure analysis to those problems. At the same time, functional devices were produced that furthered the research goals of the project, utilizing materials not commonly found in university fabrication courses. Many of the students involved in these projects have gone on to obtain jobs in the semiconductor industry, in major part because of the learning experiences gained during their time working with the group.

The hands-on experiences gained provided students with an understanding of the processing issues they may need to consider in research or job-related future tasks. There are many aspects of the learning process that are most effectively learned by solving problems or developing processing conditions for new materials. Table 1 summarizes semiconductor processes and materials investigated over the course of the granting period, that allowed students opportunities to encounter and solve processing problems.

Table 1. Semiconductor processes and materials processed at Boise State University.

Material →	Dielectrics		Chalcogenides						Metals							Other Materials			
Process ↓	Si_3N_4	SiO_2	Ge_2Se_3	GeTe	SnSe	SnTe	Doped Ge_xSe_{x-100}	$Ge_xSb_yTe_z$ alloys	W	Cr	Al	Ag	Ni	Cu	Ta	TiAlN	PCMO	ZnO	TCNQ*
Wet Etch	X	X							X	X	X								
Dry Etch -Oxford Plasmalab 100	X	X							X	X									
Dry Etch -Veeco ME 1001 Ion Beam Etcher	X	X	X	X	X	X	X	X	X	X	X	X	X	X	X	X	X	X	
Industries SE-600-RAP Thermal Evaporator			X	X	X	X	X				X	X		X					X
Deposition - CrC 150 Sputter Tool									X			X	X	X					
Deposition - AJA RF Magnetron Sputter Tool	X		X						X	X	X	X		X			X		
Planarization - Strasbaugh		X						X											
	*TCNQ = 7,7',8,8'-Tetracyanolquinodimethane, an organic compound used as an organic counterion to a variety of metals																		

The practical aspects of designing photolithography masks may not be taught in engineering device design courses or fabrication lab courses. During the granting period, several mask sets were designed by students, and updated or improved as problems and issues were encountered while using the masks (see Table 2). The iterative process of design, test and redesign was a valuable hands-on opportunity for students to learn from experience in a laboratory environment.

Table 2. Photolithography layout designs completed at Boise State University.

Mask Set Name, Date	Design Layers				
Single Device - Original, 2007	Met1	OVGL	ViaD	Met2	
Single Device - updated 2008	Level 1 BE	Level 2 Via	Level 3 TE	Level 4 Pad opening	Level 5 Via + Pad opening
Single Device - top electrode and Mask 5 via modification 2009			Mask 3 TE variable stub length		Mask 5 Via + Pad opening
NASA1-ZFS-SAW - 3 mask, 3 projects - 2008	Bottom Electrode	Via	Top Electrode		
Switching array - 2 mask 150 x 150 - 2008	Metal 1	Via			
Switching Array - modified - 3 mask 150 x 150 - 2009	Metal 1	Via 1	Metal 2		
Switching Array - modified - remake of Metal 1 and 2 due to frame shorting error - 2009	Metal 1		Metal 2		
Crosspoint Array 10 x 10 - 3 mask - 2010	M1 Bottom	Via	M2 Top		

3. Synthesis of exotic chalcogenide glasses for materials characterization and device fabrication. Work involving synthesis of chalcogenide glasses produced a wide range of stoichiometries of glass-forming chalcogenides from germanium and selenium precursors, in large enough quantities for both characterization and device fabrication. The unique capability of producing the desired exotic materials for fabrication of experimental memory devices allowed exploration of a wide variety of memory mechanisms, including phase change and ion conduction. Glasses doped with a wide range of transition and main group metals were also made and studied for memory applications.

Glass synthesis also provided valuable learning opportunities for students, to explore the techniques required for successful preparation of samples for synthesis, and to learn operation of the rocking furnace as well as the characterization tools, including electron paramagnetic resonance (EPR) spectrometer, Raman confocal microscope, Differential Scanning Calorimeter and the broadband spectroscopy thin film characterization tool, the n&k 1280.

Detailed discussions of the major areas of research are provided in Appendix A. Drafts of papers submitted or in preparation for publication are provided in Appendix B. This includes efforts of student that have prepared thesis and/or dissertations based resulting from this work.

Personnel Supported and/or Associated with the Research Effort

Faculty at Boise State University:

1. Dr. Kristy Campbell, Associate Professor, Electrical and Computer Engineering
2. Dr. Jeffrey Peloquin, Assistant Professor, Chemistry and Biochemistry (Deceased)

Associated People:

1. Dr. Art Edwards, Senior Research Physicist, AFRL Space Vehicles Directorate
2. Dr. P. Craig Taylor, Professor of Physics, Colorado School of Mines, Assoc. Director, Colorado Energy Research Institute
3. Dr. Michael Paesler, Professor of Physics, North Carolina State University
4. Dr. Rene Rodriguez, Professor of Chemistry, Idaho State University

Post-Docs:

1. Dr. Pulok Pattanayak, Electrical and Computer Engineering, Boise State University
2. Dr. Jennifer Regner, Electrical and Computer Engineering, Boise State University

Graduate Students:

1. Morgan Davis, Materials Science and Engineering, Boise State University (**graduated MS Materials Science and Engineering, 2010**)
2. Jared Barclay, Electrical and Computer Engineering, Boise State University (**graduated MS EE, 2009, currently a Ph.D. student**)
3. Beth Cook, Electrical and Computer Engineering, Boise State University (**graduated MS EE 2011**)
4. Antonio Oblea, Electrical and Computer Engineering, Boise State University (**graduated MEngr EE 2011**)
5. Archana Devasia, Microelectronics Engineering, Rochester Institute of Technology (**graduated Ph.D., 2010**)

Undergraduates:

1. Shan Lyons, Chemistry and Biochemistry, Boise State University
2. Cliff Cszimar, Chemistry and Biochemistry, Boise State University
3. Jamie Minick, Chemistry and Biochemistry, Boise State University
4. Jason Durand, Electrical and Computer Engineering, Boise State University
5. Jayme Christensen, Electrical and Computer Engineering, Boise State University
6. Robert Scott, Electrical and Computer Engineering, Boise State University
7. Kolton Drake, Electrical and Computer Engineering, Boise State University

Publications

Submitted Manuscripts and Conference Proceedings:

1. Pattanayak,P.; Campbell, K.A. Raman studies of bulk Ge_xSe_{100-x} and metal doped $Ge_{40}Se_{60}$ chalcogenide glasses. *Submitted to the Journal of Non-Crystalline Solids (September 2011)*.
2. Pattanayak,P.; Campbell, K.A. EPR studies on certain transition metal doped chalcogenide glasses. Manuscript in preparation.
3. Davis, M.G.; Pattanayak,P.; Campbell, K.A. Effect of metal doping on structural and thermal properties of Ge-Se glasses. Manuscript in preparation.
4. Campbell, K.A.; Cook, B.R. Ge_2Se_3/SnSe-Based Ion-Conducting Robust Memristive, Non-Volatile Memory Device. *Submitted to IEEE Electron Device Letters, August 2011*.
5. Campbell, K.A.; Cook, B.R. Electrical switching properties of Ge_2Se_3/metal-Se/Ag-based ion-conducting memristive devices. Manuscript in preparation.
6. Edwards, Arthur H.; Taylor, P. C; Kristy A. Campbell; Pineda, Andrew C. First-principles study of 75As NQR in arsenic-chalcogenide compounds. Journal of Physics: Condensed Matter (2011), 23(5), 055502/1-055502/11.
7. Devasia, Archana; Kurinec, Santosh; Campbell, Kristy A.; Raoux, Simone Influence of Sn Migration on phase transition in GeTe and Ge2Se3 thin films, Applied Physics Letters (2010), 96(14), 141908/1-141908/3.
8. Jarvis, K.; Carpenter, R. W.; Davis, M.; Campbell, K. A. An investigation of amorphous Ge2Se3 structure for phase change memory devices using fluctuation electron microscopy. Journal of Applied Physics (2009), 106(8), 083507/1-083507/5.
9. Oblea, A.; Timilsina, A.; Moore, D.; Campbell, K.A. Silver chalcogenide memristor devices. IEEE World Conference on Computational Intelligence. July 18-23, 2010, Barcelona, Spain.
10. Pino, R.; Bohl, J.W.; McDonald, N.; Wysocki, B.; Rozwood, P.; Campbell, K.A.; Oblea, A.; Timilsina, A.Compact method for modeling and simulation of memristor devices Ion conduction chalcogenide-based memristor devices. NanoArch Conference, July 2010.
11. Devasia, A.; Bai, F.; Davis, M.G.; Campbell, K.A.; Kurinec, S. "Analyzing Residual Stress in Bilayer Phase Change Memory Films," *Thin Solid Films*, 2009, doi:10.1016/j.tsf.2009.04.017
12. "A New Approach to the Design, Fabrication, and Testing of Chalcogenide-Based Multi-State Phase-Change Nonvolatile Memory," Ande, H.K.; Busa, P.; Balasubramanian, M.; Campbell, K.A.; Baker, R.J., the 51st IEEE International Midwest Symposium on Circuits and Systems, August 10-13, 2008, Knoxville, TN, USA.
13. "Investigation of phase transition in stacked Ge-Chalcogenide/Sn-Chalcogenide phase-change memory films," Bai, F.; Gupta, S.K.; Devasia, A.-M.; Kurinec, S.; Campbell,

K.A. *Proceedings of the Materials Research Society Fall 2007 Meeting*, Boston, MA, **HH11.70**, November 26-30 (2007).

Interactions/Transitions

Technology assists, transitions, and transfers.

Government Transition:

Results from the reconfigurable electronics based devices have resulted in a grant with the Space Vehicles Directorate, Air Force Research Laboratory (FA9453-08-2-0252), and a grant (FA8751-10-P-0064) **with the Emerging Computing Technology Branch AFRL/RITC. In addition, an Educational Partnership Agreement was established with AFRL/RITC.**

Industrial Transition:

Results from memory device development led to the discovery of a potential continuously variable resistor technology. This idea was submitted as an SBIR proposal (under AF073-100) and funded as a Phase I with Nu-Trek, Inc. as the primary and Boise State University as the collaborating partner.

Results from the memristive-device work resulted in an STTR with Bio-Inspired Technologies (under FA8750-11-C-0112), a Boise, ID start-up company established by researchers that propose to use this technology in neuromorphic computing.

New discoveries, inventions, or patent disclosures.

During electrical testing of new memory devices, four invention disclosures were filed. One of these has been filed at the U.S. Patent Office and the other three are currently in preparation. These inventions are listed below along with a brief description of the invention:

1. ***Programmable Capacitor.*** A metal-chalcogenide device that exhibits capacitance in the range of 20 fF to 500 pF, tunable by application of a short (ns) low amplitude (<1 V) pulse. The capacitance is selected by the pulse amplitude. US patent application filed in 2010.
2. ***Programmable Capacitor Electronic Memory.*** The metal-chalcogenide programmable capacitor used as either a semi-volatile memory or non-volatile memory. Disclosed to Boise State University August 2009.
3. ***Electrostatic Discharge Integrated Circuit Device.*** An integrated circuit device that can protect a circuit from electrostatic discharge (ESD) on chip was discovered. This device is based on a metal-doped chalcogenide which acts as an ion-conductor and changes resistance from GOhms to kOhms (and is programmably reversible) under certain bias conditions. Disclosure filed at Boise State University.
4. ***Structure and Method to Achieve Multiple Resistance States in a Resistance Variable Material***, disclosed by K. Campbell.
5. ***Detector for terahertz frequency signals***, disclosed by K. Campbell.
6. ***Wideband Sensor***, inventor, K. Campbell, patent application filed July 2009.

Change in AFOSR program manager, if any: Gernot Pomrenke

Appendix A. Research Details and Data

1. Materials Samples Prepared and Characterized

Table 1. List of samples prepared and characterized in tabular form.

Glass Composition				Raman	MDSC	EPR
	Metal (M)	**x**	**y**			
Ge_xSe_{100-x}		10, 15, 20, 23, 25, 30, 33.33, 35, 40 & 45		all	all	$Ge_{40}Se_{60}$
$(Ge_{40}Se_{60})_{100-y}M_y$	V		y = 0.1, 1 & 3	all	all	
	Cr		y = 0.01, 0.1, 1 & 3	all	all	y = 0.1
	Mn		y = 0.01, 0.1, 1 & 3	all	all	y = 0.1
	Fe		y = 0.1	all		y = 0.1
	Co		y = 0.01, 0.1, 1 & 3	all	all	y = 0.1
	Ni		y = 0.01, 0.1 & 1	all		
	Cu		y = 0.01, 0.1, 1 & 3	all	all	
	Zn		y = 0.01, 0.1, 1 & 3	all	all	
	Ag		y = 0.01, 1 & 3	all	all	
	W		y = 0.1 & 3	all	all	
$(Ge_xSe_{100-x})_{100-y}Mn_y$		20, 23, 25, 30, 33.33, 35	0.01, 0.1, 1 & 3	all		

Sample preparation method:

Bulk chalcogenide glasses were prepared by the conventional melt quenching technique (see experimental set up in Figures 1 and 2). Proper quantities of high purity elements (≥ 99.99+%; Alfa-Aesar) were sealed into evacuated quartz tubes. The sealed tubes were then placed into a rocking tube furnace and heated to 1000 ^oC with a heating rate of 30 ^oC/min, at which point rocking was initiated. The tubes were left at this condition for approximately 6 hours, after which the tubes were rapidly quenched in an ice/water bath to get the desired glasses. Sources of metal dopants were elemental metals and as well as, metal-Se compounds, and there was no evident difference in the measured Raman and Electron Paramagnetic Resonance (EPR) spectra.

Fig. 1. Quartz ampoule set-up sealing set up.

Fig. 2. View of rocking furnace in hood next to quartz ampoule sealing equipment.

Raman spectroscopy, method and results

(a) Method:

The Raman spectroscopy investigations were performed with a backscattering configuration using a Renishaw Invia Raman Microscope with a resolution of 1 cm^{-1}. The scattered light was dispersed by a spectrometer fitted with a 1200 lines/mm grating. The excitation wavelength was 785 nm produced by a single-mode wavelength stabilized laser diode

(Innovative Photonic Solutions). In order to avoid local laser damage on glass samples, the beam power was kept to approximately 0.5 mW the output of the laser with a 10 s total exposure time. The Raman spectra were measured three times on different points for each sample with a 20x objective lens (Leica, N.A. = 0.40) for all room temperature measurements. The beam spot size was approximately 10 µm at this configuration. The spectra of the three measurements for each sample were identical, as expected due to the homogeneity of the glasses.

Fig. 3. The Renishaw InVia Raman Confocal Microscope.

(b) Results

(i) Ge_xSe_{100-x} glasses:

Raman spectra of Ge_xSe_{100-x} are shown in fig. 4 below. Peaks deducted from the spectra are listed in the table 2. Peaks are assigned as per references 1-4. It is clear from the graph that the strength of the peaks related to Se-Se bonds (250 cm^{-1}) reduces very fast with increase in Ge. Peaks correspond to Ge-Se bonds (193 and 210 cm^{-1}) gain strength. A peak (179 cm^{-1}) which relates to Ge-Ge bonds, appears for glasses with Ge $\geq$ 33.33.

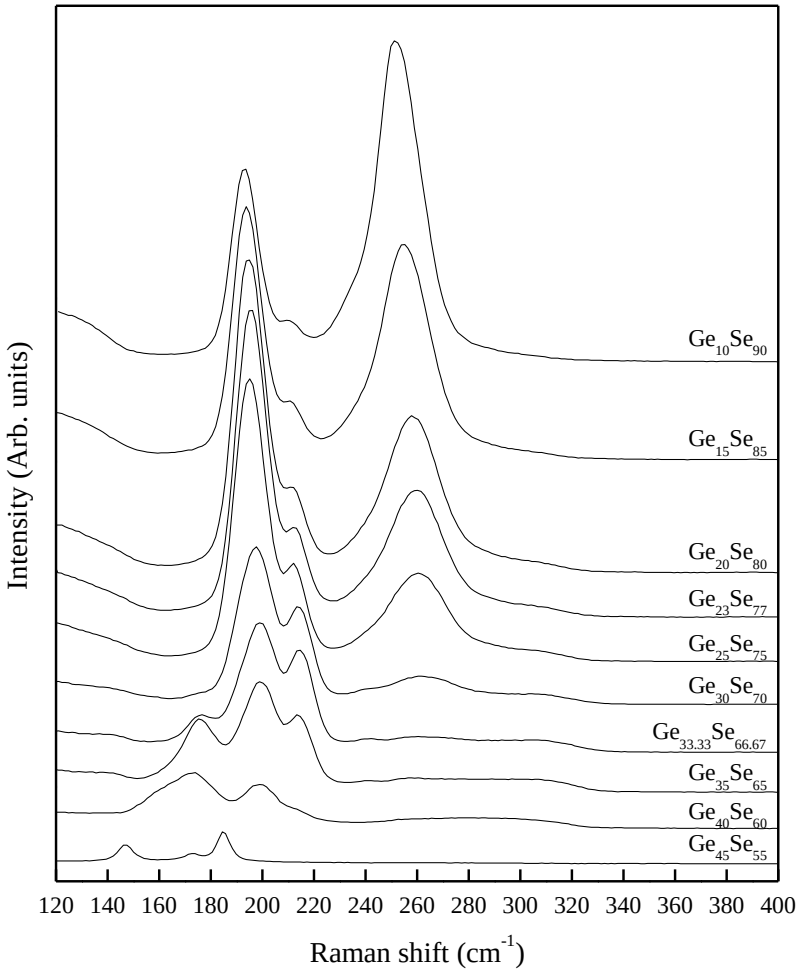

Fig. 4. Raman spectra of Ge_xSe_{100-x} glasses.

Table 2. Raman peaks seen Ge_xSe_{100-x} glasses; peaks are attributed to (a) - F_2 antisymmetric vibration modes of $GeSe_{4/2}$ based structural units, (b) - symmetric stretching vibrations of Se-Se bonds, (c) - Se_8 rings, (d) - Se rings fragments or Se_n chains, (e) - A_1^C breathing vibrations of edge-shared $Ge_2Se_{8/2}$ bi-tetrahedra, (f) - A_1 vibration or the stretching mode of the corner-sharing $GeSe_{4/2}$ tetrahedra, (g) - vibrating of $Se_3Ge–GeSe_3$ units or ethane-like Ge_2Se_6 units, (h) unassigned, and (i) - unresolved lattice modes or the vibrations of structural units similar to the compound GeSe with a Ge-to-Se ratio of approximately 1.

Sample	Raman Peaks (cm^{-1})
$Ge_{10}Se_{90}$	193 (f), 210 (e), 236 (d), 252 (c), 262 (b), 292 (a)
$Ge_{15}Se_{85}$	193, 210, 239, 255, 269, 291
$Ge_{20}Se_{80}$	194, 211, 236, 256, 271, 291
$Ge_{23}Se_{77}$	194, 211, 234, 257, 284, 308
$Ge_{25}Se_{75}$	195, 212, 237, 260, 288, 310
$Ge_{30}Se_{70}$	136 (i), 179 (g), 197, 214, 243, 263, 280, 305
$Ge_{33.33}Se_{66.67}$	134, 175, 199, 215, 240, 263, 282, 308
$Ge_{35}Se_{65}$	133, 175, 198, 215, 236, 258, 281, 307
$Ge_{40}Se_{60}$	132, 160 (h), 175, 198, 210, 237, 257, 277, 303

(ii) $Ge_{40}Se_{60-y}M_y$

Spectra of metal doped $Ge_{40}Se_{60}$ glasses are shown in Fig. 5-13. Other than 3 % V, Co and W doped $Ge_{40}Se_{60}$ samples, all metal doped samples are very similar in nature. Intensity of the most of the sample reduces with dopant concentration. This is due to the reduction in Ge-Ge and Ge-Se bonds as the metal is incorporated into the glass. The metal dopant atoms will bond with the Se atoms [5] reducing the number of Se atoms that are available to make a bond with Ge effectively decreasing the intensity of those peaks.

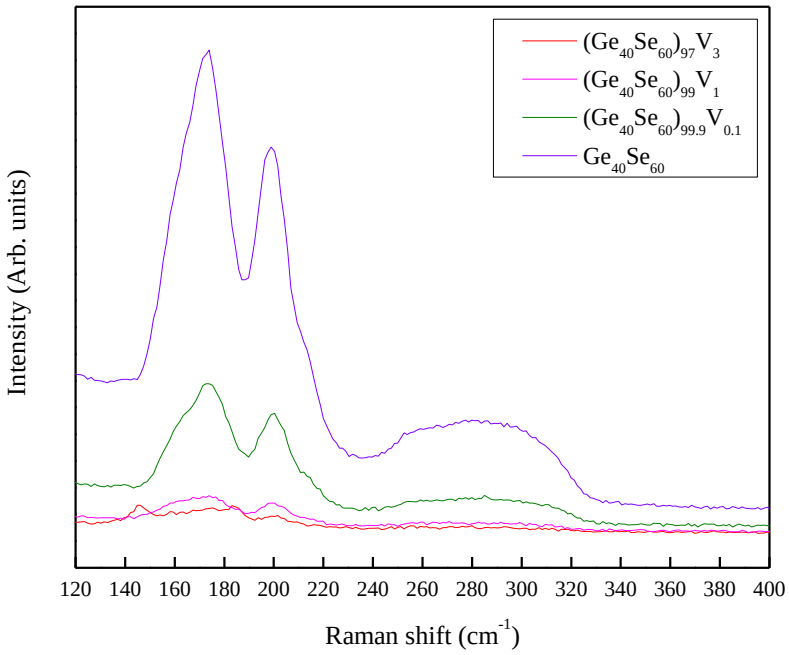

Fig. 5. Raman spectra of $(Ge_{40}Se_{60})_{100-x}V_x$ glasses.

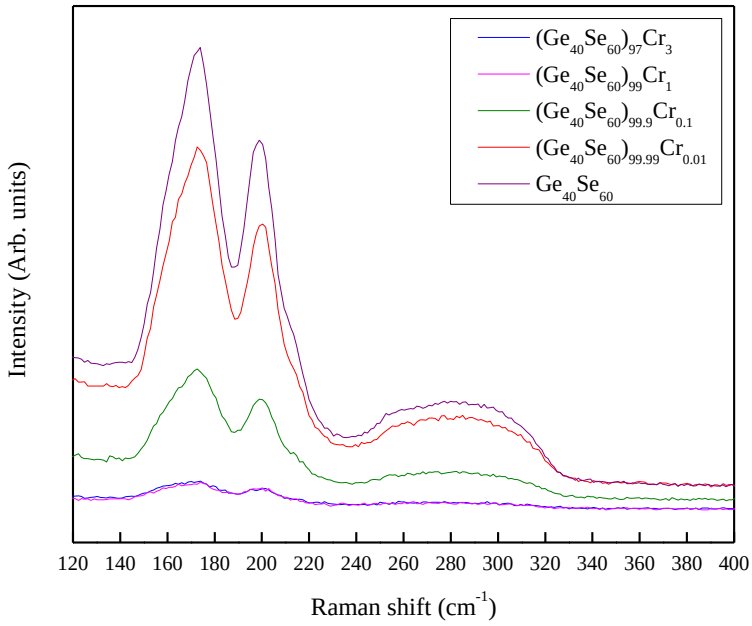

Fig. 6. Raman spectra of $(Ge_{40}Se_{60})_{100-x}Cr_x$ glasses.

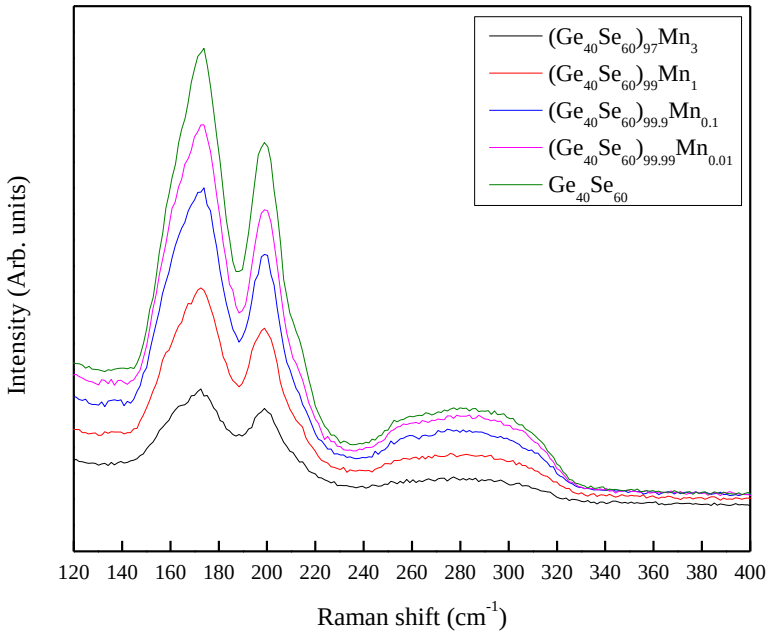

Fig. 7. Raman spectra of $(Ge_{40}Se_{60})_{100-x}Mn_x$ glasses.

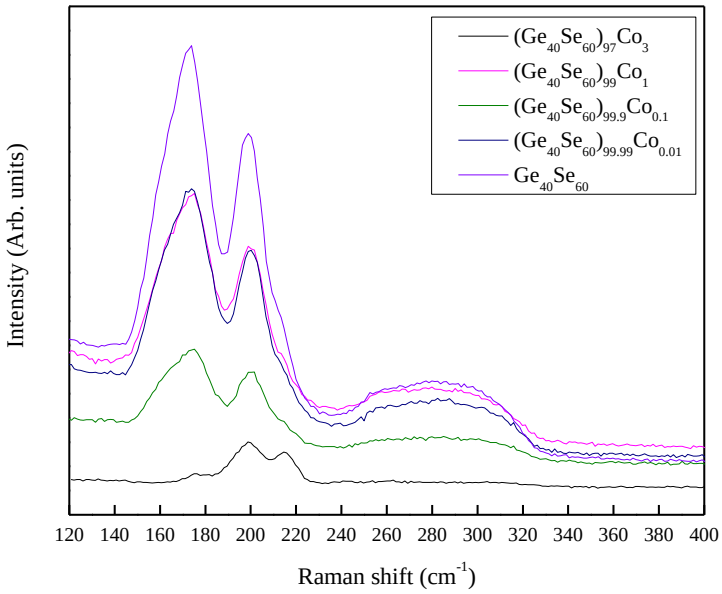

Fig. 8. Raman spectra of $(Ge_{40}Se_{60})_{100-x}Co_x$ glasses

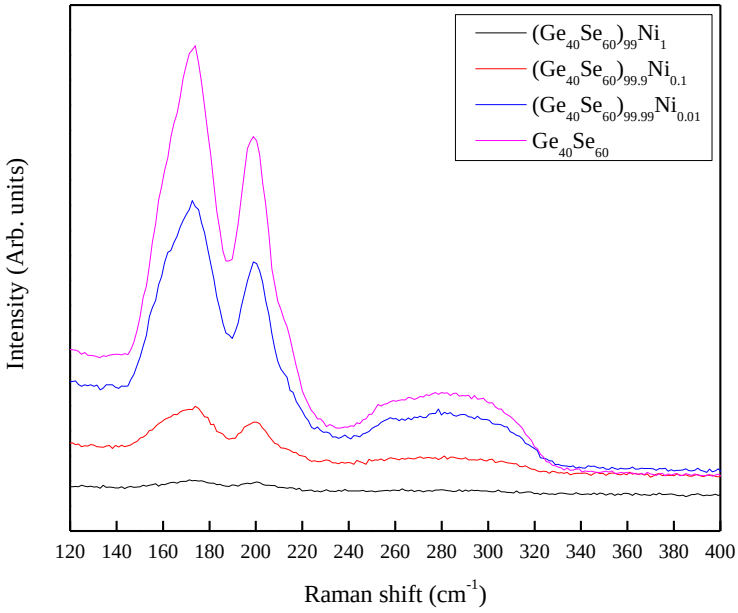

Fig. 9. Raman spectra of $(Ge_{40}Se_{60})_{100-x}Ni_x$ glasses

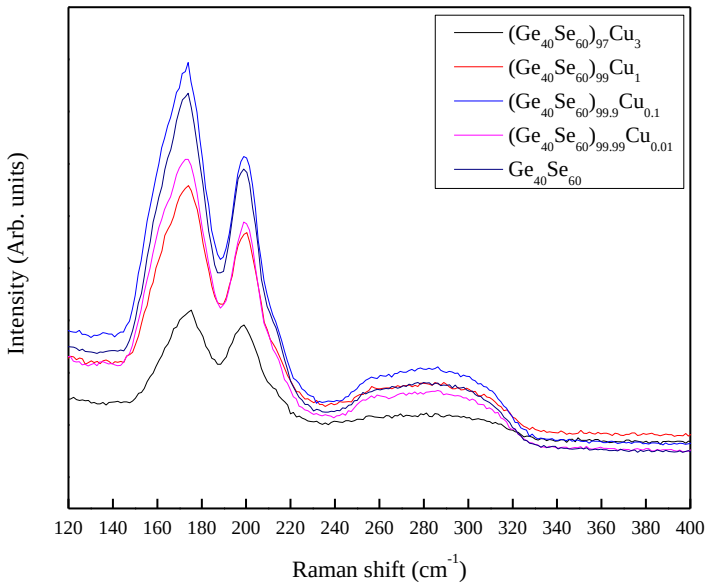

Fig. 10. Raman spectra of $(Ge_{40}Se_{60})_{100-x}Cu_x$ glasses

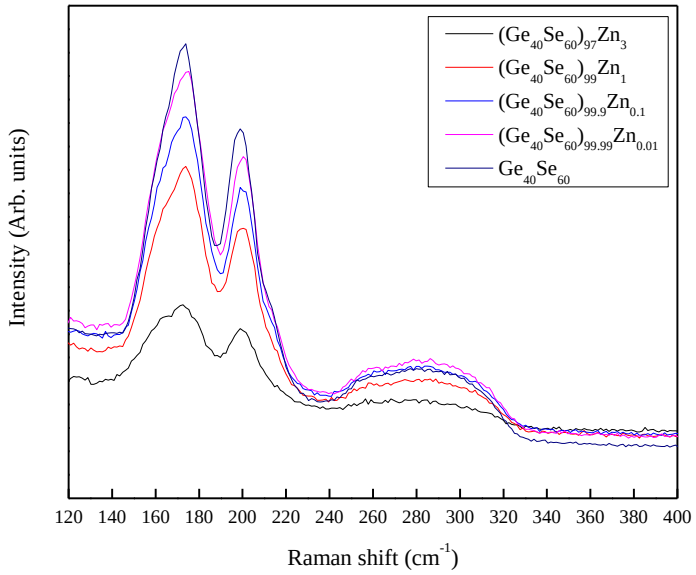

Fig. 11. Raman spectra of $(Ge_{40}Se_{60})_{100-x}Zn_x$ glasses

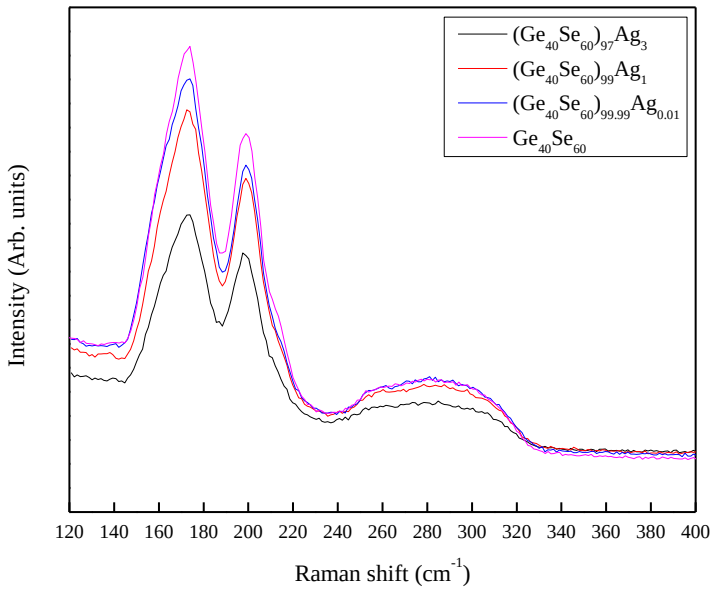

Fig. 12. Raman spectra of $(Ge_{40}Se_{60})_{100-x}Ag_x$ glasses

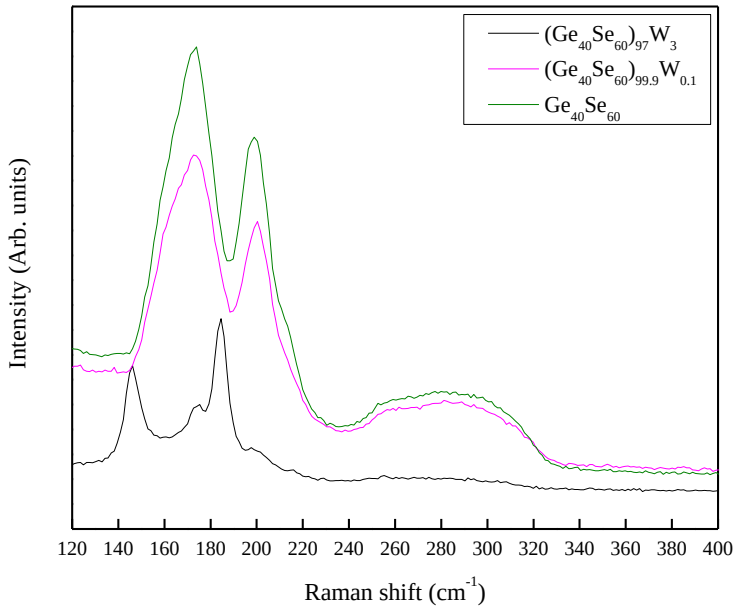

Fig. 13. Raman spectra of $(Ge_{40}Se_{60})_{100-x}W_x$ glasses

(iii) $Ge_xSe_{100-y}Mn_y$

Raman spectra for $Ge_xSe_{100-y}Mn_y$ are shown in Fig. 13-19. Red-Shift in peak due to Se-Se bonds (250 cm^{-1}) is clearly visible with increase in Mn content for $Ge_{20}se_{80}$ and $Ge_{23}Se_{77}$ glasses. On the other hand, Raman peaks in $Ge_{40}Se_{60}$ glass do not show significant shift with the variation in dopant concentration.

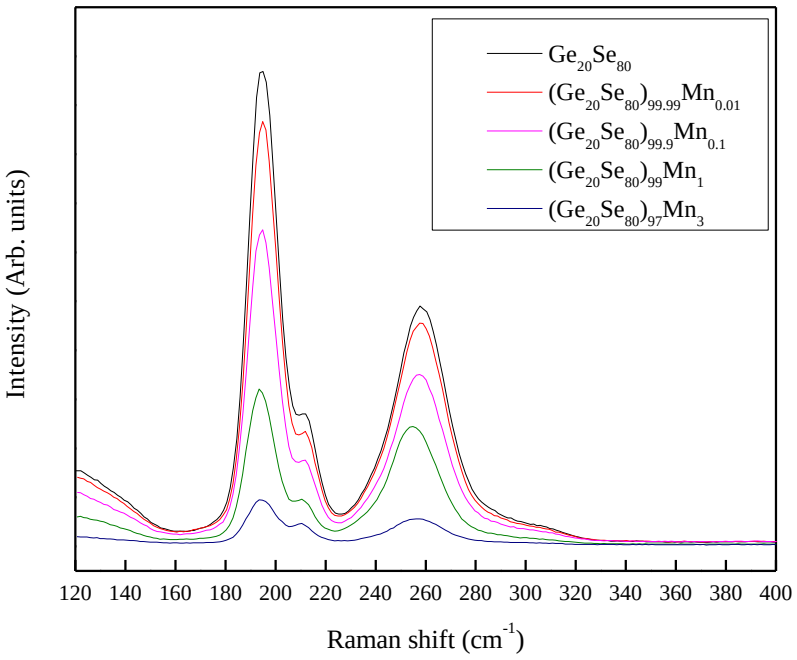

Fig. 13. Raman spectra of $(Ge_{20}Se_{80})_{100-}Mn_x$ glasses

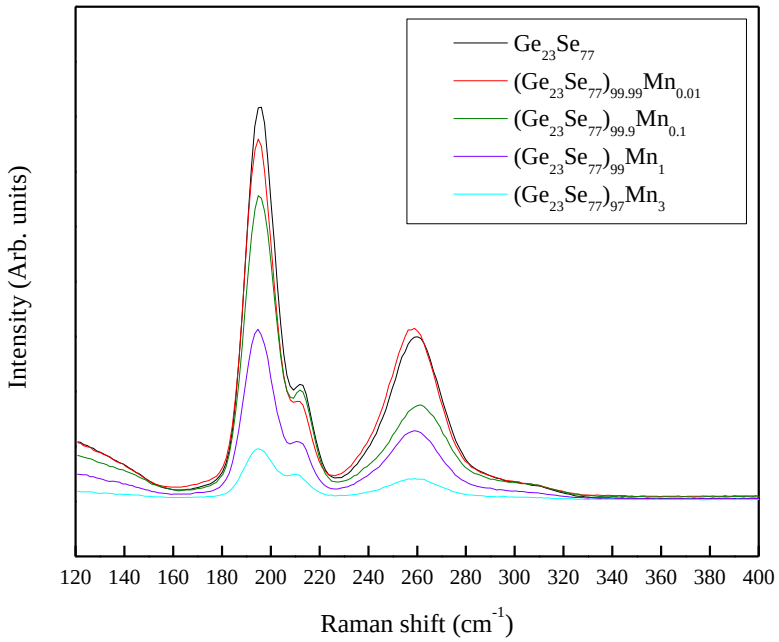

Fig. 14. Raman spectra of $(Ge_{23}Se_{77})_{100-}Mn_x$ glasses

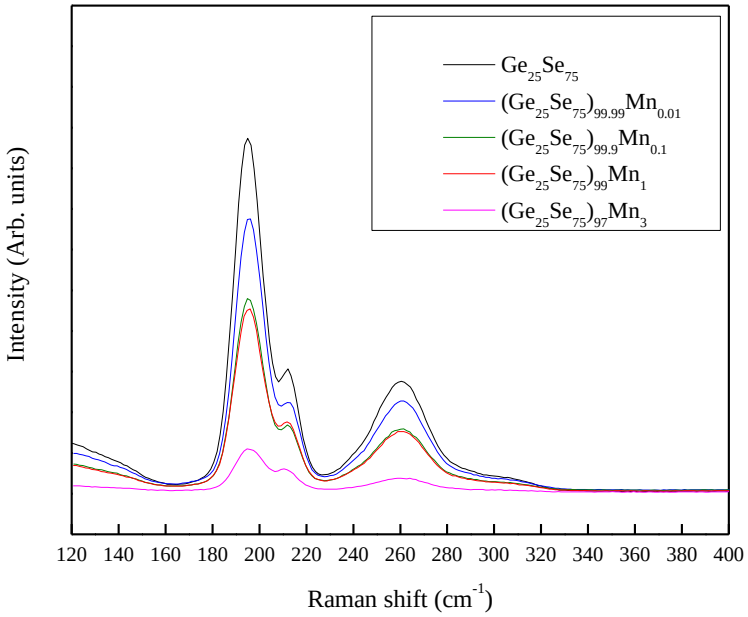

Fig. 15. Raman spectra of $(Ge_{25}Se_{75})_{100-}Mn_x$ glasses

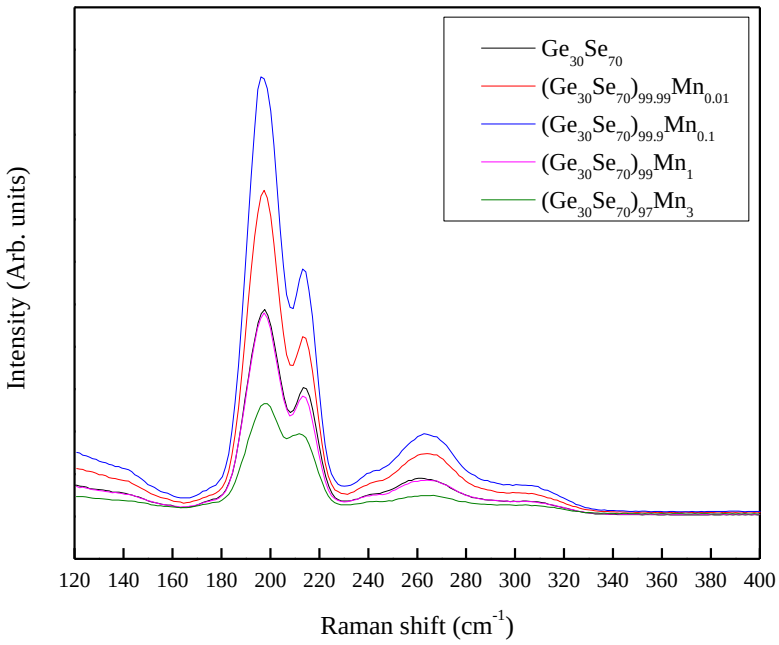

Fig. 16. Raman spectra of $(Ge_{30}Se_{70})_{100-}Mn_x$ glasses

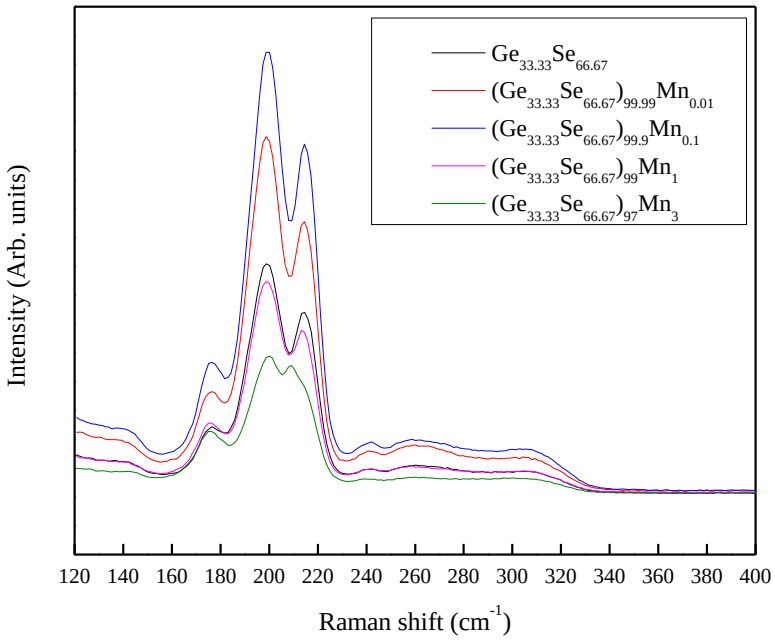

Fig. 17. Raman spectra of $(Ge_{33.33}Se_{66.67})_{100-}Mn_x$ glasses

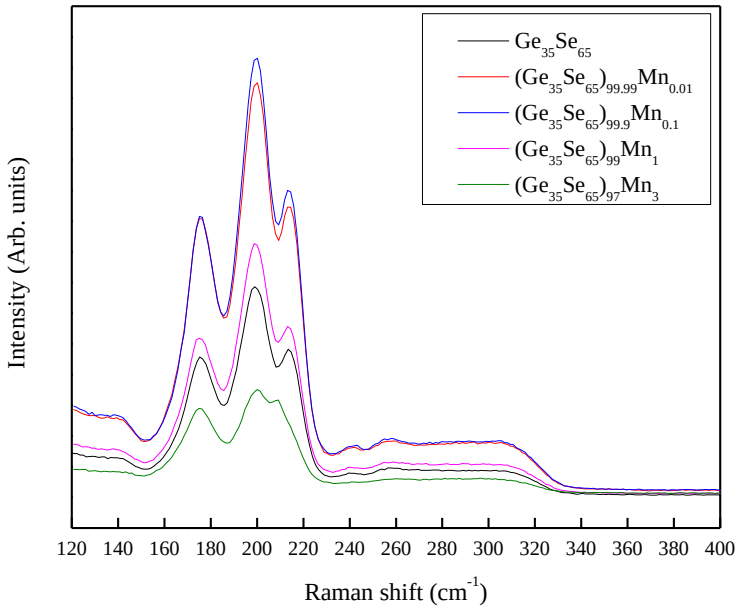

Fig. 18. Raman spectra of $(Ge_{35}Se_{65})_{100-}Mn_x$ glasses

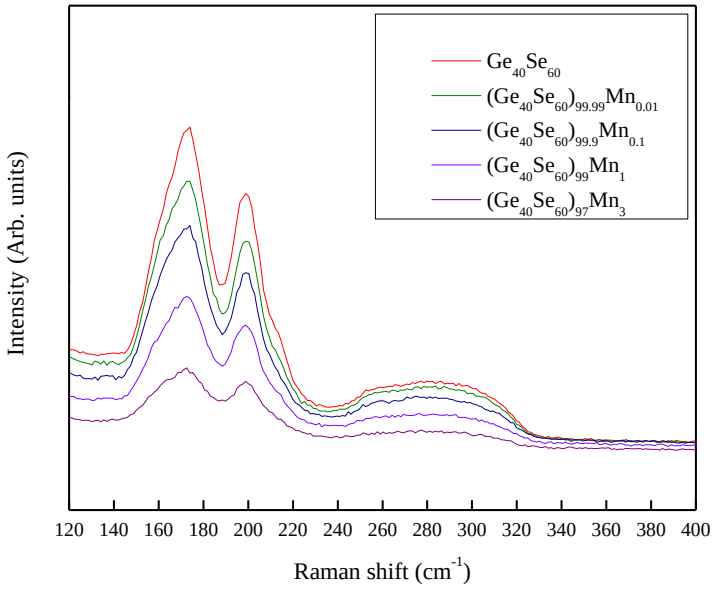

Fig. 19. Raman spectra of $(Ge_{40}Se_{60})_{100-}Mn_x$ glasses

Modulated Differential Scanning Calorimetry (MDSC), method and results

(a) Method:

Thermal analysis is carried out by MDSC (model Q2000, TA Instruments). MDSC scans of all samples are taken at a 3 °C min^{-1} scan rate and 1 °C min^{-1} modulation rate. Glass transition temperatures are deduced from the inflection point of the reversing heat flow curves and crystallization peaks from the nonreversing curves; typical error in the measurements is within ±2 °C.

Fig. 20. The TA Instruments Q2000 differential scanning calorimeter.

(b) Results:

(i) Ge_xSe_{100-x}

MDSC curves for $Ge_{23}Se_{77}$ and $Ge_{40}Se_{60}$ are shown in Fig. 21 and 22 below as examples. The deducted glass transition temperatures, T_gs are plotted in Fig. 23 against the composition along with related co-ordination number <r>. The quantity <r> is formally defined as $\frac{\sum n_i r_i}{N}$, where n_i represents the number of atoms having a coordination r_i and $N = \sum n_i$ gives the total number of atoms in a network. T_g reaches at the maximum for $Ge_{33.33}Se_{66.67}$ and starts to reduce for the composition Ge > 33.33. The observation can be explained through the nano-phase separation effect due to stress in these rigid glasses [6]. Crystallization temperature, T_c at 450 ^{0}C also starts to appear from the composition, $Ge_{30}Se_{70}$ which might an indication of same nano-phase separation phenomenon in these glasses.

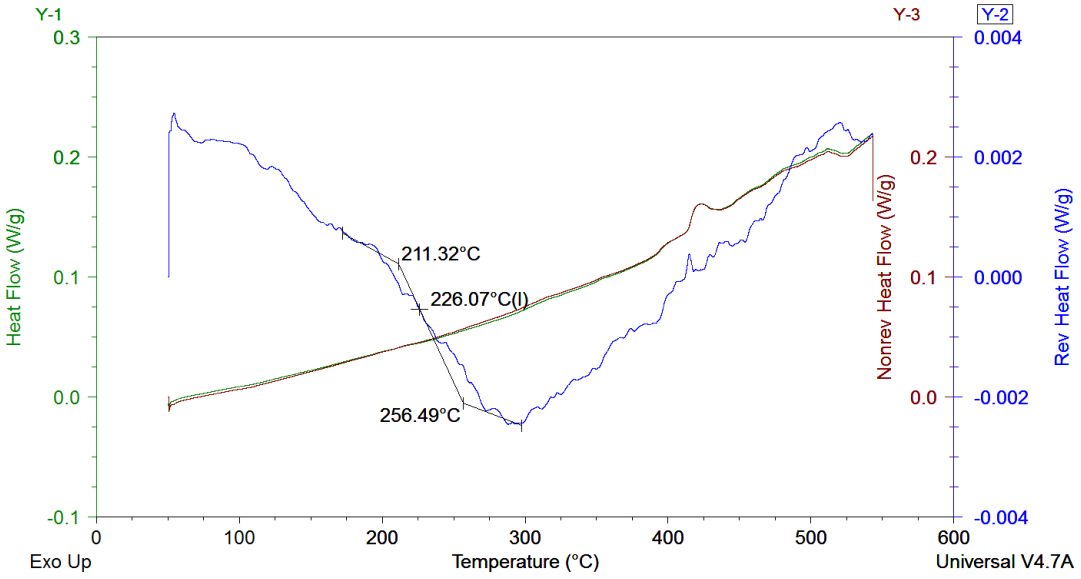

Fig. 21. Total, reversible and nonreversible curves for $Ge_{23}Se_{77}$ glass. T_g is calculated from reversible curve whereas T_c is calculated from nonreversible curve.

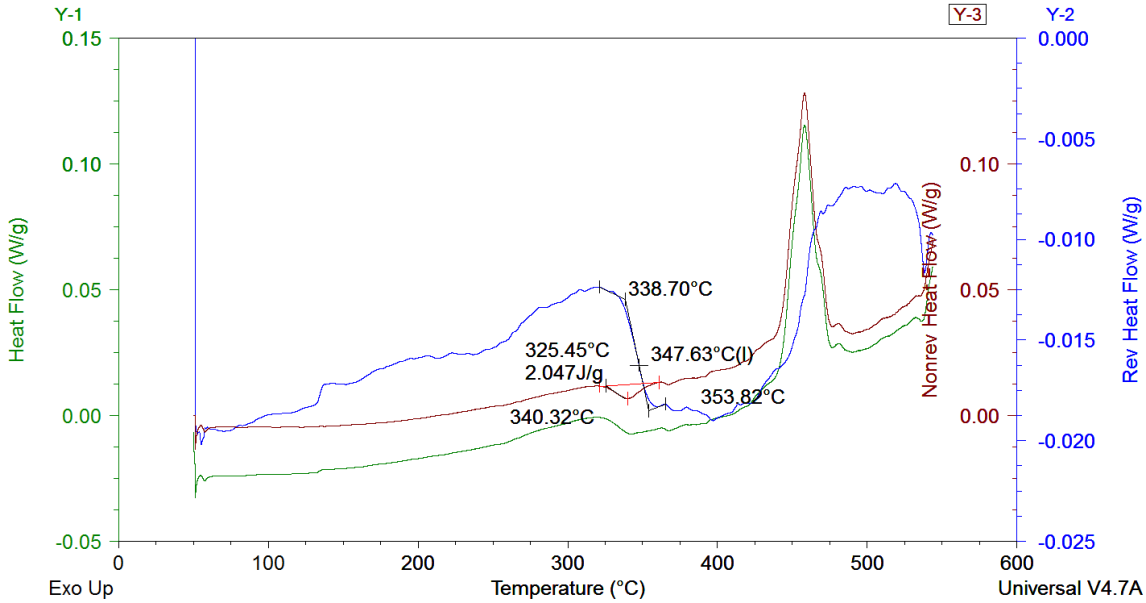

Fig. 22. Total, reversible and nonreversible curves for $Ge_{40}Se_{60}$ glass. T_g is calculated from reversible curve whereas T_c is calculated from nonreversible curve. Change of heat enthalpy at T_g can also be calculated from nonreversible curve.

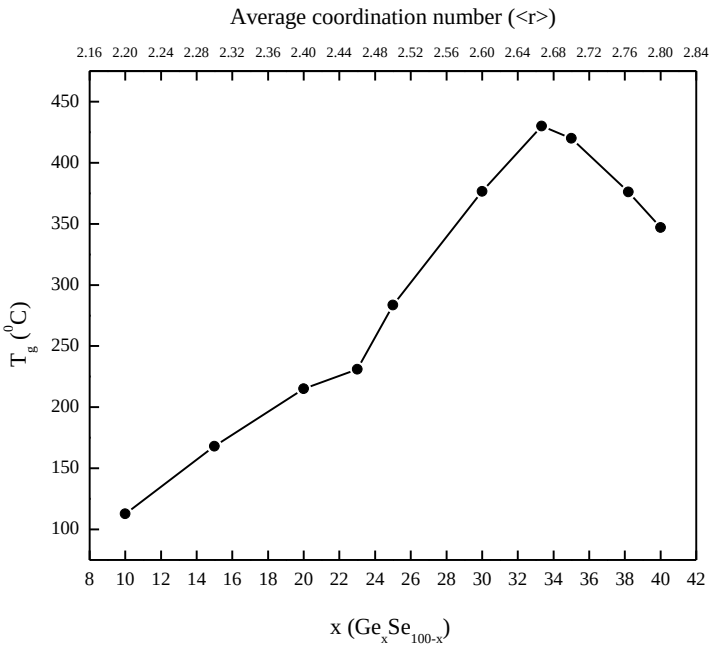

Fig. 23. Compositional variation of T_g in Ge-Se glasses.

(ii) $(Ge_{40}Se_{60})_{100-y}M_y$:

Metal doped samples with two or more crystallization temperatures may have potential to use as multi-states phase change memory [7].

$(Ge_{40}Se_{60})_{97}V_3$

V-doped samples show mainly one T_g and T_c. 3 % V doped sample shows a hint of second T_c approximately at 510 ^oC.

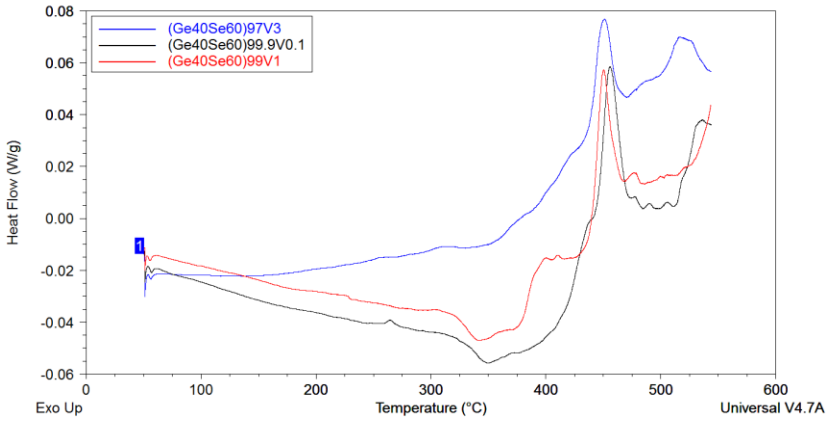

Fig. 24. Total heat flow curves of $(Ge_{40}Se_{60})_{100x}V_x$ glass.

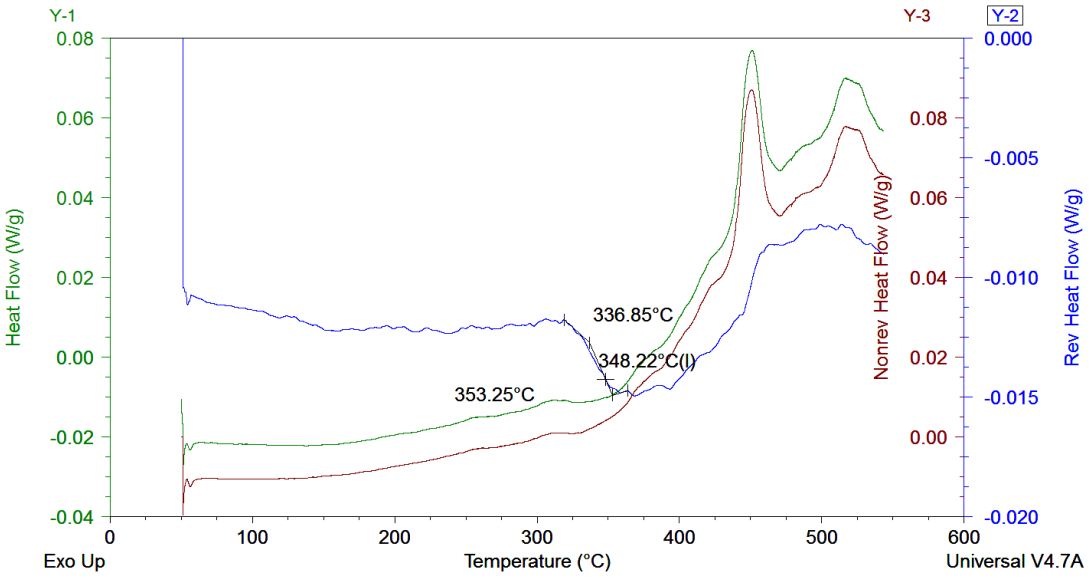

Fig.25. Total, reversible and nonreversible curves for $(Ge_{40}Se_{60})_{97}V_3$ glass.

$(Ge_{40}Se_{60})_{97}Cr_3$

All Cr doped samples show one T_g and at least two T_cs. 3 % doped Cr sample shows one minor T_c approximately at 510 ^oC.

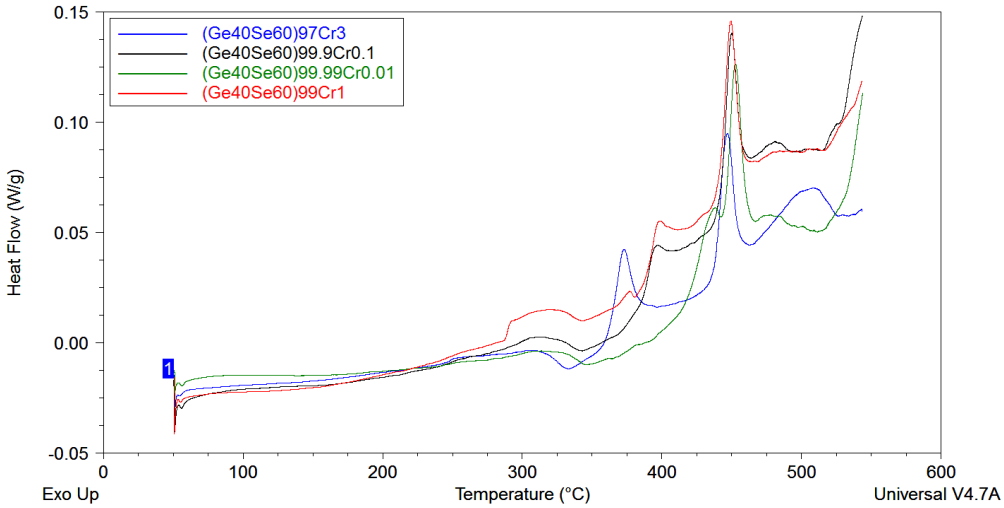

Fig. 26. Total heat flow curves of $(Ge_{40}Se_{60})_{100x}Cr_x$ glass.

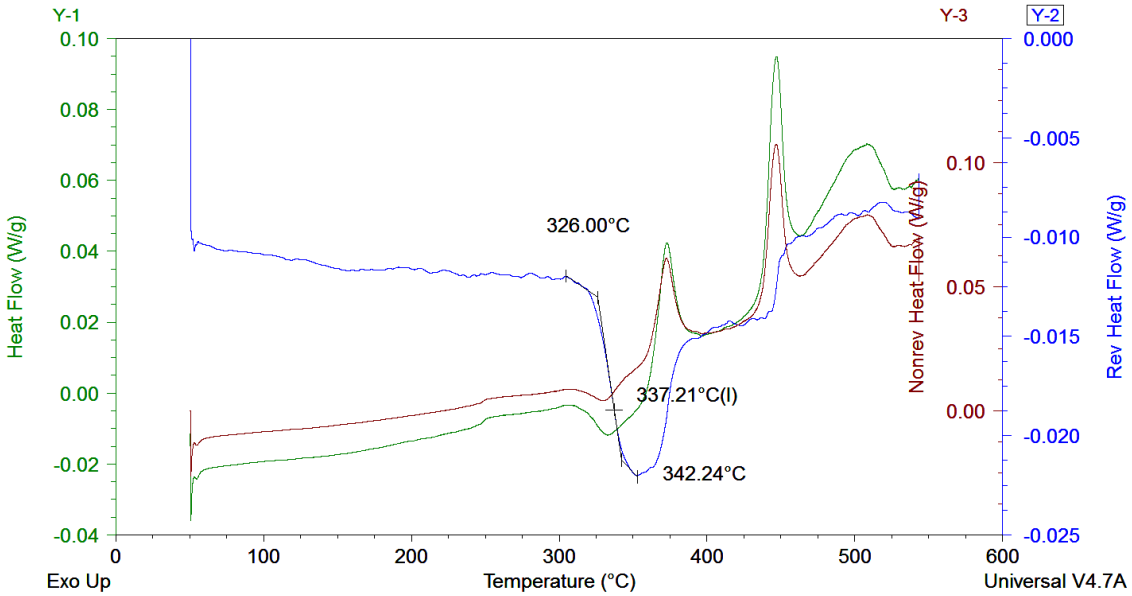

Fig. 27. Total, reversible and nonreversible curves for $(Ge_{40}Se_{60})_{97}Cr_3$ glass.

$(Ge_{40}Se_{60})_{97}Mn_3$

All Mn doped samples appear to have one T_g. $Mn_{0.1}$ and Mn_3 doped samples show two T_cs whereas Mn_1 doped sample has surprisingly one T_c.

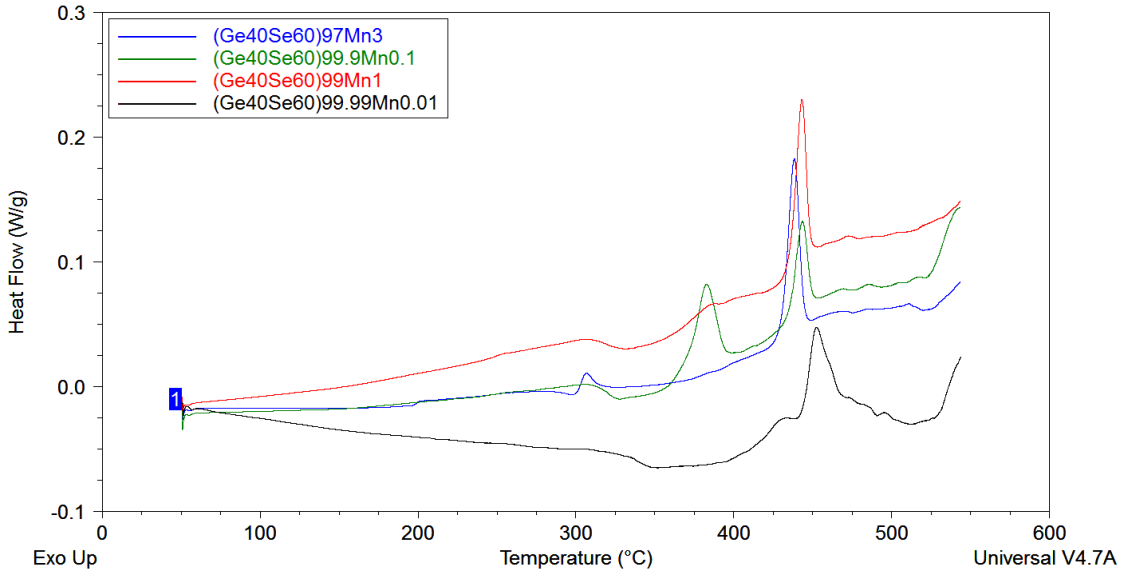

Fig. 28. Total heat flow curves of $(Ge_{40}Se_{60})_{100x}Mn_x$ glass.

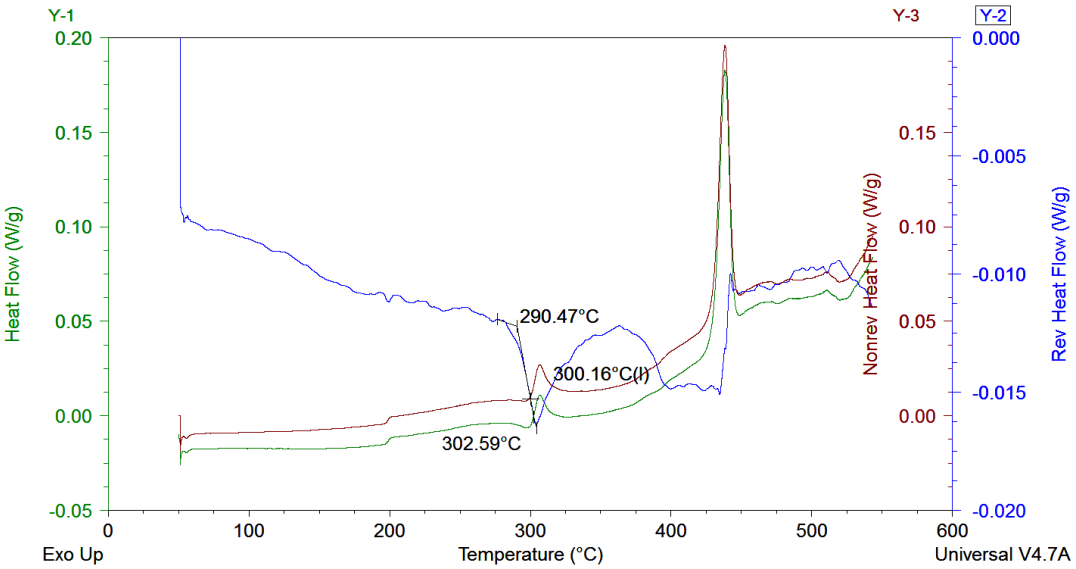

Fig. 29. Total, reversible and nonreversible curves for $(Ge_{40}Se_{60})_{97}Mn_3$ glass.

$(Ge_{40}Se_{60})_{97}Co_3$

All Co doped sample show one T_g and one major T_c peaks.

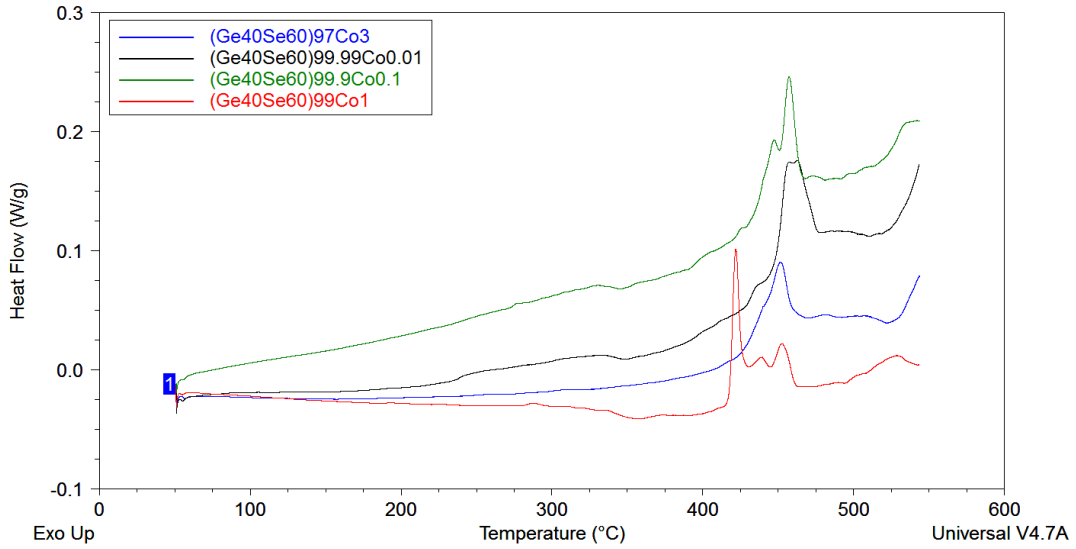

Fig. 30. Total heat flow curves of $(Ge_{40}Se_{60})_{100x}Co_x$ glass.

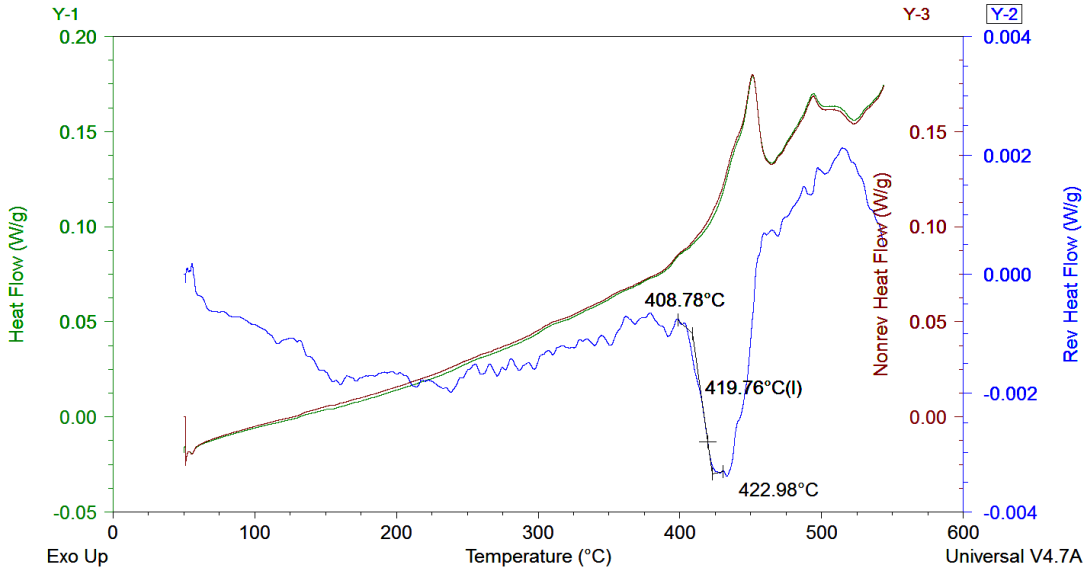

Fig. 31. Total, reversible and nonreversible curves for $(Ge_{40}Se_{60})_{97}Co_3$ glass.

$(Ge_{40}Se_{60})_{97}Cu_3$

Cu_3-doped sample has three T_cs whereas all other samples have one T_c.

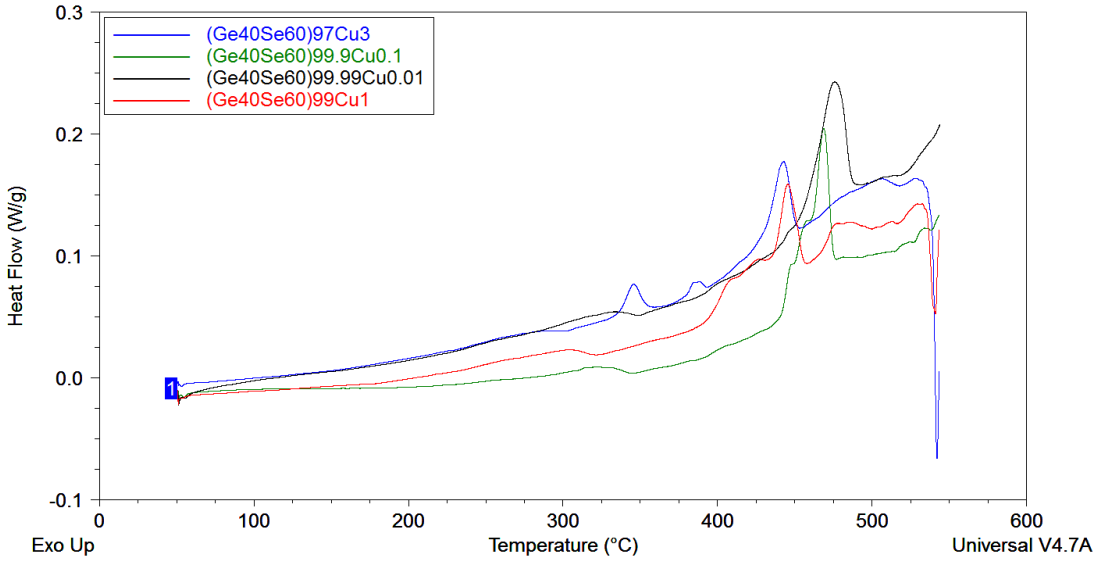

Fig. 32. Total heat flow curves of $(Ge_{40}Se_{60})_{100x}Cu_x$ glass.

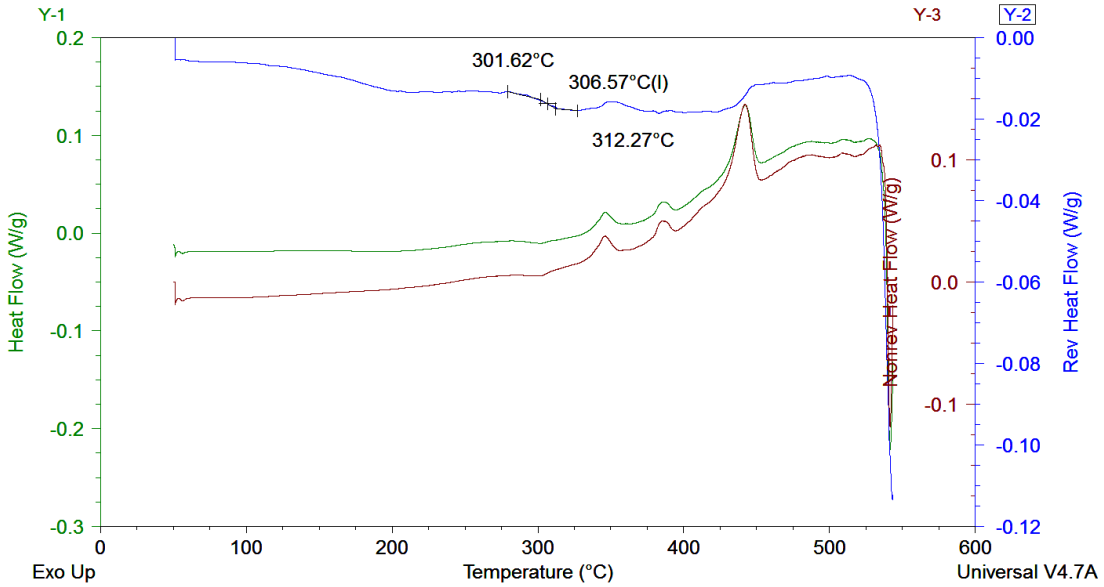

Fig. 33. Total, reversible and nonreversible curves for $(Ge_{40}Se_{60})_{97}Cu_3$ glass.

$(Ge_{40}Se_{60})_{97}Zn_3$

This series of glasses show the evolution of T_c with dopant concentration most elegantly. $Zn_{0.01}$ doped glass has only one T_c; indication of 2nd T_c appears for $Zn_{0.1}$ doped glass. Third T_c appears in Zn_1 doped glass. Zn_3 doped glass has prominent presence of all three T_cs. All samples have only one T_g.

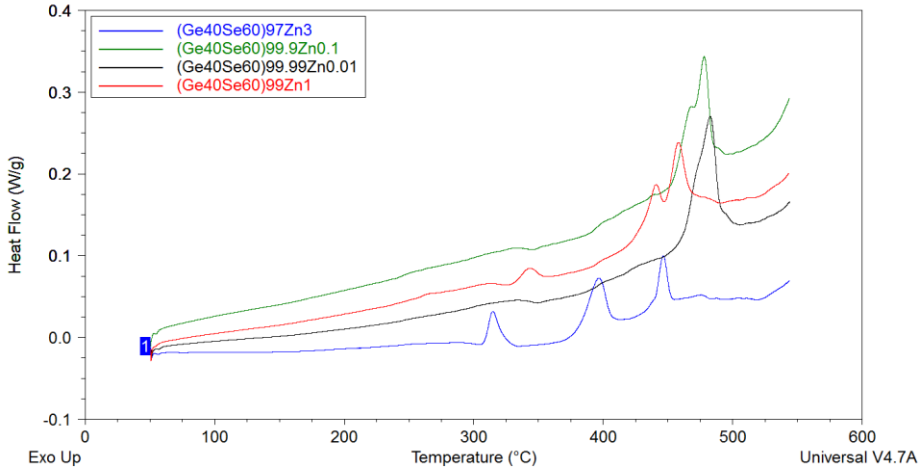

Fig. 34. Total heat flow curves of $(Ge_{40}Se_{60})_{100x}Zn_x$ glass.

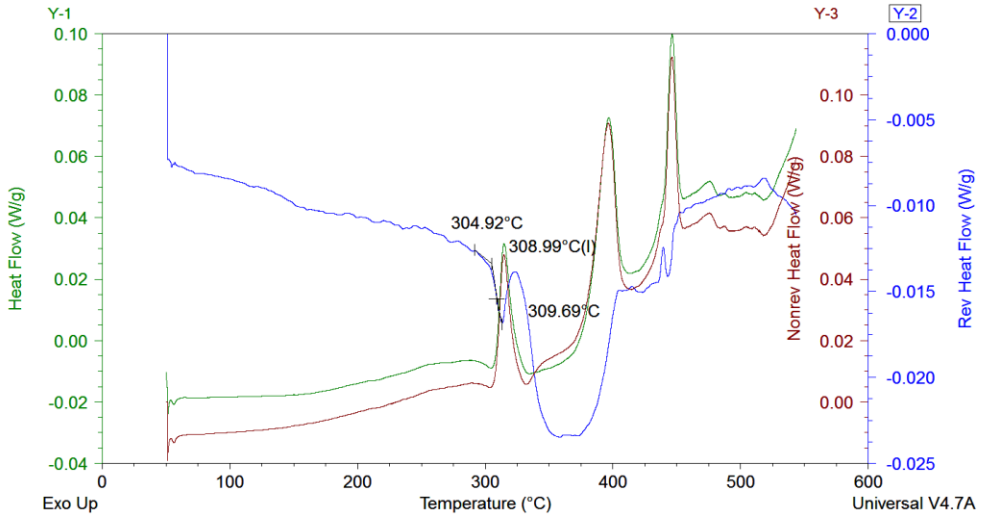

Fig. 35. Total, reversible and nonreversible curves for $(Ge_{40}Se_{60})_{97}Zn_3$ glass.

$(Ge_{40}Se_{60})_{97}Ag_3$

Ag-doped samples show one T_c. One meting dip appears for $(Ge_{40}Se_{60})_{97}Ag_3$ glass at 415 ^oC which might be an indication of phase-separation in this composition.

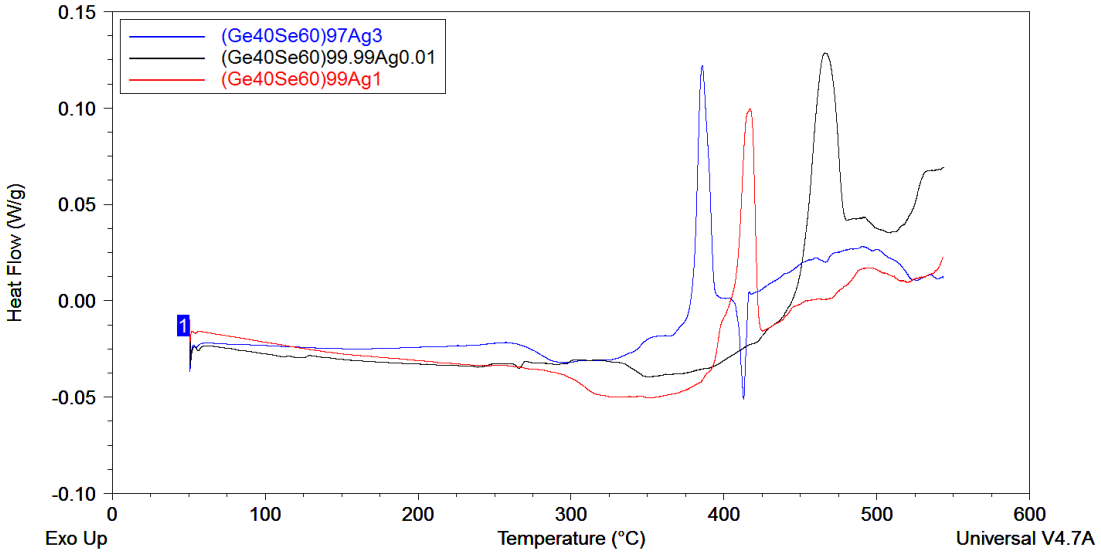

Fig. 36. Total heat flow curves of $(Ge_{40}Se_{60})_{100x}Ag_x$ glass.

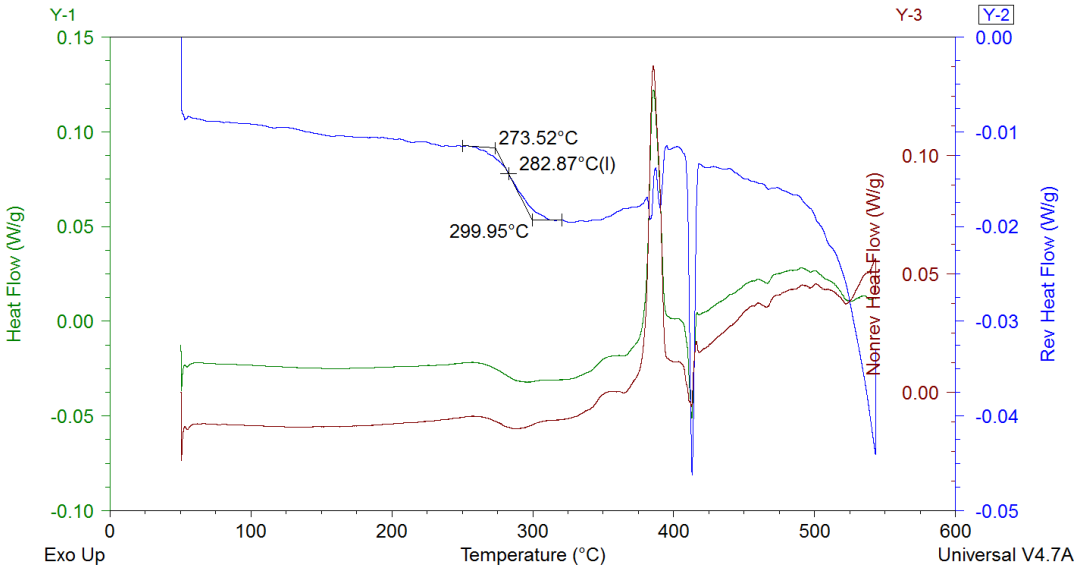

Fig. 37. Total, reversible and nonreversible curves for $(Ge_{40}Se_{60})_{97}Ag_3$ glass.

$(Ge_{40}Se_{60})_{97}W_3$

All W-doped samples appear to have one T_c and one T_g.

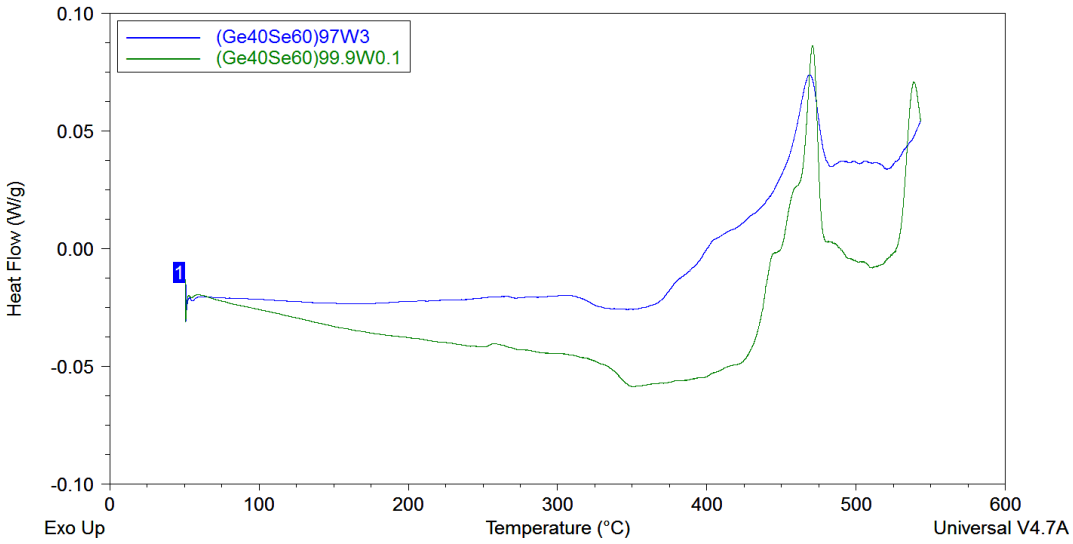

Fig. 38. Total heat flow curves of $(Ge_{40}Se_{60})_{100x}W_x$ glass.

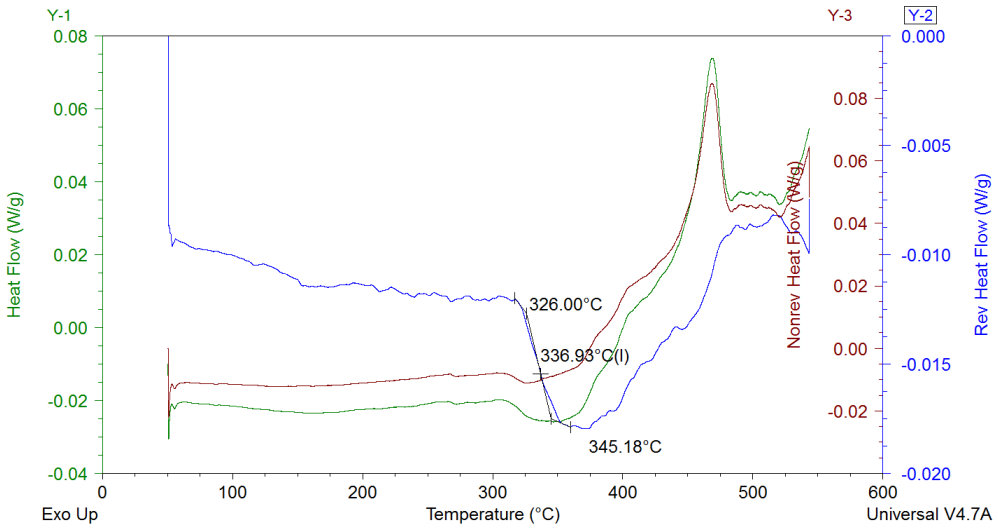

Fig. 39. Total, reversible and nonreversible curves for $(Ge_{40}Se_{60})_{97}W_3$ glass.

Electron Paramagnetic Resonance (EPR) spectroscopy, method and results

(a) Method:

The EPR spectra of chalcogenide glasses were recorded on a Bruker ESP 300E spectrometer operating at X-band microwave frequency. A dual mode microwave cavity (Bruker, 4116M/0705) was used in order to allow spectra recording with perpendicular (H1 ⊥ H) or parallel (H1 ∥ H) polarization of the magnetic field vector H1 of the microwave relative to the static magnetic field H. Cryogenic temperatures were obtained with an Oxford ESR900 liquid helium cryostat. The temperature was controlled with an Oxford ITC503 temperature and gas flow controller.

Glassy samples crushed into small pieces were taken in EPR-grade quartz tubes (Wilmad, 707-SQ). Dopant concentration was kept constant at 0.1 % in order to compare the effects of all dopants and also, as it was found that 0.01 % of dopant was too low to detect any ESR signal whereas 1 % doping was too concentrated and created an unwanted dipole-dipole interaction in the sample. Dewar flask (Wilmad, WG-819-B) was used to carry out the measurement at 77 K in liquid nitrogen.

The photoinduced EPR spectra were studied using a Dolan-Jenner MI-150R light source with EKE 21 V 150 W halogen lamp of color temperature 3250 K. Light was transmitted from the light source into the dual-mode cavity optical port through Dolan-Jenner B460 fiber with 6.35 mm output diameter, 152.4 cm length, 0.4 to 2.0 microns spectral transmittance and maximum 10 %/ft. at 0.6 microns transmission losses. EPR spectra were recorded on all samples in dark conditions, followed by spectra recording during in-situ illumination. Subsequently, ESR spectra was measured at dark and also, after 15 min of annealing at 300 K.

Fig. 40. The electron paramagnetic resonance system.

(b) Results:

(i) $Ge_{40}Se_{60}$:

Room temperature (RT) EPR spectra collected in the perpendicular mode on $Ge_{40}Se_{60}$ glasses shows a broad signal at g = 2.14 which is quite similar reported earlier and also, has been seen in other chalcogenide glass such as Se, P_4Se_4 etc. [8]. This broad peak could be assigned to intrinsic paramagnetic centers present in these glasses. One additional minor peak is also seen around g = 1.97. According to our knowledge, observation of this additional peak without illumination was not reported earlier anywhere else. No obvious light induced signals were observed in $Ge_{40}Se_{60}$ at room temperature (Fig. 41).

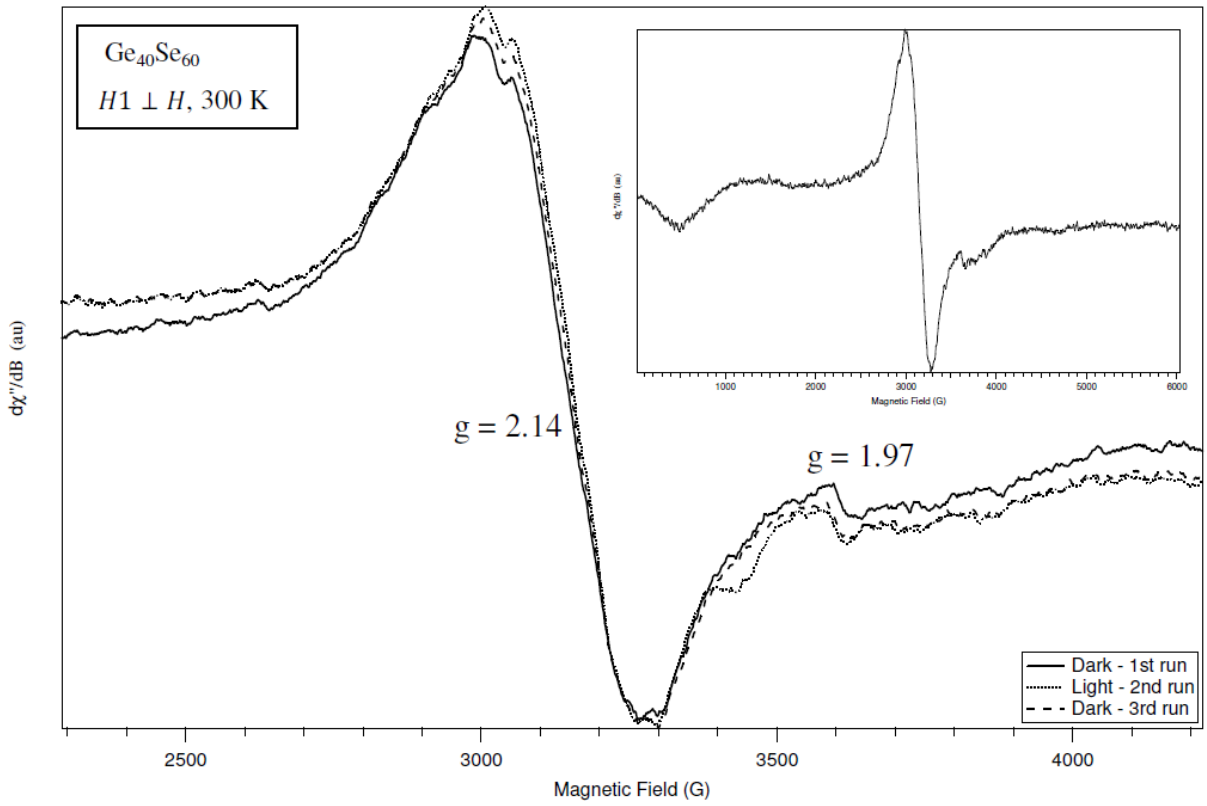

Fig. 41. EPR results on $Ge_{40}Se_{60}$ glass at 300 K with microwave frequency = 9.59 GHz; illumination shows no photo-generated signal. Full scan result is shown in inset.

EPR measurement on $Ge_{40}Se_{60}$ glass at 77K replicates the pattern of 300 K. Light illumination at this temperature enhances the minor peak at g = 1.97 which was found to be frozen even after the excitation light was turned off for 30 minutes (Fig. 42). Annealing at room temperature for about 15 minutes restores the initial state of the material. It is important to mention here that annealing at room temperature destroys the light-induced EPR centers seen at 77 K for all samples studied.

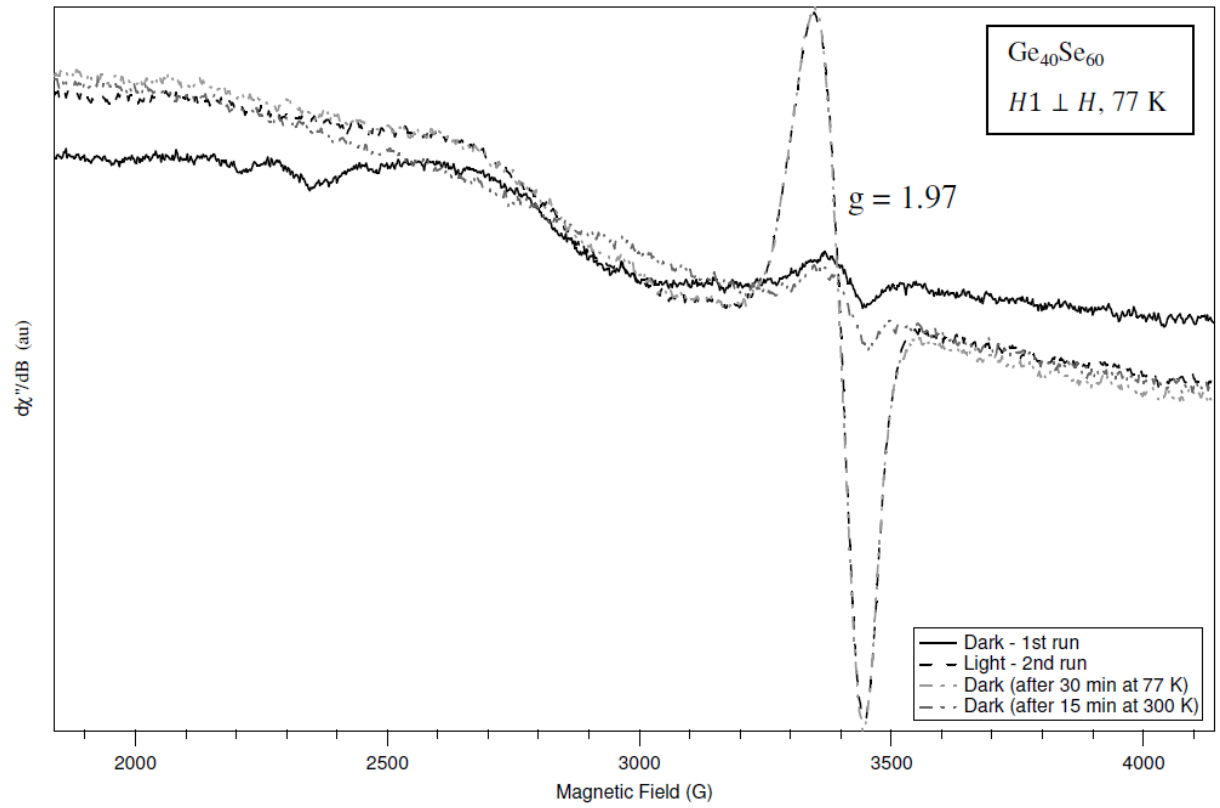

Fig. 42. Light-induced EPR spectra of $Ge_{40}Se_{60}$ glass; enhanced peak at g = 1.97 becomes frozen at 77 K and goes back to its initial state after 15 min of annealing at 300 K.

Parallel mode EPR response of $Ge_{40}Se_{60}$ glass at 300 K is shown in Fig. 43. Light illumination does not create any additional peak. It is important to mention here that similar results were obtained for $Ge_{40}Se_{60}$ glass at 77 K and as well as for other glasses at both temperatures other than the Co-doped glasses at 77 K which will be discussed in later part of the paper.

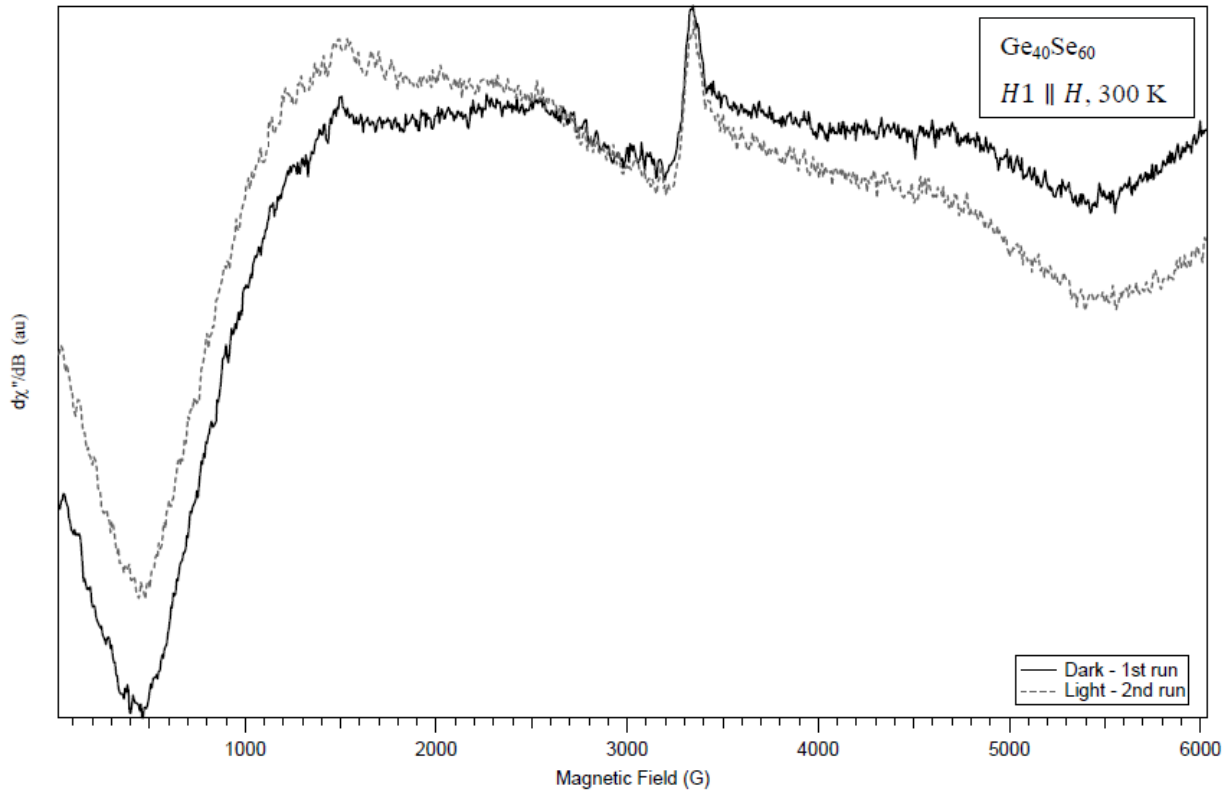

Fig. 43. Parallel mode EPR runs with microwave frequency = 9.43 GHz on $Ge_{40}Se_{60}$ glass do not show any peak at 300 K (as well as at 77 K, not shown), with or without illumination (peak around 3300 G is due to the cavity).

(ii)$(Ge_{40}Se_{60})_{99.9}Cr_{0.1}$

$(Ge_{40}Se_{60})_{99.9}Cr_{0.1}$ shows one major (g = 1.98) and one very minor (g = 5.18) EPR signals at 300 K (Fig. 44). The low-field resonance at g = 5.18 is generally assigned to the isolated Cr^{3+} ions in distorted sites [9, 10]. g = 1.98 line may be due to both exchange coupled Cr^{3+} ions and isolated Cr^{3+} ions [10]. EPR spectrum at 77 K is exactly similar to the 300 K spectra. No light induced signal was observed for this glass at 77 K which indicates that the signal due to Cr^{3+} ions smears out all other signals. This observation also suggests that Cr does not become a part of chalcogenide glass network, i.e. Cr ions stay mostly as isolated or coupled ions in the glassy network.

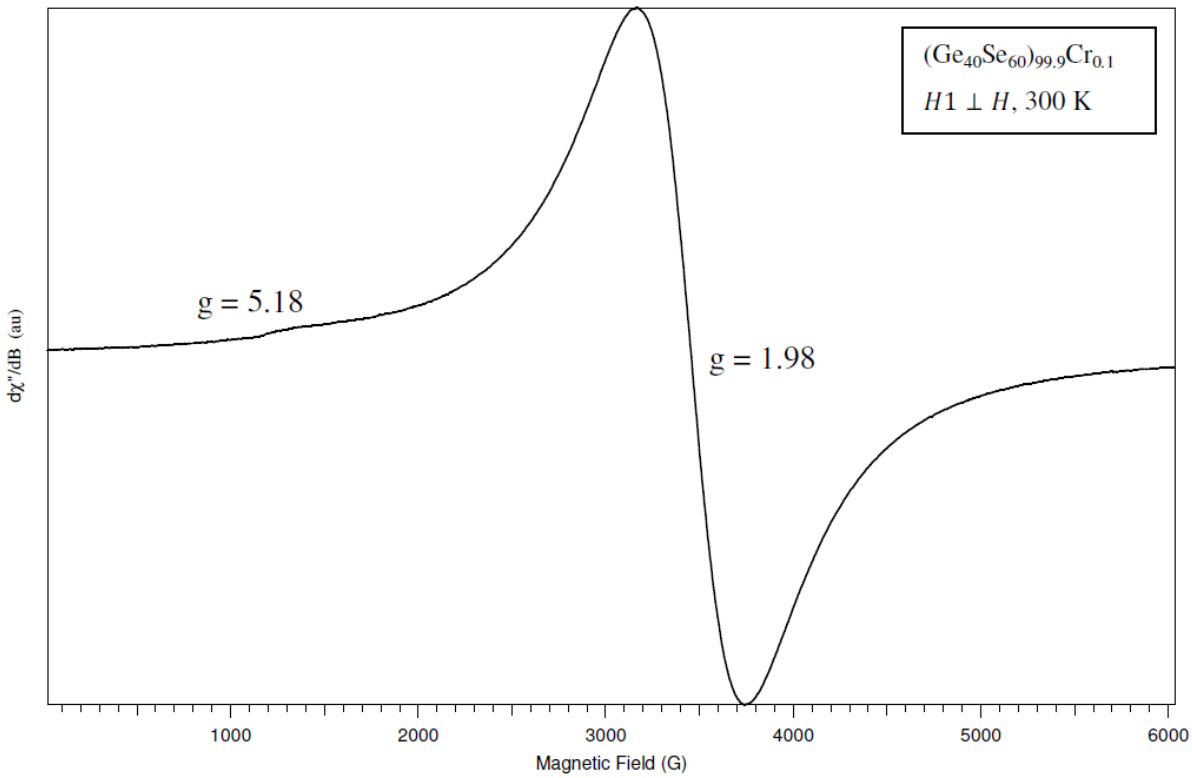

Fig. 44. 300 K perpendicular mode EPR spectrum of $(Ge_{40}Se_{60})_{99.9}Cr_{0.1}$ glass.

300 K parallel mode EPR spectrum of $(Ge_{40}Se_{60})_{99.9}Cr_{0.1}$ does not show any peak (Fig. 45).

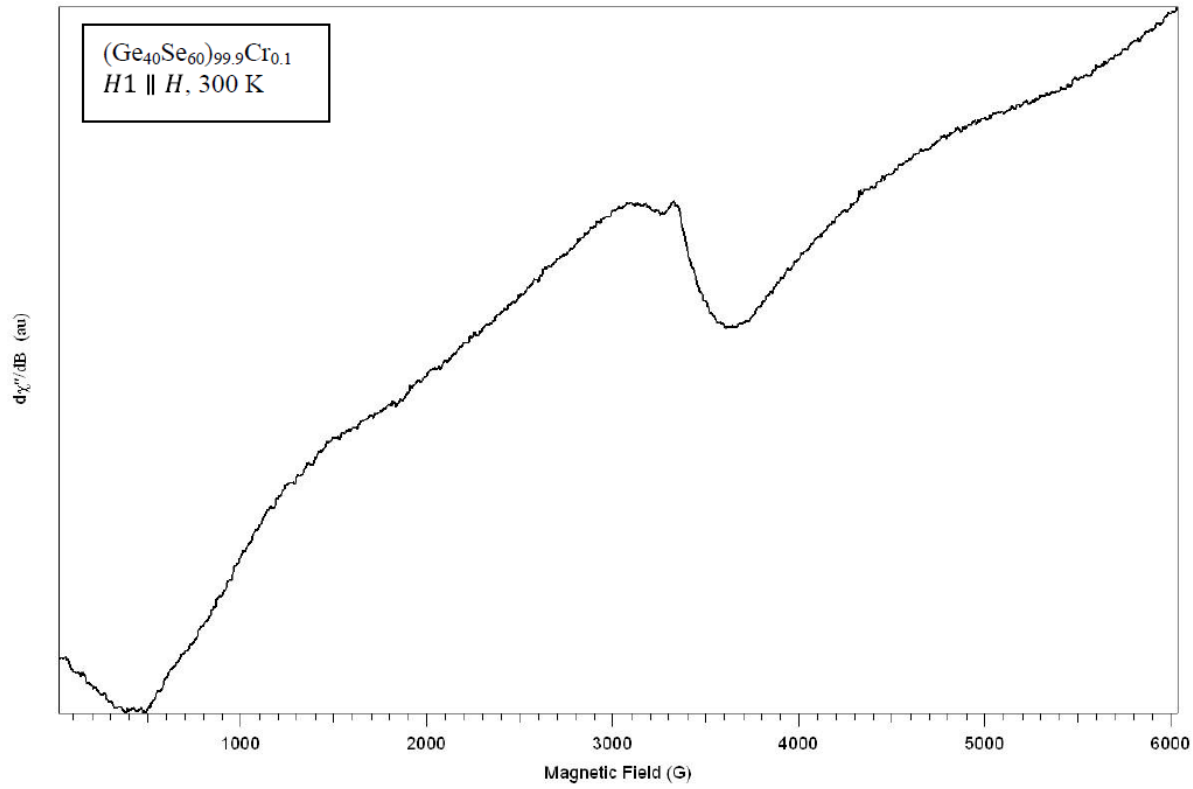

Fig. 45. Parallel mode EPR spectrum of $(Ge_{40}Se_{60})_{99.9}Cr_{0.1}$ glass without any peak at 300 K (as well as at 77 K, not shown), with or without illumination.

Three absorption lines are seen in parallel ESR spectrum of $(Ge_{40}Se_{60})_{99.9}Cr_{0.1}$ at 77 K with g = 10.2, g = 8.37 and g = 1.99 (Fig. 46). Exchange coupled Cr^{3+} ions and isolated Cr^{3+} ions are behind the appearance of g = 1.99 signal. Although other two peaks are not reported earlier, those can be assigned to Cr^{3+} ions.

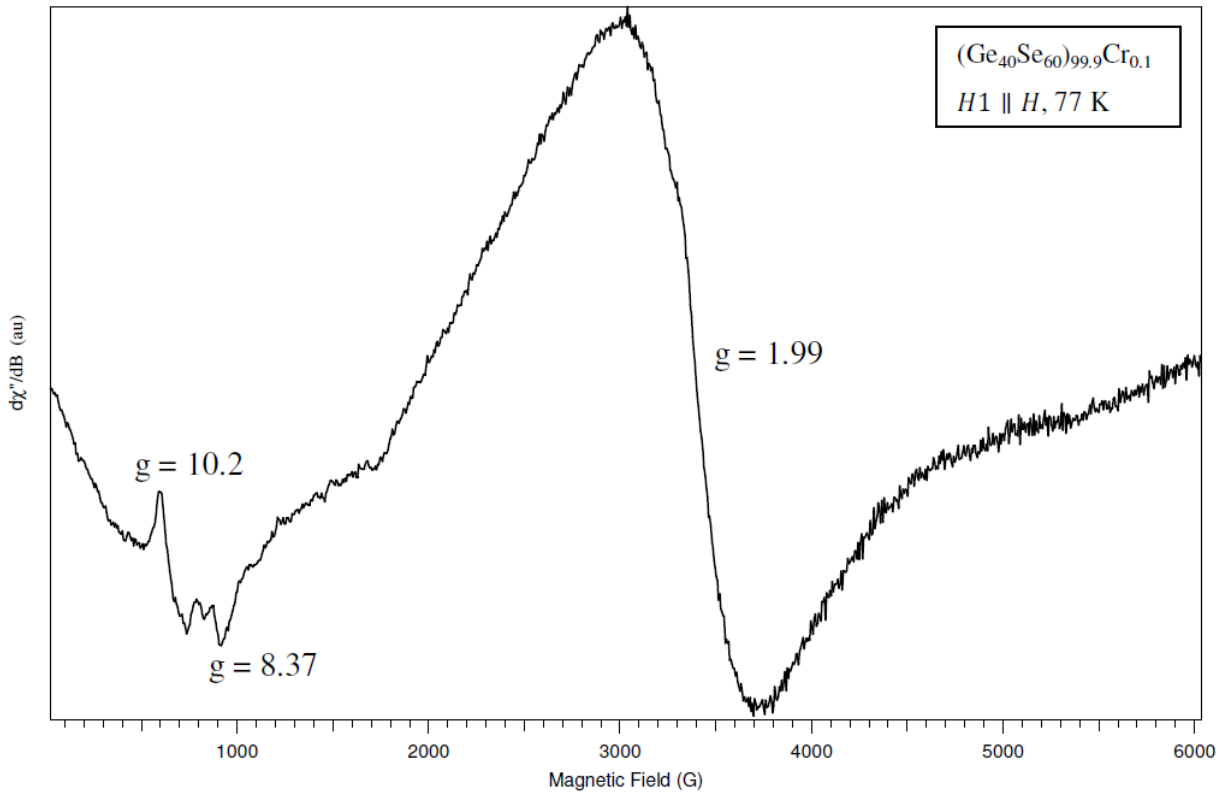

Fig. 46. Three peaks can be seen in 77 K EPR parallel mode spectrum of $(Ge_{40}Se_{60})_{99.9}Cr_{0.1}$ glass.

$(Ge_{40}Se_{60})_{99.9}Mn_{0.1}$

Sources of Mn dopants were MnSe and Mn, and there was no difference in EPR responses out of these two sources and this fact is found to be true for all of the dopants used in this study. Parallel mode 300 K EPR spectrum of $(Ge_{40}Se_{60})_{99.9}Mn_{0.1}$ glass is shown in Fig. 47 and two peaks are seen with g = 4.13 and g = 1.97 which are similar to the already reported values [11-14]. Light illumination does not create any additional peak.

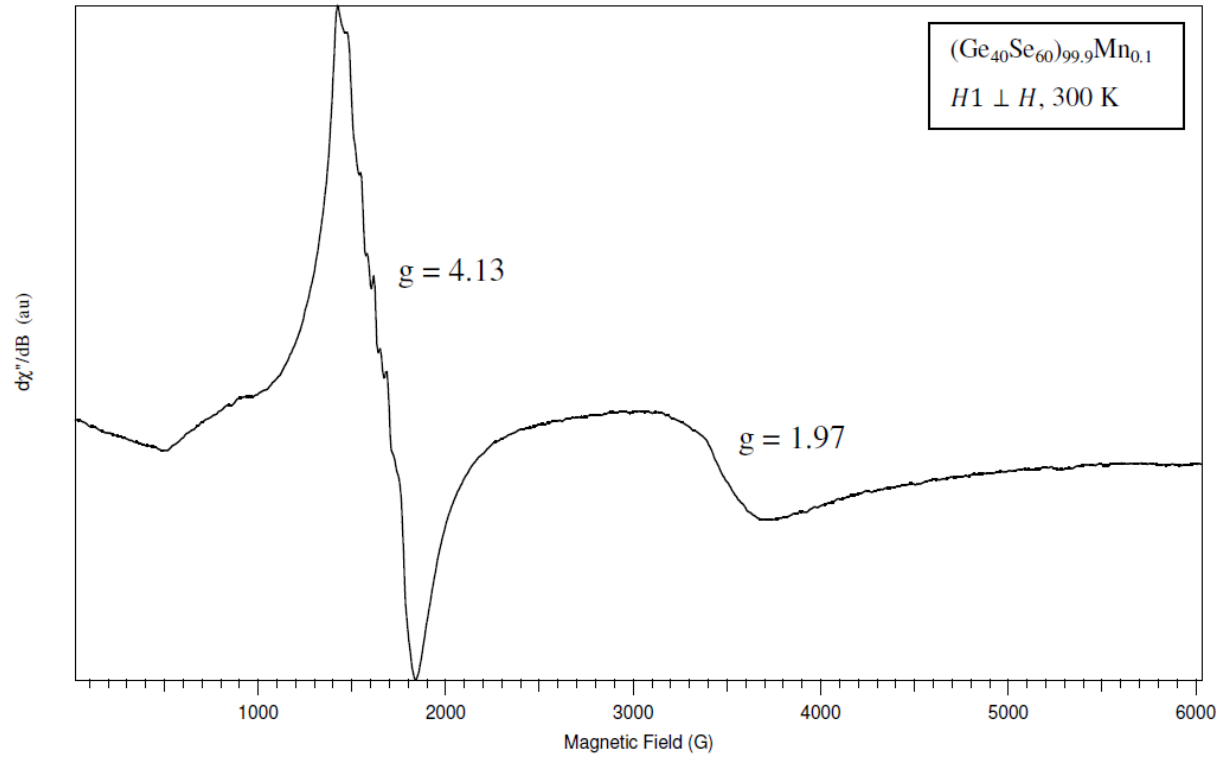

Fig. 47. EPR results on $(Ge_{40}Se_{60})_{99.9}Mn_{0.1}$ glass at 300 K with peaks around g = 4.13 and g = 1.97; g = 4.13 line has resolved hyperfine structure.

Two absorption peaks seen in these glasses are due to different Mn^{2+} centers. Depending upon the Mn concentration and strength of dipole-dipole interaction in the host lattice, these lines may exhibit resolved hyperfine structure. The g = 1.97 line is mainly due to the Mn^{2+} ions forming Mn-chalcogen particles, microcrystalline inclusion or Mn-O due to oxygen contamination of the material particles at the surface. The g = 4.13 line is caused by the Mn^{2+} ions incorporated into the glass network. The appearance of resolved hyperfine structure at g = 4.13 may be attributed to the Mn^{2+} occupying sites similar to Ge in an environment with approximately orthorhombic symmetry as the line with g = 4.3 is characteristic of transition metal ions ($S = \frac{5}{2}$) incorporated in the amorphous network [13].

EPR spectrum of $(Ge_{40}Se_{60})_{99.9}Mn_{0.1}$ glass taken at 77 K is very similar to the 300 K spectrum. Light illumination creates a hump around g = 1.97 which is most probably due to the photo-induced defect centers as discussed before for $Ge_{40}Se_{60}$ glasses (Fig. 48).

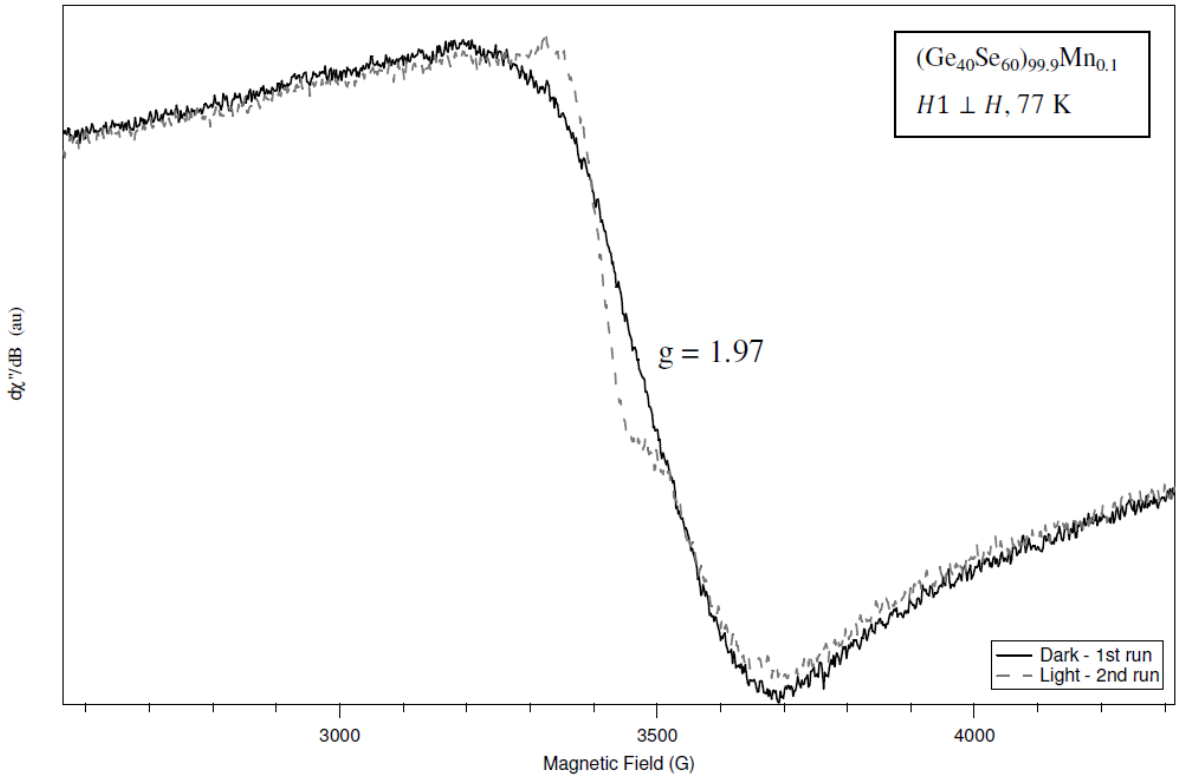

Fig. 48. 77 K EPR spectrum of $(Ge_{40}Se_{60})_{99.9}Mn_{0.1}$ glass; appearance of a light-induced hump can be seen around g = 1.97.

300 K parallel mode EPR spectrum of $(Ge_{40}Se_{60})_{99.9}Mn_{0.1}$, shown as an example in Fig. 49, is found to be very similar to the spectrum obtained for $Ge_{40}Se_{60}$ (Fig. 43). Parallel mode 77 K spectrum is also found to be very similar to the 300 K spectrum.

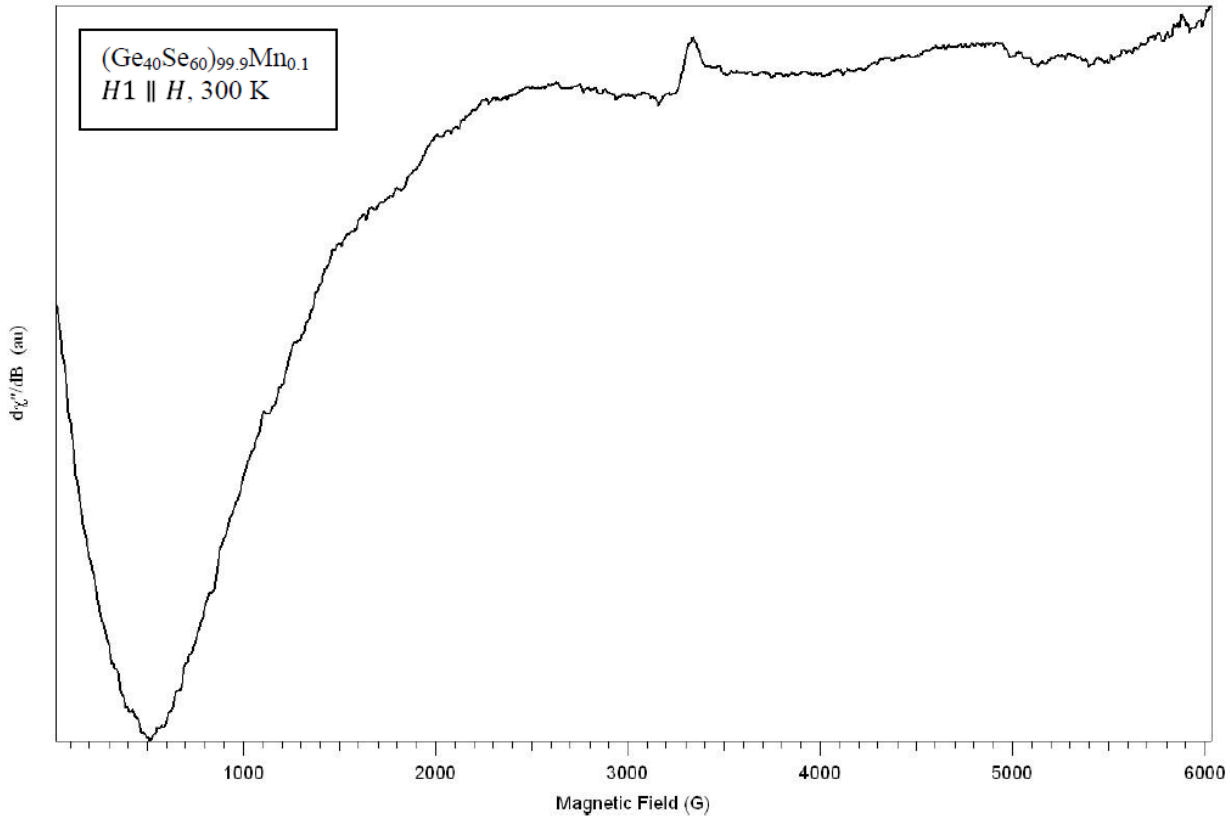

Fig. 49. Parallel mode EPR spectrum of $(Ge_{40}Se_{60})_{99.9}Mn_{0.1}$ glass do not show any peak at 300 K (as well as at 77 K, not shown), with or without illumination.

$(Ge_{40}Se_{60})_{99.9}Fe_{0.1}$

$(Ge_{40}Se_{60})_{99.9}Fe_{0.1}$ EPR spectrum shows two lines, a broad peak with g = 3.04 and a small sharp peak with g = 2.13 (Fig. 50). g = 2.13 can be identified with the iron ions being coupled by strong exchange interactions [15, 9]. There is no report of Fe spectrum with g = 3.04 which may be a result of superimposed signal of reported g ≈ 4.3 line of Fe and g = 2.17 broad line seen in $Ge_{40}Se_{60}$ glass.

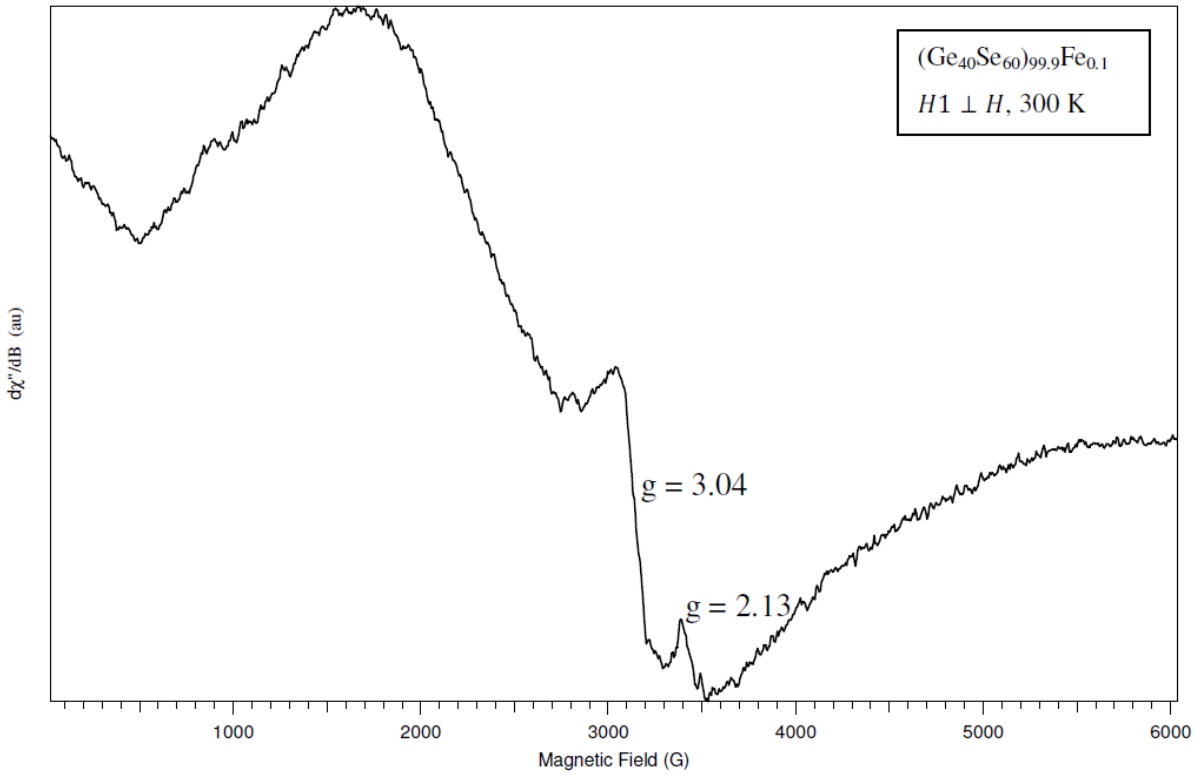

Fig. 50. EPR spectrum of $(Ge_{40}Se_{60})_{99.9}Fe_{0.1}$ glass at 300 K.

77 K EPR spectrum of Fe-doped glass indicates the presence of three peaks (Fig. 51). First peak which is around g = 4.22, can be attributed to the presence of Fe^{3+} ions situated in low symmetry crystalline fields provided by tetrahedral or octahedral surrounding of selenium atoms and is seen in chalcogenide and as well as in other glasses too [16]. Second major peak around g = 2.08 is as mentioned before, due to the iron ions being coupled by strong exchange interactions. A weak peak is also seen around g = 1.98 which intensifies under light illumination. This peak can be assigned to the charge defects of base chalcogenide glass and photo-induced transition follows equations (1) and (2) as in the case of $Ge_{40}Se_{60}$ glass.

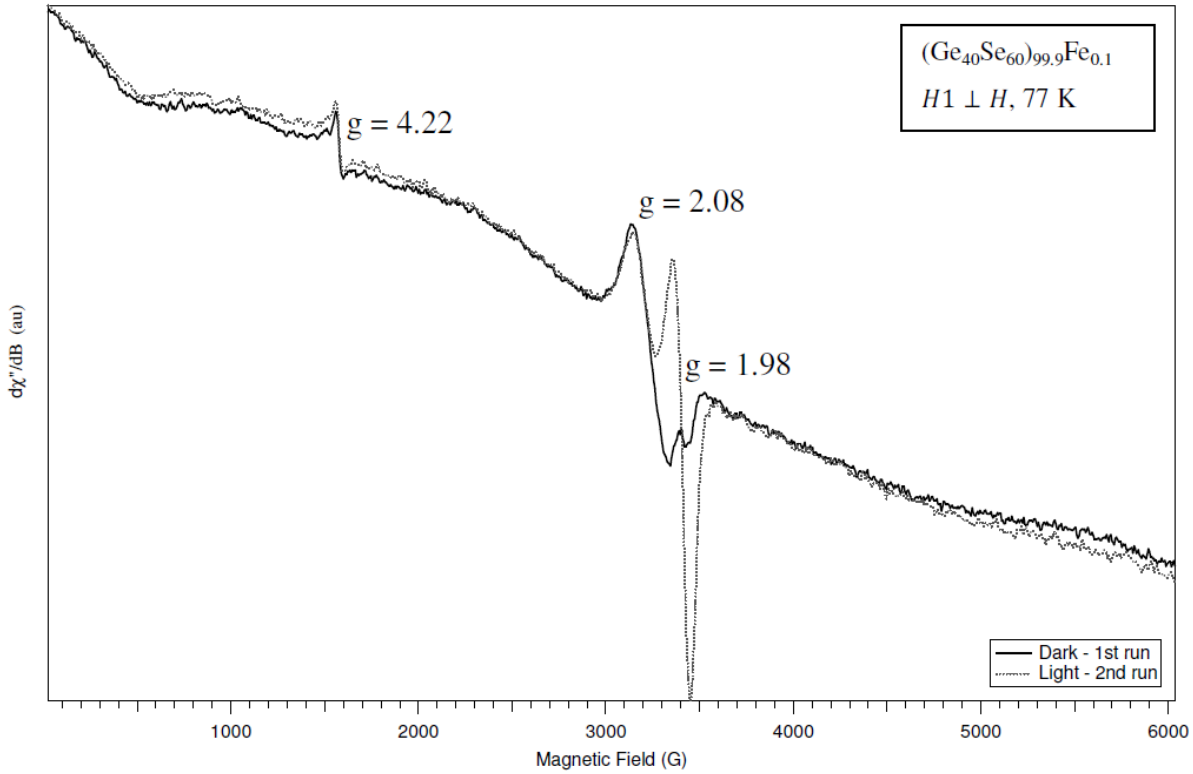

Fig. 51. EPR spectrum of $(Ge_{40}Se_{60})_{99.9}Fe_{0.1}$ glass at 77K showing three peaks. Light illumination causes enhancement of the peak with g = 1.98.

Parallel mode EPR spectrum of $(Ge_{40}Se_{60})_{99.9}Fe_{0.1}$ taken at 300 K shown in Fig. 52 as an example, resembles the spectra of other glasses at the same temperature and as well as, the spectrum taken for the same glass at 77 K.

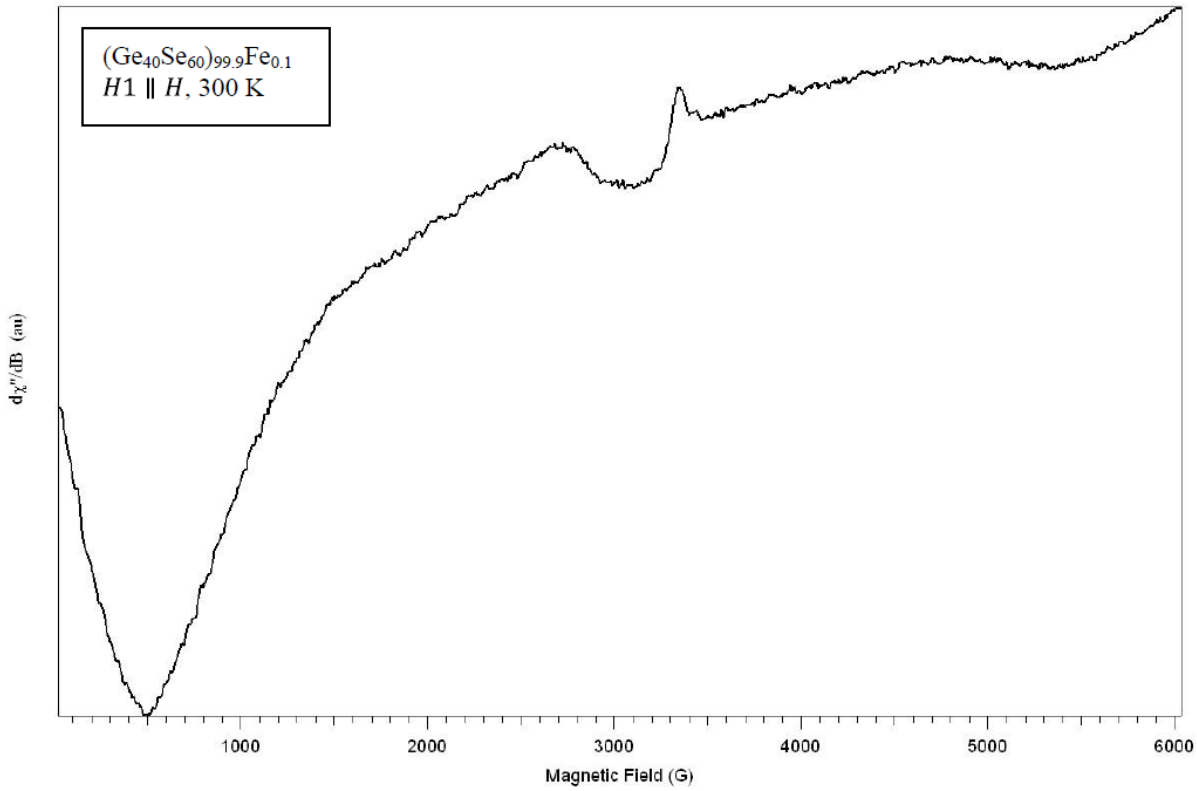

Fig. 52. 300 K parallel mode EPR spectrum of $(Ge_{40}Se_{60})_{99.9}Fe_{0.1}$ without any peak, with or without illumination; 77 K spectra has similar characteristics (not shown).

$(Ge_{40}Se_{60})_{99.9}Co_{0.1}$

Room temperature EPR spectrum of $(Ge_{40}Se_{60})_{99.9}Co_{0.1}$ shows two peaks (Fig. 53). First peak which is at g = 2.17, corresponds to Co (II) substitution into a tetrahedral environment whereas the second peak at g = 1.96, is most likely to be due to the presence of oxygenated cobalt or defects the structure in the form of microcrystalline inclusions [17, 18].

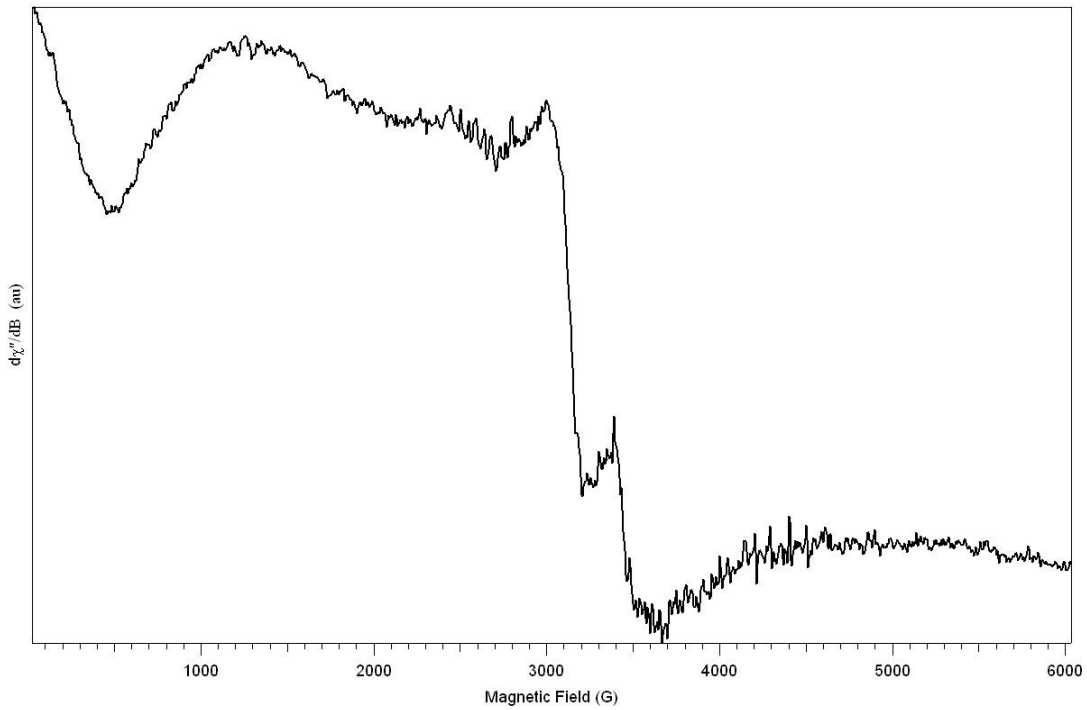

Fig. 53. 300 K EPR spectrum of $(Ge_{40}Se_{60})_{99.9}Cr_{0.1}$ shows two peak, at g = 2.17 and g = 1.96.

Light illumination at 77 K enhances the g = 1.96 peak as in the case of $Ge_{40}Se_{60}$ glasses which is due to the creation of photo-induced defects (Fig. 54).

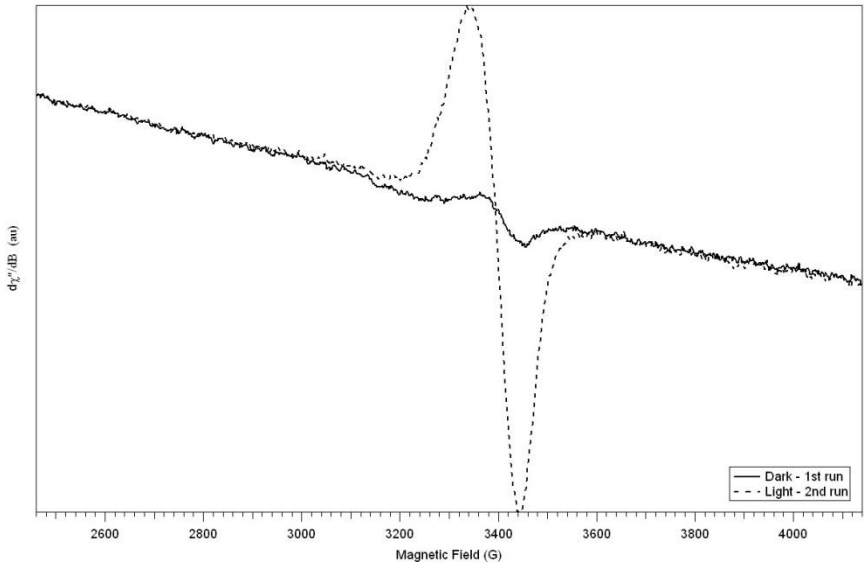

Fig. 54. Light induced enhancement of the g = 1.96 peak for $(Ge_{40}Se_{60})_{99.9}Cr_{0.1}$ at 77 K.

Parallel mode EPR spectrum of $(Ge_{40}Se_{60})_{99.9}Cr_{0.1}$ at 300 K is very similar to the other glasses (Fig. 55). Spectrum taken at 77 K imitates the 300 K spectrum.

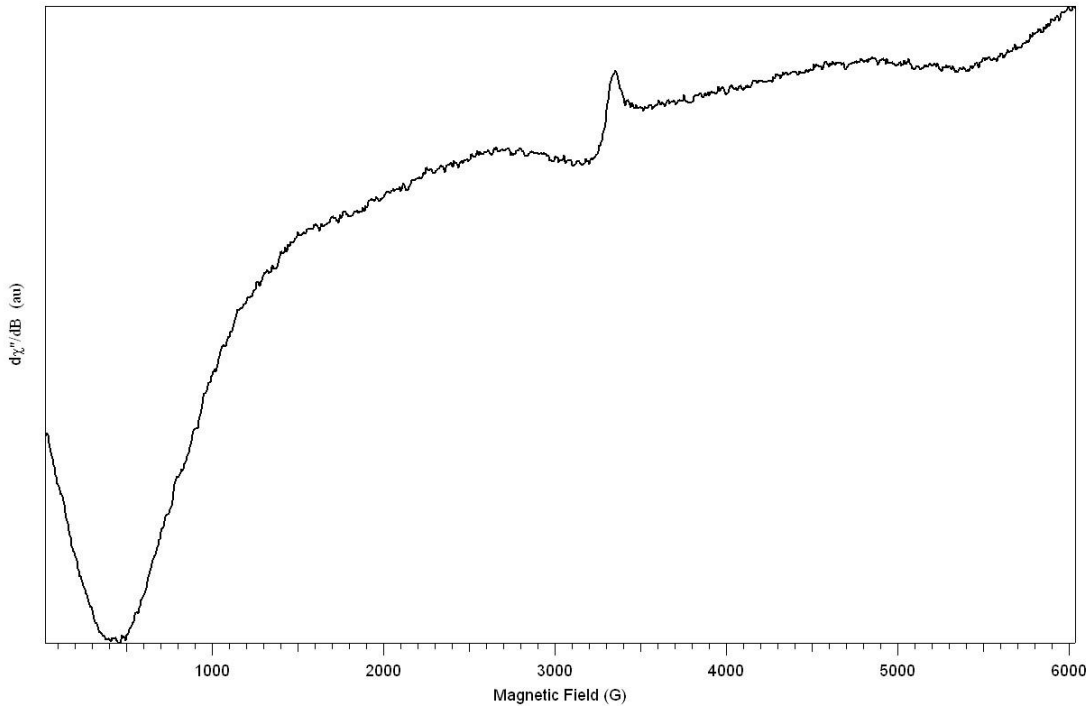

Fig. 55. EPR spectrum of $(Ge_{40}Se_{60})_{99.9}Cr_{0.1}$ taken in parallel mode and at 300 K is shown as an example.

4. References:

[1] X. Feng, W.J. Bresser, P. Boolchand, Phys. Rev. Lett. 78 (1997) 4422.

[2] Y.Wang , O.Matsuda, K.Inoue, O.Yamamuro, T.Matsuo, K.Murase, J. Non-Cryst. Solids 232-234 (1998) 702.

[3] G. Lucovsky, A. Mooradian, W. Taylor, G.B. Wright, R.C.Keezer, Solid State Commun. 5 (1967) 113.

[4] R.K. Pan, H.Z. Tao, H.C. Zang, X.J. Zhao, T.J. Zhang, J. Alloys Compd. 484 (2009) 645.

[5] T. Ikari, T. Tanaka, K. Dra, K. Maeda, K. Futagami, S. Shigetomi, Phys. Rev. B 47 (1993) 4984.

[6] Punit Boolchand, Daniel G. Georgiev, Tao Qu, Fei Wang, Liuchun Cai, Swapnajit Chakravarty, C. R. Chim. 5 (2002) 713.

[7] Kristy A. Campbell, Morgan G. Davis, Jeffrey M. Peloquin, Mater. Res. Soc. Symp. Proc. 997 (2007) 0997-I12-10.

[8] L.N. Blinov, Glass Phys. Chem. 29 (2003) 203–223.

[9] C. Legeint, J.Y. Buzarkt, J. Emery, C. Jacobonit, J. Phys.: Condens. Mat. 7 (1995) 3853-3862.

[10] A. Murali, J. Lakshmana Rao, J. Phys.: Condens. Matter 11 (1999) 1321-1331.

[11] Rakhim R. Rakhimova, David E. Jones, J. Chem. Phys. 113 (2000) 1575-1579.

[12] E.A. Zhilinskaya, V.N. Lazukin, J. Non-cryst. Solids 50 (1982) 163-172.

[13] S.K. Malik, K.L. Bhatia, N. Kishore, J.S. Phor, J. Non-cryst. Solids 142 (1992) 55-62.

[14] J.W.H. Schreurs, J. Chern. Phys. 69 (1978) 2151-2156.

[15] E.A. Zhilinskaya, V.N. Lazukin, E.A. Bychkov, I.L. Likholit, J. Non-cryst. Solids 119 (1990) 263-268.

[16] K.J. Rao, B.G. Rao, Proc. Indian Acad. Sci. (Chern. Sci.) 95 (1985) 169-188.

[17] A.M. Beale et al., Phys. Chem. Chem. Phys. 7 (2005) 1856-1860.

[18] D. Skrzypek, I. Madejska, J. Habdas, Solid State Sci. 9 (2007) 295-302

EXAFS spectral analysis performed at Argonne National Laboratory July 2009.

In July 2009, EXAFS analysis of individual devices containing GST phase change material within a switching array device via, was performed at the Argonne National Laboratory Advanced Photon Source by Dr. Leonardo Miotti, a member of collaborator Dr. Michael Paesler's group at North Carolina State University.

Details of device fabrication were included in the 2009 annual report, but a basic summary of the devices designed and fabricated is included in this report for completeness. The devices were fabricated at Boise State University's Idaho Microfabrication Laboratory by members of Dr. Kris Campbell's group, with the exception of the GST and silicon nitride deposition steps, which were completed by Dr. Craig Taylor's group at the Colorado School of Mines. After completion, several devices were electrically probed. While there were issues with the fabrication which prevented fully functional arrays, some devices were switched and erased, and a representative set of these devices were identified and sent to the Paesler Group for EXAFS analysis.

Switching array layout and fabrication. A 150 x 150 cross point array layout was designed for this project, containing three design layers, Metal 1, Via and Metal 2. The three individual layers are shown in Figure 1. Figure 2 shows all three layers aligned to each other.

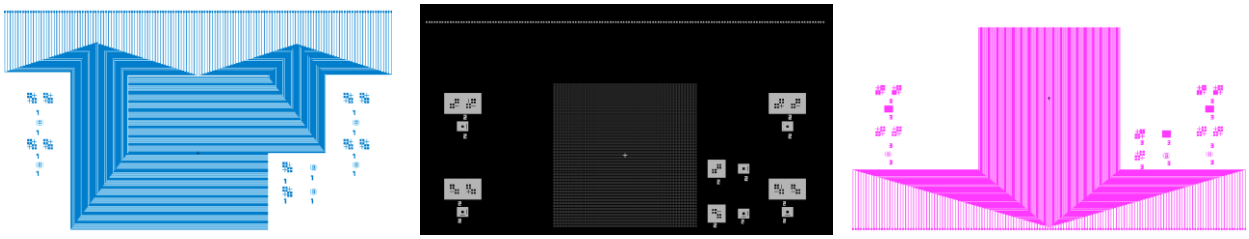

Design layer 1: Metal 1 (bottom) Design layer 2: Via Design layer 3: Metal 2 (top)

Figure 1. Three design layers for the switching array devices.

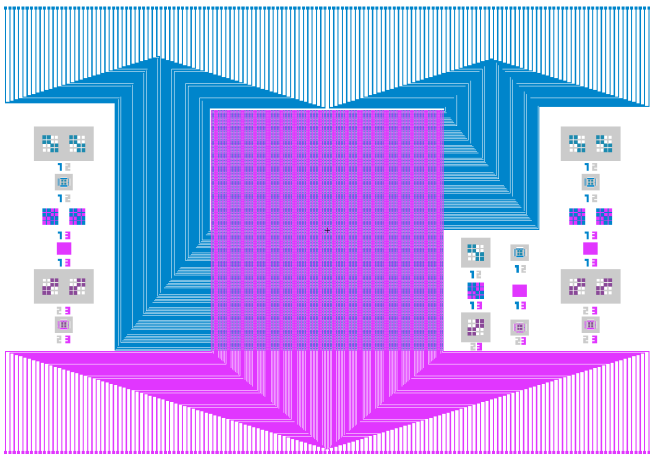

Figure 2. Three design layers for the switching array devices aligned to each other.

Figure 3 shows an expanded view of the array. Each via is 4μ x 4μ, each metal line is 24μ wide and each via is 50μ center to center.

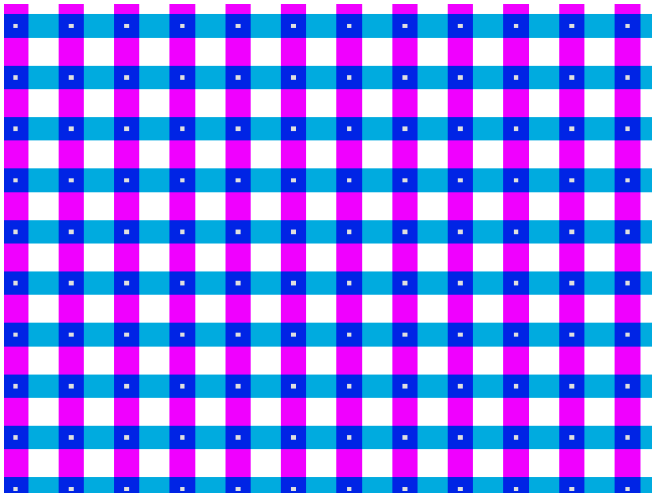

Figure 3. Three design layers aligned for the switching array, expanded view of array.

The process flow utilized to fabricate the switching array devices containing $Ge_2Sb_2Te_5$ (GST) is summarized in Figure 4.

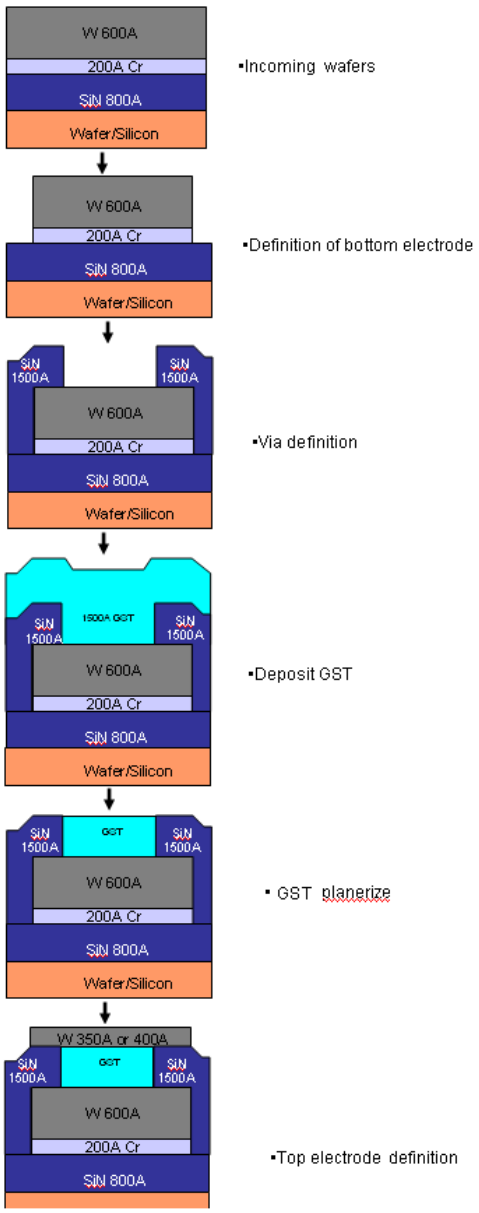

Figure 4. Schematic of Switching Array process flow.

Geometry of samples and probing depth of analysis. The crossection geometry of via samples analyzed is described in Figure 5. At 9886 eV (Ge K alpha 1 fluorescence), the tungsten absorption length is 5.2µ, and the GST absorption length is 12.6µ. At 11,150 eV (above the Ge K edge), the tungsten absorption length is 2.8µ, and the GST absorption length is 14.0µ (the density of GST is 5.8 g/cm^3). Therefore all absorption lengths for the EXAFS analysis are much greater than the film thicknesses as shown in Figure 5, and the beam probed the whole volume of the device with similar sensitivity. Figure 6 shows a partial top down view of the array of completed device vias and the numbering scheme used to locate probed devices. Figure 7 shows the die numbering scheme utilized on the 100 mm wafers used for fabrication.

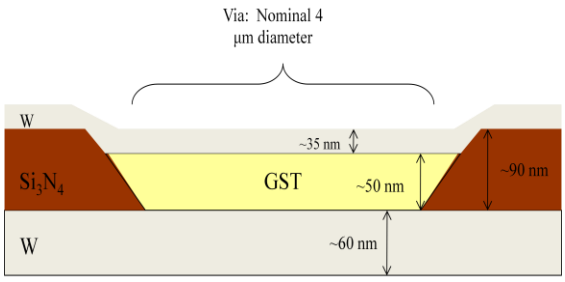

Figure 5. Sample geometry for GST cross point array vias.

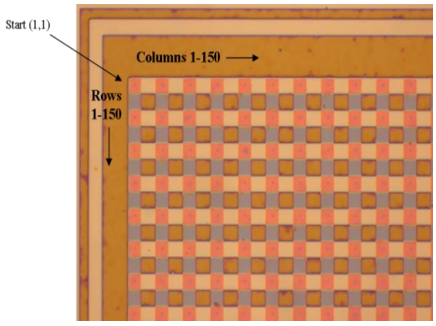

Figure 6. Optical image of completed array.

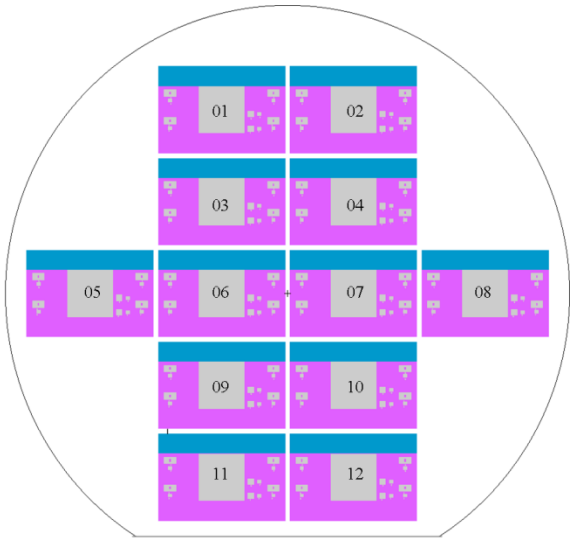

Figure 7. Sample geometry for GST cross point array vias.

NEXAS Experiment setup conditions. The solid state detector was in fluorescence mode, with beam incidence and fluorescence detection at ±45° to the sample normal. The Ge K edge was at 11,150 eV. The beam spot and photon flux deteriorate at the Te and Sb edges, above 30,000 eV. The W L2 edge was at 11,544 eV and the L3 edge was at 10,207 eV nearby.

Array samples analyzed. Table 1 below lists the samples analyzed by EXAFS. The samples analyzed were from BSU lot 090520-1A slot 1, die 4 and die 6. The probed devices were located by counting from the (1,1) position (see Figure 6 above). The GST films were deposited in the amorphous, high resistance state. Two devices were switched to the low resistance, crystalline state. Three other devices on die #4 were read to verify they were unswitched (as deposited).

Table 1. Device via locations and die numbers from 090520-1A slot 1.

Die #	Row & Column	Device Status
6	9,76	Switched
6	2,76	Switched
4	26,76	Unswitched
4	4,76	Unswitched
4	9,77	Unswitched

Contour maps. Figure 8 shows a contour map at the (1,1) position at an energy below the Ge K edge. The contrast is due to the tungsten L3 edge with the Ge K edge overlaid. Figure 9 shows a contour map on a device at row 2 column 76 above the K edge, 11150 eV. Again, the contrast is due to the Ge K edge on top of the tungsten L3 edge.

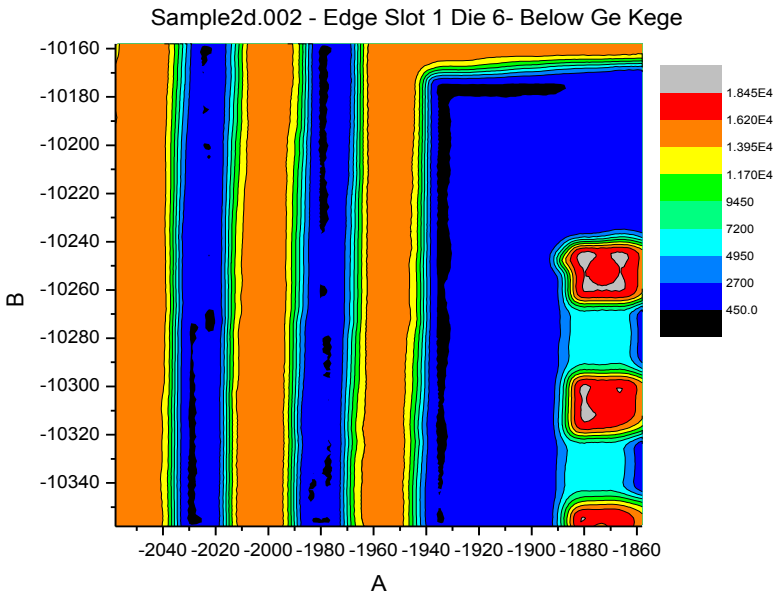

Figure 8. Contour map obtained at energy below the Ge K edge, 11,150 eV.

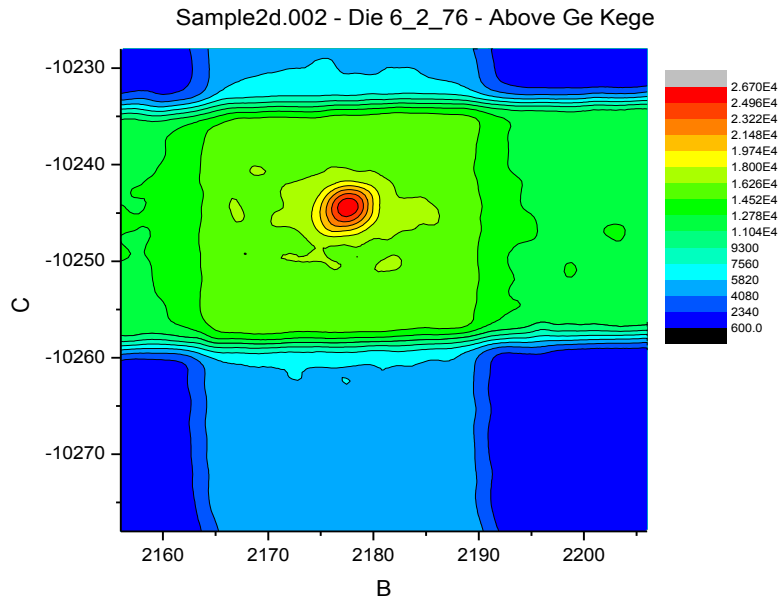

Figure 9. Contour map obtained at energy above the Ge K edge, 11,150 eV.

Figure 10 shows a an expanded view contour map of a switched device via above the Ge K edge, 11,150 eV with more detail of the device via.

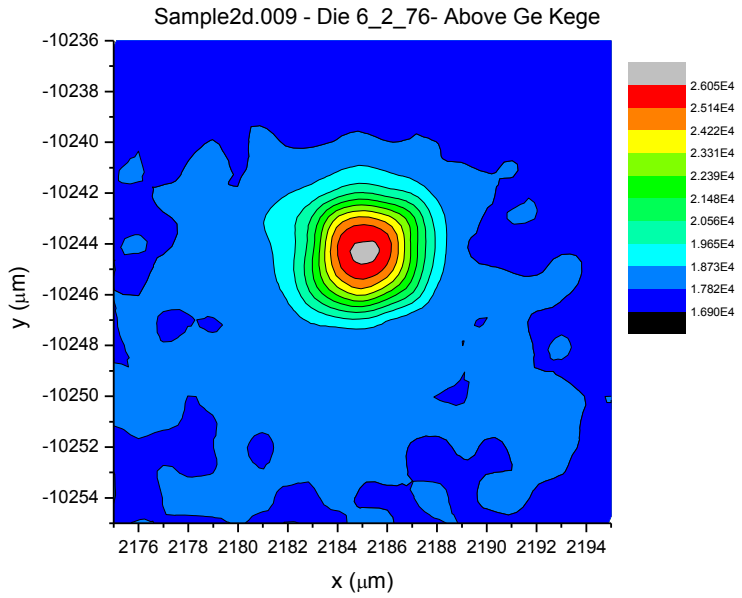

Figure 10. Contour map obtained at energy above the Ge K edge, 11,150 eV.

EXAFS data plotted. Figures 11 through 16 all show the Ge K edge data for array samples as compared to other materials. Figure 11 compares the Ge K edge at 11,150 eV for all samples analyzed. All spectra appear similar. Figure 12 compares one switched and two

unswitched (as deposited) array samples from Figure 11 to a reference PVD amorphous GST thin film. This reference film was deposited with a different tool than the array samples. The array samples absorbed at a significantly different energy when compared to the amorphous reference film. A thin film reference sample was not available from the Colorado School of Mines sputter tool that was used for the array sample depositions.

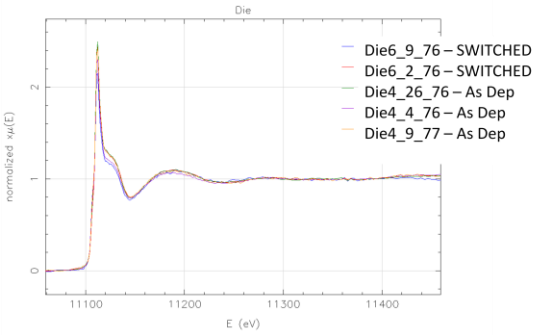

Figure 11. Ge K edge, 11,150 eV, all samples, all similar.

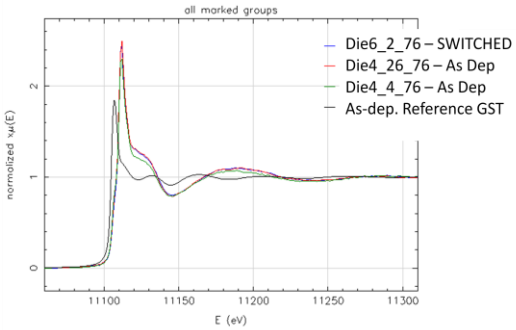

Figure 12. Ge K edge, 11,150 eV three samples compared to a reference amorphous GST film.

Figure 13 compares one switched and two unswitched (as deposited) array samples compared to a reference switched (crystalline) GST thin film sample, again not from the same tool that deposited the array samples. None of the array samples compares well with the crystalline GST film sample. For comparison with another germanium-containing phase change material, Figure 14 compares the same switched and unswitched array samples with an amorphous as-deposited Ge10Se90 thin film sample deposited at Boise State University. Again, the amorphous Ge-containing reference film absorbs at a different energy than any of the array samples.

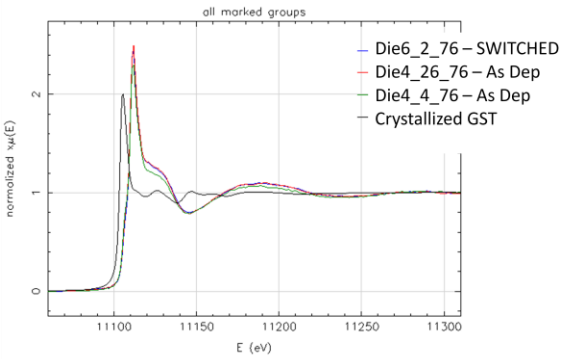

Figure 13. Ge K edge, three array samples compared to a reference crystallized GST film.

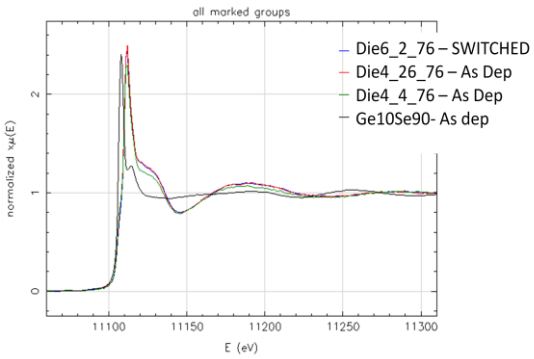

Figure 14. Ge K edge, three array samples compared to a thin film amorphous Ge10Se90 sample.

Figure 15 compares the same switched and unswitched array samples with a reference germanium oxide thin film sample. The absorptions are much more similar than the comparison samples in Figures 12-14. This would indicate that the germanium in the GST film deposited in

the array samples was significantly oxidized at the time of analysis. Figure 15 shows a shoulder on the absorption peak that corresponds to unoxidized GST, indicating that some unoxidized material was present in the array samples.

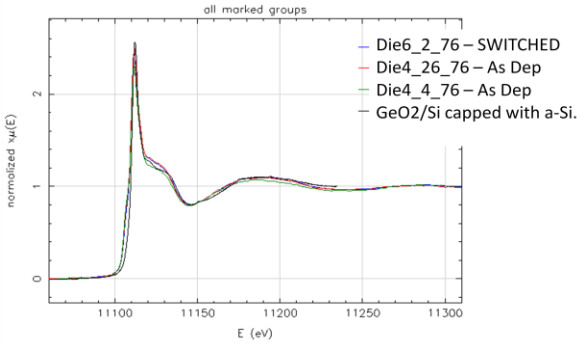

Figure 15. Ge K edge, three array samples compared to a reference GeO_2 film.

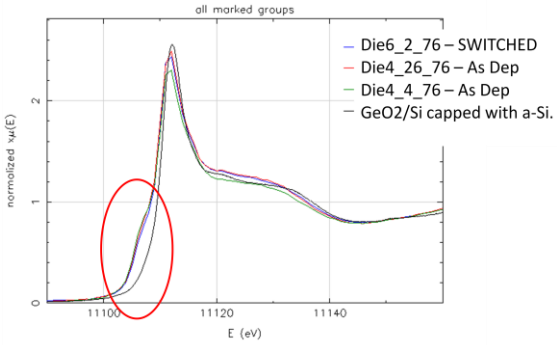

Figure 16. Figure 15 with expanded x axis to show a shoulder on the Ge edge, evidence of amorphous/crystalline GST.

It is not clear why significantly oxidized devices were capable of switching. Dr. Miotti theorized that enough unoxidized GST material was present, that the devices were switchable and may have responded to the electrical characterization as shown in Figure 17, below. It is not possible to determine the percentage of material oxidized in the array samples from the EXAFS data, and the volume proportion indicated in the cartoon cannot be confirmed.

The GST could have been partially oxidized during the planarization process, which involved aqueous slurry directly in contact with the GST material. This would be expected to be a surface phenomenon, however, and would not be expected to oxidize the bulk of the material. The GST may potentially have been oxidized during the physical vapor deposition process. Dr. David Baker, post-doctoral research associate working in Dr. Craig Taylor's group at the Colorado School of Mines, indicated in discussion that the longer than usual evacuation time noted during the deposition of the array samples, could have contributed to an oxidized state for some of the GST material deposited. No further analysis of this data has been completed at this time.

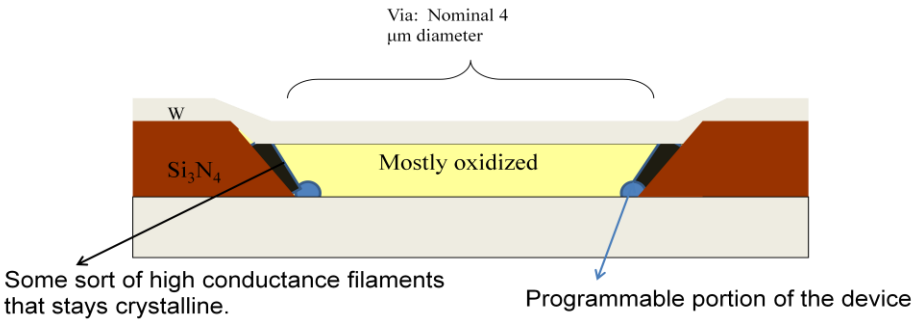

Figure 17. Cartoon depicting possible explanation for switching behavior in array sample devices containing mostly oxidized GST.

Thin film sample preparation. Thin film samples deposited at Boise State University were also analyzed by EXAFS in July 2009. The thin film samples prepared are listed in Table 2

below. Undoped germanium selenide in four different stoichiometries, two stoichiometries of germanium selenide doped with manganese at 3% and one stoichiometry of germanium selenide doped with tin and one doped with zinc at 3% each were synthesized by the standard rocking furnace method. Thin film samples were prepared by thermal evaporation from the synthesized bulk materials. Each film was deposited on quartz slides in triplicate and also on a 200 mm Si wafer for ICP elemental analysis and on several wafer fragments for additional analysis if needed, during the same deposition run by including all substrates within the chamber. In this way all replicate films were identical. Samples were annealed as shown in Table 2, using a RTP-600S Rapid Thermal Processor (RTP). Table 3 shows the annealing profile used for both argon and oxygen atmosphere anneals.

Table 2. Film samples prepared at Boise State University for EXAFS analysis.

	Samples							
Substrate, Sample processing	Substrate →	8" wafer	Quartz Slides (as deposited)	Quartz Slides (annealed at 150 ^{0}C in Ar environment, 20 min)	Quartz Slides (annealed at 150 ^{0}C in O_2 environment, 20 min)	EXAFS Data Completed		
Purpose		ICP analysis	UV-Vis-IR, Raman; EXAFS	UV-Vis-IR, Raman; EXAFS	UV-Vis-IR, Raman; EXAFS	Ge K edge	Se K edge	Dopant edge
	$Ge_{23}Se_{77}$	1	2	2	2	✓ 7/22/09	✓ 7/22/09	
	$(Ge_{23}Se_{77})_{97}Mn_3$	1	2	2	2	✓ 7/22/09	✓ 7/22/09	Mn K edge 7/22/09
	$Ge_{40}Se_{60}$	1	2	2	2	✓ 7/22/09	✓ 7/22/09	
	$(Ge_{40}Se_{60})_{97}Mn_3$	1	2	2	2	✓ 7/22/09	✓ 7/22/09	Mn K edge 7/22/09
	$Ge_{10}Se_{90}$	1	2	2	2	✓ 7/22/09	✓ 7/22/09	
	$Ge_{50}Se_{50}$	1	2	2	2	✓ 7/22/09	✓ 7/22/09	
	$(Ge_{40}Se_{60})_{97}Sn_3$	1	2	2	2	✓ 7/22/09	✓ 7/22/09	
	$(Ge_{40}Se_{60})_{97}Zn_3$	1	2	2	2	✓ 7/22/09	✓ 7/22/09	
Total		8	16	16	16			

Table 3. Annealing profile used to anneal thin films under argon or oxygen atmosphere.

Step:	1	2	3	4	5	6
Condition:	idle	idle	Ramp	Hold	Ramp	Stop
Time (sec):	60	15	300	1200	300	
Temp (°C):			150	150	30	
Flow rate (SLPM):	10	3	3	3	3	

In addition to the thin film samples, samples of all three manganese oxides were prepared at North Carolina State University for comparison to the doped manganese in the thin film samples. Table 4 lists the samples prepared, as powders on adhesive, and the data collected.

Table 4. Manganese oxides prepared for EXAFS, and data collected.

	Samples							
Substrate, Sample processing	Mn (II), Mn (III) and Mn (IV) oxide	EXAFS Data Completed						
Purpose		Ge K edge	Se K edge	Sb edge	Te edge	Dopant edge	L2 Edge	Other
	Mn (II) Oxide							Mn K edge 7/22/09
	Mn (III) Oxide							Mn K edge 7/22/09
	Mn (IV) Oxide							Mn K edge 7/22/09

Model 1 fixed and fitted parameters. For the fixed parameters, the first shell coordination number was 4 for Ge and 2 for Se. Bond distances of Ge-Se, Ge-Ge and Se-Se were set according to Zhou et al. (Zhou, W., Paesler, M. and D.E. Sayers Phys Rev. B 43(3) 1991 p 2315-2321). The Debye-Waller factor was greater than that used in Zhou et al., whose data was collected at 80°K. This data was collected at room temperature. The fitted parameters used were for the Ge edge, the ratio of Ge-Se to Ge-Ge bonds; for the Se edge, the ratio of Se-Ge to Se-Se bonds. The Se and Ge edges fit independently.

EXAFS Ge K edge data for doped and undoped thin films. Figures 18 through 23 show Ge K edge data plotted in the R space. Annealing at 150°C does not change the Ge coordination. The only significant change with annealing is for the $Ge_{50}Se_{50}$ composition. There is a significant change in the amplitude of the R space for different compositions. This is due to differences in the first neighbors of Ge and the slightly different mean coordination number. Ge and Se first neighbors in Ge_xSe_{1-x} compounds have very similar contribution in EXAFS, making it difficult to distinguish among Ge and Se. Doping at 3% of the metals represented does slightly change the EXAFS of the Ge K edge.

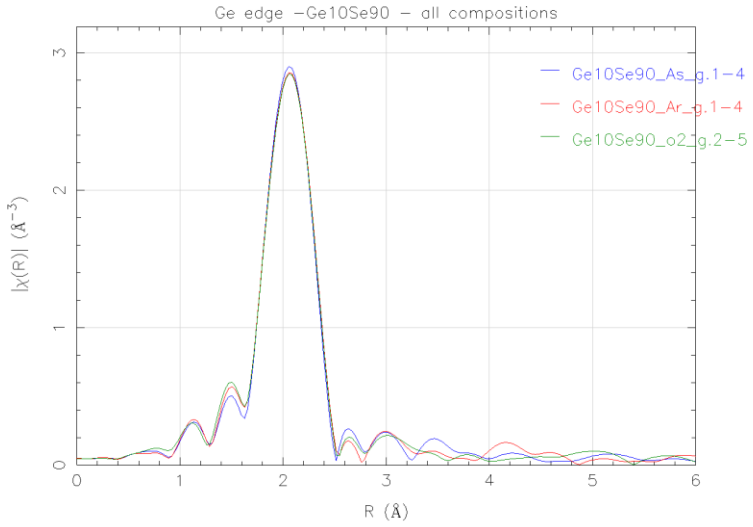

Figure 18a. Ge K edge for $Ge_{10}Se_{90}$ undoped film, as deposited (blue) and argon- (red) and oxygen-annealed (green).

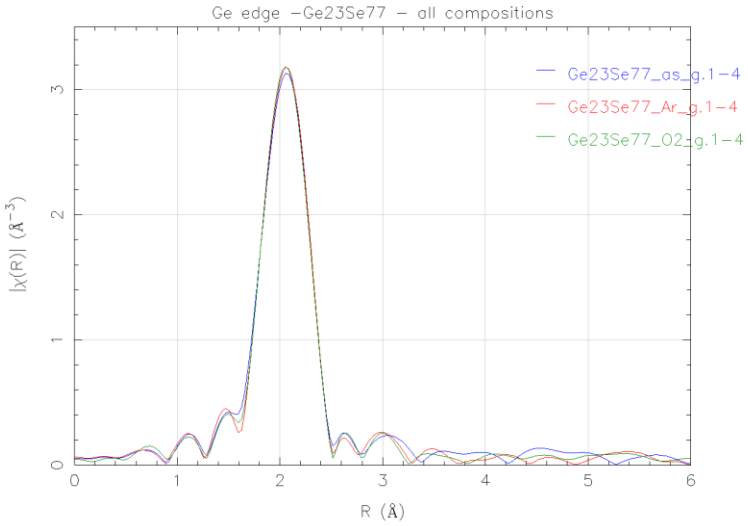

Figure 18b. Ge K edge for $Ge_{23}Se_{77}$ undoped film, as deposited (blue) and argon- (red) and oxygen-annealed (green).

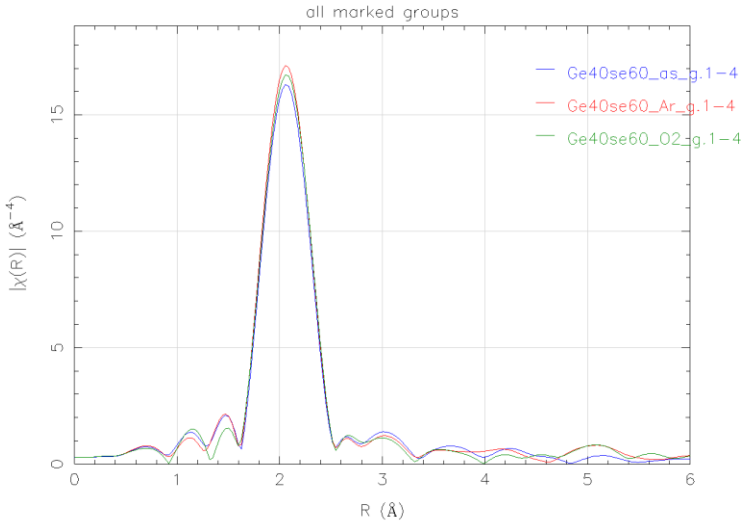

Figure 19. Ge K edge for $Ge_{40}Se_{60}$ undoped film, as deposited (blue) and argon- (red) and oxygen-annealed (green).

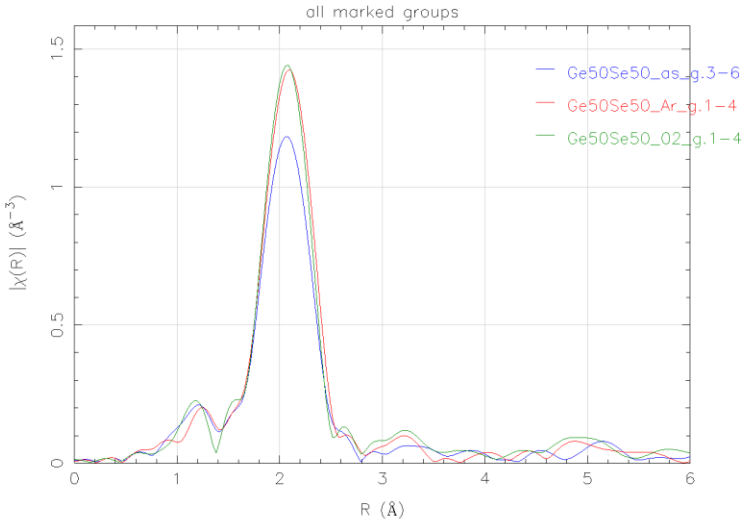

Figure 20. Ge K edge for $Ge_{50}Se_{50}$ undoped film, as deposited (blue) and argon- (red) and oxygen-annealed (green).

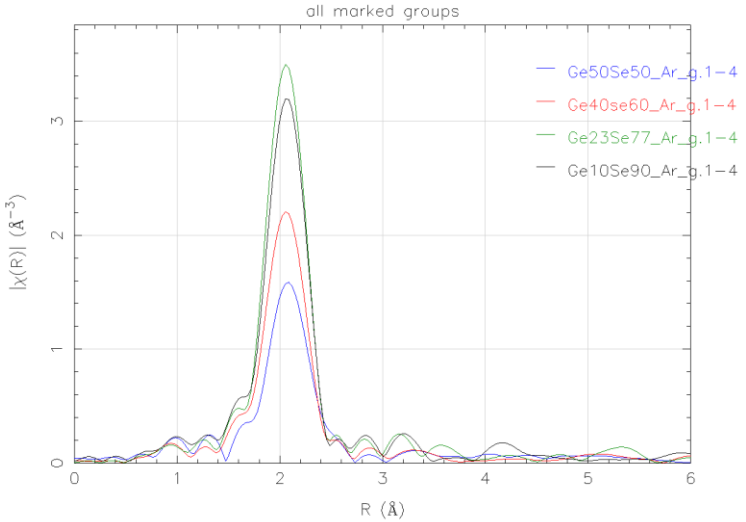

Figure 21. Comparison of the Ge K edge for all four undoped germanium selenide films, argon-annealed.

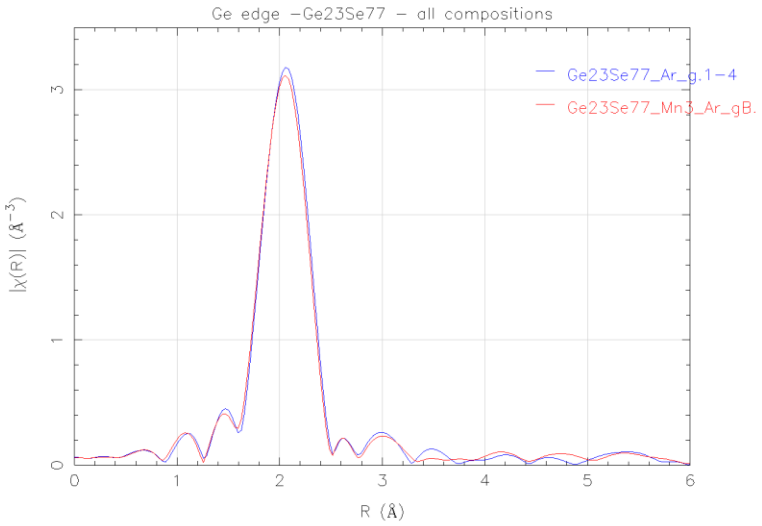

Figure 22. Ge K edge for $Ge_{23}Se_{77}$ undoped film (blue), compared to$(Ge_{23}Se_{77})_{97}Mn_3$ (red), both argon-annealed.

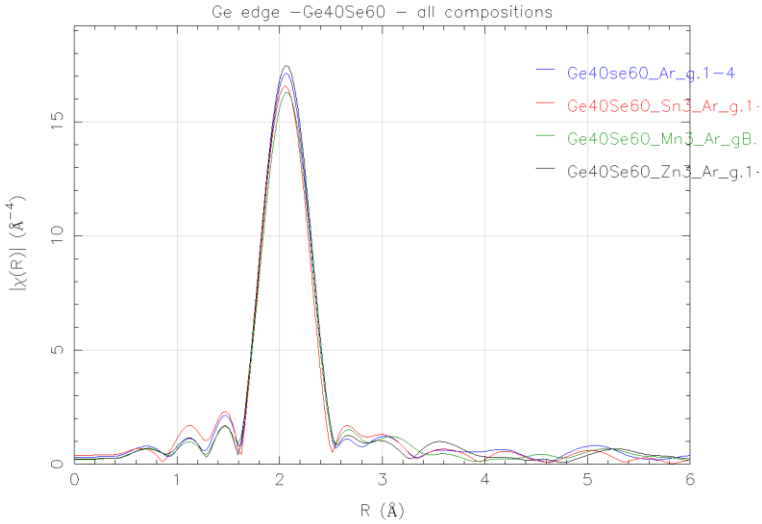

Figure 23. Ge K edge for $Ge_{40}Se_{60}$ undoped film (blue), compared to $(Ge_{40}Se_{60})_{97}Sn_3$ (red), $(Ge_{40}Se_{60})_{97}Mn_3$ (green) and a$(Ge_{40}Se_{60})_{97}Zn_3$ (black), all argon-annealed.

EXAFS Se K edge data for doped and undoped thin films. Figures 24 through 30 show Se K edge data plotted in the R space. Apart from the $Ge_{50}Se_{50}$ sample, annealing at 150°C does not change the EXAFS of the Se K edge. The amplitude of the EXAFS in the R space is strongly different for different compositions, although there is not a significant change in the R position. Doping at 3% does slightly change the EXAFS of the Se K edge.

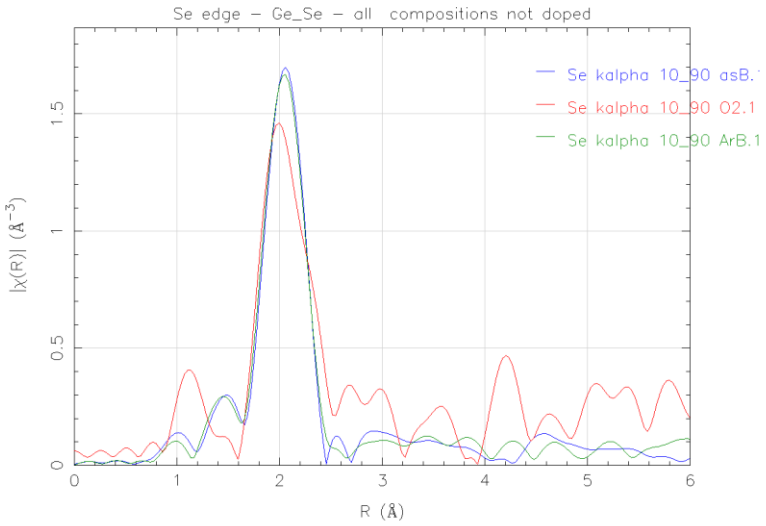

Figure 24. Se K edge for $Ge_{10}Se_{90}$ undoped film, as deposited (blue) and oxygen- (red) and argon-annealed (green).

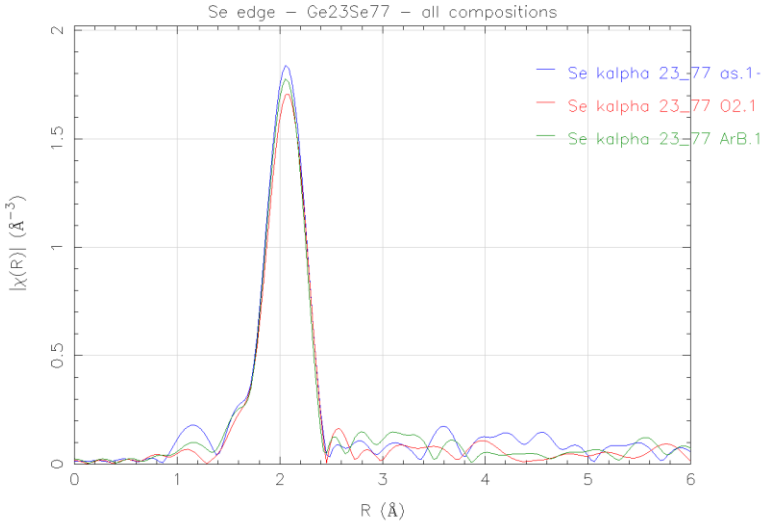

Figure 25. Se K edge for $Ge_{23}Se_{77}$ undoped film, as deposited (blue) and oxygen- (red) and argon-annealed (green).

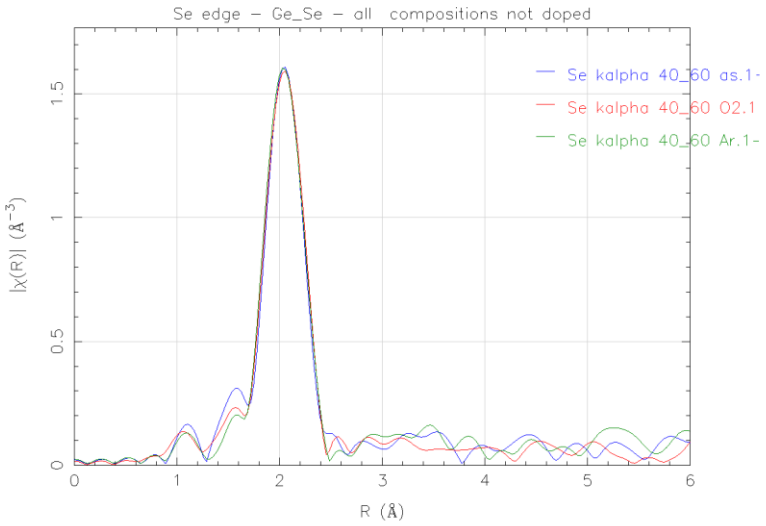

Figure 26. Se K edge for $Ge_{40}Se_{60}$ undoped film, as deposited (blue) and oxygen- (red) and argon-annealed (green).

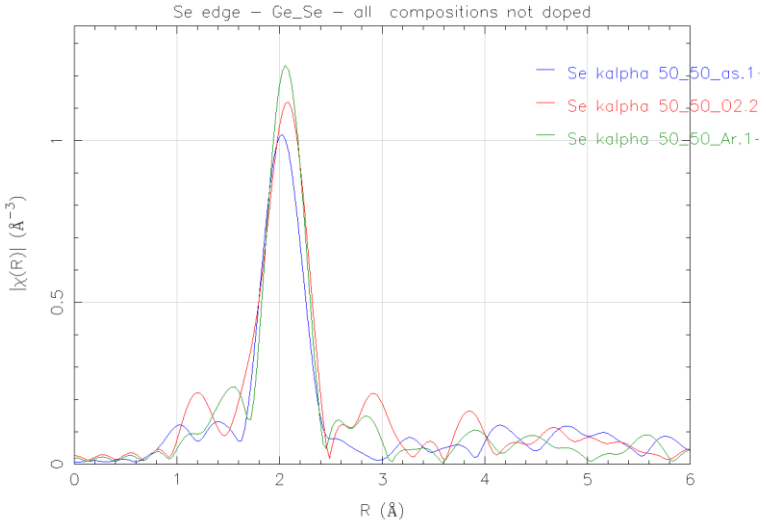

Figure 27. Se K edge for $Ge_{50}Se_{50}$undoped film, as deposited (blue) and oxygen- (red) and argon-annealed (green).

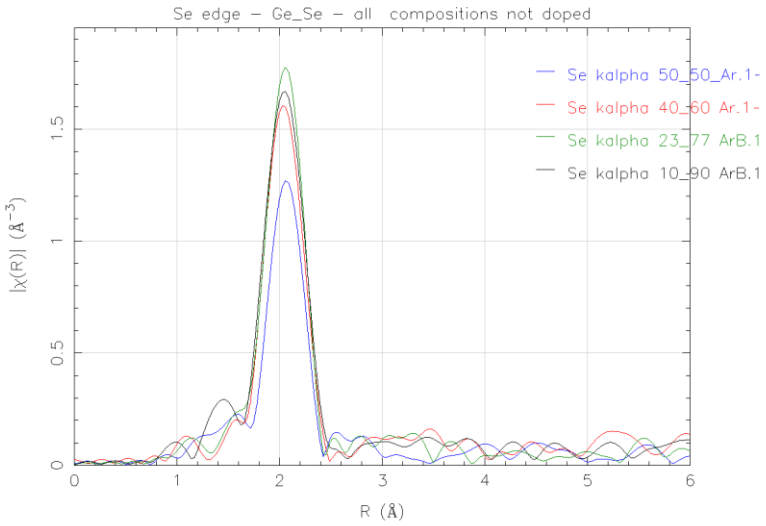

Figure 28. Comparison of the Se K edge for all four undoped germanium selenide films, argon-annealed.

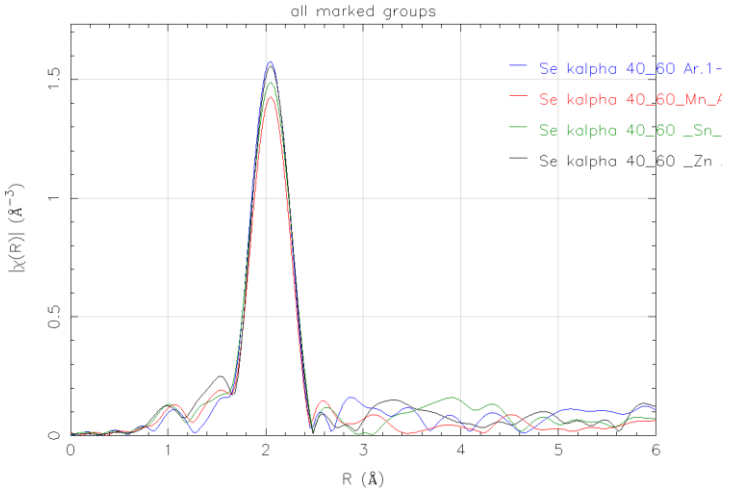

Figure 29. Se K edge for $Ge_{40}Se_{60}$ undoped film (blue), compared to $(Ge_{40}Se_{60})_{97}Mn_3$ (red), $(Ge_{40}Se_{60})_{97}Sn_3$ (green) and a$(Ge_{40}Se_{60})_{97}Zn_3$ (black), all argon-annealed.

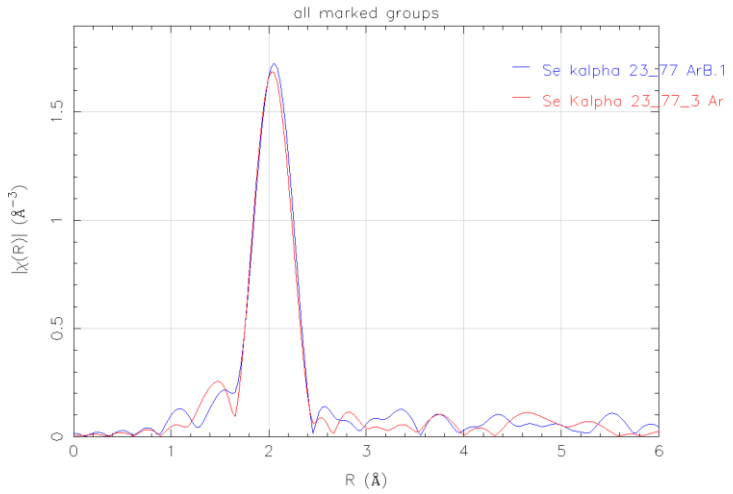

Figure 30. Se K edge for $Ge_{23}Se_{77}$ undoped film (blue), compared to$(Ge_{23}Se_{77})_{97}Mn_3$ (red), both argon-annealed.

EXAFS Mn K edge data for doped and undoped thin films and manganese oxides. Figures 31 and 32 show Mn K edge data plotted in the R space for thin films. Figure 33 presents the manganese oxide data. The Mn K edge data plotted comparing the manganese oxides to the manganese doped germanium selenide films indicates that the manganese is present in a mixed valence state, or in similar concentration of both Mn^{+2} and Mn^{+3}.

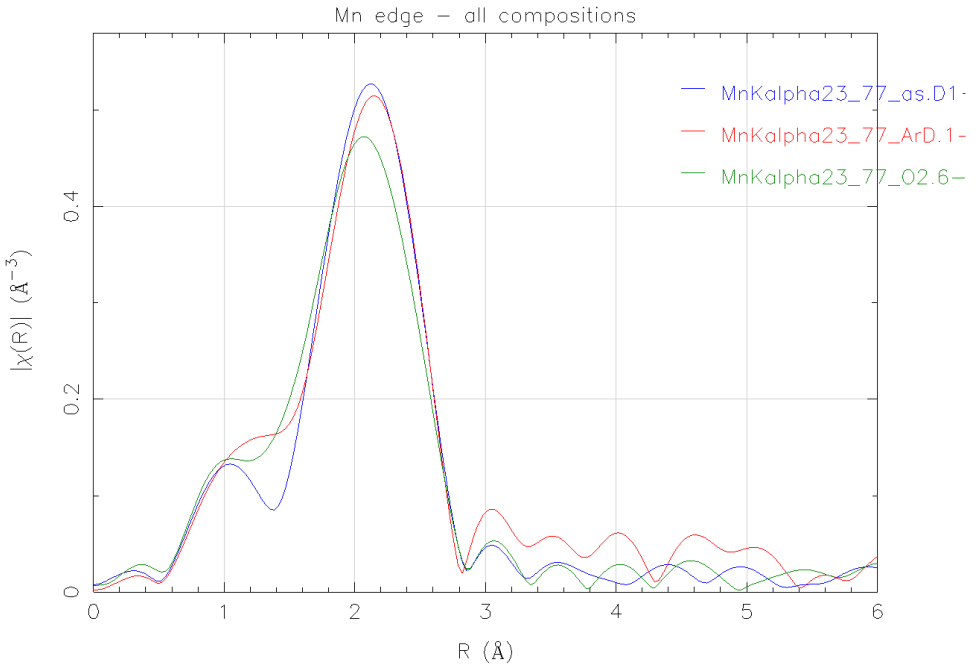

Figure 31. Mn K edge for $(Ge_{23}Se_{77})_{97}Mn_3$ as deposited (blue), argon-annealed (red) and oxygen-annealed (green).

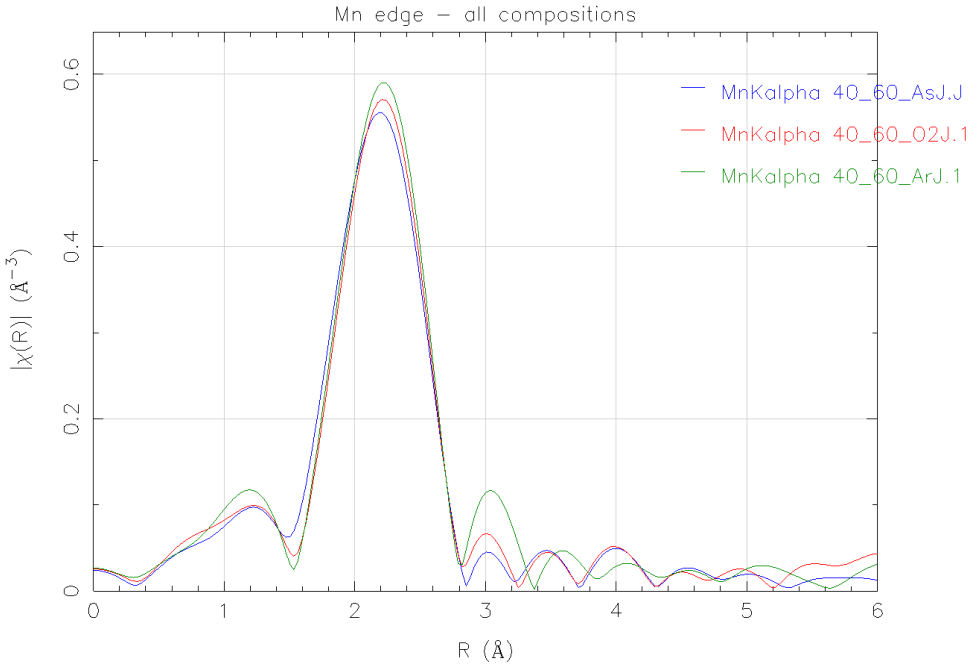

Figure 32. Mn K edge for $(Ge_{40}Se_{60})_{97}Mn_3$ as deposited (blue), oxygen-annealed (red) and argon-annealed (green).

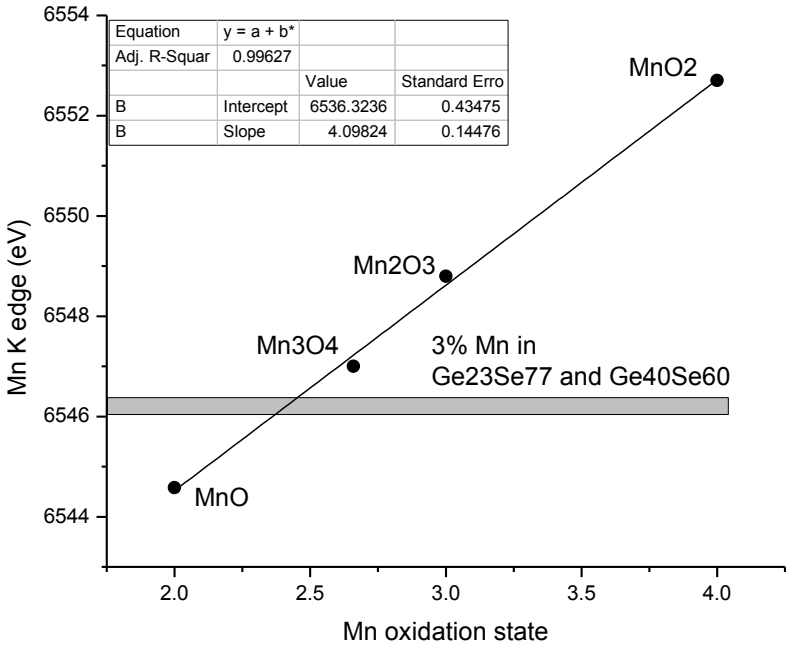

Figure 33. Mn K edge energy for various Mn oxides and for $Ge_{23}Se_{77}$ and $Ge_{40}Se_{60}$ as dopant.

EXAFS spectral analysis performed at Argonne National Laboratory October 2009

Some of the same films with data shown above were annealed at a higher temperature and re-analyzed by EXAFS at Argonne National Laboratory in October, 2010. This data is awaiting analysis and utilization of the ICP-AES data recently obtained.

i. Supplemental ICP-AES data. Table 5 shows the elemental analysis of the 8 film samples analyzed by EXAFS. This data was recently obtained and will be utilized to model the EXAFS data collected in October 2009. The films were etched off wafer pieces using a blend of sulfuric, nitric and hydrofluoric acids and diluted for analysis.

Table 5. Elemental analysis of thin films by ICP-AES.

Film	Ge (mol%)	Se (mol%)	Mn (mol%)	Sn (mol%)	Zn (mol%)	Mass Recovery (%)
(Ge40Se60)97Zn3	41.7	58.3			<0.2	91.2
(Ge40Se60)97Mn3	40.9	57.9	1.2			86.5
(Ge23Se77)97Mn3	24.3	72.9	2.9			100
Ge40Se60	41.0	59.0				86.1
Ge23Se77	24.4	75.6				95
Ge50Se50	49.8	50.2				86.3
Ge10Se90	10.5	89.5				101.4
(Ge40Se60)97Sn3	40.6	58.0		1.4		112

Device Fabrication and Electrical Characterization. Phase Change Memory Devices Based on GeSeSn Materials

Device Fabrication Details.

Selected Masks used for Fabrication:

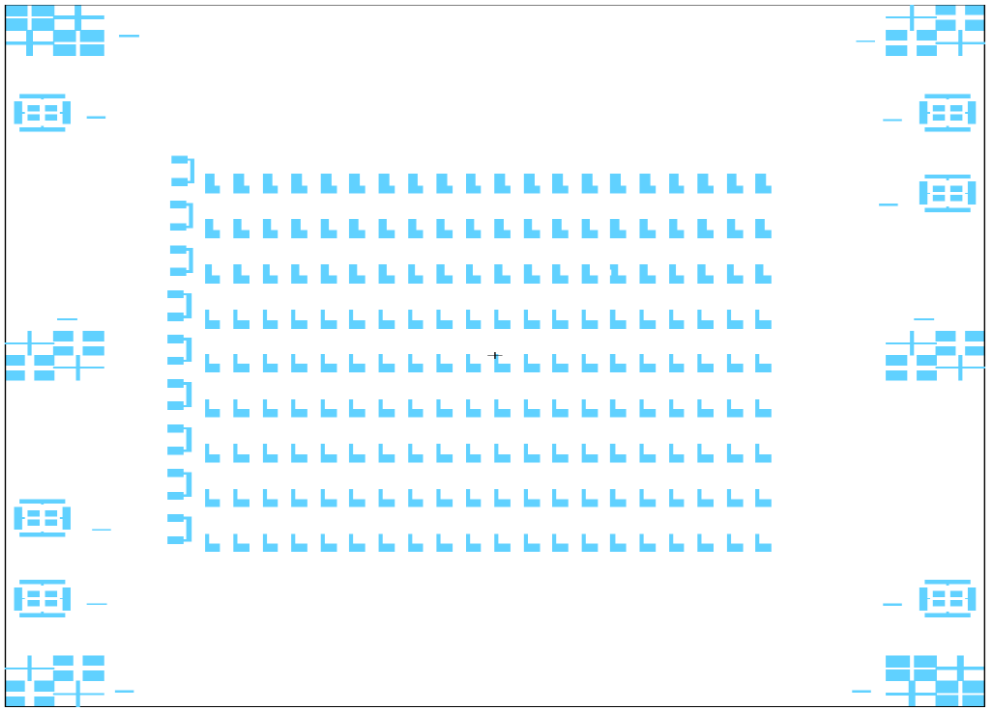

Fig. 34. Metal 1, Bottom Electrode (Mask 1).

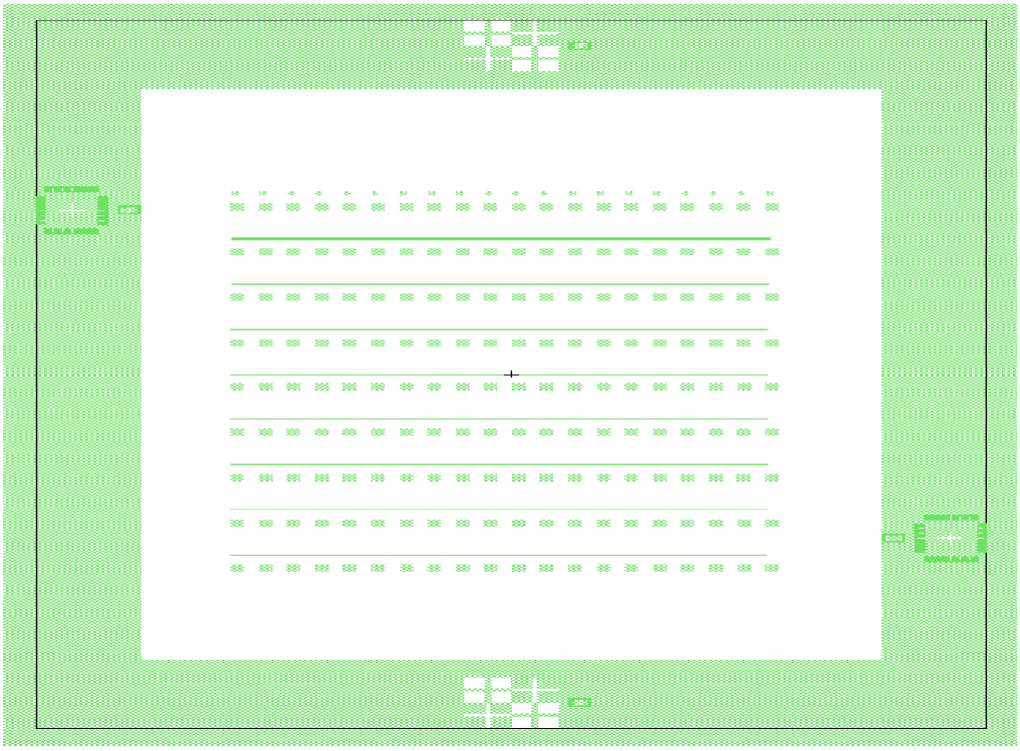

Fig. 35. Via + Bond Openings (Mask 5).

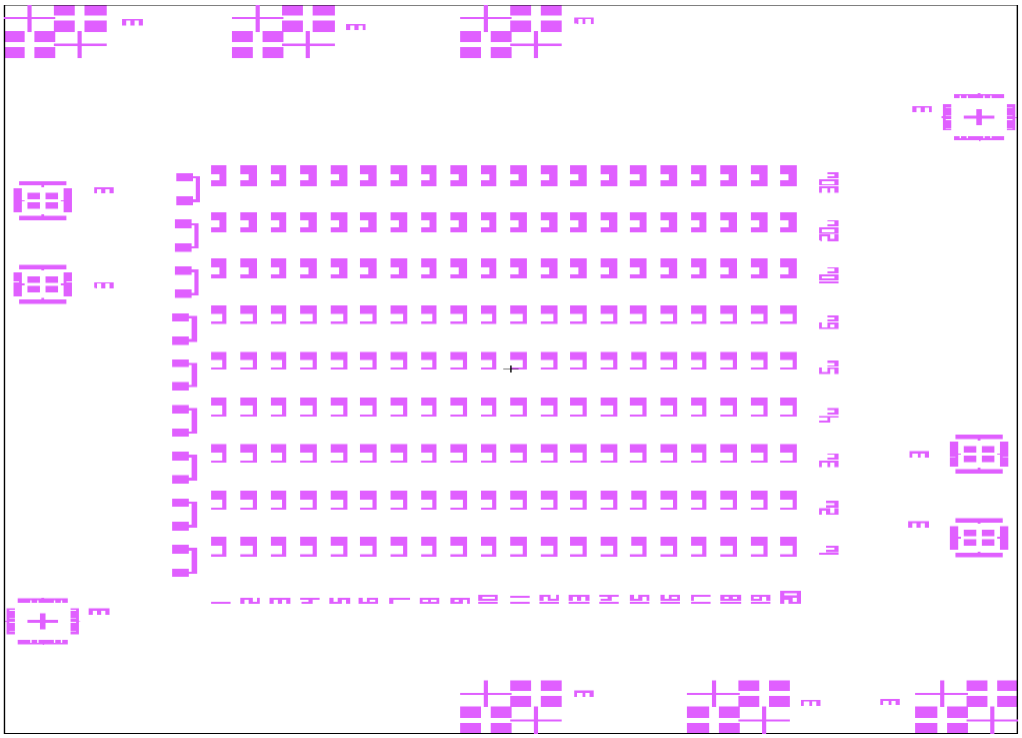

Fig. 36. Metal 2, Top Electrode (Mask 3).

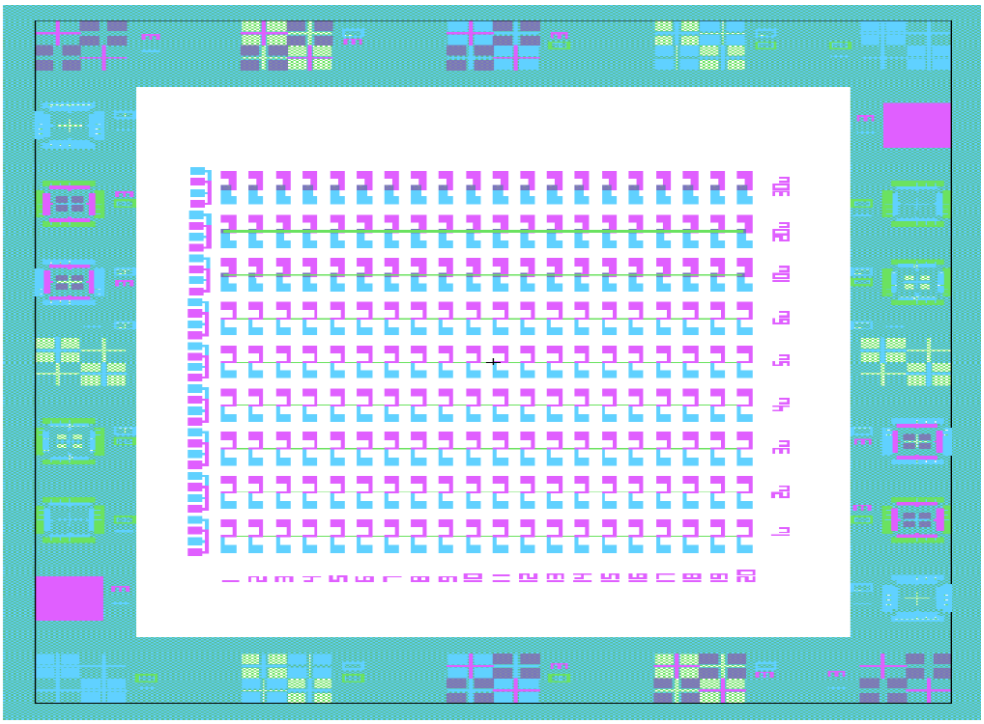

Fig. 37. All 3 Mask Layers Aligned.

Device Fabrication:

A cross-sectional cartoon of a device used in this study is shown in Fig. 38. At first, W/Cr bottom electrodes were defined out of W/Cr/SiN/Si wafer by ion-milling with a Veeco ion-mill after the required photolithography step. Insulating SiN layer was then deposited by CVD method and then, patterned through deep reactive-ion etching with an Oxford Plasma Lab System.

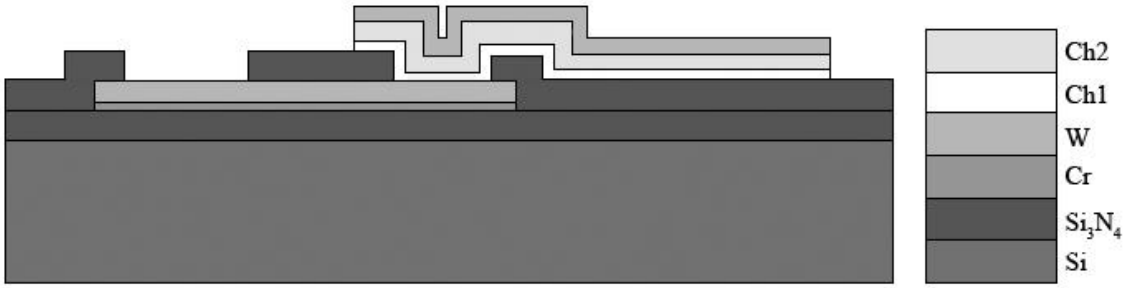

Fig. 38. Cross-sectional cartoon of the fabricated device

The two Chalogenide layers (at first, metal doped $Ge_{40}Se_{60}$ layer, then SnSe) were deposited without breaking the vacuum by thermal evaporation using a CHA Industries SE-600-

RAP thermal evaporator. After the sputtered deposition of the top W layer, ion-mill dry-etch was performed to form fully functional devices.

Optical microscope example images of the completed devices are given in Fig. 39.

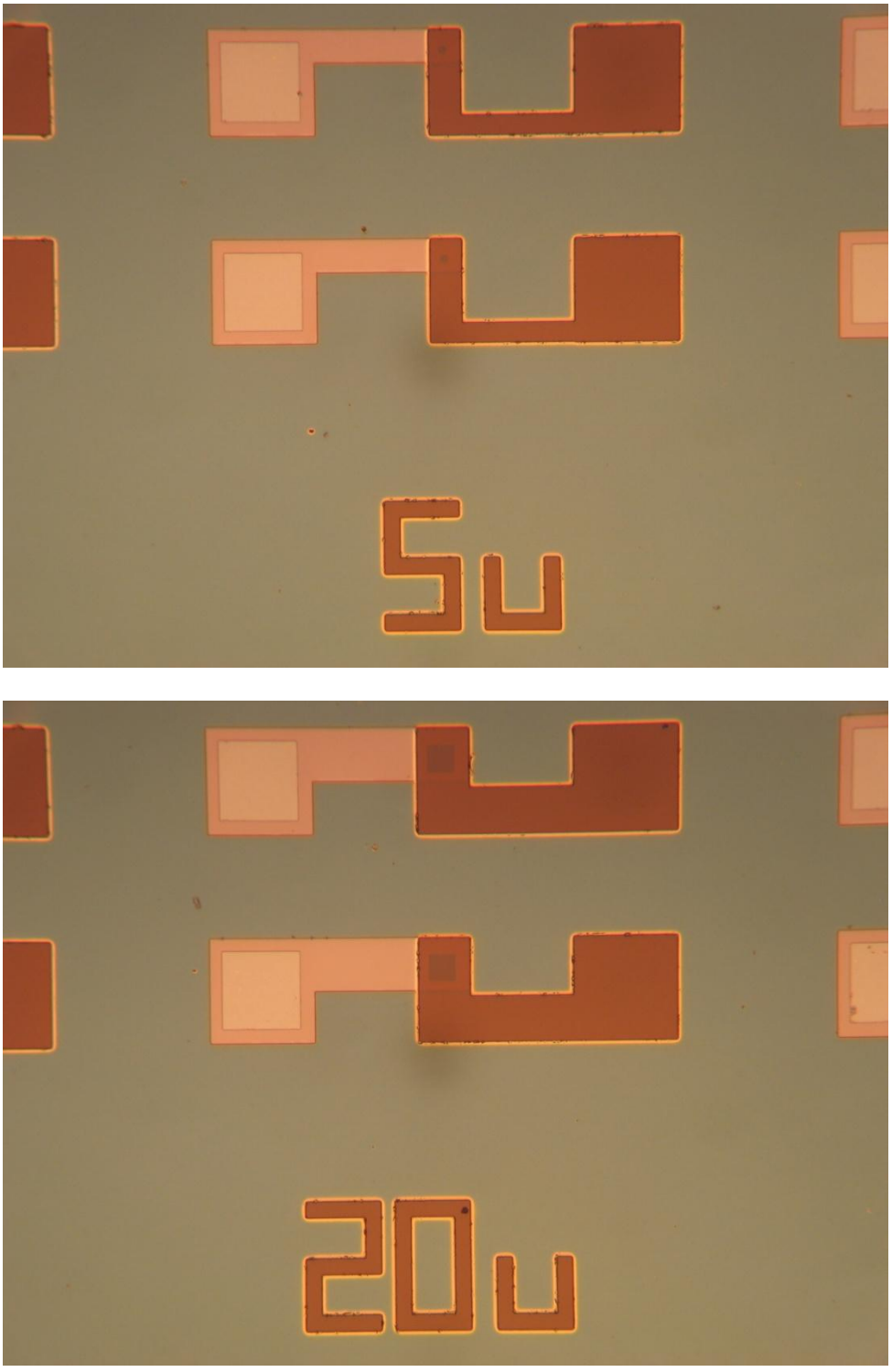

Fig. 39. Optical microscope example images of the completed devices.

Process Development:

Time frame of total process development is given below in tabular form:

Single Device Processing Completed on 9/21/09: Isolated Bottom Electrode New Single Devices
Note: Lot 09717-1A, wafers as purchased have 600Å W with ~200Å Cr adhesion film on 800Å Si3N4 on Si.

Wafer Description			Bottom Electrode				shipping	Processing at ISU	shipping	Via Patterning & Etch into Nitride at BSU			Chalcogenide Stack Deposition			Top Electrode Patterning & Etch at BSU			
Lot#.Slot#	Substrate	Split description	Photolitho-graphy: W Bottom Electrode	Plasma Etch W, hard stop on Cr	Tungsten Ar^+ Ion Mill Etch BE Chromium	Photoresist Strip	to ISU	PE-CVD Si_3N_4	returned to BSU	Via Photolitho-graphy	Plasma Etch Vias	Photoresist Strip	Ar^+ Ion Mill BE Sputter Clean	Evap	Stack Description	Tungsten Sputter 350Å	Photolitho-graphy: Top Electrode	Tungsten Ar^+ Ion Mill Etch TE	Photoresist Strip
090717-1A.03	W/Cr/SiN/Si	Isolated Bottom Electrode New Single Devices using W on Insulator wafers	8/5/09	8/5/09	8/5/09	8/6/09-8/7	8/11/09	→	8/19/09	8/25/09	8/26/09	9/10/09	09/11/09	09/11/09	$(Ge_{40}Se_{60})_{97}Sn_3$/SnSe	09/11/09	09/15/09	09/21/09	
090717-1A.04	W/Cr/SiN/Si		8/5/09	8/5/09	8/5/09	8/6/09-8/7	8/11/09	→	8/19/09	8/25/09	8/26/09	9/10/09	09/11/09	09/11/09	$(Ge_{40}Se_{60})_{97}Sn_3$/SnSe	09/11/09	09/15/09	09/21/09	
090717-1A.05	W/Cr/SiN/Si		8/5/09	8/5/09	8/6/09	8/6/09-8/7	8/11/09	→	8/19/09	8/25/09									
090717-1A.06	W/Cr/SiN/Si		8/5/09	8/5/09	8/6/09	8/6/09-8/7	8/11/09	→	8/19/09	8/25/09	8/26/09	9/10/09	09/11/09	09/11/09	$(Ge_{40}Se_{60})_{97}Sn_3$	09/11/09	09/15/09	09/21/09	
090717-1A.07	W/Cr/SiN/Si		8/5/09	8/5/09	8/6/09	8/6/09-8/10	8/11/09	→	8/19/09	8/25/09	8/26/09	9/10/09	09/11/09	09/14/09	$(Ge_{40}Se_{60})_{97}Zn_3$/SnSe	09/14/09	09/15/09	09/21/09	
090717-1A.08	W/Cr/SiN/Si		8/5/09	8/5/09	8/6/09	8/6/09-8/7	8/11/09	→	8/19/09	8/25/09	8/26/09	9/10/09	09/11/09	09/14/09	$(Ge_{40}Se_{60})_{97}Zn_3$/SnSe	09/14/09	09/15/09	09/21/09	
090717-1A.09	W/Cr/SiN/Si		8/5/09	8/5/09	8/6/09	8/6/09-8/7	8/11/09	→	8/19/09	8/25/09	8/26/09	9/10/09	09/11/09	09/14/09	$(Ge_{40}Se_{60})_{97}Zn_3$	09/14/09	09/15/09	09/21/09	
090717-1A.10	W/Cr/SiN/Si		8/5/09	8/5/09	8/6/09	8/6/09-8/10	8/11/09	→	8/19/09	8/25/09	8/26/09	9/10/09							
090717-1A.11	W/Cr/SiN/Si		8/5/09	8/5/09	8/6/09	8/6/09-8/7	8/11/09	→	8/19/09	8/25/09	8/26/09	9/10/09							
090717-1A.12	W/Cr/SiN/Si		8/5/09	8/5/09	8/6/09	8/6/09-8/10	8/11/09	→	8/19/09	8/25/09	8/26/09	9/10/09							
090717-1A.13	W/Cr/SiN/Si		8/5/09	8/5/09	8/6/09	8/6/09-8/7	8/11/09	→	8/19/09	8/25/09									
090602-1.14	W/Cr/Si	Si_3N_4 witness/test wafer	n/a	n/a	n/a	n/a	8/11/09	→	8/11/09	8/25/09	8/26/09								

Slot 4 & 8 were used for SEM cross-sectional studies.
Studies on slot 6 & 9 are yet not complete.

090717-1A:

Slot 3: $(Ge_2Se_3)_{97}Sn_3$ (~ 30 nm)/SnSe (~ 38 nm)
Slot 7: $(Ge_2Se_3)_{97}Zn_3$ (~ 32 nm)/SnSe (~ 42 nm)

SEM Images of the Control wafers:
$(Ge_2Se_3)_{97}Sn_3$/SnSe:

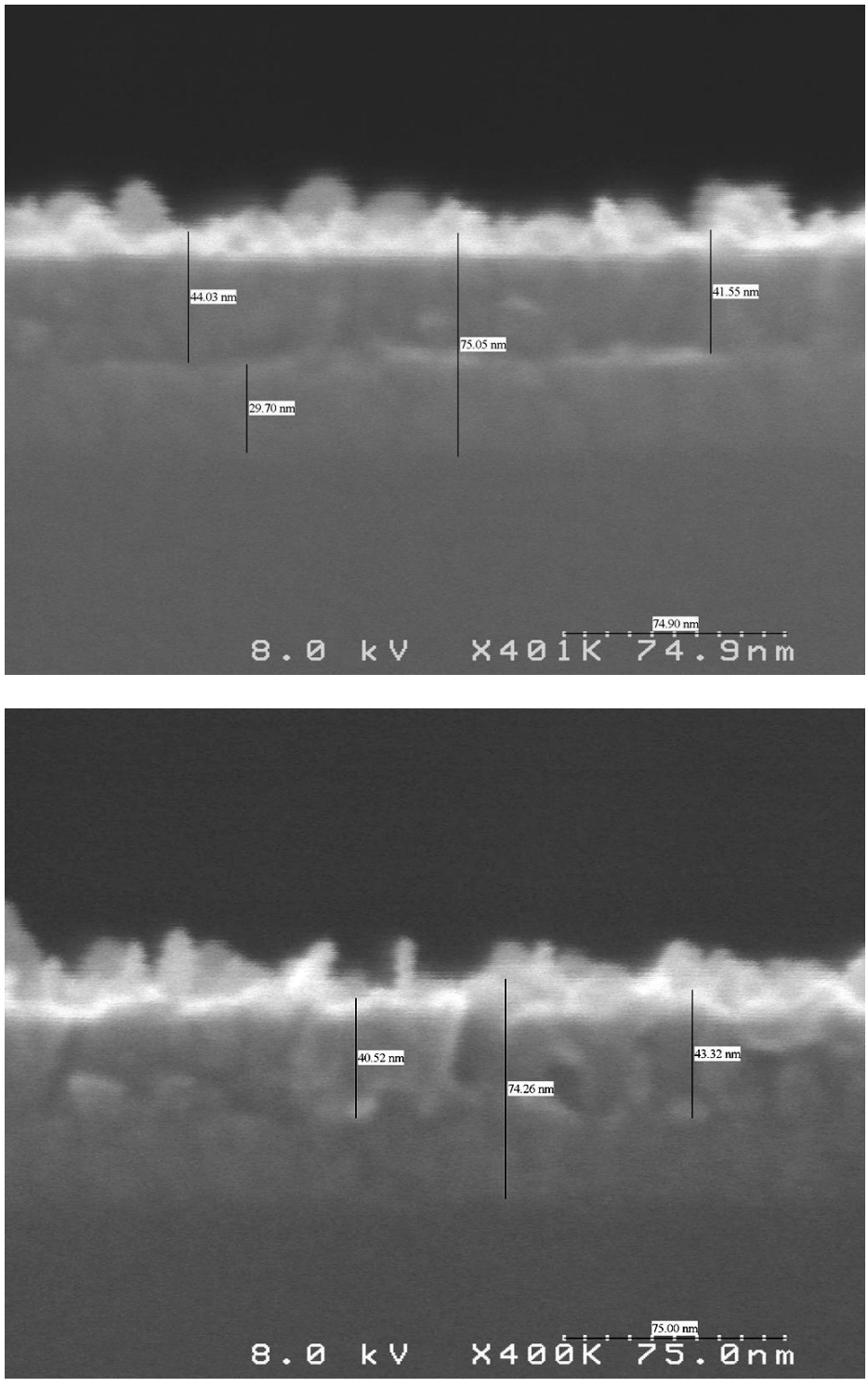

Fig. 40. SEM images of the deposited $(Ge_2Se_3)_{97}Sn_3$/SnSe films, used to determine thickness and film morphology.

$(Ge_2Se_3)_{97}Zn_3$ /SnSe:

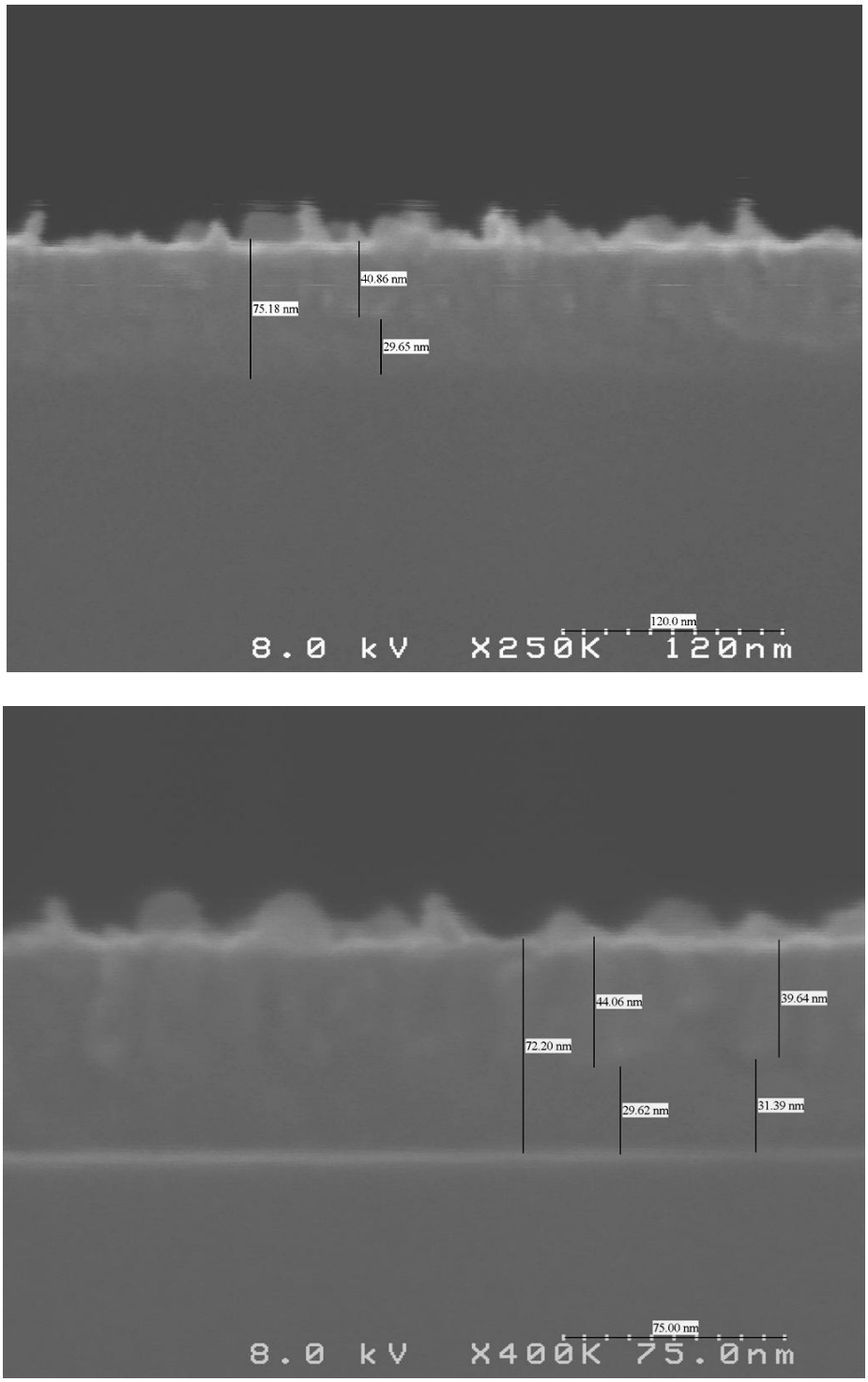

Fig. 41. SEM images of deposited $(Ge_2Se_3)_{97}Zn_3$ /SnSe films.

Switching Results:

Electrical measurements were made using a Micromanipulator 6200 microprobe station equipped with Agilent B1500A Semiconductor Device Analyzer, and American Probe's probes with 1.5 μm W tips (model: 73CT-APTA/15).

Single Two-Terminal Devices:

Slot 3: $(Ge_2Se_3)_{97}Sn_3$ (~ 30 nm)/SnSe (~ 38 nm)

Stacks	$(Ge_{40}Se_{60})_{97}Sn_3$/SnSe																	
Slot No	Slot 3																	
VIA size	1 μm		2 μm		3 μm		4 μm		5 μm		6 μm		10 μm		20 μm		30 μm	
Nature of the current sweep (100 μA, $V_{compliance}$ = 20 V, 1001 steps)	Positive sweep	Negative sweep	Positive sweep	Negative sweep	Positive sweep	Negative sweep	Positive sweep	Negative sweep	Positive sweep	Negative sweep	Positive sweep	Negative sweep	Positive sweep	Negative sweep	Positive sweep	Negative sweep	Positive sweep	Negative sweep
Threshold voltages, V_{th} (V)	7.31	12.36	9.92	12.73	6.86	10.54	7.17	8.79	5.14	8.49	5.25	9.02	6.37	7.21	5.38	9.21	4.03	8.8
	9.57	8.92	9.93	11.12	8.94	12.19	5.37	8.6	4.95	9.16	5.18	7.31	5.37	8.01	5.26	8.18	4.67	8.55
	10.19	9.22	9.23	12.52	6.62	8.29	6.79	9.32	7.05	7.93	6.37	9.51	5.5	8.64	4.88	7.68	5.57	8.32
	6.02	9.64	10.26	11.87					6.34									
	9.77	13.95	10.5	13.09					6.27									
	12.43	15.05	9.84	14.65														
	11.19	13.27	10.58															
	10.23	12.42	10.17															
Average V_{th} (V)	9.58875	11.85375	10.05375	12.66333	7.473333	10.34	6.443333	8.903333	5.95	8.526667	5.6	8.613333	5.746667	7.953333	5.173333	8.356667	4.756667	8.556667

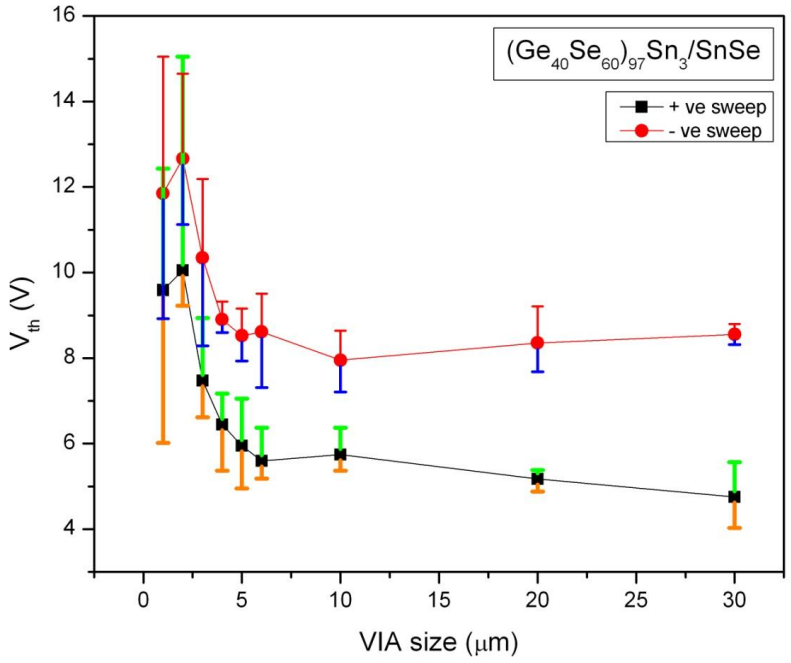

Fig. 42. Variation of threshold voltage (V_{th}) with respect to via size for two-terminal devices with (Ge2Se3)97Sn3/SnSe films for phase change memory operation.

Slot 7: $(Ge_2Se_3)_{97}Zn_3$ (~ 32 nm)/SnSe (~ 42 nm)

$(Ge_{40}Se_{60})_{97}Zn_3$/SnSe																	
Slot 7																	
1 µm		2 µm		3 µm		4 µm		5 µm		6 µm		10 µm		20 µm		30 µm	
Positive sweep	Negative sweep	Positive sweep	Negative sweep	Positive sweep	Negative sweep	Positive sweep	Negative sweep	Positive sweep	Negative sweep	Positive sweep	Negative sweep	Positive sweep	Negative sweep	Positive sweep	Negative sweep	Positive sweep	Negative sweep
11.24	9.25	6.52	8.61	6.8	8.42	7.89	8.93	7.47	8.05	7.4	9.05	6.74	8.69	7.12	9.19	6.27	8.42
9.44	10.81	5.81	8.51	7.36	8.09	7.9	8.68	7.65	8.67	7.37	8.87	7.04	8.39	7.16	8.79	6.99	8.93
9.82	11.04	6.94	7.92	6.99	8.26	7.64	8.97	6.85	8.57	7.42	8.83	7.2	6.63	6.72	8.81	6.72	9.13
8.66	9.63	8.67	9.16			7.73	8.8					5.43	5.84				
7.96	9.47	8.63	9.44			7.6	8.7					5.37	8.62				
9.55	9.75	8.48	9.18			7.55	8.69					5.53	8.47				
													8.57				
													8.33				
9.445	9.991667	7.508333	8.803333	7.05	8.256667	7.718333	8.795	7.323333	8.43	7.396667	8.916667	6.218333	7.9425	7	8.93	6.66	8.826667

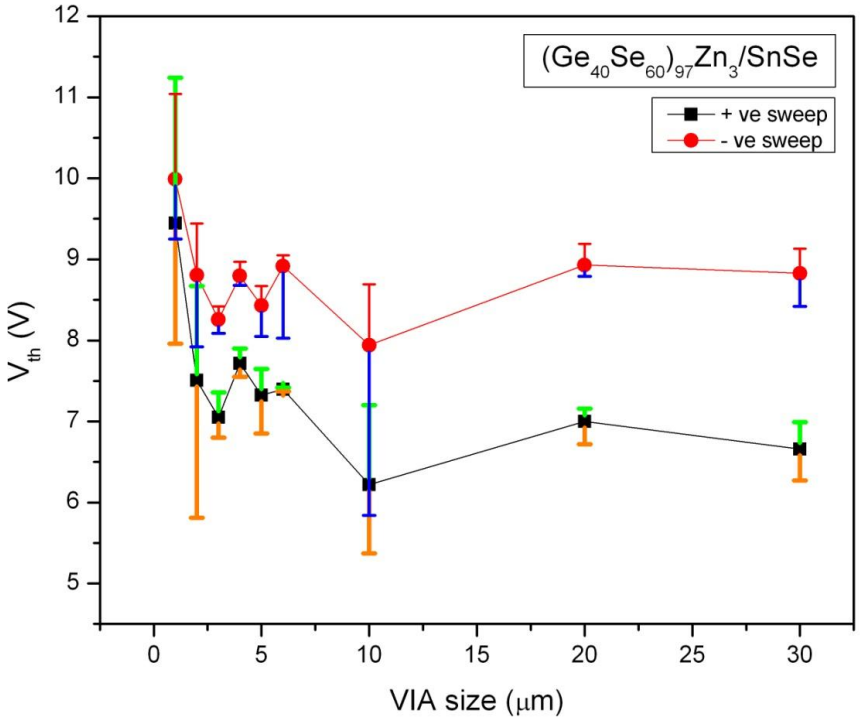

Fig. 43. Variation of threshold voltage (V_{th}) with respect to via size for the (Ge2Se3)97Zn3/SnSe phase change two-terminal devices.

Examples:

$(Ge_{40}Se_{60})_{97}Sn_3$/SnSe – 1 μm

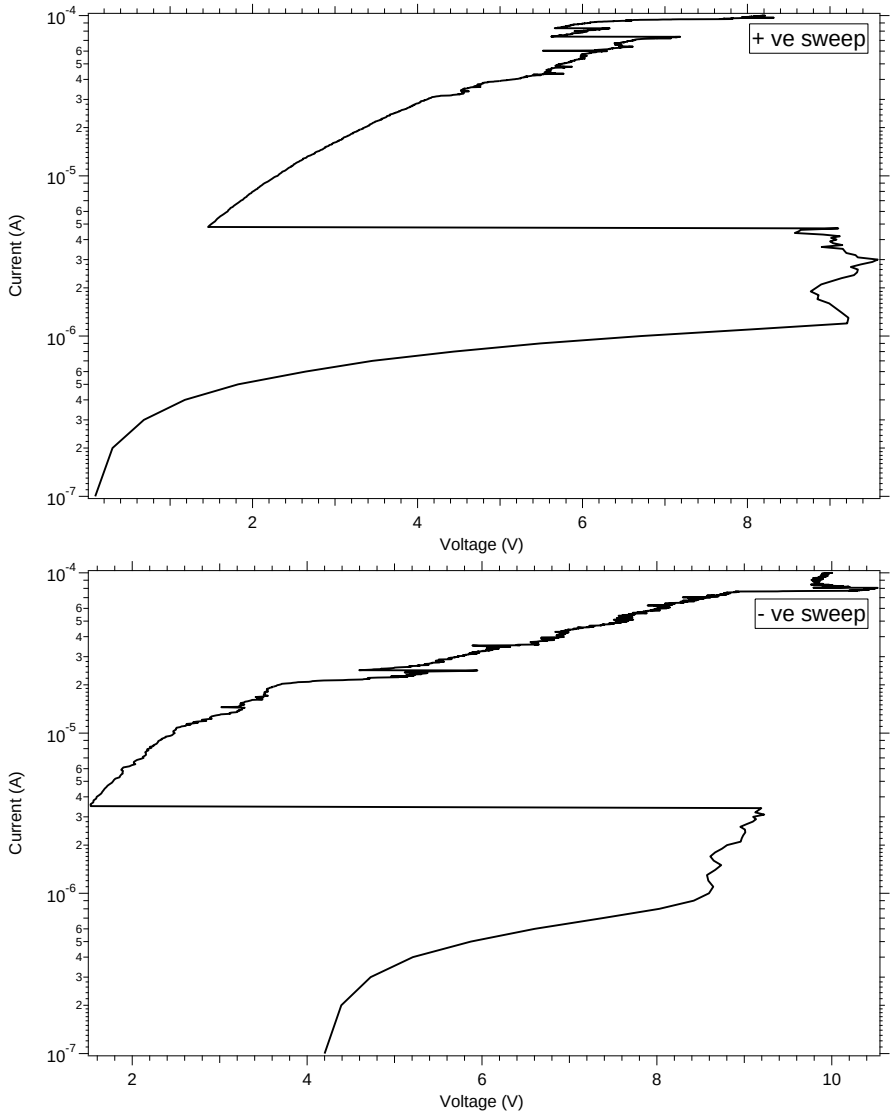

Fig. 44. Electrical switching results for positive potential on the top electrode (top graph) and the bottom electrode (bottom graph) for the $(Ge_{40}Se_{60})_{97}Sn_3$/SnSe 1 μm device size.

$\underline{(Ge_{40}Se_{60})_{97}Sn_3/SnSe}$ – 3 μm

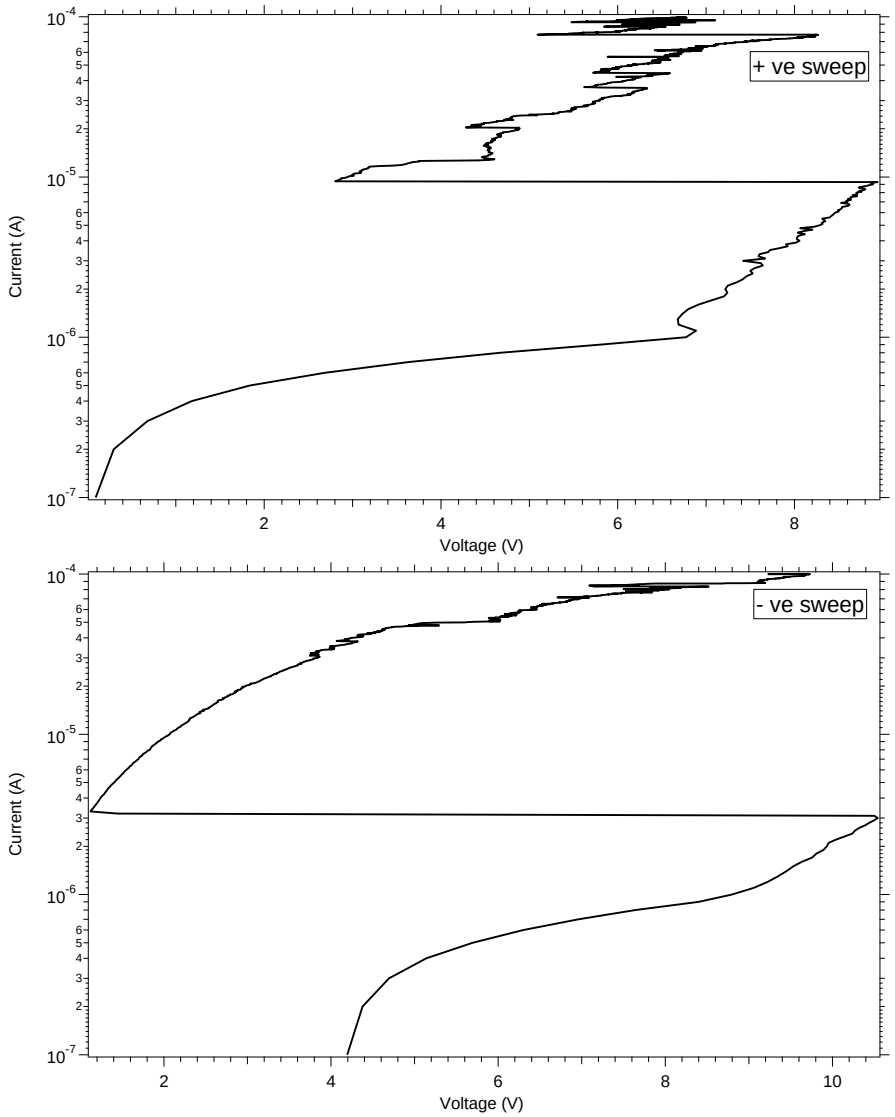

Fig. 45. Electrical Electrical switching results for positive potential on the top electrode (top graph) and the bottom electrode (bottom graph) for the $(Ge_{40}Se_{60})_{97}Sn_3/SnSe$ 3 μm device size. .

Study of effect of temperature on threshold voltage (V_{th}):

A cryogenic Probe Station (LakeShore; model: Model CRX-4K) is used to study the effect of the temperature on threshold voltage (V_{th}) in the range of 5-300 K. Results for the via size of 2 μm of slot 3 ($(Ge_{40}Se_{60})_{97}Sn_3$/SnSe) are shown in graphical form in Fig. 46. General trend of decrease in Vth with increase in temperature can be clearly seen from the figure. Analysis and study on other devices are underway.

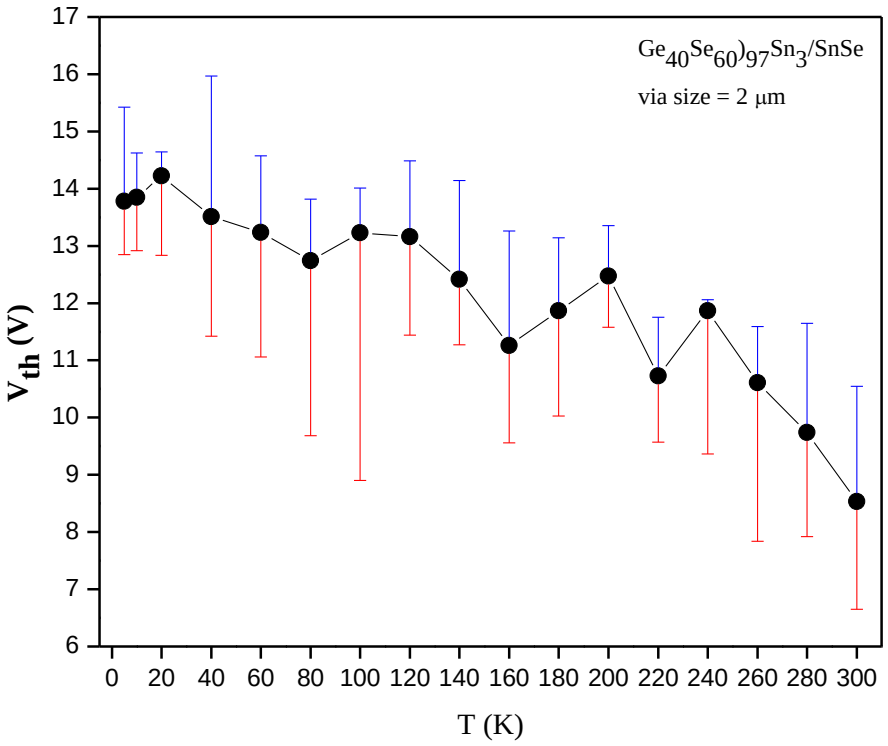

Fig. 46. V_{th} vs. T plot with maximum and minimum of V_{th} at each temperature.

Electrical Characterization of Devices

Electrical characterization is performed on one of three microprobe station in the characterization lab. The first set is basic semiconductor analysis instruments consisting of a Cascade-Microtech manual probe station and an Agilent 4156A or B1500A semiconductor analyzer (shown below).

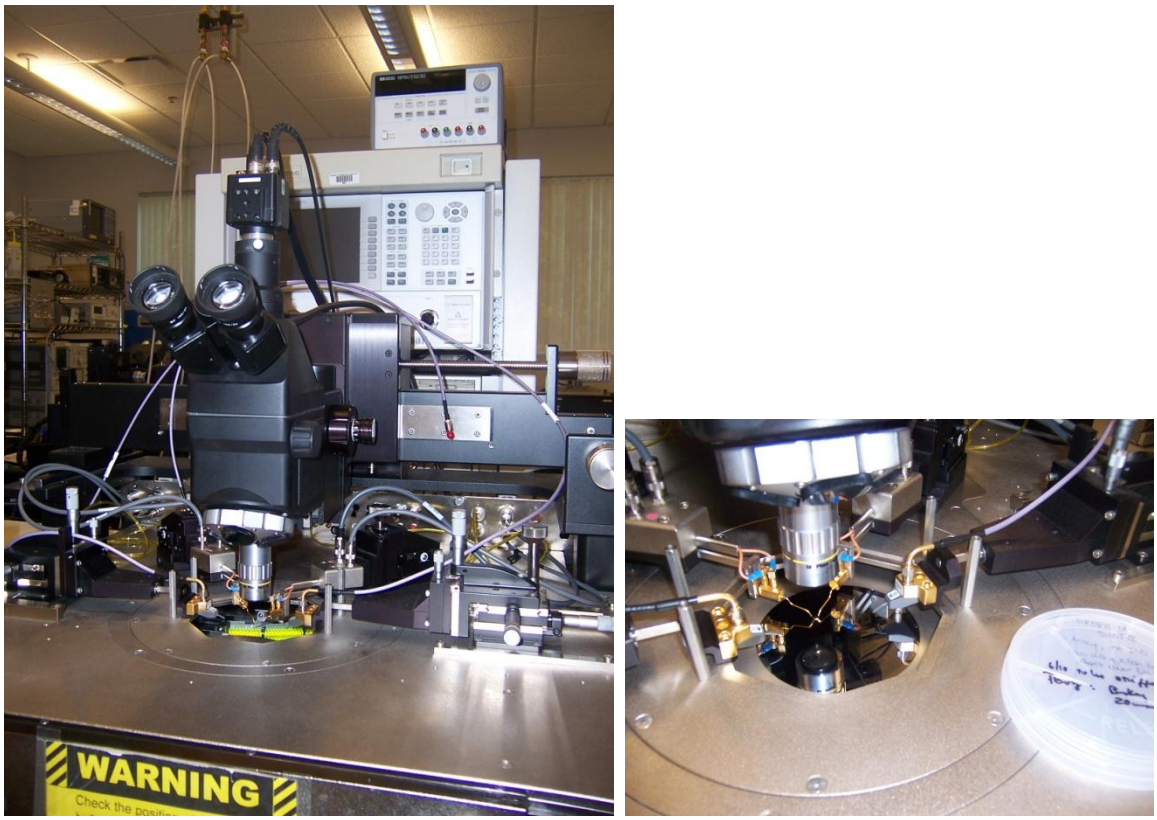

Fig. 47. One of the microprobe stations at Boise State University.

The second set of equipment is used for the automated test execution, which is responsible for recording the pre and post write resistance values, as well as automatically applying the write voltage to each bit in the arrays to be tested (shown below).

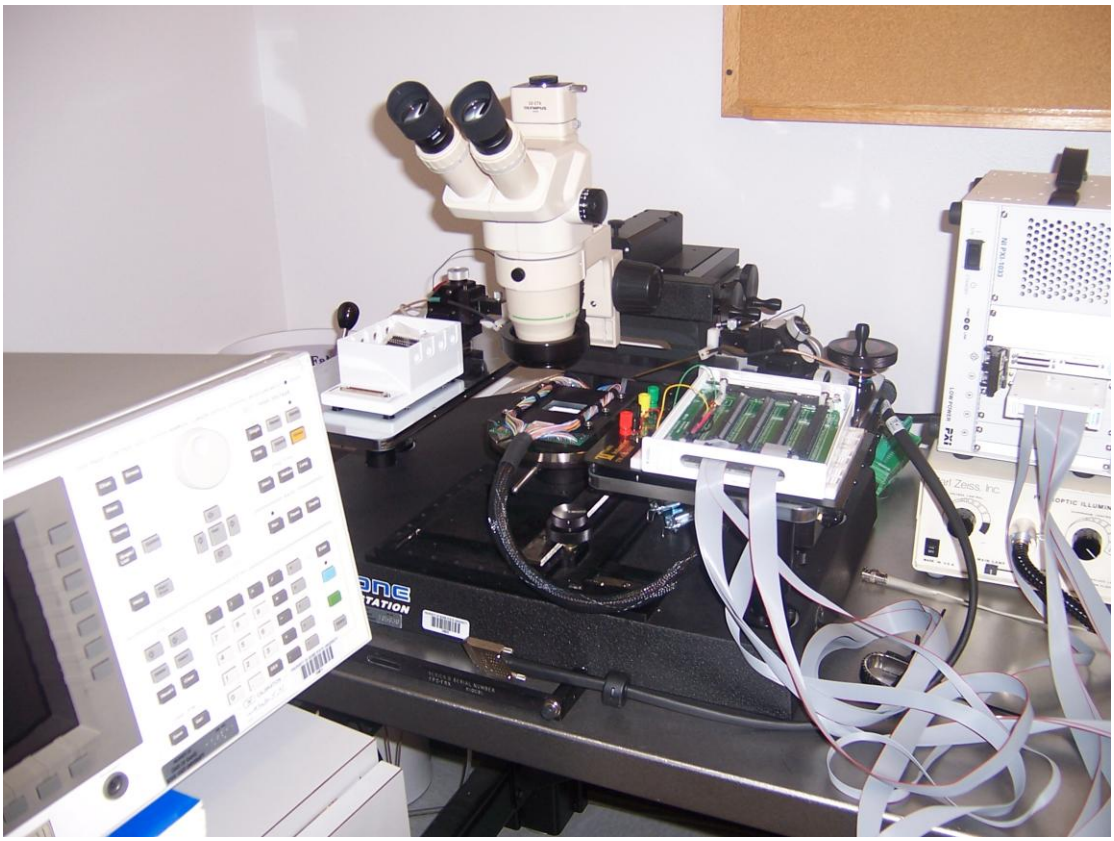

Fig. 48. Probe station for array programming.

This collection of hardware is controlled by the custom designed software interface (described below). The electrical measurement sequence is executed by an Agilent 4156A semiconductor parameter analyzer controlled through a PCI modulated GPIB interface. Data is reported to a desktop PC through the measurement BUS. The addressing (and bit isolation) is executed through a PCI controlled National Instruments PXI-1033 measurement BUS containing a PXI-2532 512 channel cross-point matrix with both a TB-2640 2wire by 256 channel converter and an SCB-204X breakout box. The breakout box is wired via 6 CN-50 connectors to a custom designed 300 pin probe card. The probe card is mounted on a Signatone S-1160 Probe station. Supplemental measurement and programming functions can be preformed using the National Instruments 7853R PXI based FPGA card mounted in the adjacent slot to the switch matrix. Supplemental software has been developed to generate write pulses using this card in the event that simple DC sweeps are insufficient or undesirable.

The automated test software is designed to execute an array of test functions from a single user interface. The purpose is to provide a platform for debugging variable segments of the completed switching array and to allow for automated write functionality. The size and number of the bits that must be effectively written precludes any attempt at a manual solution.

Software Design for Phase-Change Memory Array Testing

The primary test interface is written in LabVIEW 8.6 and is shown in Fig. 49.

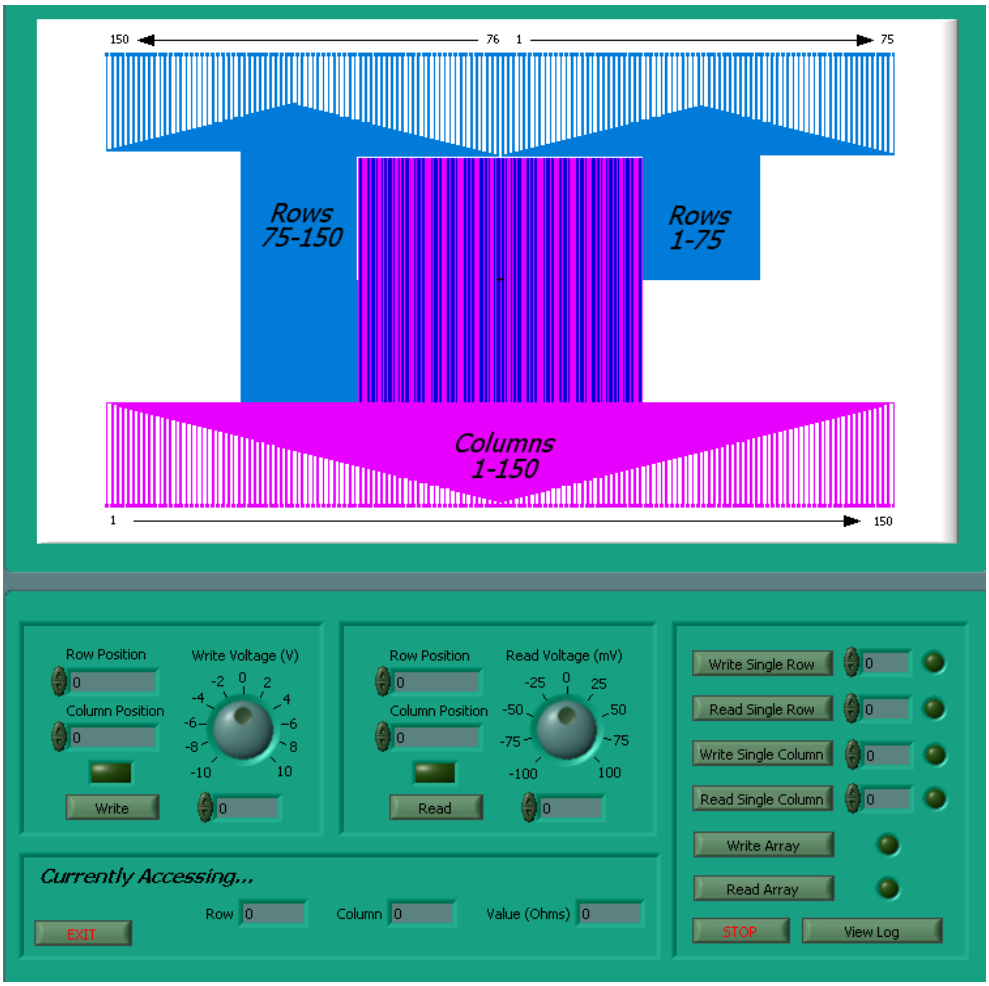

Fig. 49. Array programming software front control panel.

The software allows a user to manually address specific bits (by row and column position), complete rows, complete columns, array segments, or complete arrays to establish operating parameters for the sample of interest. Resistance of a bit(s) may be sampled, or the bit(s) may be written and the results recorded in a log file. Once operating parameters for the samples are known, an entire programming sequence may be initiated. The write mode sequence contains first, a pre-write resistance check at some user defined sampling voltage, followed by a voltage sweep to write the bit at some maximum voltage value, followed finally by a post-write resistance check to verify the bit has been programmed correctly. The measurement sequence executes a measurement group for each bit contained in the test array. The value at which the bit was written is determined by triggering the test instruments to abort at a predefined current compliance value and return the recorded voltage at the end of the measurement sequence. Results are stored during run-time in a log file and after the experiment is completed the data is exported directly to MS Excel, facilitating analysis.

For each bit tested, the results contain the position (row and column), the pre-write resistance value, the voltage value for the write, and the post-write resistance value. Any bit that was not fully written during the test process may be identified from the log file and re-written using the single write functions of the interface. During the file save procedure, additional identification is included such as lot/wafer identifiers and the die number. This methodology provides for positive identification of each bit as well as verification of the state of each bit. Supplemental information can also be gathered to aid further process development work and analysis such as the distribution of pre and post write resistance values and the distribution of the required write voltages. Much of the information is a valuable aid to the understanding and development of any future work.

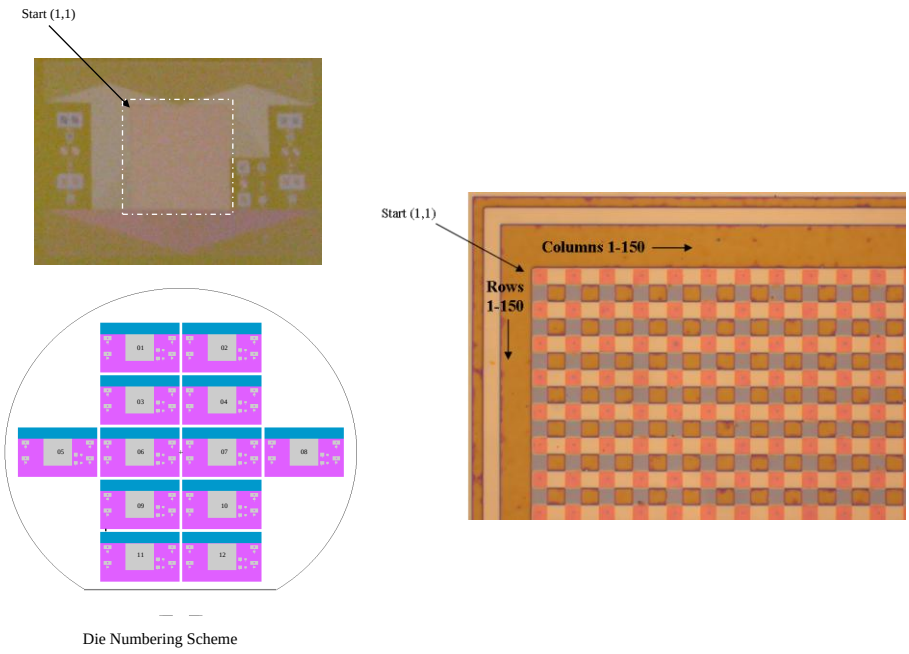

Fig. 50. Optical image of processed array edge (right), wafer layout showing individual array die on a 100 mm wafer (bottom left) and optical image of one array showing bond pad connections (top left).

Memristor Devices

Memristor devices based on silver chalcogenide materials were fabricated and packaged (Fig. 51) at Boise State University.

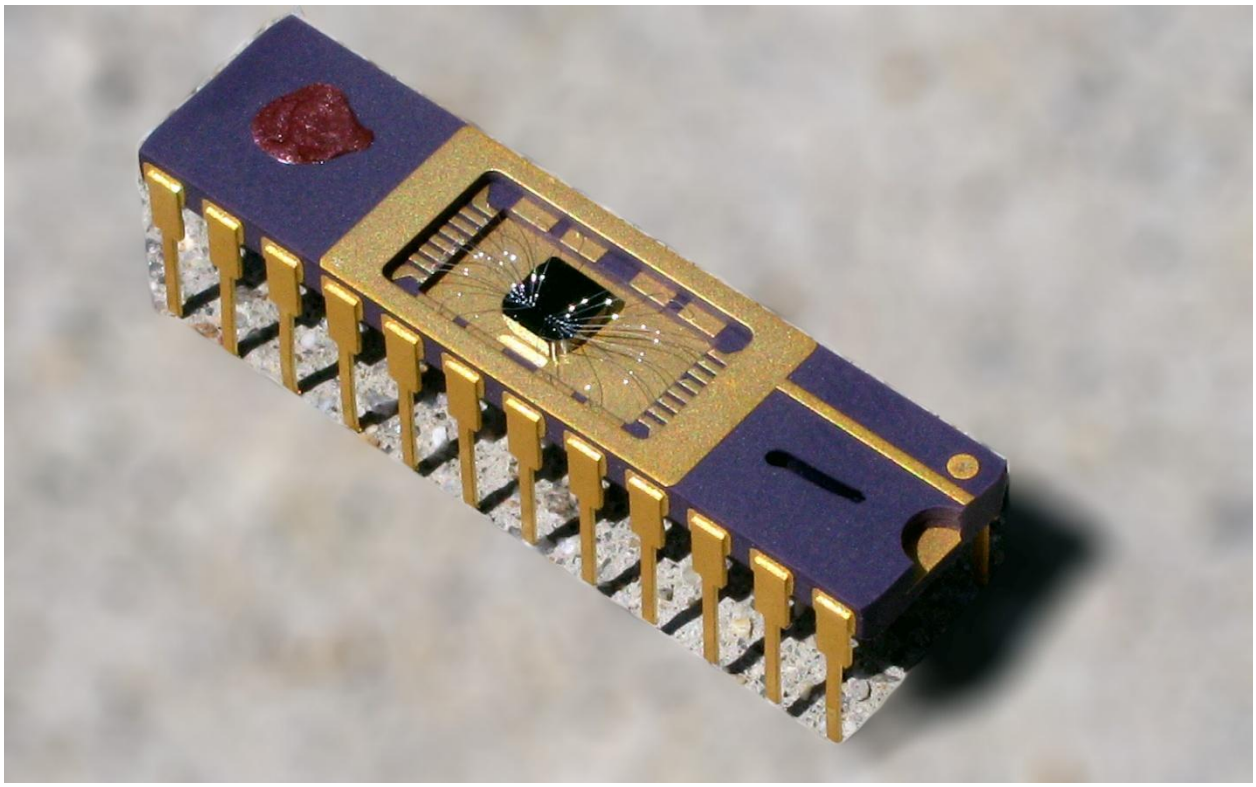

Fig. 51. Packaged memristor device used for application in intelligent computing circuits.

Memristor Background.

The memristor device postulated in 1971 by Leon Chua [1] as the fourth basic circuit element has received much attention in the research community since the publication of Strukov's 2008 paper titled "The missing memristor found." [2] The memristor name is a contraction for memory resistor [1] because that is exactly its function: to remember its resistance state [3]. The memristor is a two terminal passive device whose resistance state depends on its previous state and present electrical biasing conditions, and when combined with transistors in a hybrid chip, memristors could radically improve the performance of digital circuits without the need for further reduction of transistor dimensions [3]. Given their two terminal structural simplicity and electronic passivity, the applications for memristor technology range from non-volatile memory, instant on computers, reconfigurable electronics and neuromorphic computing [3,4].

In this work, Ag-chalcogenide devices are presented that exhibit memristor electrical characteristics. DC and AC electrical characterization is presented and observations discussed.

Experimental Details

Memristor devices were fabricated on 200 mm p-type Si wafers. Isolated W bottom electrodes were patterned on the wafers and a planarized nitride layer was used for device isolation. Vias were etched through the nitride layer to provide contact to the bottom electrode and to define the device active region. Prior to deposition of the memristor materials, the wafers received an Ar^+ sputter clean to remove residual material and potentially remove any oxides that might have

formed over the W electrode. The memristor device structure consists of the layers (from bottom electrode contact side to top electrode contact): 300 Å Ge_2Se_3/500 Å Ag_2Se/100 Å Ge_2Se_3/500 Å Ag/100 Å Ge_2Se_3, see Fig. 1. The 100 Å Ge_2Se_3 layers are needed for device processing only since Ag cannot be deposited directly on Ag_2Se and since W (for the top electrode) does not adhere well to Ag in this material stack. The layers were deposited by thermal evaporation using a CHA Industries SE-600-RAP thermal evaporator equipped with three 200 mm wafer planetary rotation. The rate of material deposition was monitored using an Infincon IC 6000 with a single crystal sensor head. The base system pressure was $1x10^{-7}$ Torr prior to evaporation. A W top electrode was created by sputtering W (350 Å) and etching to define the device top contact and bond pad. Etching was performed with a Veeco ion-mill by etching through the W and the memristor device materials and stopping on nitride. The top and bottom electrode bond pad contacts were 80 μm x 80 μm.

Electrical measurements were performed with either an HP4145B or an Agilent B1500A semiconductor parameter analyzer. A Micromanipulator 6200 microprobe station equipped with a temperature controllable wafer chuck was used for the wafer-level device measurements. Probe tips were either Micromanipulator W size 7B or American Probe and Technologies 73CT-APTA probe tips. The tested devices were 180 nm in diameter as defined by the via etched through the nitride layer to the bottom electrode, Fig. 52.

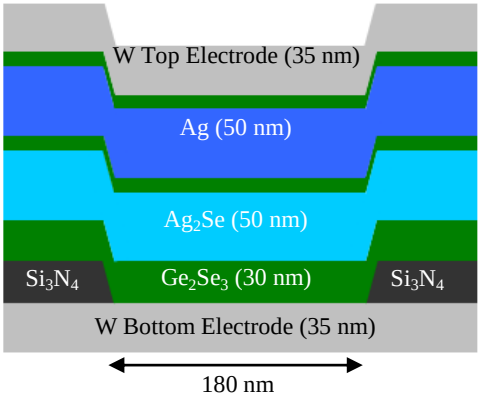

Fig. 52. Schematic representation of the fabricated device illustrating the material layers and dimensions. The unmarked layers are Ge_2Se_3 (10 nm).

Memristor Theory

A basic mathematical definition of a memristor is that of a voltage-controlled, one-port device in the generalized class of nonlinear dynamical systems called memristive systems described by (1) and (2). Here, x can be a set of state variables, G is a device conductance, and f is a generalized function [4]. Time, device current, and device voltage are represented by t, i, and v.

$$i = G(x, v, t)v \qquad (1)$$

$$\frac{dx}{dt} = f(x, v, t) \qquad (2)$$

In [2], Strukov et al. expounded on the mathematical memristor model and identified a state variable as the width, *w*, of a doped semiconductor region, illstrated in Fig. 53. This doped

region represents a region of low resistance, R_{ON}, while the undoped region supplies a high resistance, R_{OFF}, and the total device resistance is the series combination of the two for a device of thickness D. Through appropriate biasing, *w* can expand or contract and the resistance (and thus conductance) of the device can be modulated, as predicted in (1). The modulated resistance in [2] is attributed to the migration of oxygen vacancies from the doped region into the undoped region due to the field applied across the device. It is worth noting that modulated device resistance due to ion migration had been observed and identified for decades [5, 6], however, Strukov et al. identified this behavior as that of a memristor and helped explain the unique electrical characteristics exhibited by the device.

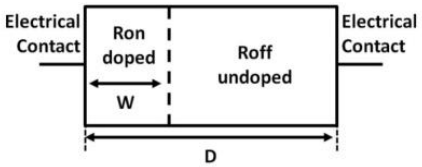

Fig. 53. Memristor device schematic illustrating the separation between the doped and undoped region. The width of the doped region, *w*, was identified as a state variable, x, from (1).

Electrical Characterization Results

Figure 54 displays the typical electrical Lissajous I-V curve behavior of the BSU memristor device under a sinusoidal input of 0.45 V and changing frequency. At 100 Hz, one can clearly observe that the memristor toggles between two states of low and high conductivity. The transition from low to high conductivity occurs near a threshold voltage of 0.24 V. In this case, Ag ions have migrated into the chalcogenide, Ge_2Se_3, layer and created a low-resistance path through the insulator. When the voltage decreases to an erase threshold of -0.32 V, the Ag ions are removed from the chalcogenide layer and the device returns to a high-resistance state. At higher frequencies, for example 100 kHz, the Ag ions cannot respond fast enough to the applied bias and the device behavior approaches that of a linear resistor. This frequency-dependent behavior was predicted in [4].

Calculating the charge and flux through the device by the time integration of the current and voltage at 100 Hz produces Fig. 55. It is clear the charge-flux behavior is not a proper function given the multiple charge values for a single flux value. This fact contradicts the original definition of an ideal memristor as originally postulated in [1]. Instead, Fig. 55 shows two distinct nonlinear charge-flux functions – the first relating charge and flux for a device initially in a high-resistance state and the second function describing a change from low resistance to high resistance. The combination of the two functions in the complete charge-flux relation suggests the device is best described as a memristive device, i.e. a device exhibiting memristance, as opposed to an ideal memristor [4, 7].

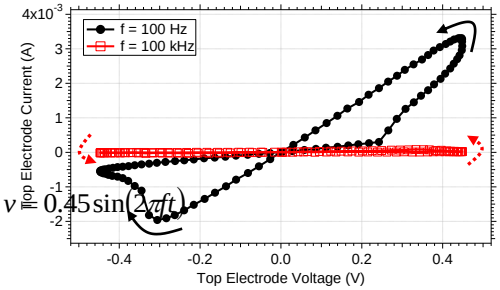

Fig. 54. Typical Lissajous I-V curve as a function of frequency for the memristor device. At low frequencies, a pinched hysteresis curve is clear. At higher frequencies, the device behavior approaches that of a linear resistor.

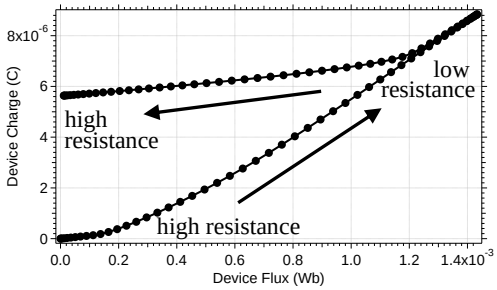

Fig. 55. Charge and flux of the device as calculated by the time integral of the 100 Hz I-V in Fig. 54. Since charge and flux are not related by a single function, the device is not an ideal memristor, strictly speaking, but is best described as a memristive device.

Another interesting characteristic of the device is the ability to continuously modulate the resistance through the application of sequential biasing. Fig. 56 shows five quasi-static DC sweeps in which the resistance of the device changes when a large enough bias is applied. For example, examining the first sweep shows a large resistance change once the voltage reaches a threshold of 0.24 V. On the second sweep only 0.17 V is needed to change the resistance, where sweep two no longer overlaps sweep one. Since a minimum threshold

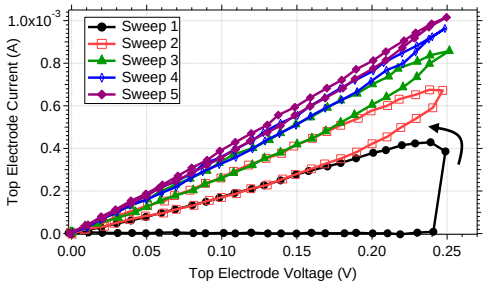

Fig. 56. Applying sequential DC sweeps to the device results in successive reduction of the device resistance. This behavior is equivalent to neurological synapses and thus a memristor can be considered an electrical synapse.

voltage is needed to change the resistance state of the device, relatively small voltages can be used to read the device without altering the resistance state. Furthermore, the multiple lower resistance states of the device based on the number of times biased is analogous to the behavior

found in a neurological synapse. Consequently, the memristor can be considered the electrical equivalent of a synapse [8].

Conditioning the device through application of several negative pulses produces a typical DC IV curve for the Ag-containing chalcogenide device as shown in Fig. 57. The memristor behavior is exhibited in the negative voltage region. Note the negative differential resistance (NDR) region between -0.2 and -0.4 V, characteristic of memristive devices.

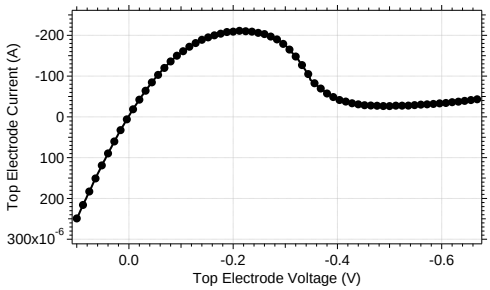

Fig. 57. Typical Ag-chalcogenide memristor DC IV curve illustrating a negative differential resistance (NDR) region.

In addition to showing a dependence on their past state, the Ag-chalcogenide devices show initial time dependence after programming wherein the device state will relax toward its initial state. After conditioning the device with negative pulses, a steady-state current (marked with *) was recorded, Fig. 58. A time dependent relaxation is observed by reading current through a device after programming with a -1.1 V, 250 ns pulse. As the read pulse time delay is increased, the current through the device increases. With this given programming pulse (-1.1 mV, 250 ns), the device reaches a higher resistance initially, but over a period of hundreds of microseconds, decays back to a lower resistance state. A time-dependent resistance (or conductance) is accounted for in (1) and complies with memristive behavior. However, this data suggests that shorter programming pulses may be insufficient to program the device into a time-stable resistance state.

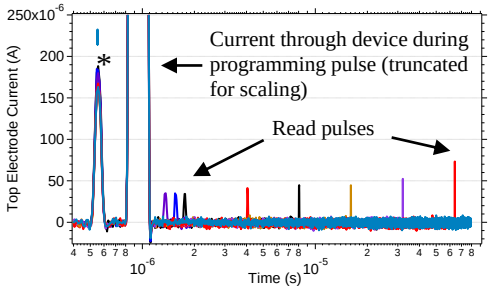

Fig. 58. After programming, a device resistance will decay. The * denotes the current through the device at steady state, prior to programming. The large truncated pulse is the current through the device during programming. The read pulses following the programming show how the device resistance changes as a function of time for the given programming conditions. Each read pulse corresponds to a different pulse test on the same device.

Conclusion

We have fabricated and tested Ag-containing chalcogenide devices that exhibit memristor

electrical characteristics. The AC characteristics presented illustrate the pinched I-V curve that approaches a linear resistor as frequency increases. DC characteristics show distinct resistance states dependent on previous states and applied voltage. Further DC data shows NDR curves characteristic of memristive devices. Pulse tests illuminate a time-dependence on the resistance state of the device. Further device characterization will explore pulse width effects and temperature effects of the device state.

REFERENCES

[1] L. Chua, "Memristor - The Missing Circuit Element," *IEEE Transactions on Circuits Theory (IEEE),* vol. 18, no. 5, 1971, pp. 507–519.
[2] D. B. Strukov, G. S. Snider, D. R. Stewart and R. S. Williams, "The missing memristor found," *Nature*, vol. 453, 2008, pp. 80-83.
[3] R. S. Williams, "How We Found the Missing Memristor," *IEEE Spectrum*, vol. 45, no. 12, 2008, pp. 28-35.
[4] L. Chua and S.M. Kang, "Memristive Device and Systems," *Proceedings of IEEE*, Vol. 64, no. 2, 1976, pp. 209-223.
[5] Y. Hirose and H. Hirose, "Polarity-dependent memory switching and behavior of Ag dendrite in Ag-photodoped amorphous As_2S_3 films," *J. of Applied Physics*, vol. 47, no. 6, 1976, pp. 2767-2772
[6] J. Blanc and L. Staebler, "Electrocoloration in $SrTiO_3$: Vacancy Drift and Oxidation-Reduction of Transition Metals," *Physical Review B*, vol. 4, no. 10, 1971, pp. 3548-3557
[7] D. B. Strukov, J. L. Borghetti, and R. S. Williams, "Coupled Ionic and Electronic Transport Model of Thin-Film Semiconductor Memristive Behavior," *Small*, vol. 5, no. 9, 2009, pp. 1058-1063.
[8] G. S. Snider, "Spike-Timing-Dependent Learning in Memristive Nanodevices," *NANOARCH 2008*, 2008, pp. 85-92.

Appendix B. Manuscripts in Preparation/Under Review Resulting From this Grant

Ge_2Se_3/SnSe-Based Ion-Conducting Robust Memristive, Non-Volatile Memory Device

Kristy A. Campbell, *Senior Member, IEEE* and Beth R. Cook

***Abstract*— A memristive/non-volatile memory ion-conducting device fabricated using layers of the chalcogenide materials Ge_2Se_3 and SnSe, with a layer of silver is described. The electrical switching properties of this device under DC and continuous wave operation over a temperature range of 300 to 423 K, and pulsed operation at room temperature, are described. Additionally, DC operation under total ionizing dose irradiation is described. This device is capable of being programmed within a continuous range of resistances from the kΩ to GΩ range.**

***Index Terms*—Memristor, Non-Volatile Memory Device, Thin Film Devices**

INTRODUCTION

ION-CONDUCTING memory devices, also referred to interchangeably as the programmable metallization cell (PMC), electrochemical metallization cell (EMC), and conductively-bridged random access memory (CBRAM), have been under development over the past ten years as one of the most promising emerging non-volatile memory technologies for replacement of Flash memory [1]. In addition to their use as memories, ion-conducting devices have been shown to exhibit memristive behavior [2], where the term 'memristive' is derived from the term "memory resistor" which was coined when the memristor was initially postulated in 1971 [3]. Operation of an ion-conducting device is based on the electric field-induced movement of a metal ion (typically silver or copper ions) into or out of a host material, such as a chalcogenide material (*e.g.* GeS) [1]. When metal ions are driven into the host material, the resistance of the host material is decreased. Electric field direction reversal removes the metal ions and increases the device resistance.

In this work, we describe a new ion-conducting device which incorporates layers of the chalcogenide materials Ge_2Se_3 and SnSe with a layer of Ag as the ion source, to facilitate stabilization of the device electrical switching properties and to improve the temperature tolerance of operational devices. In our previous work, a phase-change device with layers of Ge_2Se_3 and SnSe was demonstrated [4]. Addition of a layer of Ag over the Ge_2Se_3 and SnSe layers creates a new ion-conducting device that is no longer capable of phase-change memory operation, but instead operates as an ion-conducting device with superior performance compared to the layered phase-change device. Unlike the existing ion-conducting devices, this device does not require photodoping and/or thermal annealing [5] or homogeneous deposition of a precisely controlled composition of a ternary material containing the active metal (*e.g.* Ge-S-Ag) [6] in order to function. In addition, device fabrication is robust and the device will tolerate wide variation in chalcogenide layers' stoichiometry and thickness, as well as having no need to precisely control the ion source layer thickness. The chalcogenide layering provides protection against total ionizing dose radiation.

The ion-conducting devices described in this work can be operated in two modes: 1) the binary mode, or non-volatile memory mode, where the programmed state does not depend on the history of the device and is programmed between 'high' and 'low' resistance states, and 2) the memristive mode, where the device resistance depends upon the resistance state history and can be programmed continuously between low and high resistance states by repeated application of programming pulses until the desired resistance state is achieved. Electrical properties of this device are provided as a function of programming potential type: DC, continuous-wave, and pulse

excitation. In addition, temperature dependence of the device operation are provided for DC and continous-wave excitation.

Experimental Details

Ion-conducting devices were fabricated on 200 mm p-type Si wafers. Isolated W bottom electrodes were patterned on the wafers and a planarized nitride layer was used for device isolation. Vias were etched through the nitride layer to provide contact to the bottom electrode and to define the device active region. Prior to deposition of the chalcogenide materials, the wafers received an Ar^+ sputter clean to potentially remove any oxide that might have formed over the W electrode. The device structure consists of the layers (from bottom electrode contact side to top electrode contact): 600 Å W/300 Å Ge_2Se_3/500 Å SnSe/150 Å Ge_2Se_3/500 Å Ag/100 Å Ge_2Se_3/350 Å W. The 300 Å Ge_2Se_3 layer in contact with the bottom W electrode is the 'active' switching layer, i.e. where the Ag^+ ions are forced or removed during resistance switching. The SnSe layer is vital for device operation; it prevents the active layer from becoming saturated with Ag which would render the device non-functional, as well as assists in the formation of the conduction path through the active layer for consistent Ag movement into the active layer during switching. The remaining Ge_2Se_3 layers are necessary for device processing, but do not participate in active switching.

The layers were deposited by thermal evaporation using a CHA Industries SE-600-RAP thermal evaporator equipped with three 200 mm wafer planetary rotation. The rate of material deposition was monitored using an Infincon IC 6000 with a single crystal sensor head. The base system pressure was $1x10^{-7}$ Torr prior to evaporation. A W top electrode was deposited by sputtering W (350 Å) and etching to define the device top contact and bond pad. Etching was performed with a Veeco ion-mill by etching through the W and the memristor device materials and stopping on nitride. The top and bottom electrode bond pad contacts were 80 um x 80 um.

Electrical measurements were performed with an HP4156A or an Agilent B1500A semiconductor parameter analyzer, an Agilent 54815A oscilloscope and an HP 33250 arbitrary waveform generator. The B1500A, equipped with the B1530A waveform generation/fast measurement unit and the B1531A remote-sense and switch unit (RSU), was used for pulsed measurements.

A Micromanipulator 6200 microprobe station equipped with a temperature controllable wafer chuck was used for the wafer-level device measurements. Probe tips were either Micromanipulator W size 7B or American Probe and Technologies 73CT-APTA probe tips. The tested devices were 250 nm in diameter as defined by the via etched through the nitride layer to the bottom electrode. Total ionizing dose radiation testing was performed at Kirtland Air Force Base using the Aracor Model 4100 Semiconductor Irradiation System with a 10 keV W target X-ray source. The devices were exposed to 283 rad(SiO_2)/s for 17.6 minutes, yielding a total ionizing dose of ~300 krad(SiO_2) before radiation testing was started. A DC write/erase programming cycle was performed during radiation exposure for a total exposure time of 18 minutes.

DC and Continuous-Wave Electrical Characteristics

Fig. 1 displays a typical DC I-V curve of the ion-conducting device at room temperature. Application of a positive potential occurs at the top electrode in order to drive Ag^+ into the 300 Å Ge_2Se_3 layer, and thus reduce the device resistance. A compliance current set on the semiconductor parameter analyzer limits the current through the device (limited to 100 μA current in Fig. 1) and also the voltage applied across the device when the compliance current limit has been reached. The positive voltage at which the current jumps to the compliance current is referred to as the 'write threshold voltage' and is marked with a single asterisk in Fig. 1. As the potential is reduced below the write threshold voltage, the programmed device begins to conduct current according to Ohm's law (the linear portion of the I-V curve) until the erase threshold voltage is reached (indicated by the double asterisk in Fig. 1). Further application of negative potential to the device beyond the erase threshold voltage causes Ag^+ to leave the Ge_2Se_3 active layer and the resistance to increase significantly (see the low current region below -0.18 V in Fig. 1).

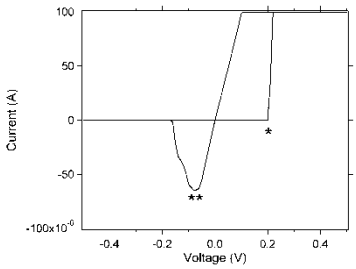

Fig. 1. Typical room temperature DC I-V curve of the layered Ge_2Se_3/SnSe/Ag ion-conducting device. '*' denotes the write threshold voltage. '**' denotes the erase threshold voltage.

During operation in binary mode, the DC write threshold voltage shifts as a function of operating temperature, Fig. 2. A similar shift is not observed in the erase threshold voltage. Devices tested under continuous-wave operation using sinusoidal waveforms up to frequencies of 1 kHz and 1 million cycles showed write and erase threshold voltages similar to the DC measurements at all temperatures tested. Threshold voltages at a given temperature did not vary depending upon the thermal history of the device.

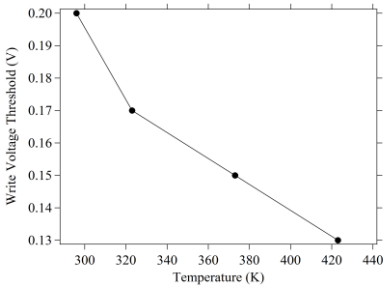

Fig. 2. Write threshold voltage as a function of temperature for a 1 mA programming compliance current. Devices were held at temperature for one hour prior to measurement.

The device can be programmed to a continuous range of resistances, depending on the programming conditions. Under DC and continuous-wave operation, limiting the current through the device will determine the resistance of the device, Fig. 3. In addition, the current through the device influences the data retention time. Table 1 lists typical data retention lifetimes for the DC and continuous-wave programming conditions. For best data retention, programming currents as high as 1 mA must be used; these conditions have shown data retention lifetimes at room temperature greater than 1 month. This has also been shown in photodoped programmable metallization cells [7].

Devices DC programmed during radiation exposure did not exhibit a shift in write or erase threshold voltages compared to the control devices. The programmed resistances between the control sample and the irradiated sample as a function of programming compliance current also did not exhibit a discernible difference (Fig. 3).

TABLE I
TYPICAL DATA RETENTION LIFETIMES UNDER DC AND CONTINUOUS-WAVE CONDITIONS AT ROOM TEMPERATURE

Programming current	Data retention lifetime
10 nA	< 10 s
100 nA	< 1 min
1 μA	< 10 min
10 μA	< 24 hr
100 μA	< 1 month
1 mA	> 1 month

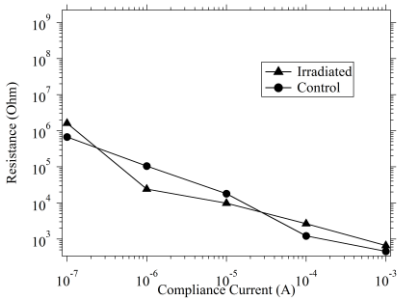

Fig. 3. Programmed resistances under variable compliance current limits. Data was collected at room temperature. Programmed resistances are shown during a DC write operation during total ionizing dose radiation exposure ('irradiated') and without exposure ('control'). The data shown is the average for five different devices programmed at each compliance current.

Pulsed Electrical Characteristics

Devices were tested under pulse conditions using the pulse sequence shown in Fig. 4. The device resistance was first measured with a 'read' pulse (leftmost pulse, top trace, Fig. 4) with the corresponding current through the device measured simultaneously with the application of the 'read' pulse (leftmost pulse, bottom trace, Fig. 4). Following the 'read' pulse, an erase, read, write, read cycle was performed.

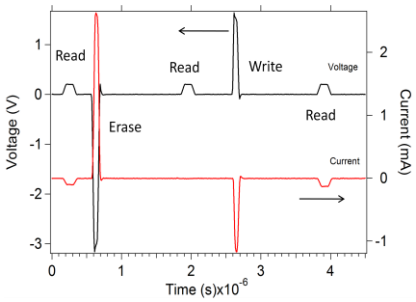

Fig. 4. Pulse sequence applied to a device (top trace, left axis) and a typical response of measured current through the device (bottom trace, right axis).

By varying the amplitude of the write pulse, the programmed resistance is varied (Fig. 5). The repeatability of the programmed resistance state can be seen in Fig. 5. The device resistance is similar for each similar programming potential, despite the order of application.

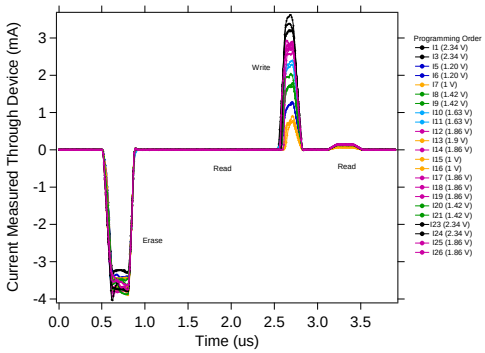

Fig. 5. Current measured through a device operated in binary mode as a function of applied pulse potential. The order that the device potential was applied is shown in the legend. The device writes to similar resistances for similar write pulses, despite the order of application.

Conclusion

A new ion-conducting variable resistance device is described that exhibits operating temperature tolerance to at least 423 K, is tolerant to total ionizing dose radiation up to 300 kRad (SiO_2), does not require photodoping or thermal annealing of the mobile metal source, and exhibits data retention at room temperature of at least 1 month. The device is capable of achieving a continuous range of resistances with good repeatability.

REFERENCES

[9] I. Valov, R. Waser, J.R. Jameson, M.N. Kozicki, "Electrochemical metallization memories – fundamentals, applications, prospects," *Nanotechnology*, vol. 22, June 2011, 254003.

[10] R.E. Pino, J.W. Bohl, N. McDonald, B. Wysocki, P. Rozwood, K.A. Campbell, A. Oblea, A. Timilsina, "Compact method for modeling and simulation of memristor devices: Ion conductor chalcogenide-based memristor devices," in *Nanoscale Architectures (NANOARCH), 2010 IEEE/ACM International Symposium*, June 2010, pp. 1-4.

[11] L. Chua, "Memristor - The Missing Circuit Element," *IEEE Transactions on Circuits Theory (IEEE)*, vol. 18, no. 5, September 1971, pp. 507–519.

[12] K.A. Campbell, C.M. Anderson, "Phase-change memory device with stacked Ge-chalcogenide/Sn-chalcogenide layers," *Microelectronics Journal*, vol. 38, Jan. 2007, pp. 52-59.

[13] F. Wang, W.P. Dunn, M. Jain, C. De Leo, N. Vickers, "The effects of active layer thickness on programmable metallization cell based on Ag-Ge-S," Solid-State Electronics, vol. 61, July 2011, pp. 33-37.

[14] H. Choi, K.-H. Nam, Y.-W. Koo, H.-B. Chung, "Characteristics on electrical resistance change of Ag doped chalcogenide thin film application for programmable metallization cell," *J. Electroceram*, vol. 23, October 2009, pp. 322-325.

[15] D. Kamalanathan, U. Russo, D. Ielmini, M.N. Kozicki, "Voltage-driven on-off transition and tradeoff with program and erase current in programmable metallization cell (PMC) memory," *IEEE Electron Device Letters*, vol. 30, May 2009, pp. 553-555.

Electrical switching properties of Ge_2Se_3/metal-Se/Ag-based ion-conducting memristive devices

Kristy A Campbell and Beth R Cook
Boise State University
Department of Electrical and Computer Engineering
1910 University Dr.
Boise, ID 83725-2075

E-mail: kriscampbell@boisestate.edu

Abstract. Ion-conducting devices that exhibit variable resistance when programmed have been fabricated using layers of the chalcogenide materials, Ge_2Se_3/M-Se (M=Sn, Pb, In, Sb, and Ag) that facilitate stable electrical switching operation and temperature tolerance over other Ag ion-conducting device types. The metal in the M-Se layer has been found to influence the formation of the conductive pathway used in device operation. The devices have been electrically characterized and shown to operate under DC and continuous-wave operation over a temperature range of 23 ºC to 150 ºC.

1. Introduction

Ion-conducting variable resistance devices have been studied for the past decade as a potentially new non-volatile memory technology [1]. Their operation relies on the movement of a mobile metal ion, such as Ag or Cu ions, into or out of an amorphous material matrix, such as a Ge_xSe_y or Ge_xS_y material. Devices are typically fabricated by either depositing a ternary material (*e.g.* Ge-S-Ag) to a desired stoichiometry [2], or by photodoping and/or thermally annealing the mobile metal into the active amorphous material matrix [3]. These fabrication methods offer deposition challenges since the amount of metal and the stoichiometry of the chalcogenide material are critical to the consistent operation of the device with respect to switching voltages, operating temperature range, achievable resistance range, number of switching cycles, as well as the degradation of all of these operating parameters as a function of the number of programming cycles.

The reliability problems associated with ion-conducting devices that have been fabricated with either the photodoping/annealing or ternary deposition methods have been shown to be significantly reduced by fabricating devices using a layered material stack consisting of a Ge_2Se_3/SnSe base structure [4]. The Ge_2Se_3 active layer material was selected due to the property of containing homopolar Ge-Ge bonds which break and form new bonds with metal from the metal chalcogenide layer [5] during the first operation of a device after fabrication. The former Ge-Ge bond sites form Ge-Metal sites and likely create a conduction pathway for programming and movement of mobile ions (e.g. Ag^+) into and out of the active material layer along a consistent pathway for all subsequent programming operations. In this paper we show that the metal in the metal-chalcogenide layer influences the properties of this first programming operation, but subsequent programming operations are independent of this metal layer and depend only on the mobile ion movement through the device. We also show that the devices can be programmed to a range of resistance values depending upon the current that is allowed through the devices during

programming. Additionally, we show that the devices are operational over the temperature range of 23 ºC to 150 ºC.

2. Device structure and fabrication

Ion-conducting devices consist of a via structure with a top and bottom electrode which extends to a metal pad for access for wirebonding or electrical probing access (figure 1). The structure consists of, in order of bottom to top electrode, 600 Å W/300 Å Ge_2Se_3/500 Å M-Se/150 Å Ge_2Se_3/500 Å Ag/100 Å Ge_2Se_3/350 Å W. The active switching layer is the 300 Å Ge_2Se_3 layer adjacent to the bottom electrode, i.e. where the Ag^+ ions are forced or removed during resistance switching. The M-Se layer is vital for device operation; it prevents the active layer from becoming saturated with Ag which would render it non-functional, as well as assists in the formation of the conduction path through the active layer for consistent Ag movement into the active layer during switching [4]. The M-Se layers used in this work are SnSe, PbSe, In_2Se_3, Sb_2Se_3, and Ag_2Se. The two other Ge_2Se_3 layers in the device stack are necessary for fabrication and are not critical to device operation. The source of metal ions during operation is from the 500 Å Ag layer.

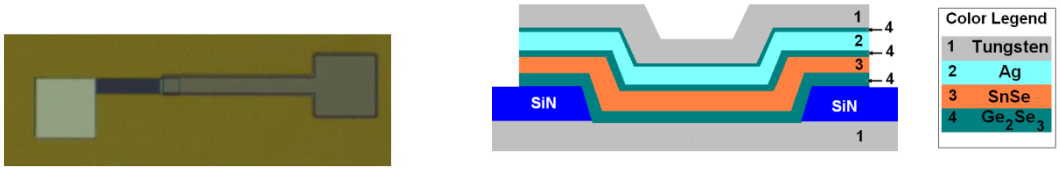

(a) (b)

Figure 1. (a) Optical top-down image of a fabricated device showing the bond pads. (b) Cross-section illustration of a fabricated device.

The devices were fabricated on 100 or 200 mm p-type Si wafers. Isolated W bottom electrodes were patterned on the wafers and a planarized nitride layer was used for device isolation. Vias were etched through the nitride layer to provide contact to the bottom electrode and to define the device active region. Prior to deposition of the chalcogenide materials, the wafers received an Ar^+ sputter clean to potentially remove any oxide that might have formed over the W electrode. The chalcogenide layers were deposited by thermal evaporation using a CHA Industries SE-600-RAP thermal evaporator equipped with three 100/200 mm wafer planetary rotation. The rate of material deposition was monitored using an Infincon IC 6000 with a single crystal sensor head. The base system pressure was $1x10^{-7}$ Torr prior to evaporation. A W top electrode was deposited by sputtering W (350 Å) and etching to define the device top contact and bond pad. Etching was performed with a Veeco ion-mill by etching through the W and the memristor device materials and stopping on nitride. The top and bottom electrode bond pad contacts were 80 μm x 80 μm.

3. Device operation

Devices are initially in a high resistance state (MΩ to GΩ range) post fabrication. The first programming operation applies a positive potential to the top electrode and forces metal from the metal chalcogenide layer into the active Ge_2Se_3 layer. Metal from the Ag layer also begins to migrate towards the active layer during this first programming operation. As the conductive channel is formed by the metal from the metal chalcogenide layer and filled with the mobile ions (Ag^+), the resistance of the device drops. It is likely that as the mobile ions migrate through the channel they are reduced and agglomerate within the

formed channel, thus leading to the reduced device resistance. However, as it is not possible to reliably observe this channel spectroscopically due to its size, the device structure, and the rapid mobility of Ag in any electron beam (especially in scanning electron microscopy (SEM) imaging) or under illumination, evidence of this type of operating hypothesis is limited to observation of device electrical response and response in altered chemical environments of the active switching material and metal chalcogenide layers.

Once a device is programmed to a low resistance state, the resistance can be increased by application of a negative potential to the top electrode, thus forcing the generation of Ag^+ and its migration back towards the top electrode. The resistance of a device is related at any time to the conductivity of the channel formed in the active switching layer, which is in turn related to the amount of silver (or other mobile metal) within the channel.

4. Measurement methodology and experiment setup

Electrical measurements were performed under DC (quasistatic) conditions with either an HP4156A or an Agilent B1500A semiconductor parameter analyzer. Continuous-wave (CW) measurements were performed with an HP33250A arbitrary waveform generator and an Agilent 54815A oscilloscope. The CW measurement circuit is shown in figure 2. A load resistor was used to limit the current through the device during CW measurements since programming current can influence the programmed resistance of the device [4] and to allow indirect measurement of the voltage drop across the ionic-conductor device.

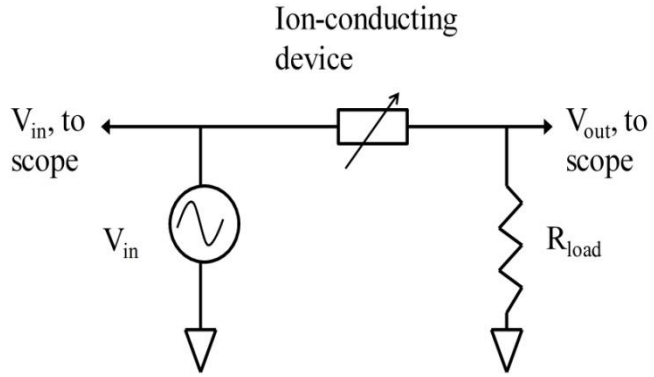

Figure 2. Continuous-wave device measurement circuit diagram.

A Micromanipulator 6200 microprobe station equipped with a temperature controllable wafer chuck was used for the wafer-level device measurements. Probe tips were either Micromanipulator W size 7B or 7A. The tested devices were 250 nm in diameter as defined by the via etched through the nitride layer to the bottom electrode (figure 1b). Temperature dependence of the device operation was performed for both DC and CW programming measurements.

DC measurements were performed in the sequence of 'Write – erase – write' where 'write' refers to programming a device to a lower resistance by application of a positive potential to the top electrode and 'erase' refers to programming a device to a higher resistance by application of a negative potential to the top electrode. A compliance current set on the semiconductor parameter analyzer limits the current through the device. The first 'write' is responsible for device conditioning and formation of the channel by incorporation of the metal from the M-Se layer into the active layer.

CW measurements were performed by cycling the device using the circuit shown in figure 2 with the oscilloscope in persistence mode (so that any deviation from the recorded traces would be observed) with waveforms saved after every measurement decade. A current limit is set in this measurement through the series load resistor.

5. Experimental results

5.1 DC room temperature I-V curves

The DC response of the devices at room temperature is shown in figures 3 and 4. In figure 3, a typical I-V curve for the devices fabricated with a metal chalcogenide layer consisting of SnSe, Sb_2Se_3, Ag_2Se, and PbSe (figure 3(a) – (d), respectively) is provided. The positive voltage at which the current first begins to increase significantly or jumps to the compliance current is referred to as the 'write threshold voltage'. An asterisk (*) is placed on each figure near the first 'write' I-V trace and the write threshold voltage. A positive potential applied to the top electrode writes the device to the low resistance state. The first write corresponds to channel forming and appears at a different potential than the second (shown in figure 3) and subsequent write threshold voltages. In the case of the SnSe and Ag_2Se-based devices, the first write potential is often at a value below the subsequent write threshold voltages (figure 3(a) and (c)). This is an indication that the first write more easily mobilizes and places metal atoms on the Ge-Ge bonding sites than the other, less mobile, metals Sb and Pb. It should be noted that the SnSe and Ag_2Se-based devices from different fabrication lots than those presented in this work have also exhibited either (1) similar first and second write potentials, or (2) a first write potential slightly higher than the second write potential. The fabrication conditions appear to influence the magnitude of the first write potential.

The typical I-V trace for the Ge_2Se_3/In_2Se_3 device is shown in figure 4 since the first write I-V sweep is significantly different than the other metal-Se devices. The Ge_2Se_3/In_2Se_3 devices did not show a clear first 'write' potential or distinct erase potential. However, the devices still changed resistance between high (MΩ) and low (kΩ) values when programmed.

Of note in each case (figures 3 and 4) is the similarity of the second 'write' potential. After conditioning with the first 'write', the second 'write' occurs in each case at approximately 0.2 V. The second 'write' (and all subsequent 'write' operations) likely use the already formed channel since the write threshold voltages are similar for each device type and all subsequent write operations.

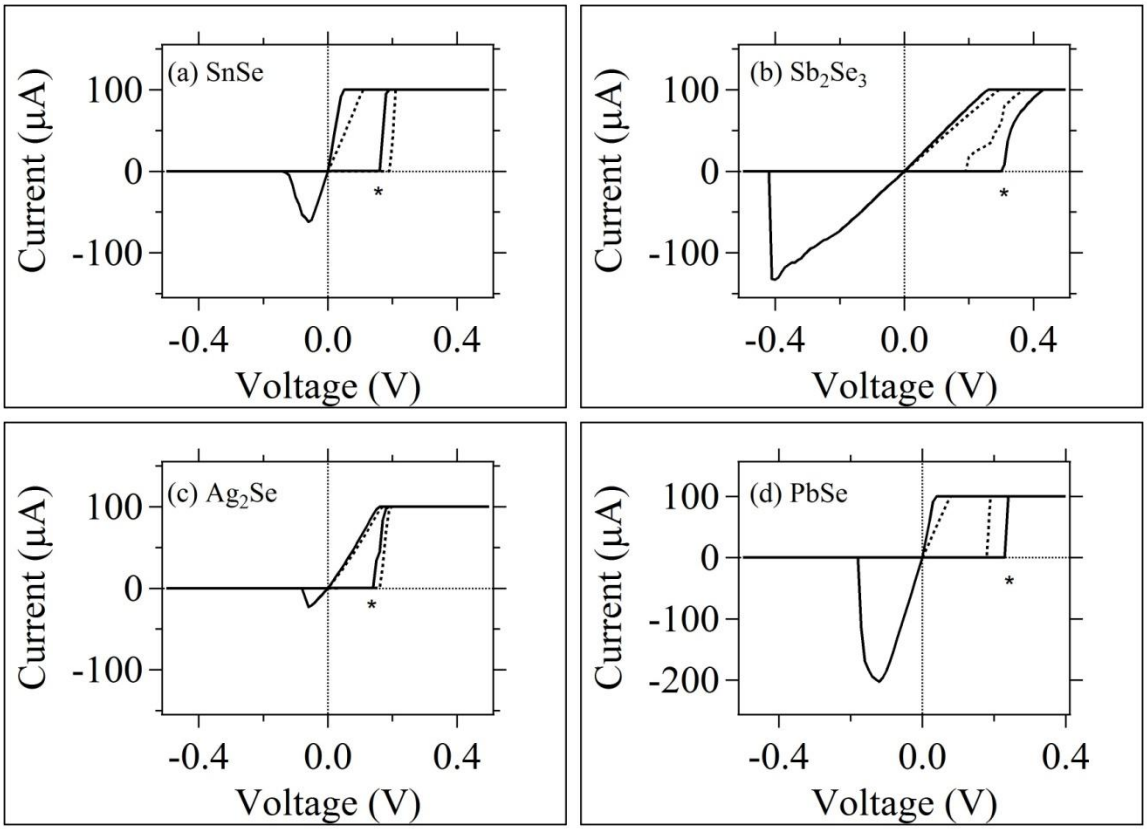

Figure 3. Typical room temperature DC response of the Ge_2Se_3/M-Se devices with M-Se given by (a) SnSe, (b) Sb_2Se_3, (c) Ag_2Se, and (d) PbSe. The programming sequence was: 'write' – 'erase' – 'write'. The asterisk (*) denotes the DC sweep corresponding to the first 'write'. The second write curve is denoted with a dashed line. A 100 μA compliance current was used during the 'write' operation in each case. The erase current was not limited to 100 μA in order to fully enable device erasure in the event of a low programmed written resistance.

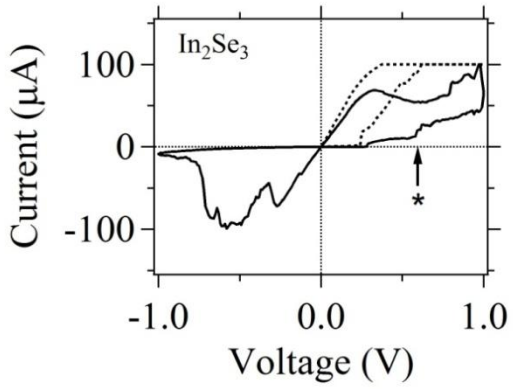

Figure 4. Typical room temperature DC response of the Ge_2Se_3/In_2Se_3 device. The programming sequence was: 'write' – 'erase' – 'write'. The asterisk (*) denotes the DC sweep corresponding to the first 'write'. The second write curve is denoted with a dashed line. A 100 μA compliance current was used during the 'write' operation.

5.2 Programmed resistance

The compliance current limit set on the parameter analyzer during a DC measurement determines the programmed resistance range for each device type. Figures 5 and 6 show the programmed resistances for each device type as a function of programming current and temperature. In each plot, the dashed line corresponds to the 'write' case where the device has been programmed to a lower resistance by application of a positive potential to the top electrode. The solid line corresponds to the resistance following an 'erase'. Each trace on the graphs corresponds to a different temperature, ranging from 23 °C to 150 °C.

As seen in figures 5 and 6, the programmed 'write' resistance has no observable dependence on temperature, but a strong dependence on the compliance current. The resistance range for all different device types as a function of compliance current is the same, 10^6 Ω to 10^3 Ω, for 100 nA to 1 mA programming current, respectively.

The erase resistance range varies with metal-Se layer type, temperature, and in some cases the previous programming compliance current. The dependence of the erase resistance on the previous programming compliance current is most notable in figure 5(a), the SnSe-based device. In this case, a 1 mA compliance current writes devices into the kΩ resistance range for each temperature, however, the devices are not erased to the GΩ range as is the case with the other compliance currents. This erase resistance dependence on the compliance current is independent of operating temperature. In the case of the Ag_2Se-based device, figure 6(b), the erase resistance has a significant dependence on the operating temperature above 100 °C. This is seen in the erase resistance data for the case of 150 °C in figure 6(b). There appears to be no trend in erased resistance as a function of compliance current in this case, but at 150 °C the devices erase to a resistance lower than any other temperature, however, this resistance change is still more than two orders of magnitude higher resistance than the programmed 'write' resistances at all temperatures.

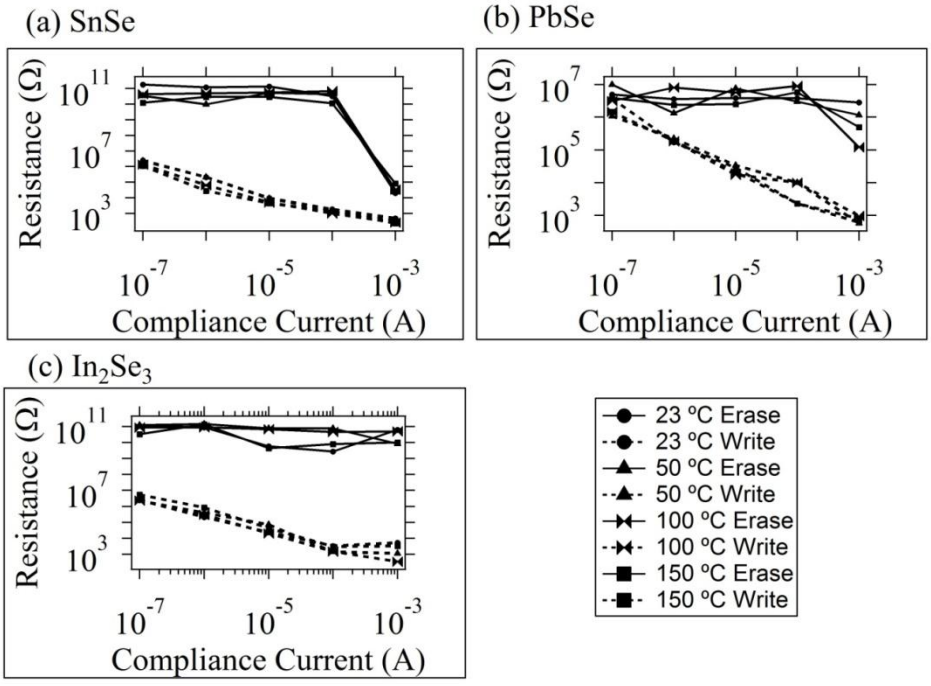

Figure 5. (a)-(c) Programmed resistance as a function of compliance current during DC measurement and device operating temperature. Each point corresponds to the average of measurements on five different devices. (a) SnSe-based device. (b) PbSe-based device. (c) In_2Se_3-based device.

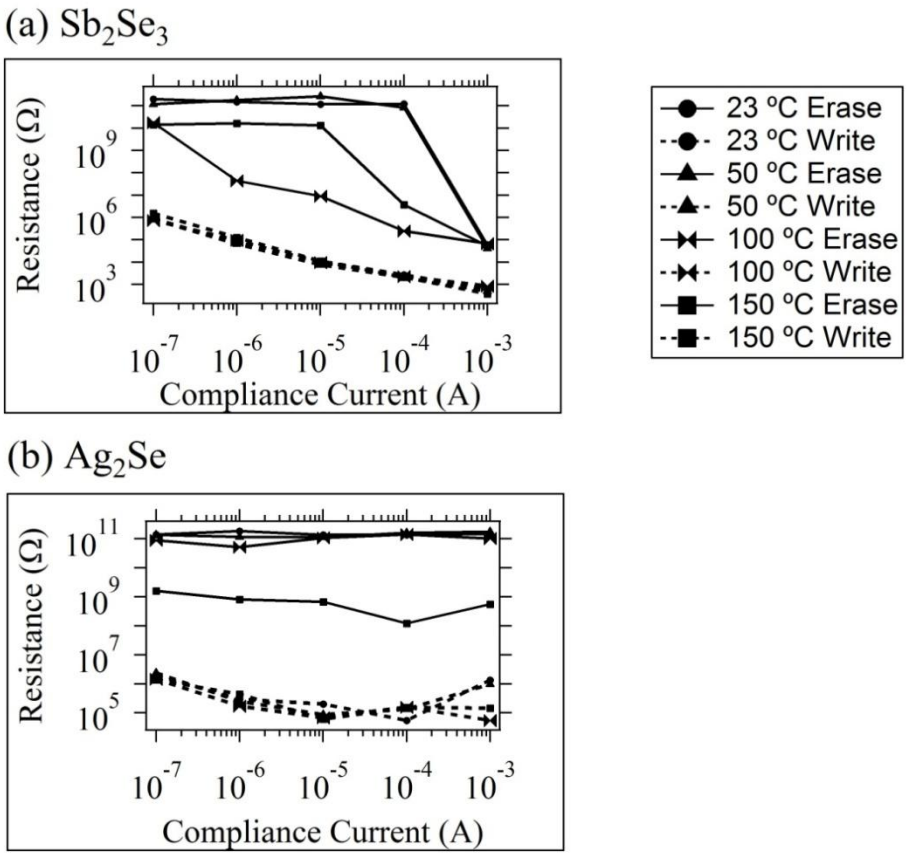

Figure 6. Programmed resistance for the Sb_2Se_3-based and Ag_2Se-based devices as a function of compliance current during DC measurement and device operating temperature. Each point corresponds to the average of measurements on five different devices. (a) Sb_2Se_3-based device. (b) Ag_2Se-based device.

5.3 DC Threshold voltage

The temperature dependence of the first and second write threshold voltages is shown in figures 7 and 8. The second write threshold voltages for the SnSe, PbSe, and Ag_2Se-based devices are similar over the temperature range of 23 to 150 °C. The In_2Se_3 and Sb_2Se_3-based devices threshold voltages appear slightly higher than the SnSe, PbSe, and Ag_2Se-based devices. However, determination of the actual switching voltage is more challenging for these device types, as can be seen from their DC I-V curves in figures 3(b) and 4, and can readily account for this deviation.

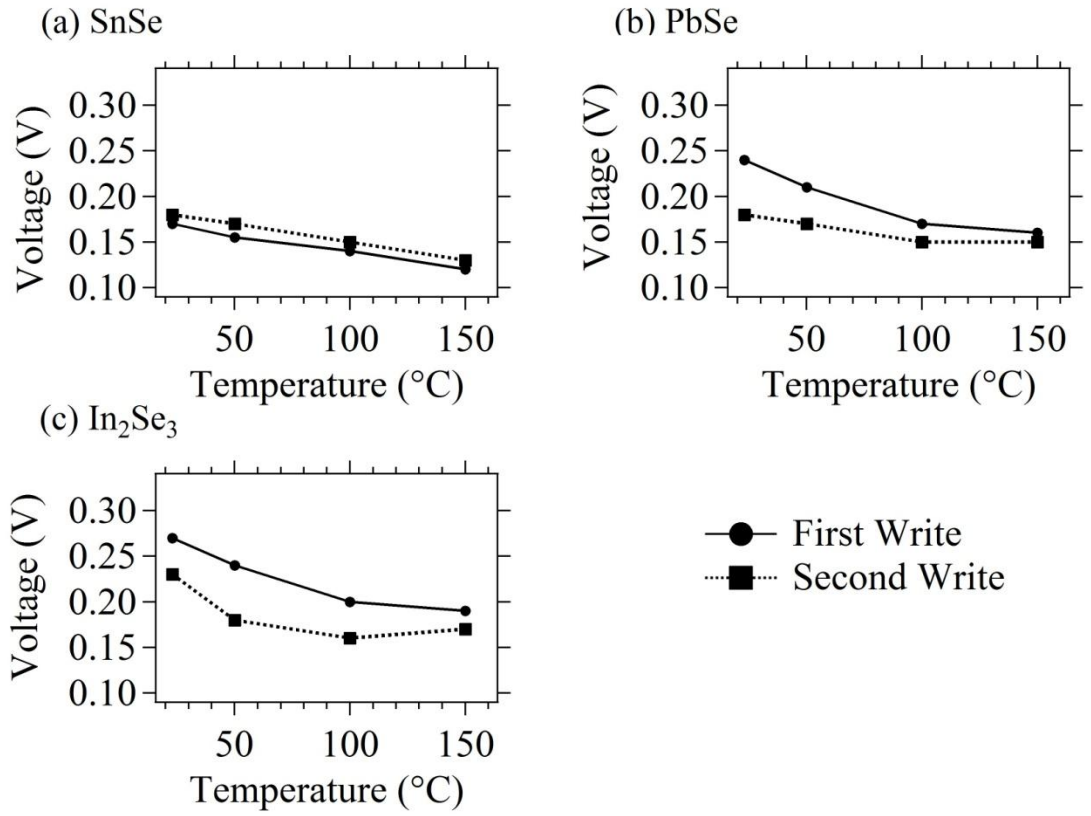

Figure 7. Temperature dependence of the first and second write threshold voltage at 100 μA compliance current. Each point corresponds to the average of measurements on five different devices. (a) SnSe-based device. (b) PbSe-based device. (c) In_2Se_3-based device.

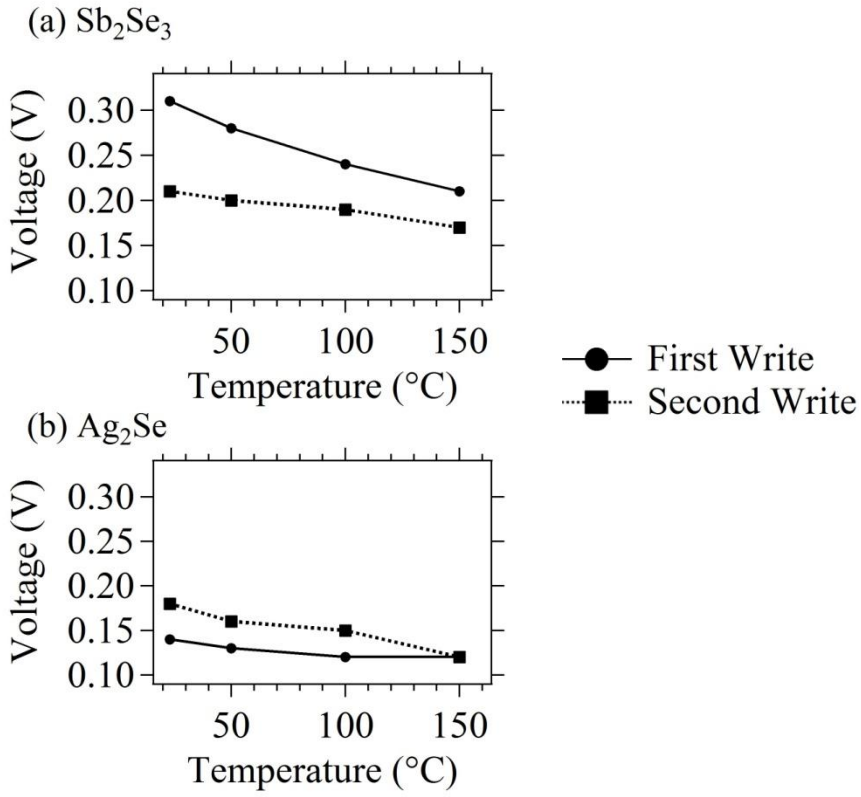

Figure 8. Temperature dependence of the first and second write threshold voltage at 100 μA compliance current. Each point corresponds to the average of measurements on five different devices. (a) Sb_2Se_3-based device. (b) Ag_2Se-based device.

The 'erase' threshold voltage as a function of temperature and device type is shown in figure 9. The SnSe and In_2Se_3 device types appear to have a slight increase in the average erase threshold voltage at 150 °C. However, this may be attributable to normal slight variation from device-to-device given the small sample size.

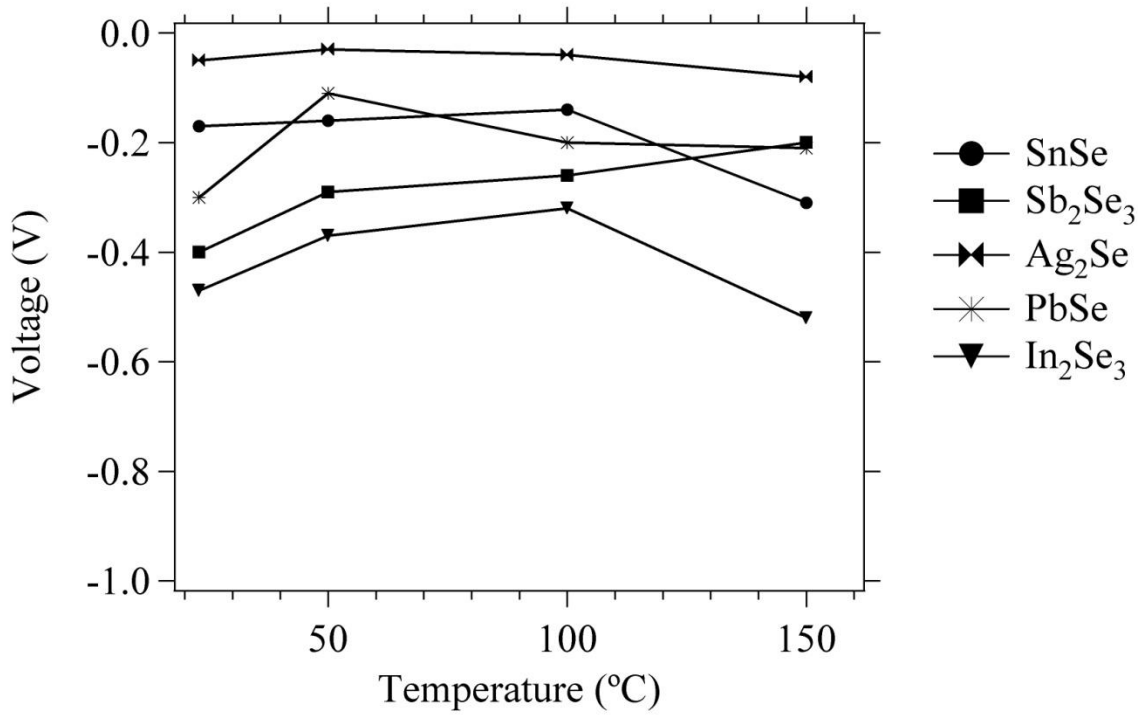

Figure 9. Temperature dependence of the DC 'erase' threshold voltage following a 100 μA compliance current programming sweep for each device type. Measurements from five devices were averaged to obtain the data points shown at each temperature.

5.4 Continuous-wave cycling

All device types except the In_2Se_3-based devices were cycled using the circuit in figure 2. Devices were measured at 23, 50, 100, and 140 °C. All devices were kept at temperature for at least one hour prior to CW measurements. The input waveforms used on each device type were of arbitrary shape and were selected to offer the best cycling endurance for the various device types. The In_2Se_3-based devices did not show cycling endurance under these test conditions and therefore could not be compared with the other device types.

The cycling input waveform and voltage across the load resistor for up to 1 million cycles is shown for an Ag_2Se-based device in figure 10 for 23 and 140 °C. The data was sampled and saved after every cycling decade. It is clear at 23 °C (figure 10a) that the first cycle has different switching behaviour than the subsequent cycles; the voltage across the load resistor shows a smooth transition in following the input signal. All of the subsequent 'writes' show a response that has a distinct jump in the voltage across the load resistor, corresponding to a distinct change in the resistance of the ion-conducting device. The voltage across the load resistor appears to follow the input signal until an erase potential is reached that allows the ion-conducting device resistance to increase (corresponding to a reduction in voltage across the load due to the majority of voltage being dropped across the large resistance of the ion-conducting device). At 140 °C, the write threshold voltage is reduced, and the jump in the voltage across the load resistor occurs at less than 100 mV, unlike the 23 °C case where it occurs above 200 mV.

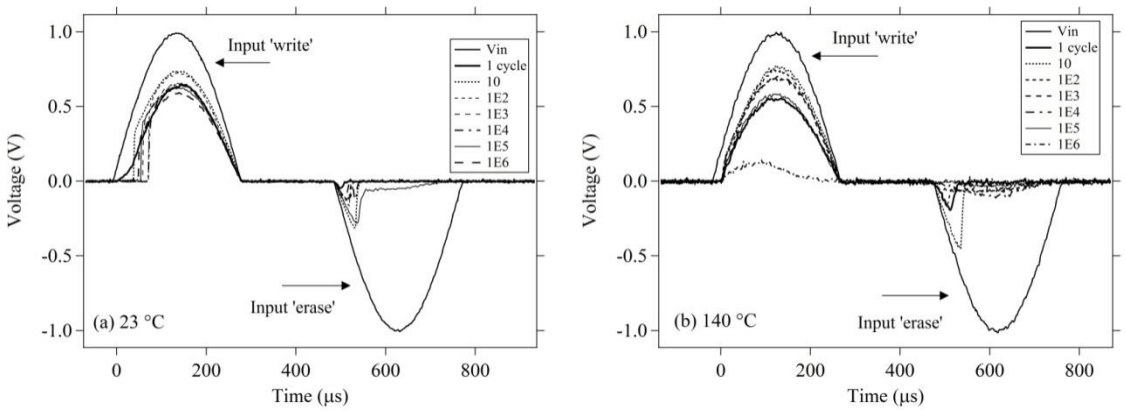

Figure 10. (a) Room temperature and (b) 140 °C CW cycling of the Ag_2Se-based device using the circuit in figure 2. The input waveform is used to write the device (positive potential) and erase the device (negative potential). The other waveforms correspond to the potential across the device load resistor in series with the ion-conducting device, sampled every decade. R_{load} = 10 kΩ.

The Sb_2Se_3-based device response, figure 11, is similar to the Ag_2Se device response. However, a noteable difference is observable in the first write cycle of the Sb_2Se_3-based device where the device switches at a higher potential for all temperatures. Since the 140 °C data for these devices (figure 11b) has a much different erase appearance than the 23 °C data (figure 11a), a 'read' pulse was added after the write and erase cycles. This small positive voltage pulse has an amplitude that was selected to be low enough not to write a device that is in the high resistance state. When the device is in the low resistance state, the voltage across the load resistor follows the input signal and appears to follow the read pulse shape (see the read pulse adjacent to the Input 'write' signal in figure 11b). When the device is in a high resistance state, the voltage across the load resistor will not appear to follow the read pulse (see the read pulse adjacent to the Input 'erase' signal in figure 11b).

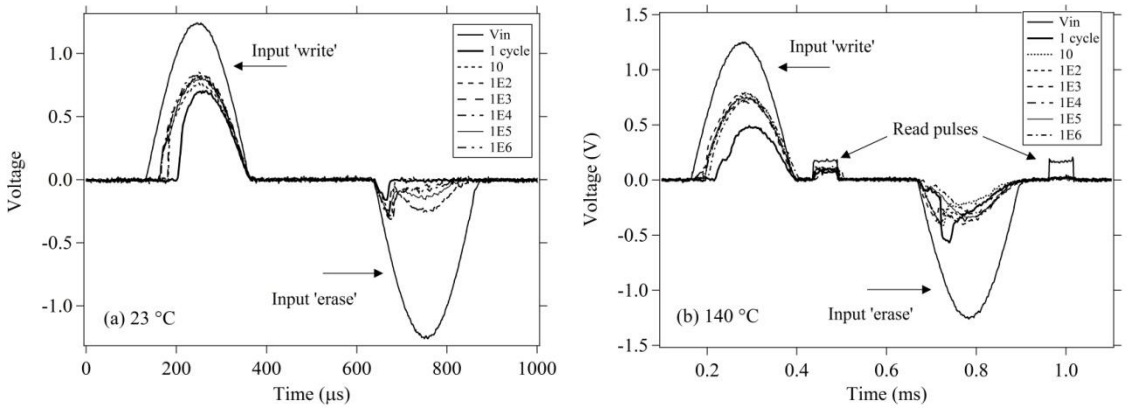

Figure 11. (a) Room temperature and (b) 140 °C CW cycling of the Sb_2Se_3-based device using the circuit in figure 2. The input waveform is used to write the device (positive potential) and erase the device (negative potential). The other waveforms correspond to the potential across the load resistor in series with the ion-conducting device, sampled every decade. R_{load} = 10 kΩ.

The CW response of the SnSe and PbSe-based devices is shown in figures 12 and 13. In both of these cases, the devices cycled better with a fast fall time, thus the falling edge of the Input 'write' and Input 'erase' pulses is 8 ns.

In all device cases, a higher voltage is required to erase the device. This is most noticeable in the SnSe and PbSe-based devices (figures 12b and 13b). During the erase signal the voltage across the load resistor follows the Input 'erase' signal until an adequate potential to erase the device is reached. This potential is between –1 V and –0.5 V at 23 °C, but between –0.25 V and –0.1 V at 140 °C.

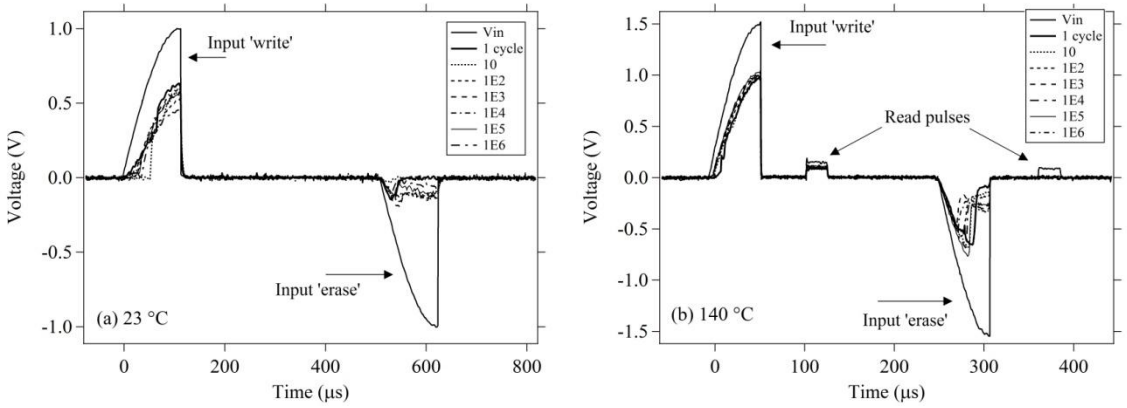

Figure 12. (a) Room temperature and (b) 140 °C CW cycling of the SnSe-based device using the circuit in figure 2. The input waveform is used to write the device (positive potential) and erase the device (negative potential). The other waveforms correspond to the potential across the load resistor in series with the ion-conducting device, sampled every decade. R_{load} = 10 kΩ.

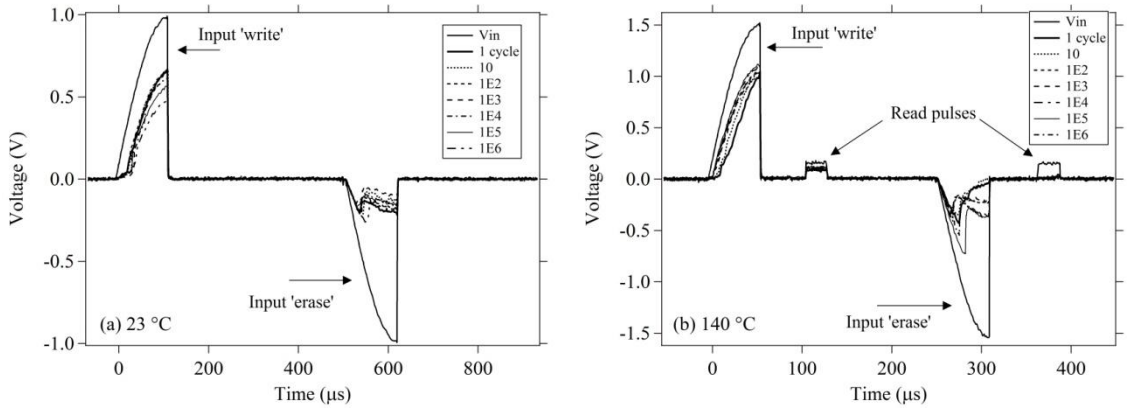

Figure 13. (a) Room temperature and (b) 140 °C CW cycling of the PbSe-based device using the circuit in figure 2. The input waveform is used to write the device (positive potential) and erase the device (negative potential). The other waveforms correspond to the potential across the load resistor in series with the ion-conducting device, sampled every decade. R_{load} = 10 kΩ.

The amplitude of the write and erase threshold voltages changes as a function of the frequency of applied input signal, as can be seen by comparison of the CW data in figures 10-13 with the DC data in figures 8 and 9. In fact, pulsing the device (rather than applying a CW signal) leads to write and erase threshold voltages than can be more than 5 times the amplitude of the DC threshold voltages and depends on pulse width and pulse rise time [4].

6. Discussion

Layered Ge_2Se_3/M-Se ion-conducting devices, where M = Sn, Pb, In, Sb, and Ag, have been demonstrated under DC and CW conditions at operating temperatures from 23 °C to 150 °C (140 °C for CW measurements). Devices show resistance switching and demonstrate the programmability of intermediate resistance states as a function of the programming current over the entire temperature range. The programmed written resistance is independent of temperature within the 23 °C to 150 °C range. However, there is temperature dependence on the erased resistance in the case of Ag_2Se-based devices operated at 150 °C. At 150 °C, the erased resistance is almost two orders of magnitude less than it is at the lower temperatures. This might be explained by the structural changes in Ag_2Se with temperature. Ag_2Se has a phase transition at 133 °C, going from the low temperature α-phase to the higher temperature superionic conductor phase (β–phase) [6]. The superionic conducting phase is likely present at 150 °C, and if Ag_2Se is present in the conductive channel, the overall erased resistance might be lower (although it is still quite high). The same effect is not observed on the written resistance as the conducting channel should be comprised of mostly Ag after programming to a lower resistance state.

The 'write' threshold voltage is temperature dependent under both DC and CW test conditions; as the temperature is increased, the 'write' threshold voltage decreases. The 'erase' threshold voltage in DC conditions has no clear temperature dependence. However, there is an observable increase in the erase voltage on the CW measurements at the highest temperature tested (140 °C). Interestingly, while the reduced 'write' threshold voltage could be explained by the increased ease with which Ag can move at higher temperatures, this doesn't explain the lack of clear temperature dependence on the 'erase' threshold voltage.

None of the device types exhibited temperature dependent failure due to Ag migration or Ag saturation of the active Ge_2Se_3 switching layer over at least 48 hours at temperature. This is likely due to the M-Se layer between the active Ge_2Se_3 layer and the Ag source layer. As the temperature in increased, the Ag does not easily migrate through the M-Se layer into the Ge_2Se_3 layer. Since the active Ge_2Se_3 layer is not saturated, photodoped, or annealed to contain Ag like the traditional methods of forming a chalcogenide-based ion-conducting device [1-3], the Ag in the cell should be confined to the conductive channel(s). Additionally, since the Ge_2Se_3 layer is not photodoped with Ag, the glass maintains a Ge_2Se_3 stoichiometry which has a higher glass transition temperature (~346 °C) than the Ge-Se-based glasses post Ag-photodoping. The Ge-Se-based glasses post Ag-photodoping have reduced glass transition temperatures [7] that can be too low for many microfabrication processes, thus making production with these materials challenging. By maintaining a higher glass transition temperature, the devices using the Ge_2Se_3 layer and M-Se layer can be easily fabricated using higher temperature processes.

7. Conclusions

Ion-conducting devices have been fabricated using layers of the chalcogenide materials Ge_2Se_3 and M-Se (M=Sn, Pb, Sb, In, and Ag), with an Ag layer as the ion source. These devices exhibit operation over the temperature range of 23 to 150 °C. All devices tested, excluding the In_2Se_3-based devices, cycle without failure over 1 million cycles at temperatures of 140 °C. No temperature dependent failure of devices was observed over 48 hours at temperature. The switching consistency and temperature tolerance of this ion-conducting device structure makes it superior to the existing chalcogenide-based ion-conducting device types which suffer from switching repeatability issues due to inhomogeneity of Ag photodoped into the chalcogenide glass or inhomogeneity from the Ag-Chalcogenide thin film deposition as well as higher temperature intolerance. The layered Ge_2Se_3/M-Se devices described in this work are easily fabricated and can be processed at temperatures as high as 300 °C without degradation in device operation.

In addition to the fabrication and device operation temperature tolerance, the devices can be easily programmed to a range of resistances from 10^6 to 10^3 Ω by controlling the amount of current allowed through the device during programming.

Acknowledgments

This work was partially funded by a grant from the United States Air Force Office of Scientific Research, DEPSCoR Grant No. FA9550-07-1-0546, and by the United States Air Force Research Laboratory, Grant No. FA9453-08-2-0252.

References

[1] Valov I, Waser R, Jameson J R, Kozicki M N 2011 Electrochemical metallization memories – fundamentals, applications, prospects *Nanotechnology* **22** 254003
[2] Wang F, Dunn W P, Jain M, De Leo C, Vickers N 2011 The effects of active layer thickness on programmable metallization cell based on Ag-Ge-S *Solid-State Electronics* **61** 33-37
[3] Kamalanathan D, Russo U, Ielmini D, Kozicki M N 2009 Voltage-driven on-off transition and tradeoff with program and erase current in programmable metallization cell (PMC) memory *IEEE Electron Device Letters* **30** 553-555
[4] Campbell K A and Cook B R Ge_2Se_3/SnSe-based ion-conducting memory device *Submitted for publication, August 2011*
[5] Edwards A E and Campbell K A **need title** *Submitted for publication*
[6] Kienle L, Duppel V, Mogwitz B, Janek J, Kreutzbruck M v, Leineweber A, and Simon A 2011 Synthesis-real structure-property: The showcase of silver-rich Ag_2Se *Crystal Growth & Design* **11** 2412-2421
[7] Feltz A 1993 *Amorphous Inorganic Materials and Glasses* (New York:VCH Publishers) p230

Raman studies of bulk Ge_xSe_{100-x} and $(Ge_{40}Se_{60})_xM_{100-x}$ (M=Ag, Co, Cr, Cu, In, Mn, Sb, Sn, V, W, Zn) chalcogenide glasses

Pulok Pattanayak, Kristy A. Campbell[1]
Department of Electrical and Computer Engineering
Boise State University, Boise, Idaho – 83706, USA

Room temperature Raman scattering experiments have been performed on bulk Ge_xSe_{100-x}($10 \leq x \leq 40$) chalcogenide glasses and $Ge_{40}Se_{60}$ chalcogenide glasses containing up to 3 at% of Ag, Co, Cr, Cu, In, Mn, Sb, Sn, V, W and Zn to investigate the bonding nature of these glasses. The presence of an intermediate phase in glasses with an average coordination number near <r> = 2.4 is indicated by a change in slope of compositional variation of Raman peaks. The appearance of two new peaks after the intermediate phase (<r> ≥ 2.60) supports this assumption indicating major structural changes beyond the intermediate phase. A reduction in the intensity of overall Raman spectra with increasing dopant concentration is seen for all the metal doped glasses. Floppy glasses are found to show major shifts in Raman peaks in temperature dependent Raman studies.

Keywords: Chalcogenide glasses, Raman spectroscopy, Intermediate phase

[1]Corresponding Author. Tel.: +1-208-426-5968; fax: +1-208-426-2470.
Email address: KrisCampbell@boisestate.edu

1. Introduction –

In recent years much attention has been paid to Ge–Se-based amorphous chalcogenide semiconductors as they are very promising materials for electronic and optoelectronic applications [[19]-[22]]. Ge-Se has also received a great deal of interest, in terms of the changes in the structural dimensionality of the glass with increasing Ge content, leading to different measurable effects in the electronic, structural, vibrational and thermal properties [[23]-[28]].

The character of a network glass undergoes a qualitative change, from being easily deformable (or, floppy) at an average coordination number, <r> < 2.4 to being rigid at <r> > 2.4 [[29], [30]]. The quantity <r> is formally defined as $\frac{\sum n_i r_i}{N}$, where n_i represents the number of atoms having a coordination r_i and $N = \sum n_i$ gives the total number of atoms in a network. <r> = 2.4, is called the rigidity percolation threshold, and for Ge_xSe_{100-x} glasses it corresponds to x = 20 using the coordination numbers of 4 for Ge and 2 for Se, conforming with Mott's (8-N) rule [13, 14]. Although the physical nature of this rigidity transition is not yet fully understood, it was recently pointed out that there is a range of chemical compositions across which the optimal requirement of rigidity transition is fulfilled in glasses [15, 16]. Previous experiments including Mössbauer spectroscopy [17], electrical switching [18], and differential scanning calorimetry [19] have shown evidence of threshold behavior in this range which is called the intermediate phase [15, 16]. From this point of view, the Ge-Se system is very attractive to study, since it allows the formation of glasses in the range x = 0 to about x = 42 corresponding to <r> = 2 to <r> = 2.84.

In this paper, the Raman spectra for Ge_xSe_{100-x} ($10 \leq x \leq 40$) glasses are investigated as Raman scattering is a useful method for clarifying the relationship between these macroscopic phenomena and the structural changes.

Raman spectra of metal (up to 3 % of Ag, Co, Cr, Cu, In, Mn, Sb, Sn, V, W and Zn) doped $Ge_{40}Se_{60}$ bulk glasses are also reported in this paper. $Ge_{40}Se_{60}$ glass was chosen as the base glass because it shows some unique properties as multi-state and multi-stack phase change memory when it is doped with certain metals [[22]]. Understanding of bonding nature of base $Ge_{40}Se_{60}$ and metal-doped $Ge_{40}Se_{60}$ glasses will allow more insight about the uniqueness of these glasses and the roles played by the metal dopants in multi-state phase change memory devices to

be gained. As a result, it would aid in potentially finding the ideal metal dopant for multi-state phase change memory devices.

Temperature dependent Raman studies have been performed to characterize the effect of temperature on the structure of the floppy and rigid glasses. One of each type of glass was chosen as representative for these studies. It is important to mention here that although some studies on Raman response of GeSe glasses with respect to change in temperature are reported earlier [20], the nature of shifts in Raman peaks due to temperature variation in floppy and rigid glasses is not mentioned in those studies.

2. Experimental details

2. (a) Sample preparation

Bulk chalcogenide glasses were prepared by the conventional melt quenching technique [21]. Proper quantities of high purity elements (≥ 99.99+%; Alfa-Aesar) were sealed into evacuated quartz tubes. The sealed tubes were then placed into a rocking tube furnace and heated to 1000 ^{o}C with a heating rate of 30 ^{o}C/min, at which point rocking was initiated. The tubes were left at this condition for approximately 6 hours, after which the tubes were rapidly quenched in an ice/water bath to get the desired glasses. Sources of metal dopants were elemental metals and as well as, metal-Se compounds, and there was no evident difference in the measured Raman spectra.

2. (b) Raman spectroscopy

The Raman spectroscopy investigations were performed with a backscattering configuration using a Renishaw Invia Raman Microscope with a resolution of 1 cm^{-1}. The scattered light was dispersed by a spectrometer fitted with a 1200 lines/mm grating. The excitation wavelength was 785 nm produced by a single-mode wavelength stabilized laser diode (Innovative Photonic Solutions). In order to avoid local laser damage on glass samples, the beam power was kept to approximately 0.5 mW the output of the laser with a 10 s total exposure time. The Raman spectra were measured three times on different points for each sample with a 20x objective lens (Leica, N.A. = 0.40) for all room temperature measurements. The beam spot size was approximately 10 μm at this configuration. The spectra of the three measurements for each sample were identical, as expected due to the homogeneity of the glasses.

For temperature dependent Raman studies, an air-cooled Linkam THMS600 temperature stage controlled by a Linkam TMS94 temperature controller was used. Raman spectra were taken at the desired temperature after 10 minutes of stabilization time and after reaching that temperature with a controlled heating rate (1 ^{0}C/min), as well as during the cooling (- 1 ^{0}C/min) in an Ar environment. For the temperature measurements, a 5x objective lens (Leica, N.A. = 0.12) was used with 30 s total exposure time due to the limitation of the working distance of temperature stage; all other conditions were similar to the room temperature experiment.

3. Results and discussion

3. (a) Raman spectra of Ge_xSe_{100-x} glasses

Unnormalized room temperature Raman spectra of bulk GeSe glasses are provided in Fig.1. Raman spectra of polycrystalline $Ge_{45}Se_{55}$ sample is also shown in the same figure for comparison. The lineshapes in Fig. 1a show the evolution of different modes of Ge-Se corner-sharing (CS) tetrahedra (193cm^{-1}) and Ge-Se edge-sharing (ES) $GeSe_{4/2}$ tetrahedra (210cm^{-1}) at the expense of the Se-Se stretch mode of Se_n-chains (CM) at about 250 cm^{-1} [20, 22]. All spectra are shown together in Fig. 1b for better comparison. In general, CS and ES modes are symmetric and could be analyzed in terms of one Gaussian each. This was not the case for the CM, however, and it required multiple Gaussians for an adequate deconvolution at all x. Examples of such deconvoluted Raman spectra for $Ge_{10}Se_{90}$and $Ge_{40}Se_{60}$ glasses are shown in Fig. 2a and 2b, respectively. The A_1 vibration (the stretching mode of the corner-sharing $GeSe_{4/2}$ tetrahedra) is at 193 cm^{-1} and the A_1 companion mode (A_1^C), indicating two adjacent $GeSe_{4/2}$ tetrahedra that are connected by sharing a common edge or the A_1^C breathing vibrations of edge-shared $Ge_2Se_{8/2}$ bi-tetrahedra, is at 210 cm^{-1}. The peak seen around 250 cm^{-1} can be deconvoluted into four Gaussians whose peaks are at 236, 252, 262 and 292 cm^{-1}. With an increase in x (i.e., Ge concentration), the intensity of the peak at 252 cm^{-1} decreases significantly whereas the intensity of the peak at 292 cm^{-1} increases only moderately. The intensities of the other two peaks remain almost the same throughout the compositional range. The peak at 252 cm^{-1}can be attributed to Se_8 rings[7, 23] and the diminution of its intensity and augmentation of the intensity of the 210 cm^{-1}peak with increasing Ge content suggests that Ge disrupts Se_8 rings to make new $GeSe_{4/2}$ tetrahedra in Ge-rich glasses. The peaks at 236 and 292 cm^{-1} are attributed to Se rings fragments or Se_n chains[[25], 23] and F_2 antisymmetric vibration modes of $GeSe_{4/2}$ based structural units

[22, 24], respectively. The presence of the 236 cm^{-1} mode in all samples indicates the presence of Se ring fragments throughout the range of composition. The fact that the 292 cm^{-1} mode intensity increases marginally with increasing Ge content supports the decision of assignment of F_2 antisymmetric vibration modes of $GeSe_{4/2}$ based structural units to it (Fig. 2a and 2b). From the study of Marquez et al [25], symmetric stretching vibrations of Se-Se bonds may be attributed to the 262 cm^{-1} mode.

Table 1 lists all the deconvoluted peaks seen in each sample. Two new peaks (136 and 179 cm^{-1}) appear for the glasses with $x \geq 30$ and another new peak (160 cm^{-1}) for the glasses with x =40. The first two peaks at 136 and 179 cm^{-1} are due to the unresolved lattice modes or the vibrations of structural units similar to the compound GeSe with a Ge-to-Se ratio of approximately 1 and the vibrating of $Se_3Ge–GeSe_3$ units or ethane-like Ge_2Se_6 units, respectively. The mode at 160 cm^{-1} is seen for the first time in this study. The deconvoluted example graph of $Ge_{40}Se_{60}$ in Fig. 2b clearly depicts the three new peaks which appear for $x \geq 30$ glasses.

Table 1: Raman peaks seen Ge_xSe_{100-x} glasses; peaks are attributed to (a) - F_2 antisymmetric vibration modes of $GeSe_{4/2}$ based structural units, (b) - symmetric stretching vibrations of Se-Se bonds, (c) - Se_8 rings, (d) - Se rings fragments or Se_n chains, (e) - A_1^C breathing vibrations of edge-shared $Ge_2Se_{8/2}$ bi-tetrahedra, (f) - A_1 vibration or the stretching mode of the corner-sharing $GeSe_{4/2}$ tetrahedra, (g) - vibrating of $Se_3Ge–GeSe_3$ units or ethane-like Ge_2Se_6 units, (h) unassigned, and (i) - unresolved lattice modes or the vibrations of structural units similar to the compound GeSe with a Ge-to-Se ratio of approximately 1.

Sample	**Raman Peaks (cm^{-1})**
$Ge_{10}Se_{90}$	193 (f), 210 (e), 236 (d), 252 (c), 262 (b), 292 (a)
$Ge_{15}Se_{85}$	193, 210, 239, 255, 269, 291
$Ge_{20}Se_{80}$	194, 211, 236, 256, 271, 291
$Ge_{23}Se_{77}$	194, 211, 234, 257, 284, 308
$Ge_{25}Se_{75}$	195, 212, 237, 260, 288, 310
$Ge_{30}Se_{70}$	136 (i), 179 (g), 197, 214, 243, 263, 280, 305
$Ge_{33.33}Se_{66.67}$	134, 175, 199, 215, 240, 263, 282, 308
$Ge_{35}Se_{65}$	133, 175, 198, 215, 236, 258, 281, 307

$Ge_{40}Se_{60}$	132, 160 (h), 175, 198, 210, 237, 257, 277, 303

For a better view of compositional evolution of the peaks mentioned in previous paragraphs and Table 1, all graphs are normalized and plotted with respect to the peak at 193 cm^{-1} of $G_{10}Se_{90}$ glass in Fig. 3 as193 cm^{-1} peak appears for all of studied glasses.

The compositional variation of the Raman peaks is plotted in Fig.4. It can be clearly seen from the figure that there is a change of slope of almost all curves for the composition range of $20 \leq x \leq 25$ ($2.40 \leq \langle r \rangle \leq 2.50$). This change of slope can be interpreted as evidence for an intermediate phase or reversibility window, first described by Boolchand [15], around an average coordination number,$\langle r \rangle = 2.4$. The term 'reversibility window' is associated with the range of glasses within this window as these glasses show loss of irreversibility of the heat flow on cycling through the glass transition temperatures. The glasses in the intermediate phase are, in that sense, stress-free.

The peak at 179 cm^{-1} for $x \geq 30$ glasses is an indication of the appearance of Ge-Ge homopolar bonds for these compositions. When $\langle r \rangle$ is greater than 2.5 (the intermediate phase maximum), Ge-Ge bonds start to appear, and as a result the glasses become rigid-stressed [26]. A gradual downward Raman shift is seen for glasses $x \geq 35$ which can be an indication of phase separation in these stressed glasses [16, 27], as the decrement in mode frequency might be a result of deprivation of network connectivity. Phase separation in Ge-Se glasses is known to appear beyond $\langle r \rangle \geq 2.67$ [26] which may result from the deprivation of network connectivity mentioned in previous sentence.

3. (b) Raman spectra of metal doped $Ge_{40}Se_{60}$glasses

Raman spectra of $Ge_{40}Se_{60}$ and $(Ge_{40}Se_{60})_{100-x}M_x$ (M = metal; Ag, Co, Cr, Cu, In, Mn, Sb, Sn, V, W and Zn) glasses are similar in nature with the exception of the Co, Cr, V and W doped samples. It is interesting to mention here that the intensity of Raman spectra and peaks for all metal doped glasses systematically reduces with increasing dopant concentration and as a result, Raman spectra become noisier with the same experimental conditions. This is due to the reduction in Ge-Ge and Ge-Se bonds as the metal is incorporated into the glass. The metal dopant atoms will bond with the Se atoms [28] reducing the number of Se atoms that are available to make a bond with Ge effectively decreasing the intensity of those peaks. Error in the deconvolution process is also increased because of these effects. As an example, Raman spectra

of different concentration of Mn-doped $Ge_{40}Se_{60}$ glasses are given in Fig. 5. The decrease of overall Raman intensity with increase in dopant concentration can be clearly seen from the figure. The intensity ratio of the two major peaks at 175 and 198 cm^{-1} does not indicate any trend contrary to the results by Ikari et al.which show that the ratio of the peaks varies with dopant concentration [28]. Low level of change in dopant concentration might be one of the reasons behind our observation.

Raman spectra of $Ge_{40}Se_{60}$ and $(Ge_{40}Se_{60})_{97}M_3$ (M = metal; Ag, Co, Cr, In, Mn, Sb, Sn, V, W and Zn) glasses are shown in Fig. 6.Intensity of Raman spectra for all metal doped glasses is invariably lower than base $Ge_{40}Se_{60}$ glass.

Peaks deducted from the spectra of Fig. 6 are shown in Table 2. Raman spectra (Fig. 6) and Raman data (Table 2) for Co, Cr, V and W-doped materials indicate that there are major structural differences in these glasses with respect to base $Ge_{40}Se_{60}$ glass. The reason for and significance of these differences is subject to future investigation.

Table 2: Raman peaks seen metal doped $Ge_{40}Se_{60}$ glasses.

Sample	**Raman Peaks (cm^{-1})**
$Ge_{40}Se_{60}$	132, 160, 175, 198, 210, 237, 257, 277, 303
$(Ge_{40}Se_{60})_{97}Ag_3$	137, 159, 174, 196, 208, 236, 261, 283, 307
$(Ge_{40}Se_{60})_{97}Co_3$	132, 176, 200, 216, 238, 270, 296, 320
$(Ge_{40}Se_{60})_{97}Cr_3$	127, 152, 172, 198, 219, 242, 263, 283, 307
$(Ge_{40}Se_{60})_{97}Cu_3$	135, 161, 176, 196, 209, 236, 260, 280, 304
$(Ge_{40}Se_{60})_{97}In_3$	124, 149, 171, 198, 208, 233, 253, 278, 300
$(Ge_{40}Se_{60})_{97}Mn_3$	129, 155, 174, 197, 212, 235, 256, 281, 305
$(Ge_{40}Se_{60})_{97}Sb_3$	130, 161, 178, 198, 217, 240, 262, 285, 303
$(Ge_{40}Se_{60})_{97}Sn_3$	132, 157, 174, 197, 211, 232, 259, 284, 305
$(Ge_{40}Se_{60})_{97}V_3$	129, 145, 163, 183, 201, 216, 256, 288, 319
$(Ge_{40}Se_{60})_{97}W_3$	129, 145, 155, 175, 197, 222, 256, 281, 305
$(Ge_{40}Se_{60})_{97}Zn_3$	127, 154, 174, 197, 210, 233, 257, 280, 305

3. (c) Temperature dependent Raman study:

The temperature dependent normalized Raman response of one floppy ($Ge_{10}Se_{90}$) and one rigid ($Ge_{40}Se_{60}$) glass are shown in Fig. 7a and 7b. Normalization of all other graphs was done with respect the peaks at 193 and 175 cm^{-1} for $Ge_{10}Se_{90}$ and $Ge_{40}Se_{60}$ glasses respectively. As the temperature increases, three major Raman modes at 193, 210 and 252 cm^{-1} of the $Ge_{10}Se_{90}$ glass show a detectable red shift and these shifts are reversible within the experimental temperature range. On the contrary, $Ge_{40}Se_{60}$ glass does not show any appreciable temperature dependence in the Raman peak at 167 cm^{-1}, and shows a slight red shift in the higher energy peaks at 197 and 265 cm^{-1} with increasing temperature. Red shift in the frequency is usually ascribed to the effects of thermal expansion and changes in phonon occupation numbers [29]. As floppy glasses usually have higher thermal expansion due to their easily deformable nature [30, 31], the red shift is more pronounced for these glasses. Although the nature of the shift is not discussed by Wang et al. [20], a similar type of shift can be clearly seen from their reported graphs. Ge_xSe_{100-x}($x \leq 15$) glasses show a clear red shift whereas Ge_xSe_{100-x} ($x > 15$) glasses show almost no shift. The opposite of this effect, a blue shift in Raman peaks, is observed when pressure is applied on the glasses [32]. A decrease in the intensity of the Raman bands with increasing temperature has also been observed for all the glasses which may be associated with the bond expansion [33].

4. Conclusions

Raman scattering experiments at room temperature on bulk Ge_xSe_{100-x} ($10 \leq x \leq 40$) chalcogenide glasses containing transition metals suggest the presence of an intermediate phase for the glasses with an average coordination number near $\langle r \rangle = 2.4$. This is seen as a fairly abrupt change in the slope of the plot generated from Raman peak position as a function of composition, the compositional variation of the Raman peaks. Glasses become more rigid and stressed beyond the intermediate phase since Ge-Ge bonds start to form. A new subtle unassigned peak at 158 cm^{-1} has been seen for Ge = 40 glasses in this study for the first time. Different metal (Ag, In, Mn, Sb, Sn and Zn, up to 3 %) doping in $Ge_{40}Se_{60}$ glasses show the reduction in intensity of overall Raman spectra with increasing dopant concentration and very

little or no shift in Raman peaks. Red shifts in the frequency in the temperature dependent Raman studies suggest a floppier nature in the glasses with $\langle r \rangle \leq 2.4$.

References:

[19] K. Sedeek, A. Adam, M.R. Balboul, L.A. Wahab, N. Makram, Mater. Res. Bull. 43 (2008) 1355.

[20] W.C. Liu, G. Hoffman, W. Zhou, R.M. Reano, P. Boolchand, Appl. Phys. Lett. 93 (2008) 041107.

[21] C. Massobrio, A. Pasquarello, Phys. Rev. B 77 (2008) 144207.

[22] K.A. Campbell, C.M. Anderson, Microelectron. J. 38 (2007) 52.

[23] B. Uebbing, A.J. Sievers, Phys. Rev. Lett. 76 (1996) 932.

[24] K. Murase, T. Fukunaga, Mater. Res. Soc. Symp. Proc. 61 (1986) 101.

[25] X. Feng, W.J. Bresser, P. Boolchand, Phys. Rev. Lett. 78 (1997) 4422.

[26] M. Tatsumisago, B.L. Halfpap, J.L. Green, S.M. Lindsay, C.A. Angell, Phys. Rev. Lett. 64 (1990) 1549.

[27] M. Taniguchi, T. Kouchi, I. Ono, S. Hosokawa, M. Nakatake, H. Namatame, K. Murase, J. Electron Spectroscopy and Related Phenomena 78 (1996) 507.

[28] A. Feltz, H. Aust, A. Blayer, J. Non-Cryst. Solids 55 (1983) 179.

[29] J.C. Phillips, J. Non-Cryst. Solids 34 (1979) 153.

[30] M.F. Thorpe, J. Non-Cryst. Solids 57 (1983) 355.

[31] S.R. Elliot, Physics of Amorphous Materials, Longmann, London, 1990, p. 61.

[32] N.F. Mott, Philos. Mag. 19 (1969) 835.

[33] P. Boolchand, D.G. Georgiev, B.J.Goodman,Optoelect. Adv. Mater. 3 (2001) 703.

[34] D. Selvanathan, W.J. Bresser, P.Boolchand, Phys. Rev. B 61(2000) 15061.

[35] P. Boolchand, P. Chen, M. Jin, B. Goodman, W.J. Bresser,Physica B: Condens. Matter 389 (2007) 18.

[36] P. Pattanayak, S. Asokan, Solid State Commun. 142 (2007) 698.

[37] D. Selvanathan, W.J. Bresser, P. Boolchand, B. Goodman Solid State Commun. 111 (1999) 619.

[38] Y.Wang , O.Matsuda, K.Inoue, O.Yamamuro, T.Matsuo, K.Murase, J. Non-Cryst. Solids 232-234 (1998) 702.

[39] K.A. Campbell, M.G. Davis, J.M.Peloquin, Mater. Res. Soc. Symp. Proc. 997 (2007) 343.

[40] P.M. Bridenbaugh G.P. Espinosa, J.E. Griffiths, J.C. Phillips, and J.P. Remeika,Phys. Rev. B 20 (1979) 4140.

[41] G. Lucovsky, A. Mooradian, W. Taylor, G.B. Wright, R.C.Keezer, Solid State Commun. 5 (1967) 113.

[42] R.K. Pan, H.Z. Tao, H.C. Zang, X.J. Zhao, T.J. Zhang, J. Alloys Compd. 484 (2009) 645.

[43] E. Marquez, P.Nagels, J.M. Gonzalez-Leal, A.M. Bernal-Oliva, E.Sleeckx, R.Callaerts, Vacuum 52 (1999) 55.

[44] W.Zhou, M.Paesler, and D.E. Sayers, Phys. Rev. B43 (1991) 2315.

[45] P.Boo1chand, D.G. Georgiev, T.Qu, F.Wang, L.Cai, S.Chakravarty, C. R. Chimie 5 (2002) 713.

[46] T. Ikari, T. Tanaka, K. Dra, K. Maeda, K. Futagami, S. Shigetomi, Phys. Rev. B 47 (1993) 4984.

[47] A.S. Pines, P.E. Tannenwald, Phys. Rev. 178 (1969) 1424.

[48] S.Mahadevan, A. Giridhar, J. Non-Cryst. Solids 5162 (1993) 294.

[49] U.Senapati, A.K. Varshneya, J. Non-Cryst. Solids 185 (1995) 289.

[50] F.Wang, S. Mamedov, P. Boolchand, B. Goodman, M.Chandrasekhar, Phys. Rev. B 71 (2005) 174201.

[51] G.Lucazeau, J. Raman Spectrosc.,34 (2003) 478.

List of figures

Fig. 1a. Room temperature unnormalized Raman spectra of Ge_xSe_{100-x} glasses; no smoothing was performed.**1b.**Waterfall version of the spectra shown in Fig. 1a for better comparison.

Fig. 2a. Example of deconvoluted Raman spectra for $Ge_{10}Se_{90}$ glass showing six Gaussians to fit three peaks.**2b.** Example of deconvoluted Raman spectra for $Ge_{38.2}Se_{61.8}$ glass showing nine Gaussians to fit four major peaks.

Fig. 3. Normalized Raman spectra of Ge_xSe_{100-x} glassesshowing compositional evolution of the peaks with respect to the peak at 193 cm^{-1} of $G_{10}Se_{90}$ glass.

Fig. 4. Compositional variation of each Raman peak seen in Ge-Se glasses. Peak assignment is provided in Table 1.

Fig. 5. Unnormalized Raman spectra of Mn-doped and base $Ge_{40}Se_{60}$ glasses showing decline in intensity with increase in metal concentration.

Fig. 6. UnnormalizedRaman spectra of all metal doped $Ge_{40}Se_{60}$ glasses studied in this article.

Fig. 7a. Temperature dependent normalized Raman response for $Ge_{10}Se_{90}$ glass; Raman modes at 193, 210 and 252 cm^{-1} show a reversible detectable red shift within the experimental temperature range. **7b.** Temperature dependent normalized Raman response for $Ge_{40}Se_{60}$ glass showing no temperature dependence.

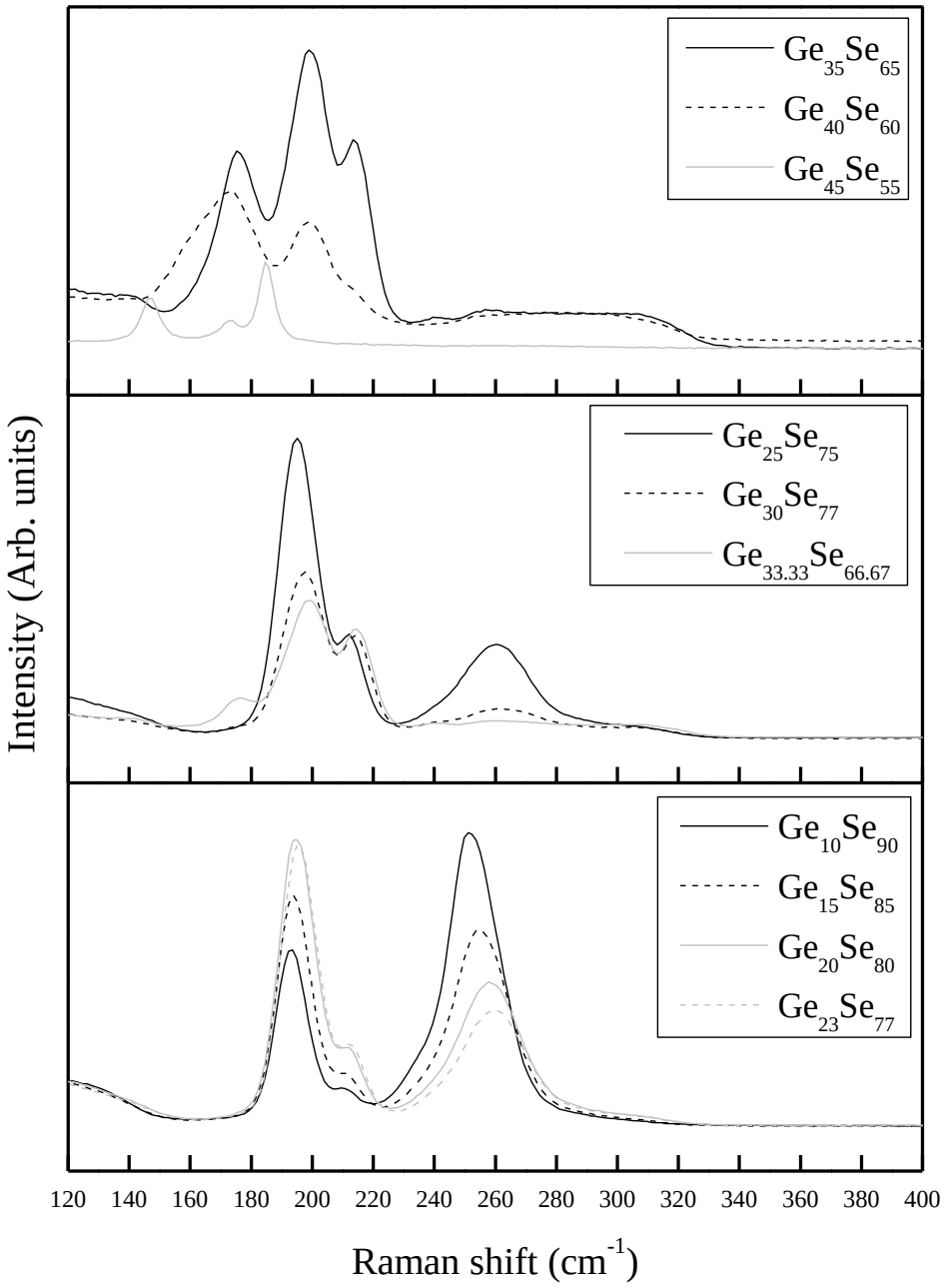
Ge35Se65
Ge40Se60
Ge45Se55
Ge25Se75
Ge30Se77
Ge33.33Se66.67
Ge10Se90
Ge15Se85
Ge20Se80
Ge23Se77
Intensity (Arb. units)
120 140 160 180 200 220 240 260 280 300 320 340 360 380 400
Raman shift (cm-1)

Fig. 1a.

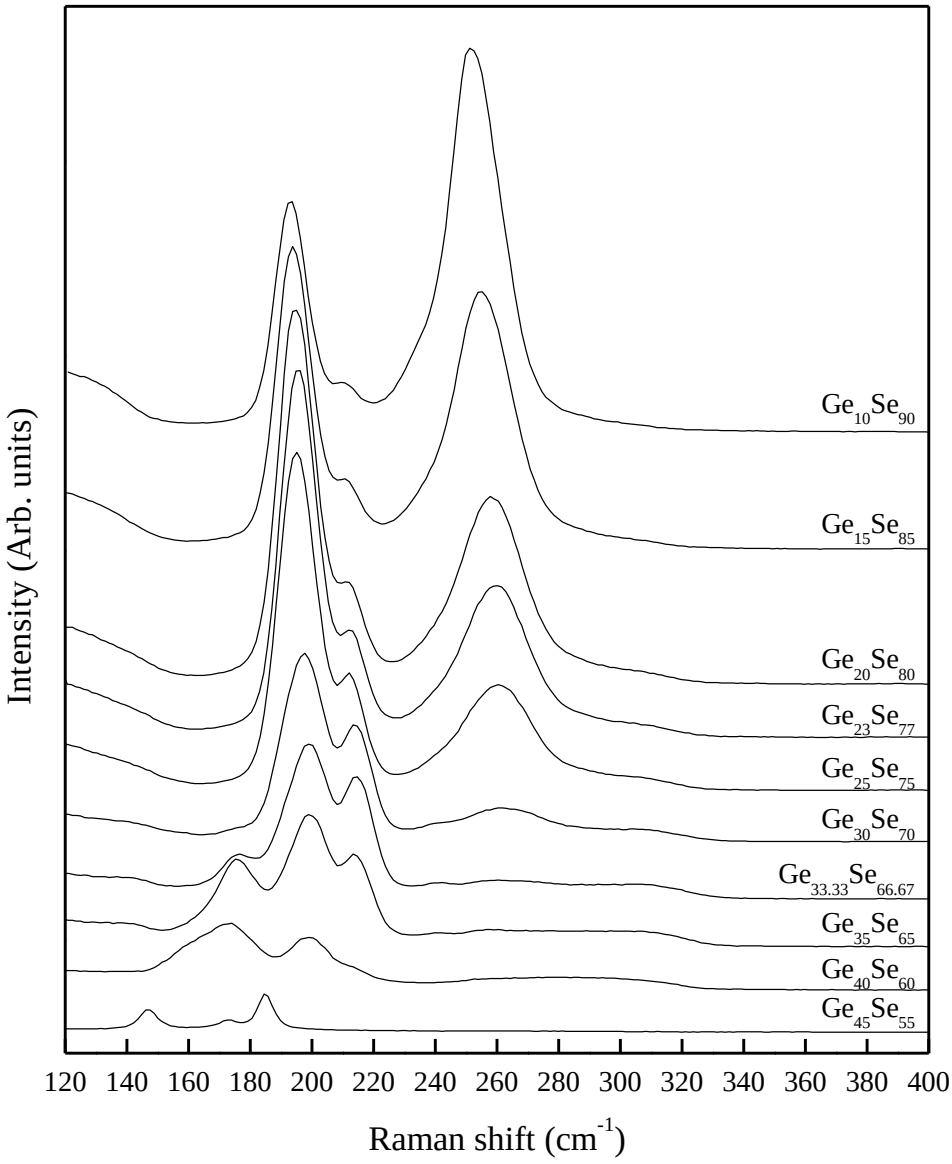
Intensity (Arb. units)
Ge10Se90
Ge15Se85
Ge20Se80
Ge23Se77
Ge25Se75
Ge30Se70
Ge33.33Se66.67
Ge35Se65
Ge40Se60
Ge45Se55
120 140 160 180 200 220 240 260 280 300 320 340 360 380 400
Raman shift (cm-1)

Fig. 1b.

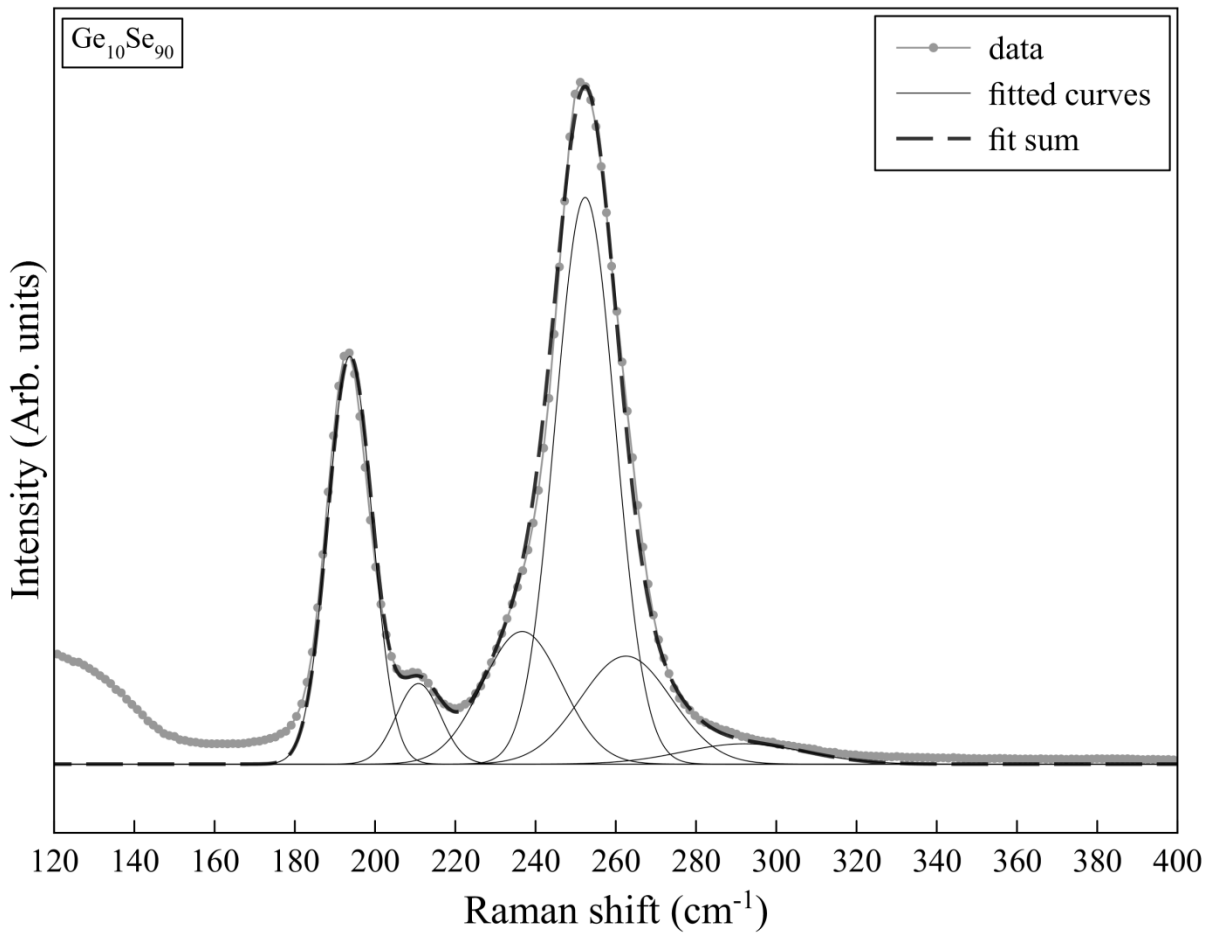
Ge10Se90
data
fitted curves
fit sum
Intensity (Arb. units)
120
140
160
180
200
220
240
260
280
300
320
340
360
380
400
Raman shift (cm-1)

Fig. 2a.

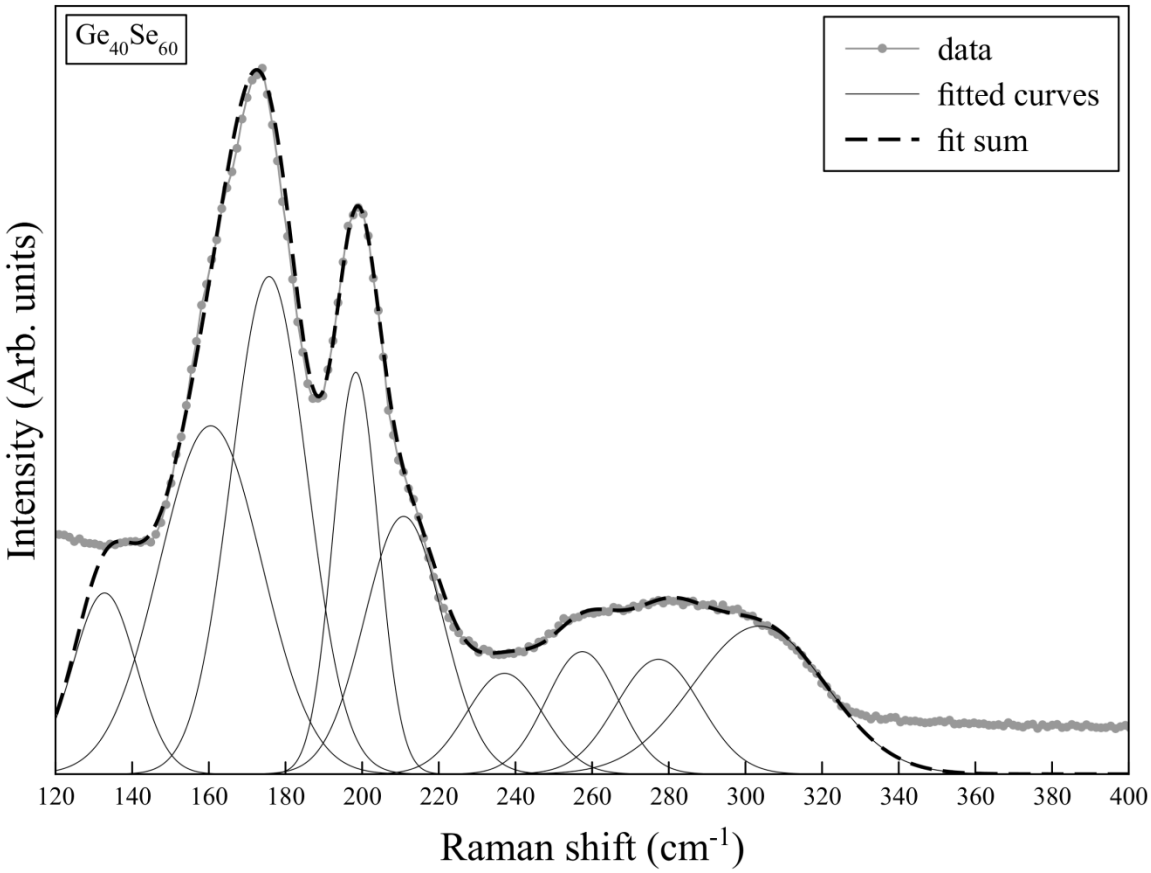
Ge40Se60
data
fitted curves
fit sum
Intensity (Arb. units)
120
140
160
180
200
220
240
260
280
300
320
340
360
380
400
Raman shift (cm-1)

Fig. 2b.

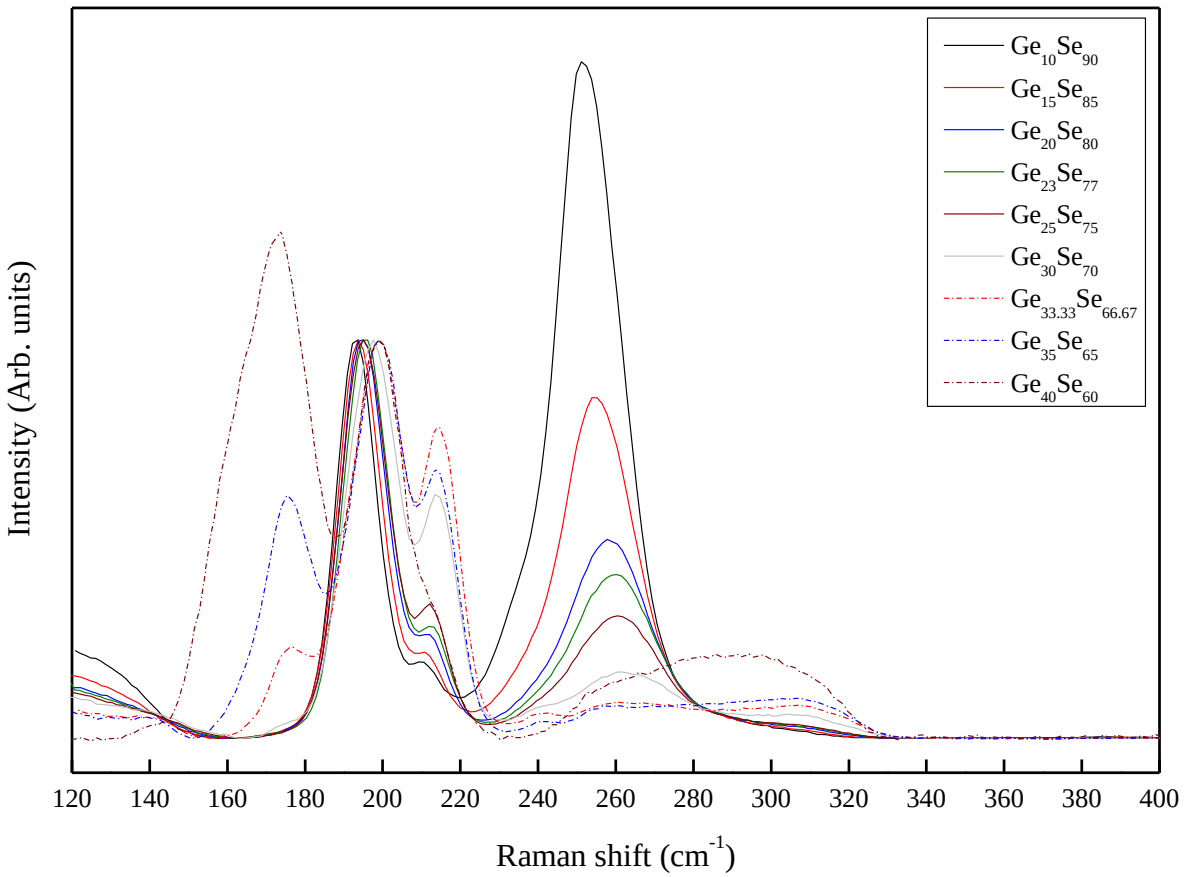
Intensity (Arb. units)
Raman shift (cm-1)
120
140
160
180
200
220
240
260
280
300
320
340
360
380
400
Ge10Se90
Ge15Se85
Ge20Se80
Ge23Se77
Ge25Se75
Ge30Se70
Ge33.33Se66.67
Ge35Se65
Ge40Se60

Fig. 3.

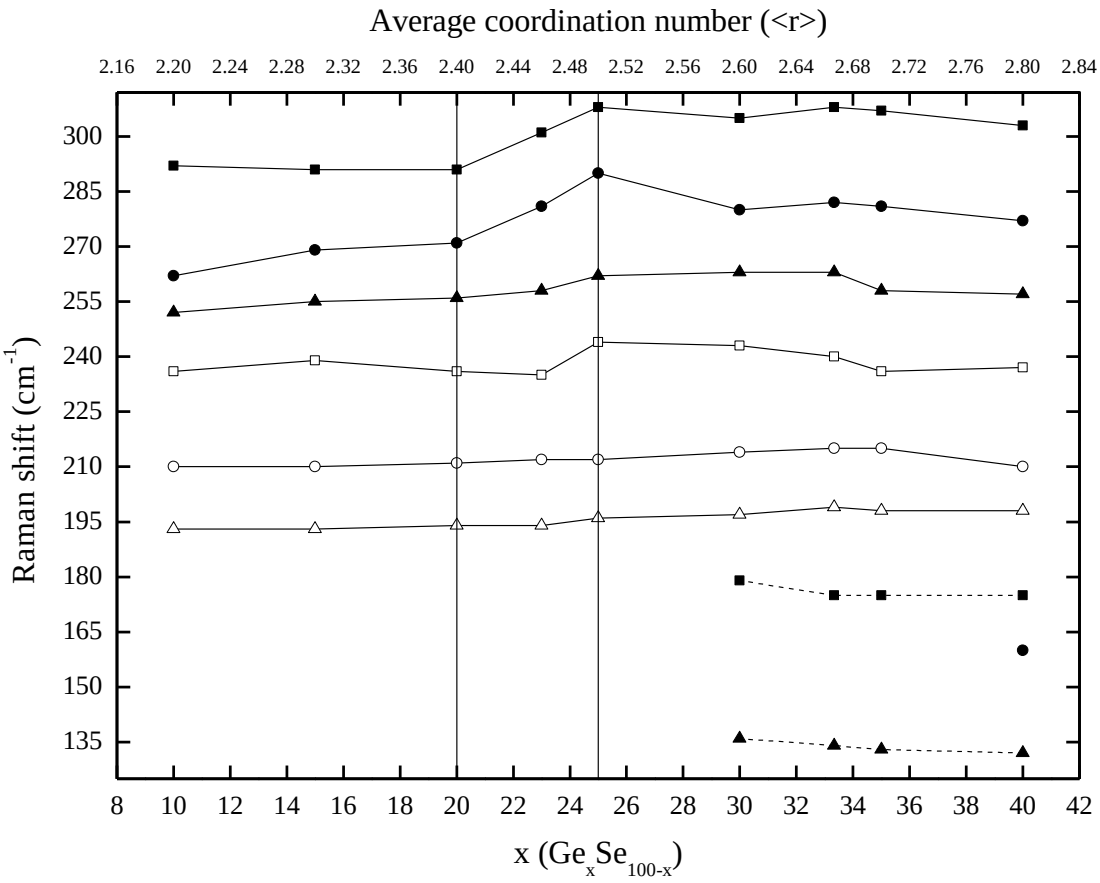
Average coordination number (<r>)
2.16 2.20 2.24 2.28 2.32 2.36 2.40 2.44 2.48 2.52 2.56 2.60 2.64 2.68 2.72 2.76 2.80 2.84
Raman shift (cm-1)
300 285 270 255 240 225 210 195 180 165 150 135
8 10 12 14 16 18 20 22 24 26 28 30 32 34 36 38 40 42
x (GexSe100-x)

Fig. 4.

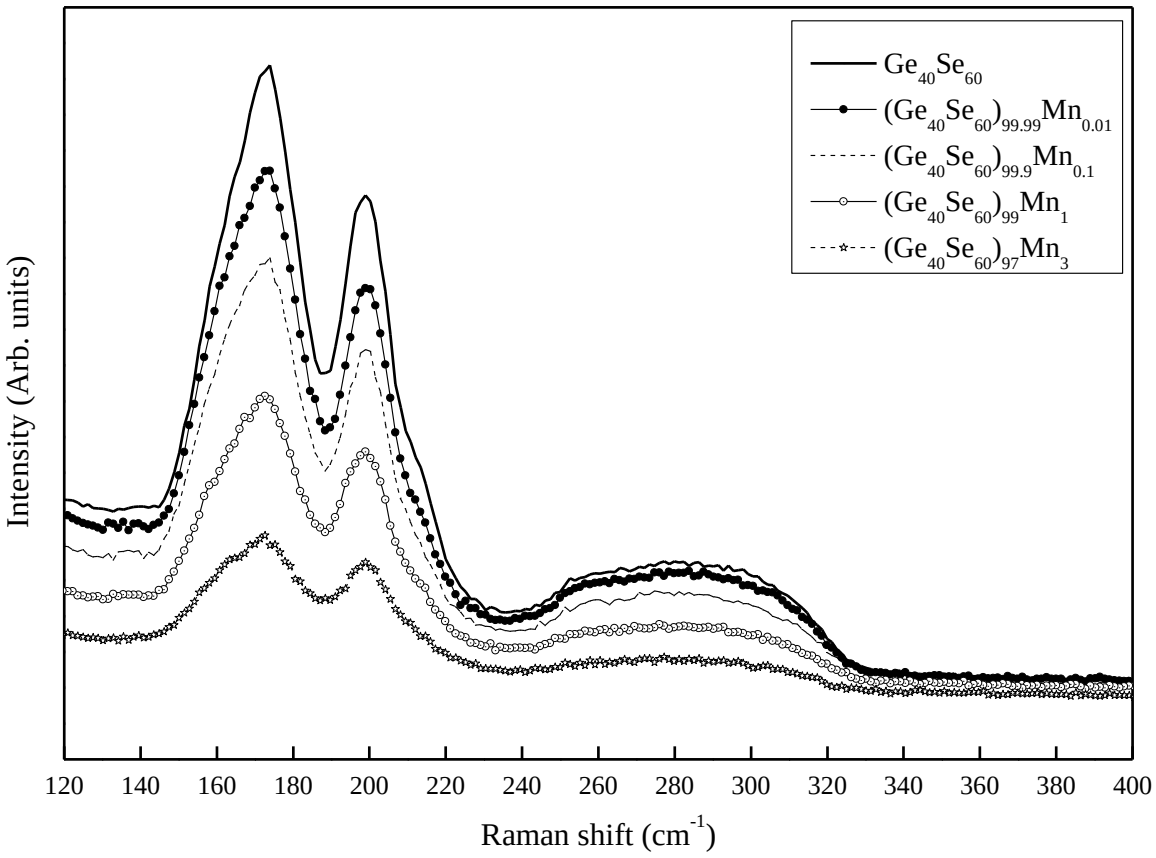
Ge40Se60
(Ge40Se60)99.99Mn0.01
(Ge40Se60)99.9Mn0.1
(Ge40Se60)99Mn1
(Ge40Se60)97Mn3
Intensity (Arb. units)
120
140
160
180
200
220
240
260
280
300
320
340
360
380
400
Raman shift (cm-1)

Fig. 5.

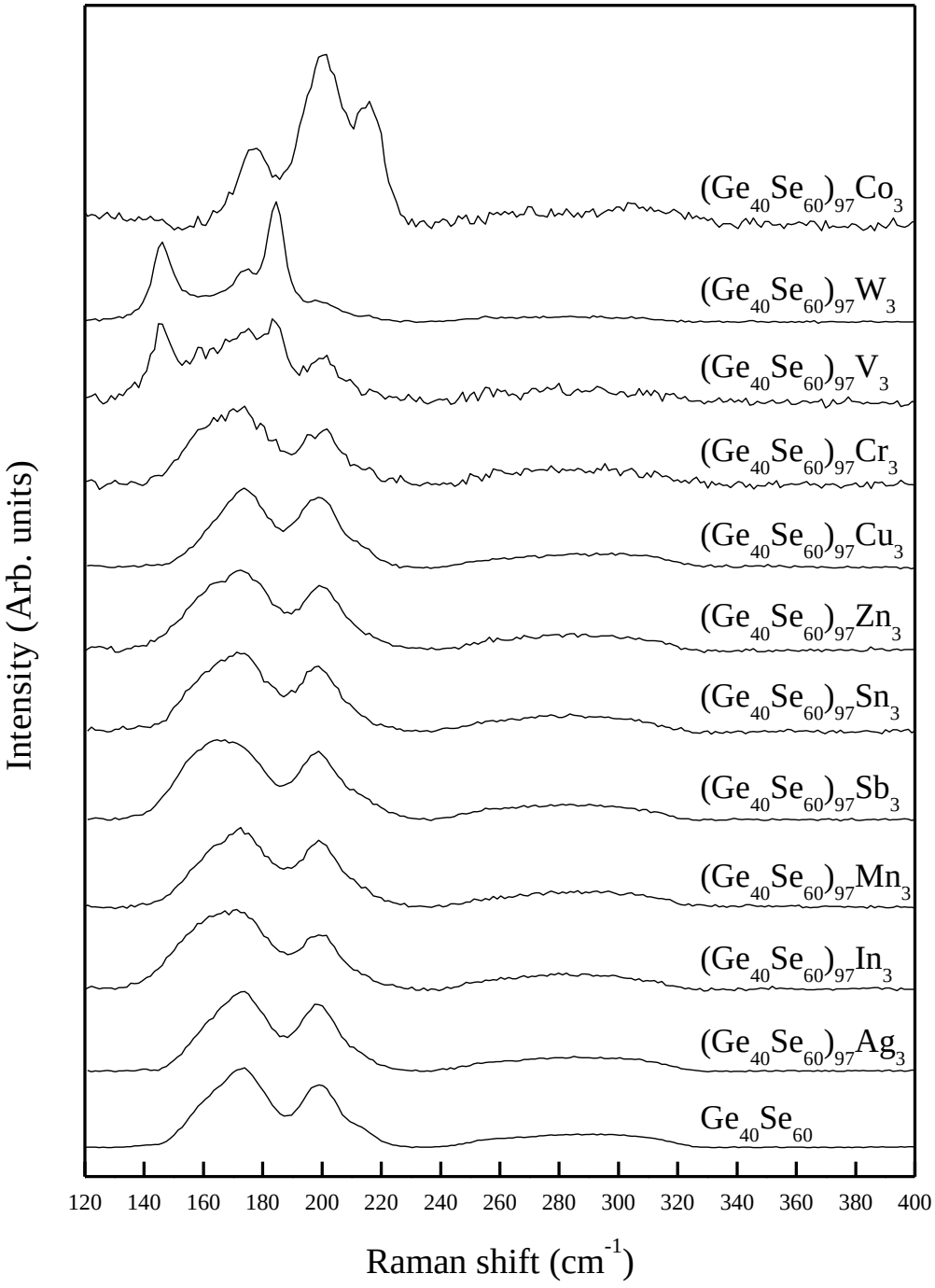
Intensity (Arb. units)
(Ge40Se60)97Co3
(Ge40Se60)97W3
(Ge40Se60)97V3
(Ge40Se60)97Cr3
(Ge40Se60)97Cu3
(Ge40Se60)97Zn3
(Ge40Se60)97Sn3
(Ge40Se60)97Sb3
(Ge40Se60)97Mn3
(Ge40Se60)97In3
(Ge40Se60)97Ag3
Ge40Se60
120 140 160 180 200 220 240 260 280 300 320 340 360 380 400
Raman shift (cm-1)

Fig. 6.

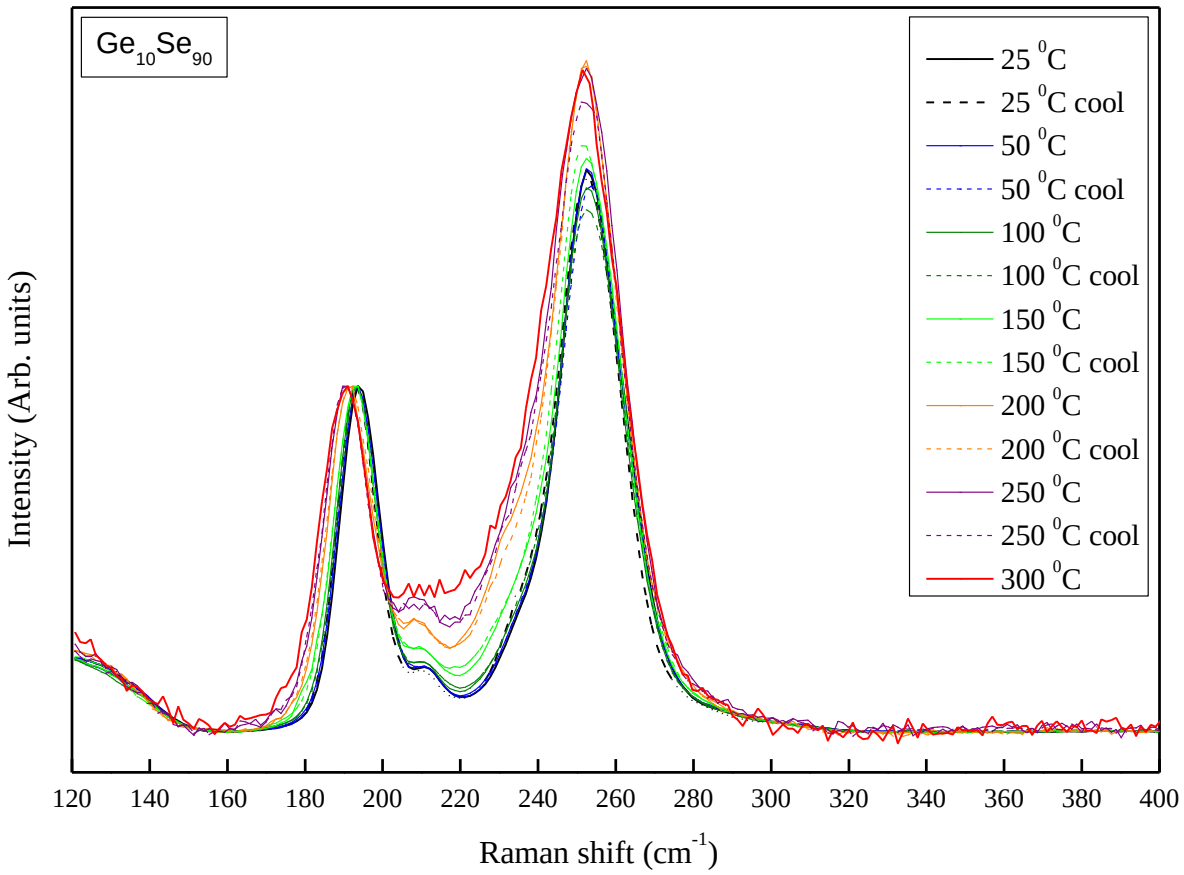
Ge10Se90
25 0C
25 0C cool
50 0C
50 0C cool
100 0C
100 0C cool
150 0C
150 0C cool
200 0C
200 0C cool
250 0C
250 0C cool
300 0C
Intensity (Arb. units)
120
140
160
180
200
220
240
260
280
300
320
340
360
380
400
Raman shift (cm-1)

Fig. 7a.

d

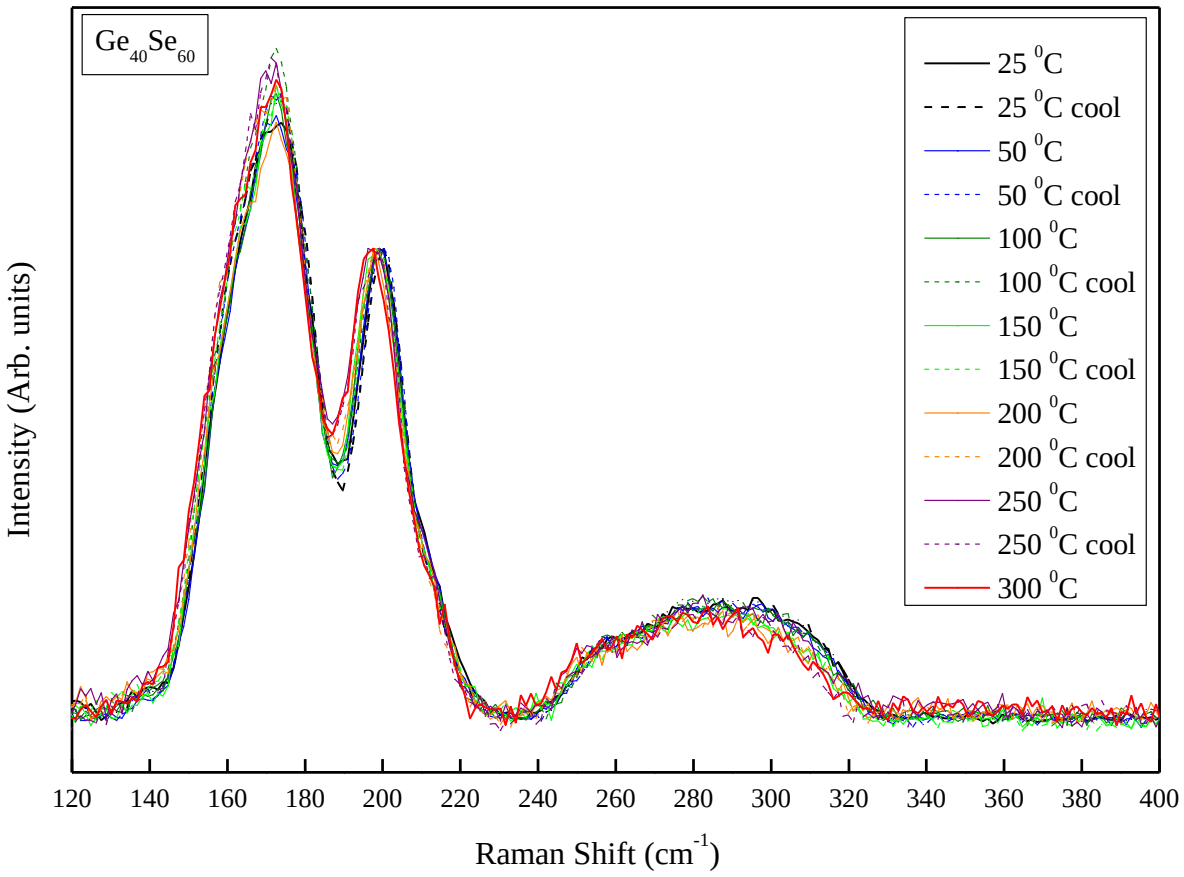
Ge40Se60
25 0C
25 0C cool
50 0C
50 0C cool
100 0C
100 0C cool
150 0C
150 0C cool
200 0C
200 0C cool
250 0C
250 0C cool
300 0C
Intensity (Arb. units)
120
140
160
180
200
220
240
260
280
300
320
340
360
380
400
Raman Shift (cm-1)

Fig. 7b.

Effect of metal doping on structural and thermal properties of Ge-Se glasses

Abstract

Ge-Se and metal doped Ge-Se glasses are synthesized and studied to elucidate the effect of doping and dopant concentration on thermal and structural properties of Ge-Se glasses. The addition of a metal dopant to $Ge_{40}Se_{60}$ glass shifts the glass and crystallization temperatures to lower temperatures. Raman data on annealed samples suggest that samples become more crystalized after crossing their crystallization peaks. The existence of multiple crystalline phases with different amounts of disorder suggests that each phase could have distinct resistivities and that these materials can be used to construct multi-bit memory.

1. Introduction

Chalcogenide based thin films are being investigated as potential materials for the next generation non-volatile memory technology [1-5]. $Ge_2Sb_2Te_5$ (GST) has been the most widely studied material for this purpose [6, 7]. Several alternate chalcogenide compositions are also being explored in an attempt to discover materials with superior performance. The use of Ge-Se/metal-Se bilayers has been reported in literature with encouraging results [5]. Investigation of memory devices employing bilayers of Ge-Se and metal-Se have revealed the possibility of obtaining multistate behavior, enhanced ability to withstand thermal cycling and use of lower voltages for achieving desired phase change response.

Resistance switching on stack structure devices such as Ge-Se/metal-Se, indicates that the formation of an alloy at the interface between the metal-Se and Ge-Se layer, as well as an alloy formed within channels created through the Ge-Se layer (caused by ion movement into the layer during electrical switching) play main role behind multi-states resistances [5, 8]. Metal ions are moved from the top metal-Se layer of the stack resulting in the formation of Ge-metal-Se solid solution. The understanding of thermal and structural properties of this alloy should, in part, determine to tune the final performance parameters of the memory bit.

In this work, we have explored the effect of modifying the metal concentration on the bulk thermal properties of ternary alloys synthesized with various compositions of metal added to the Ge-Se material. These bulk materials are used to explore the thermal and structural properties of the potential alloys that may form in-situ when a metal migrates into the Ge-Se glass layer during operation of the stacked-layer phase-change memory device. Differential scanning calorimetry (DSC) is used to observe

the glass transition and crystallization temperatures of the alloys and, Raman spectroscopy to investigate the bonding structure of the alloy.

2. Experimental details

Bulk chalcogenide glasses were prepared by the conventional melt quenching technique. Proper quantities of high purity elements (≥ 99.99+%; Alfa-Aesar) were sealed into evacuated quartz tubes. The sealed tubes were then placed into a rocking tube furnace and heated to 1000 ^{o}C with a heating rate of 30 ^{o}C/min, at which point rocking was initiated. The tubes were left at this condition for approximately 6 hours, after which the tubes were rapidly quenched in an ice/water bath to get desired glasses.

Differential scanning calorimetry (DSC) scans were collected using a Shimadzu DSC- 50 equipped with a TA50-WS thermal analyzer. Samples were hermetically sealed into aluminum pans and then heated at a rate of 15 ^{o}C/min from ambient temperature to 600 ^{o}C. Raman spectra were collected using a Thermo-Nicolet Nexus 670 ESP FT-Raman module.

Samples were annealed at 20 ^{o} above glass transition and crystallization temperatures for 10 min in sealed aluminum pans and then studied for Raman response to see the structural evolution with respect to temperature.

3. Results and discussion

Figure 1 compares the DSC scans for 1% and 3% doped $Ge_{40}Se_{60}$ materials taken at a heating rate of 15 °C/min with the undoped $Ge_{40}Se_{60}$ material. The undoped sample has a glass transition at 425 °C and an asymmetrical crystallization peak with a maximum at 480 °C and a shoulder at 430 °C. The addition of 1% metal cation leads to an immediate change in the crystallization peak where it begins to split into two distinct peaks. The addition of 3% metal cation leads to the clear formation of two crystallization peaks for all dopants except Zn, which splits into three crystallization peaks.

Table 1 summarizes the glass transition and melting point data. The initial addition of metal results in a small reduction in the depth of the glass transition (ΔW_{gt}) as the sample progresses through the glass transition but the further addition of metal results in an increase of ΔW_{gt} relative to the undoped sample. It is interesting to note that in the 1% In doped sample there appears to be two melting points whereas in the 3% In doped sample there is only one. This effect has been repeated and suggests that the 1% In doped sample may be more heterogeneous than the 3% In doped sample. Lastly, except for the 1% and 3% Zn samples, the addition of the metal dopant has no appreciable effect on heat of melting, ΔH_{mp}.

Table 1. Summary of glass transition and melting point data.

	T_{gt} (°C)	ΔW_{gt} (W/g)	T_{mp} (°C)	ΔH_{mp} (J/g)
Undoped	354	0.01558	585	42.02
1% Sn	327	0.01305	577	46.94
1% Sb	340	0.0128	575	43.8
1% In	329	0.01168	562/574	52.4
1% Zn	333	0.01267	580	35.76
3% Sn	282	0.01665	575	45.16
3% Sb	324	0.01617	563	41.03
3% In	306	0.01466	565	46.99
3% Zn	328	0.01981	578	60.59

T_{gt} – Glass Transition
T_{mp} – Melting Point
ΔW_{gt} Depth of Glass Transition
ΔH_{mp} – Heat of Melting

Table 2 summarizes the crystallization transition data. For purposes of clarity, the crystallization peaks are numbered in order of decreasing temperature. Except for 1% Sb, the addition of the metal dopant results in a decrease in the crystallization temperature relative to the undoped material.

Table 2. Summary of crystallization transition information.

	T_{c1} (°C)	T_{c2} (°C)	T_{c3} (°C)	A_{c1} (kJ/mol)	A_{c2} (kJ/mol)	A_{c3} (kJ/mol)	ΔH_{c1} (J/g)	ΔH_{c2} (J/g)	ΔH_{c3} (J/g)	Sum of all Heats of Crystallization (J/g)
Undoped	486			267			72.31			72.31
1% Sn	489	467		323	287					59.25
1% Sb	493	470		228	337					56.45
1% In	468	443		324	173					57.64
1% Zn	487	474	364	229	229	285			5.94	49.88
3% Sn	460	396		395	395		20.59	35.7		56.32
3% Sb	460	400		256	482		22.33	39.87		62.20
3% In	456	390		397	254		17.7	42.6		60.29
3% Zn	470	422	326	414	333	480	22.57	21.8	11.2	55.48

T – Crystallization Temperatures
A – Activation Energy of Crystallization
H – Heat of Crystallization
The individual Heats of Crystallization are not shown for the first two peaks of the 1% doped samples because of peak overlap

Figure 2 compares the Raman spectra of 1% and 3% doped $Ge_{40}Se_{60}$ materials with the undoped $Ge_{40}Se_{60}$ material. All the materials show the classic $Ge_{40}Se_{60}$ Raman spectra with peaks at 195 and 210 cm^{-1} attributable to the breathing modes of Ge-Se corner sharing units and Ge-Se edge sharing units, respectively [9-12]. Further all the materials contain a shoulder near 170 cm^{-1} and a broad peak near 300 cm^{-1} due to the Ge-Ge stretching mode.

This effect is more clearly seen in Figure 3, which compares the Raman spectra of 1% and 3% doped $Ge_{33}Se_{67}$ materials with the undoped $Ge_{33}Se_{67}$ material. The addition of the metal to the $Ge_{33}Se_{67}$ results in a clear increase in the contribution of the Ge-Ge stretching mode relative to the Ge-Se modes. It is likely the addition of the metal results in the formation of M-Se bonds leading to the disruption of the Ge-Se edge sharing and corner sharing units. The removal of any Ge-Se bonds should result in a compensating increase in Ge-Ge bonds.

Figure 4A compares the Raman spectra of undoped $Ge_{40}Se_{60}$ after annealing of the sample at specific temperatures just past the glass transition and its crystallization temperature. Not too surprising heating just past the glass transition results in no significant change in the Raman spectra but heating beyond the crystallization temperature does result in significant change. Figure 4B compares the Raman spectra of undoped $Ge_{40}Se_{60}$ material with the 3% Sn, In and Zn samples in which all the samples have been annealed at a temperature past their last crystallization temperature and as a result all the samples are in their crystalline phase. Comparison of the Raman spectra of all the crystalline forms shows that the addition of metal dopant does slightly alter the Raman spectra of the 3% In and 3% Zn samples. The addition of 3% Sn does somewhat significantly alter the Raman in that the peaks are significantly broader in the 3% Sn sample. The increase in breadth is most likely due to some disorder in the crystalline phase.

Figure 5 compares the Raman spectra of 3% Sn, In, Sb and Zn doped $Ge_{40}Se_{60}$ samples in which the samples have been annealed at temperatures just past their glass transitions as well as each of their crystallization peaks. As with the undoped sample, annealing past the glass transition has little effect on the Raman spectra. However, annealing past the first crystallization peak does result in a significant change in which the Raman spectra significantly but not completely transforms toward the Raman spectra of the fully crystalline material. In all cases, the two main peaks are significantly broader than they are in the fully crystalline forms and the spectra are missing a small peak at 210 cm^{-1}.

4. Conclusions

The addition of a metal dopant to $Ge_{40}Se_{60}$ glass results in a shift of the glass and crystallization temperatures to lower temperatures and except in the case of Sb and Zn, results in an increase in the activation energy of the crystallization process. Further, the introduction of the Sn, In and Sb dopant results in two crystallization peaks and the introduction of the Zn dopant results in three crystallization

peaks. The Raman data indicate that as the metal doped materials are heated through their crystallization peaks that the crystalline phase becomes more ordered. The existence of crystalline phases with different amounts of disorder suggests that each phase could have distinct resistivities and that these materials can be used to construct multi-state memory. The significant increase in the activation barrier for the crystallization process following the addition of the metal dopant is important as it serves as a predictor that the amorphous and first crystallization phases will be highly stable, which is important for a non-volatile memory.

References

1. Philip Wong H S, Raoux Simone, Kim Sang Bum, Liang Jiale, Reifenberg John P, Rajendran Bipin, Asheghi Mehdi and Goodson Kenneth E 2010 Proceedings of the IEEE **98** 0018
2. Sedeek K, Adam A, Balboul M R, Wahab L A and Makram N 2008 Mater. Res. Bull. **43** 1355
3. Liu W C, Hoffman G, Zhou W, Reano R M and Boolchand P 2008 Appl. Phys. Lett. **93** 041107
4. Massobrio C and Pasquarello A 2008 Phys. Rev. B **77** 144207
5. Campbell K A and Anderson C M 2007 Microelectron. J. **38** 52
6. Shang Fei, Zhai Jiwei, Song Sannian, Song Zhitang and Wang Changzhou 2010 Appl. Phys. Lett. **96** 203504
7. Lee Suyoun, Jeong Doo Seok, Jeong Jeung-hyun, Zhe Wu, Park Young-Wook, Ahn Hyung-Woo, Kim Won Mok and Cheong Byung-ki 2009 Appl. Phys. Lett. **95** 093504
8. Devasia Archana, Kurinec Santosh, Campbell Kristy A and Raoux Simone 2010 Appl. Phys. Lett. **96** 141908
9. Feng X, Bresser W J and Boolchand P 1997 Phys. Rev. Lett. **78** 4422
10. Wang Y, Matsuda O, Inoue K, Yamamuro O, Matsuo T and Murase K 1998 J. Non-Cryst. Solids **232-234** 702
11. Bridenbaugh P M, Espinosa G P, Griffiths J E, Phillips J C and Remeika J P 1979 Phys. Rev. B **20** 4140
12. Lucovsky G, Mooradian A, Taylor W, Wright G B and Keezer R C 1967 Solid State Commun. **5** 113
13. Pan R K, Tao H Z, Zang H C, Zhao X J and Zhang T J 2009 J. Alloys Compd. **484** 645

List of Figures

Figure 1. DSC traces of $(Ge_{40}Se_{60})_{100-x}M_x$ materials where M = Sn, Sb, In or Zn. Exothermic events results in negative peaks. The * marks the glass transition.

Figure 2. Comparison of Raman spectra of $(Ge_{40}Se_{60})_{100-x}M_x$ glasses where x = 0, 1 and 3 and M = Sn, In, Sb and Zn.

Figure 3. Comparison of Raman spectra of $(Ge_{33}Se_{67})_{100-x}M_x$ glasses where x = 0, 1 and 3 and M = Sn, In, Sb and Zn

Figure 4. A) Comparison of the Raman spectra of undoped $Ge_{40}Se_{60}$ material annealed at various temperature. **B)** Comparison of the Raman Spectra undoped $Ge_{40}Se_{60}$ material and $(Ge_{40}Se_{60})_{100-x}M_x$ materials annealed after their last crystallization peak, where x = 3 and M = Sn, In and Zn.

Figure 5. Comparison of the Raman spectra of $(Ge_{40}Se_{60})_{97}M_3$ materials annealed at specific temperature peak, where M = Sn, In, Sb and Zn.

Figure 6. Comparison of DSC traces of undoped $Ge_{40}Se_{60}$ material with 3% Sn and 0.1 % Mn doped $Ge_{40}Se_{60}$ material.

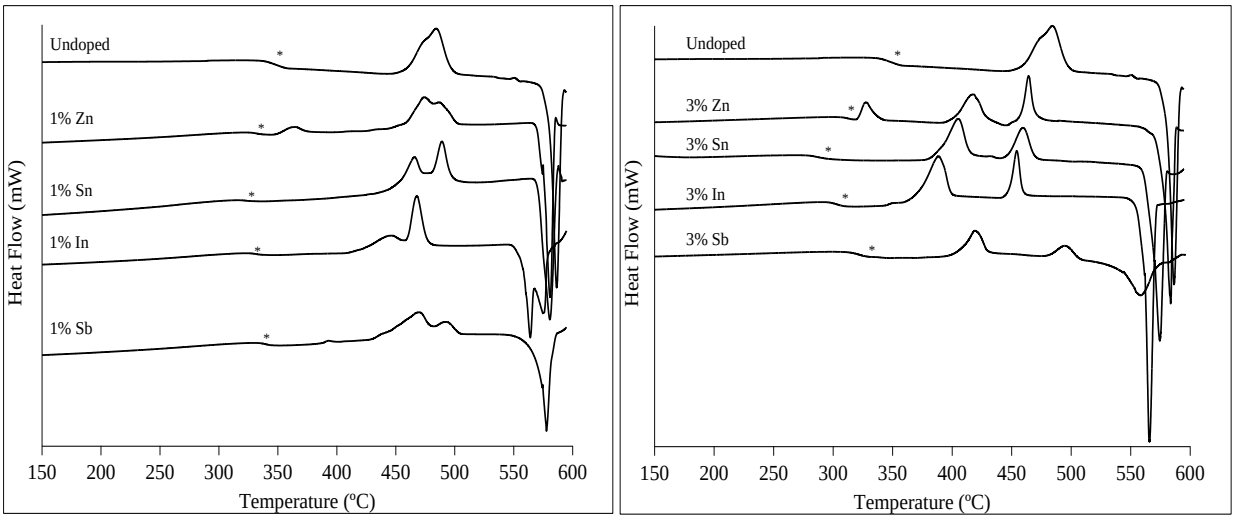
Undoped
1% Zn
1% Sn
1% In
1% Sb
Heat Flow (mW)
150 200 250 300 350 400 450 500 550 600
Temperature (ºC)
Undoped
3% Zn
3% Sn
3% In
3% Sb
Heat Flow (mW)
150 200 250 300 350 400 450 500 550 600
Temperature (ºC)

Figure 1.

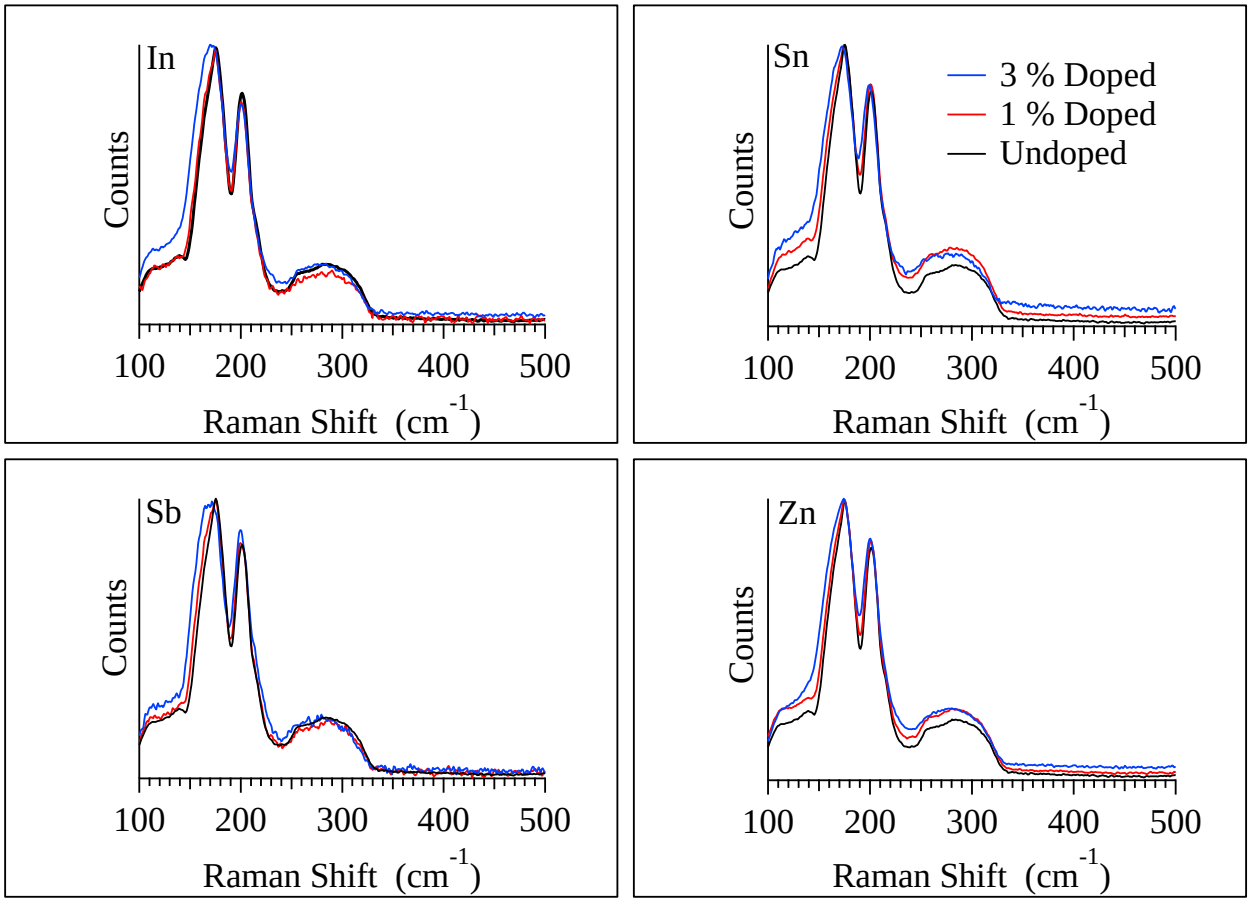
In
Sn
Sb
Zn
Counts
Raman Shift (cm-1)
100
200
300
400
500
3 % Doped
1 % Doped
Undoped

Figure 2.

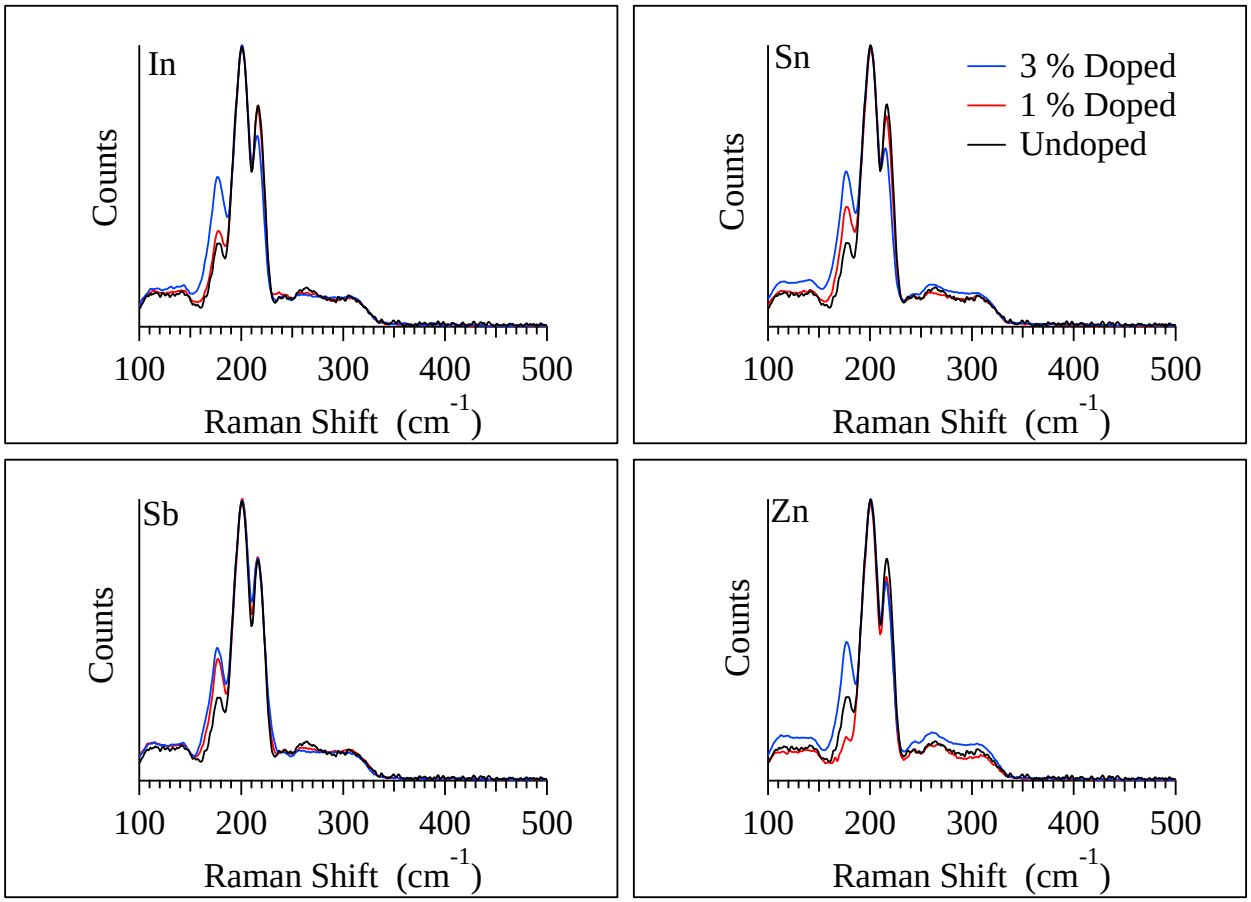
In
Sn
Sb
Zn
Counts
Raman Shift (cm-1)
100
200
300
400
500
3 % Doped
1 % Doped
Undoped

Figure 3.

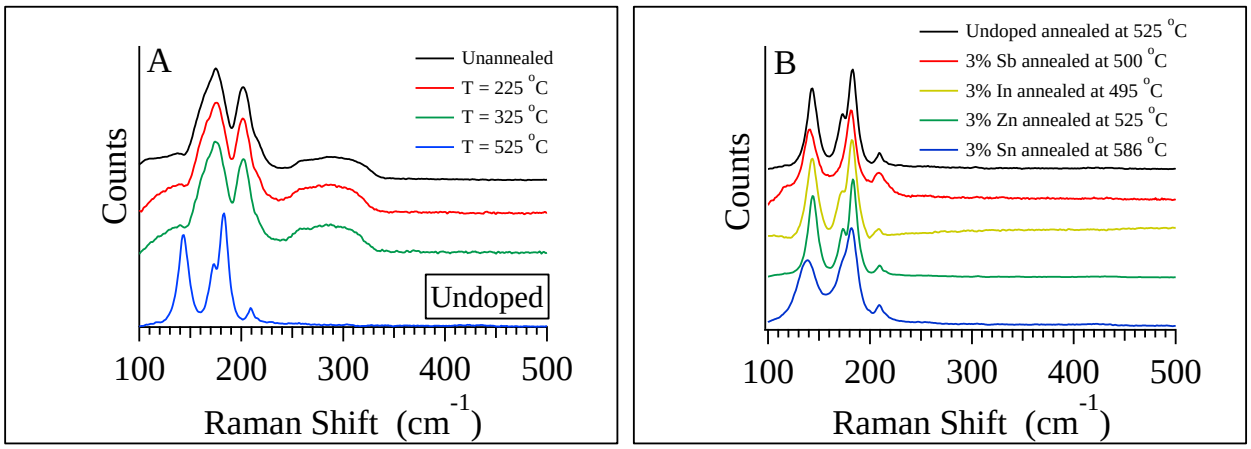
A
Unannealed
T = 225 °C
T = 325 °C
T = 525 °C
Undoped
Counts
100
200
300
400
500
Raman Shift (cm-1)
B
Undoped annealed at 525 °C
3% Sb annealed at 500 °C
3% In annealed at 495 °C
3% Zn annealed at 525 °C
3% Sn annealed at 586 °C
Counts
100
200
300
400
500
Raman Shift (cm-1)

Figure 4.

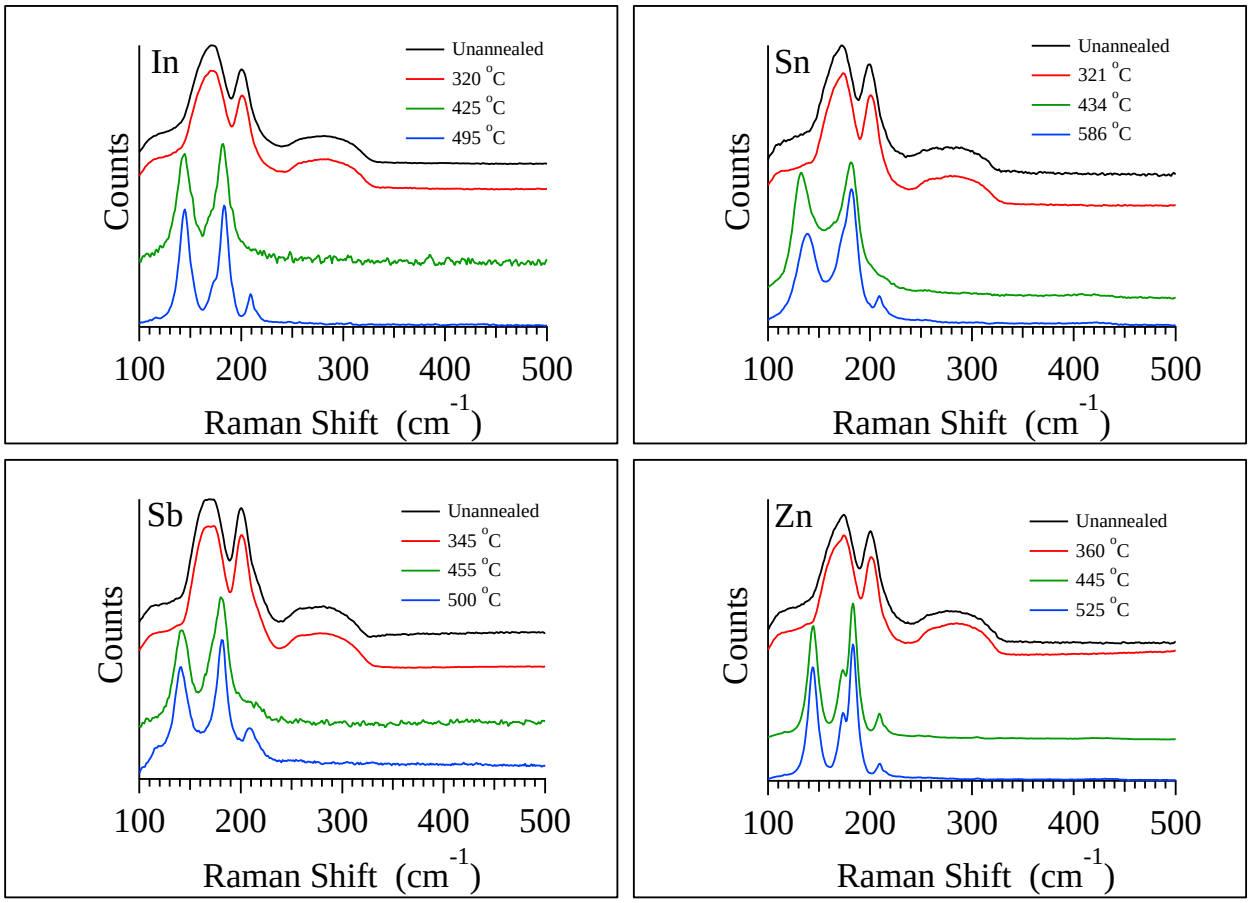
In
Unannealed
320 °C
425 °C
495 °C
Counts
100
200
300
400
500
Raman Shift (cm-1)
Sn
Unannealed
321 °C
434 °C
586 °C
Counts
100
200
300
400
500
Raman Shift (cm-1)
Sb
Unannealed
345 °C
455 °C
500 °C
Counts
100
200
300
400
500
Raman Shift (cm-1)
Zn
Unannealed
360 °C
445 °C
525 °C
Counts
100
200
300
400
500
Raman Shift (cm-1)

Figure 5.

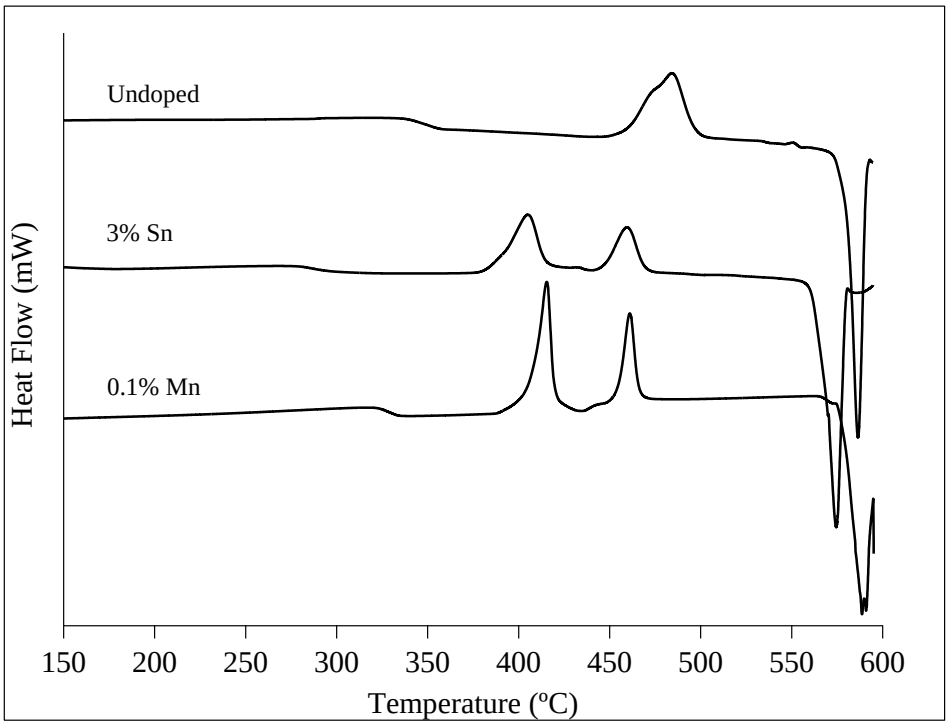
Undoped
3% Sn
0.1% Mn
Heat Flow (mW)
150
200
250
300
350
400
450
500
550
600
Temperature (ºC)

Figure 6.